Sensitivity of High Pressure Nozzle Guide Vane Capacity to Trailing Edge Cooling



Daniel Burdett

University College

University of Oxford

A thesis submitted for the degree of

Doctor of Philosophy

Hilary Term 2021

Acknowledgments

I am indebted to Prof. Tom Povey for his support, advice, and encouragement throughout the course of this work and indeed since I first arrived in Oxford as an undergraduate all the way back in 2011. I also have to thank Dr. Roderick Lubbock for teaching me many of the secret ways of experimentation, and especially Dominic Harris without whose technical expertise and problem solving in the workshop the work presented here simply would not have been possible. Finally, everyone at the lab who has provided that little bit of inspiration when it has been needed, or simply dragged me away from my desk when that too has been needed.

I am grateful to Rolls Royce for supporting the work presented in this integrated thesis.

The work presented in this integrated thesis is not substantially the same as any that I have submitted, or, is being concurrently submitted for a degree, diploma, or other qualification at the University of Oxford or any other University or similar institution. This integrated thesis consists primarily of a series of five journal papers. Whilst these papers are multi-authored, they are all substantially my own work as described after each paper. The submission status of these five papers is as follows:

1. *Analysis of ultra-low uncertainty gas turbine flow capacity measurement techniques*: Accepted for publication in Proceedings of the IMechE, Part A: Journal of Power and Energy, and published online on 8th March 2020 at https://doi.org/10.1177/0957650920909718.
2. *Understanding Capacity Sensitivity of Cooled Transonic Nozzle Guide Vanes: A Parametric Experimental and Computational Study of the Impact of Trailing Edge Geometry*: Accepted for publication in ASME Journal of Turbomachinery, and published online on 30th March 2021 at https://doi.org/10.1115/1.4050068.
3. *Analysis of averaging methods for non-uniform total pressure fields*: Submitted to ASME Journal of Turbomachinery (paper number TURBO-20-1403), currently in review.
4. *Experimental and numerical analysis of loss characteristics of cooled transonic nozzle guide vanes*: Submitted to ASME Journal of Turbomachinery (paper number TURBO-21-1040), currently in review.
5. *Impact of trailing edge overhang length on the loss characteristics of fully cooled transonic nozzle guide vanes*: Submitted to ASME Journal of Turbomachinery (paper number TURBO-21-1060), currently in review.

Abstract

High pressure (HP) nozzle guide vane (NGV) capacity is one of the most important parameters for setting overall turbine power output, for stage matching, and for understanding turbine performance. In accelerated engine development programmes in particular, accurate and early assessment of NGV capacity is a significant advantage. Whilst the capabilities of computational methods have improved rapidly in recent years, the accuracy of absolute capacity prediction capability is lower than experimental techniques by some margin. Thus, experimental measurement of NGV capacity is still regarded as an essential part of many engine programmes.

The semi-transient capacity measurement technique has been developed and refined at the University of Oxford over the last ten years. It allows rapid and accurate measurement of engine component (typically fully-cooled NGVs) capacity at engine-representative conditions of Mach number, Reynolds number, and coolant-to-mainstream pressure ratio. The technique has been demonstrated to offer considerable advantages over traditional (industrial steady-state) techniques in terms of accuracy, time and operating cost.

The present work describes in detail improvements made to the semi-transient method to optimise its uncertainty, and presents a detailed uncertainty analysis of the updated facility which is shown to achieve a bias uncertainty of ±0.495% (to 95% confidence) and a precision uncertainty of ±0.025%. The extremely low precision uncertainty in particular allows very small changes in capacity to be resolved. This, combined with rapid interchangeability of test modules, allows studies of the sensitivity of capacity to secondary influences with much greater flexibility than was previously possible.

In the present work, this capability is used to examine the effect of changing trailing edge (TE) geometry—particularly suction side (SS) TE overhang length—on the flow capacity. Experimental measurements and complementary numerical predictions of capacity are presented for four geometries bridging the gap between a classical *centred ejection* design and a *SS-overhang* design. A monotonic increase in capacity is observed as TE overhang length reduces, but with a greatly reduced gradient when overhang length becomes very short. Strong agreement was achieved between experiment and

CFD in terms of both absolute capacity prediction (average error of 0.67%) and capacity changes between TE geometries (average error of 0.20%).

Comprehensive examination is given to the fundamental mechanisms responsible for the observed capacity changes. Two models of the vane are proposed which describe the interactions between multiple controlling areas which can be defined from the physical geometry. Whilst these models are incomplete, they represent an important aspect of the changing flow interactions between different TE geometries and help to explain the change in flow behaviour when overhang length becomes very short. Further insight is gained by studying the area and static pressure changes at several controlling areas, although this approach is demonstrated to be somewhat arbitrary. Whilst the capacity trend *can* be explained by considering particular controlling areas in this way, a more complete system description is provided by holistically analysing the aerodynamic change in the entire *controlling region* of the vane passage.

The SS-overhang TE design has generally been favoured by HP NGV designers in recent years because it has been presumed to be aerodynamically advantageous on account of providing a thinner ultimate TE than the equivalent centred ejection geometry (at the cost of increased cooling requirement for the overhanging length). The prior literature is not in consensus on this point, however, and so the present work re-examines the impact of TE overhang length on NGV aerodynamic loss characteristics.

High-fidelity experimental traverse measurements downstream of the HP NGV cascade are presented, and compared against steady and unsteady RANS CFD predictions. This is a highly useful data set for benchmarking typical CFD methods for absolute loss prediction of cooled engine components. URANS CFD under-predicts the rate of mixing out of the non-uniform flow-field, and significantly over-predicts the profile loss coefficient in a particular axial plane by an average of 17.9%. The agreement for mixed-out loss coefficient is much better, differing by just 4.0%. Detailed examination is given to local distributions of loss coefficient. A significant feature of the experimentally-measured flow-field is a radial non-uniformity caused by internal cooling features within the TE slot. This sort of effect would be very difficult to detect without testing engine components. Significant differences in local loss coefficient distributions between different radial

sections are also observed due to the 3D shaping (lean, sweep, turning) of the engine component geometry. Analysis of the development of these distributions provides the basis for a model of wake profile decay based on streamwise path length.

Detailed analysis of aerodynamic loss measurements are then brought together with comparison of the parametric set of TE designs with four different TE overhang lengths. Unsteady pressure fluctuations in the wake predicted by URANS CFD show a large rise in magnitude, and fall in shedding frequency, when overhang length becomes short. This is attributed to a change in shedding mode from one in which small vortices are shed at relatively high frequency from the overhanging SS TE, to one in which larger vortices are shed at lower frequency from the entire base region. Experiment and CFD are largely in agreement regarding the trend in mixed-out average loss coefficient, corrected for changes in TE thickness, between TE geometries: loss coefficient gradually rises before plateauing at short overhang length. However, the experimental data show an additional large increase in loss coefficient at intermediate overhang length which is not predicted by URANS. This discrepancy is attributed to the shedding of pressure waves associated with vortex shedding in the transonic range, which is not captured in the CFD simulations (a known limitation of the URANS method). Analysis of the base region pressure distributions predicted by URANS shows that the PS base region pressure falls substantially with reducing overhang length, whilst the SS base pressure is almost insensitive to overhang length. The differing behaviours of the PS and SS base regions are explained by interactions with changes in the entire vane aerodynamic at their different locations. There does not seem to be a simple relationship between changes in base region pressure and loss coefficient, suggesting that the overall loss trend cannot be understood without studying the aerodynamic change in the entire passage more holistically.

The experimental and numerical study of NGV aerodynamic loss characteristics presented in this work additionally provided the opportunity to consider a more fundamental aspect of performance evaluation in complex 3D flows. Performance parameters such as total pressure or kinetic energy loss coefficients can be represented in various different ways ranging from line and plane averages to fully mixed-out values. There are further considerations to be made for each of these representations such as

weighting methods, mixing methods and so forth. The present work analyses the sensitivities of a range of different representations of performance parameter to axial measurement location, radial averaging range, and exit Mach number, in order to provide guidance on the accuracy of each method in a relevant, practical application. In particular, the area-weighted-average, despite its simplicity (which makes it a common choice in the literature), is demonstrated to be strongly sensitive to axial plane which makes it an extremely poor choice for comparing between CFD and experiment or between different experiments.

Contents

1 Introduction and Thesis Outline **1**

1.1 Cooled trailing edge design and trailing edge overhang length 2

1.2 Introduction to nozzle guide vane capacity 4

1.3 Introduction to nozzle guide vane efficiency and aerodynamic loss 7

1.4 Research objectives 11

2 Review of Related Literature **13**

2.1 Nozzle guide vane capacity measurement techniques and influencing factors 13

2.2 Nozzle guide vane aerodynamic performance and sensitivity to trailing edge cooling 19

2.2.1 Introduction to nozzle guide vane efficiency and loss 19

2.2.2 Representation and evaluation of loss coefficient 21

2.2.3 Relationship between trailing edge loss and total loss 26

2.2.4 Influence of trailing edge coolant ejection on trailing edge loss 29

2.2.5 Relationship between base pressure and trailing edge loss 31

2.2.6 Trailing edge flow in transonic turbine cascades 34

2.2.7 Unsteady behaviour of turbine wakes 35

2.3 Cooled trailing edge geometries 39

2.3.1 Analysis of trailing edge cooled nozzle guide vane performance and sensitivity of loss coefficient to trailing edge blowing rate 40

2.3.2 Comparisons of different trailing edge geometries 47

2.3.3 Summary of cooled trailing edge literature 54

2.3.4 Other recent developments in cooled trailing edge geometry 55

2.4 Studies of nozzle guide vane aerodynamic performance in high-TRL experimental environments 56

2.5 Reference list for literature review 61

3 **Analysis of Ultra-low Uncertainty Gas Turbine Flow Capacity Measurement Techniques** **67**

3.1 Introduction 68

3.2 Experimental facility 70

3.3 Vane module construction and sealing 71

3.4 Mass flow rate measurement 74

3.5 Mass flow rate unsteady correction 74

3.6 Inlet total pressure and temperature measurement 75

3.7 Exit static pressure measurement 75
3.8 Capacity definition for fully cooled nozzle guide vanes 76
3.9 Evaluation of vane capacity characteristic 80
3.10 Evaluation of bias uncertainty in capacity measurement 81
3.11 Summary of uncertainties and comparison to original and proposed upgraded facilities 89
3.12 Conclusions 90
3.13 References 91
3.14 Appendix I: Propagation of uncertainty in a simple summation 92

4 Understanding Capacity Sensitivity of Cooled Transonic Nozzle Guide Vanes: A Parametric Experimental and Computational Study of the Impact of Trailing Edge Geometry 96
4.1 Introduction 96
4.2 Experimental capacity measurement 98
4.3 Variation of trailing edge geometry 99
4.4 Numerical method 100
4.5 Experimental and numerical capacity characteristics 101
4.6 Analysis 102
4.6.1 Analysis of coolant stream capacity changes 102
4.6.2 Analysis of changes in surface boundary layer profiles due to aerodynamic changes 102
4.6.3 Simplistic analysis of vane total pressure loss 103
4.6.4 Incomplete models of the controlling region 103
4.6.5 Analysis of the aerodynamic flow field in the controlling region 104
4.7 Summary and conclusions 109
4.8 Appendix A: Changes in vane capacity due to changes in coolant stream capacities 110
4.9 Appendix B: Changes in passage mass flow deficit due to changes in surface boundary layer profiles 111
4.10 Appendix C: Application of simplistic area-total pressure loss model 111
4.11 References 114
4.12 Addendum: Specification of mass flow inlet boundary conditions for film and TE slot coolant flows 115

5 Analysis of Averaging Methods for Non-Uniform Total Pressure Fields 118
5.1 Introduction 118

5.2 History of total pressure performance parameters, averaging and mixing methods 119
5.3 Definitions for averaging and mixing methods 120
5.4 Experimental measurement process 122
5.5 Numerical method 123
5.6 Comparison of averaging methods 123
5.6.1 Plane-average weighting functions 124
5.6.2 Sensitivity to radial averaging range 127
5.6.3 Comparison of plane-average and mixed-out methods 128
5.6.4 Effect of Mach number 129
5.7 Summary and conclusions 130
5.8 References 131

6 Experimental and Numerical Analysis of Loss Characteristics of Cooled Transonic Nozzle Guide Vanes 135
6.1 Introduction 135
6.2 Overview of experimental facility 136
6.3 Instrumentation and measurement process 137
6.4 Numerical methods 138
6.5 Definitions of loss coefficient and efficiency 139
6.6 Experimental and computational results 140
6.7 Sensitivity of loss coefficient to exit Mach number 149
6.8 Summary and conclusions 150
6.9 References 152
6.10 Appendix A: Methods for distinguishing profile and endwall loss coefficients 156

7 Impact of trailing edge overhang length on the loss characteristics of fully cooled transonic nozzle guide vanes 160
7.1 Introduction and literature review 160
7.2 Overview of experimental facility 162
7.3 Instrumentation and measurement process 163
7.4 Loss coefficient definitions 163
7.5 Trailing edge geometries 164
7.6 Numerical method 164
7.7 Unsteady behaviour of numerical results 165
7.8 Local loss coefficient distributions 166
7.8.1 Sensitivity of secondary flow cores to trailing edge geometry 168

7.8.2 Radial profiles of kinetic energy loss coefficient and whirl angle 168
7.9 Analysis of wake circumferential profiles 171
7.10 Analysis of wake mixing rate 172
7.11 Analysis of overall aerodynamic performance 174
7.12 Boundary layer loss, base pressure and vortex shedding mechanisms 175
7.12.1 Boundary layer loss 175
7.12.2 Base pressure drag 175
7.12.3 Vortex shedding mode and transonic vortex shedding 177
7.13 Conclusions 177
7.14 References 179
7.15 Appendix A: Method for loss coefficient scaling to account for trailing edge thickness 180

8 Discussion and conclusions 186
8.1 Analysis of ultra-low uncertainty gas turbine flow capacity measurement techniques 186
8.2 Impact of trailing edge geometry on the flow capacity of transonic turbine nozzle guide vanes 188
8.3 Analysis of averaging methods for non-uniform total pressure fields 192
8.4 Experimental and numerical analysis of loss characteristics of cooled transonic nozzle guide vanes 196
8.5 Impact of trailing edge overhang length on the loss characteristics of fully cooled transonic nozzle guide vanes 199

List of Figures

2 Review of Related Literature

Figure 2.1 (a) Predicted capacity characteristics for two vanes of different loading distributions, compared against the 1D isentropic characteristic; contours of Mach number in the controlling region of the vane passage for (b) forward-loaded vane; and (c) aft-loaded vane. 15

Figure 2.2 (a) CFD-predicted capacity characteristic for an uncooled vane; predicted Mach number contours through the vane passage for (b) uncooled and (c) cooled vanes. 17

Figure 2.3 h-s charts showing the expansion process across an NGV row for: (a) uniform exit static pressure (linear cascade situation); (b) radial profile of exit static pressure (annular cascade situation). 21

Figure 2.4 Diagram of key planes in the process of determining mixed-out loss coefficients for a turbine cascade. 23

Figure 2.5 Diagram of the secondary flow structure of a turbine NGV cascade. 27

Figure 2.6 Contributions to total profile loss coefficient as functions of exit Mach number, for a Reynolds number of 10^6 29

Figure 2.7 (a) Turbine trailing edge shock structure in supersonic flow; (b) schematic illustration of vortex formation and shedding in the wake of a bluff body. 36

Figure 2.8 Schlieren image of a vortex sheet shed from a solid, round TE at a nominal exit Mach number of 0.65. 37

Figure 2.9 Diagrams of basic cooled trailing edge geometries. 39

Figure 2.10 Normalised trends in KE loss coefficient with TE coolant-to-mainstream mass-flux ratio, for different TE overhang lengths. 52

Figure 2.11 Normalised trends in KE loss coefficient with TE slot blowing rate for different TE designs, at an exit Mach number of 0.97. 54

3 Analysis of Ultra-Low Uncertainty Gas Turbine Flow Capacity Measurement Techniques

Figure 3.1 Schematic diagram of the capacity test core installed in the Oxford ECAT test bed. 71

Figure 3.2 Pressure (a), temperature (b), and vane pressure ratio (c) characteristics during a typical blowdown run. 71

Figure 3.3 De-featured section schematic of the vane module assembly showing potential leak paths and associated wet seal locations. The main components are: (1)

case front support ring; (2) case rear mount ring; (3) hub front support ring; (4) hub rear mount plate. 72

Figure 3.4 (a) Coolant capacity characteristics measured in dynamic leak tests in four ECAT test campaigns over a 12-month period, compared against bench-test data; (b) percentage standard deviation between different ECAT test sets, and percentage difference between ECAT and bench-test data. 73

Figure 3.5 (a) Overall mass flow rate characteristics for a typical blowdown test (rescaled to an arbitrary maximum of 19.0 kg s^{-1}); (b) overall mass accumulation rate in intermediate plena. 75

Figure 3.6 Locations of inlet condition measurements for mainstream and coolant flows, viewed from downstream. 75

Figure 3.7 Simplified view of a vane pair exit platform instrumented with eight static pressure tappings per passage. 75

Figure 3.8 Example of a typical measured circumferential static pressure profile on three instrumented vane pair platforms. The *x*-axis represents the tapping locations shown in Figure 3.7. 76

Figure 3.9 Schematic of a typical HP vane cooling system mainstream flow (1), film cooling flow (2), and trailing edge coolant flow (3). 76

Figure 3.10 Schematic diagram of the fully mixed, multi-stream, single controlling area model. 77

Figure 3.11 Schematic diagram pf the unmixed, multi-stream, multiple controlling area model. 78

Figure 3.12 Surface of capacity, as a function of both vane pressure ratio, p_{exit}/p_{01}, and coolant-to-mainstream pressure ratio, p_{02}/p_{01}. The sensitivity to p_{02}/p_{01} has been exaggerated by a factor of 10. 78

Figure 3.13 Schematic diagram of a hybrid model involving fully mixed mainstream and film cooling flows (1, 2) and unmixed trailing edge coolant (3). 79

Figure 3.14 Contours of percentage difference in capacity defined according to equations (4) and (9), as a function of coolant-to-mainstream mass flow ratio and temperature ratio. 79

Figure 3.15 Contours of percentage difference in capacity defined according to equations (7) and (9), as a function of coolant-to-mainstream mass flow ratio and mainstream-to-coolant temperature ratio. 79

Figure 3.16 (a) Capacity characteristics from a typical HP NGV showing 17 repeat runs, and the mean-line trend; (b) number of repeat tests conducted as a function of p_{exit}/p_{01}; (c) standard deviation and precision uncertainty in the mean capacity trend. 81

Figure 3.17 CFD-predicted circumferential static pressure profiles at vane exit (single axial position) for a range of operating pressure ratios. 85
Figure 3.18 CFD-predicted variation in circumferentially-averaged pressure ratio as a function of axial interrogation plane for a range of p_{exit}/p_{01}. 85
Figure 3.19 Normalised maximum difference between the underlying circumferentially-averaged pressure, and the average pressure as measured by a particular number of evenly-spaced circumferential sample points. Each line represents a different number of sample points. 86
Figure 3.20 Normalised credible interval for average pressure measured by a particular number of—nominally—evenly-spaced circumferential sample points subject to random spatial variation of ±1.5 mm both axially and circumferentially. Results are for a single instrumented platform. Each line represents a different number of samples. 87
Figure 3.21 Bias uncertainty in p_{exit} from each of the three principal sources, along with the overall bias uncertainty, as functions of p_{exit}/p_{01}. Dashed and solid lines represent the uncertainties associated with single platform and 12 platform measurements, respectively. 88
Figure 3.22 Contours of the sensitivity coefficients S_1 (defined in equation (17)) and S_2 (defined in equation (20)) as functions of p_{exit}/p_{01} and p_{02}/p_{01}. 88
Figure 3.23 Visualisation of the propagation of bias uncertainty through to the final capacity measurement, for each of the three considered facilities. 90
Figure 3.24 Percentage uncertainty in the sum of two variables, x and y, as a function of the relative sizes and relative percentage uncertainties of x and y. 92

4 Understanding Capacity Sensitivity of Cooled Transonic NGVs: A Parametric Experimental and Computational Study of the Impact of Trailing Edge Geometry

Figure 4.1 Simplified diagram of a meridional cross-section through the ECAT facility working section. 98
Figure 4.2 Trends from a typical experiment of (a) mass flow rates; (b) vane exit-static to inlet-total pressure ratio. 98
Figure 4.3 Diagram showing the four tested TE geometries. The inset in the top-left shows the context of the full vane. l is the baseline SS-overhang length. 99
Figure 4.4 Diagram of the NGV cascade assembly with ground steel fixtures. 99
Figure 4.5 TE thickness and passage width parameters. 100
Figure 4.6 Geometry for 3D numerical simulations. 100
Figure 4.7 Normalised vane capacities for CFD solutions with 18 M, 33 M, and 57 M cells. 100

Figure 4.8 Midspan section through the mesh for Geometry 1. 100
Figure 4.9 Detail of the midspan sections through TE region meshes. 101
Figure 4.10 Experimental capacity characteristics (solid lines) and CFD-predicted capacity (single points) for each TE geometry, normalised with respect to Geometry 1 at the design condition (p_{exit}/p_{01} = 0.542). 101
Figure 4.11 Percentage capacity changes between Geometries 1–2, 1–3, and 1–4 as functions of vane pressure ratio. 101
Figure 4.12 Change in vane capacity relative to Geometry 1 as a function of TE overhang length, for p_{exit}/p_{01} = 0.542. 102
Figure 4.13 Schematic diagrams representing models (a) (common controlling area) and (b) (independent controlling areas). 103
Figure 4.14 Contours of Mach number in a section through the controlling region of the vane passage at the midspan radius for each TE geometry. The M = 1.0 contour is highlighted in red. The locations of the w_{PS} and w_{SS} areas are indicated by dashed lines. 104
Figure 4.15 Normalised vane surface isentropic Mach number distributions at midspan, for each TE geometry. 105
Figure 4.16 Contours of Mach number in planes w_{PS} and w_{SS} for each TE geometry. 106
Figure 4.17 Contours of normalised total pressure in planes w_{PS} and w_{SS} for each TE geometry. 106
Figure 4.18 Midspan profiles in planes w_{PS} and w_{SS} of: (a) normalised total pressure; (b) normalised static pressure; (c) Mach number; (d) whirl angle; (e) deviation angle; (f) normalised local capacity; and schematics of: (g) controlling areas; and (h) angle definitions. 107
Figure 4.19 Change in non-dimensional local capacity, J', as a function of cross-passage location for each geometry. 108
Figure 4.20 Streamlines in a midspan section for (a) Geometry 1 and (b) Geometry 3. 109
Figure 4.21 Mainstream (a) and coolant (b) capacity terms for each TE geometry, normalised with respect to the experimental overall capacity for Geometry 1 at the design pressure ratio. 110
Figure 4.22 Normalised PS and SS boundary layer velocity profiles in the w_{PS} plane at midspan for each TE geometry. 111
Figure 4.23 SS and PS boundary layer displacement thicknesses as functions of wall-normal integration height, y, for each TE geometry. 111
Figure 4.24 Schematic diagram of the *repeating area unit*. 112
Figure 4.25 Experimentally-measured and CFD-predicted circumferential profiles of local total pressure loss coefficient, at midspan, 0.50 C_x downstream of the TE. 112

Figure 4.26 Percentage change in circumferentially-averaged Y_p with respect to Geometry 1, as a function of TE overhang length. 113
Figure 4.27 Comparison of capacity changes predicted by quasi-2D model and those determined by CFD and experiment. 114

5 Analysis of Averaging Methods for Non-Uniform Total Pressure Fields

Figure 5.1 Tree of possible performance metric calculations. 119
Figure 5.2 *h-s* chart showing the simplified turbine expansion process. 120
Figure 5.3 Simplified diagram of an axisymmetric cross-section through the ECAT facility working section. 122
Figure 5.4 Locations of the three experimental axial traverse planes. 123
Figure 5.5 Example traverse blocking arrangement for a single area-survey. Six separate tests are represented by the six blocks. Dashed lines show the wake locations. 123
Figure 5.6 (a) CFD geometry; (b) midspan mesh cross-section. 123
Figure 5.7 Experimentally-measured and CFD-predicted local distributions of kinetic energy loss coefficient, ζ, in the axial planes: (a) $x/C_x = 0.25$, (b) $x/C_x = 0.50$, (c) $x/C_x = 0.75$. 124
Figure 5.8 Experimental and CFD weighting functions in axial plane 1 for: (a) area-weighting, (b) volume-flow-weighting, (c) mass-flow-weighting. 125
Figure 5.9 Normalised midspan weighting functions for each of the three in-plane averaging methods for experimental and CFD data at planes 1, 2, and 3. Dashed lines show approximate wake centre locations in each plane. 126
Figure 5.10 Circumferential distributions of whirl angle at midspan for experiment and CFD in planes 1, 2, and 3. Dashed lines show approximate wake centre locations in each plane. 126
Figure 5.11 CFD-predicted midspan contours of: (a) normalised total pressure; and (b) normalised static pressure. 127
Figure 5.12 Axial trends at midspan of: (a) peak value of ζ in the wake centre; (b) wake width; and (c) static pressure along the wake centreline and in the free-stream. 127
Figure 5.13 Mass-flow-weighted average ζ as a function of radial averaging range for experiment and CFD, in three axial planes. 128
Figure 5.14 Axial trends in $\overline{\zeta}$ based on average total pressure according to a number of methods, for experimentally-measured and CFD-predicted flows. 128
Figure 5.15 CFD-predicted plane-average and mixed-out KE loss coefficient, $\overline{\zeta}$, at $x/C_x = 1.00$, as functions of vane exit Mach number. 129
Figure 5.16 Variation of $\overline{\zeta}$ with axial distance for three exit Mach numbers: $M_2 = 0.76$, 0.97, and 1.11. 130

6 Experimental and Numerical Analysis of Loss Characteristics of Cooled Transonic Nozzle Guide Vanes

Figure 6.1 Axisymmetric cross-section schematic of the ECAT facility working section 136

Figure 6.2 (a) Vane exit-static to inlet-total pressure ratios during a typical regulated (steady-state) run. 137

Figure 6.3 Photographs of the traverse probe tips: (a) five-hole probe; (b) Pitot probe. 137

Figure 6.4 Schematic of experimental traverse planes and circumferential limits. 137

Figure 6.5 Typical traverse pattern for a steady-state area survey, showing six individual traverse sections. NGV wake locations are marked by bold dashed lines. 138

Figure 6.6 Typical traverse patterns for a blowdown midspan circumferential traverse: (a) in (θ, r)-space; (b) in (θ, M_2)-space, showing two runs. Wake locations are marked by dashed lines. 138

Figure 6.7 Geometry for CFD simulations. 138

Figure 6.8 Section through the mesh at midspan. 139

Figure 6.9 Detail of TE slot internal cooling geometry. 139

Figure 6.10 Local distributions of KE loss coefficient, ζ', from experiment and cooled URANS in planes 1, 2, and 3. 141

Figure 6.11 Comparison of case ((a)–(c)) and hub ((d)–(f)) secondary loss cores between experiment, cooled RANS, and cooled URANS. 141

Figure 6.12 Circumferential profiles of ζ' extracted from experimental traverse measurements at planes 1–3 at: (a) 75% span; (b) 50% span; (c) 25% span. 142

Figure 6.13 Comparison of midspan circumferential profiles of ζ' between experiment and three CFD methods at: (a) plane 1; (b) plane 2; and (c) plane 3. 143

Figure 6.14 Experimentally-measured radial profiles of circumferentially-mass-flux-averaged KE loss coefficient, ζ''', in three axial planes. 143

Figure 6.15 Radial profiles of circumferentially-mass-flux-averaged ζ''' for experiment and three CFD methods at plane 2. 144

Figure 6.16 Circumferential profiles of whirl angle at midspan for experiment and three CFD methods, in three axial planes. 145

Figure 6.17 Radial profiles of circumferentially-mass-flux-averaged flow turning angle, β, for: (a) experiment; and (b) cooled URANS, in three axial planes. 145

Figure 6.18 Circumferential variation of local KE loss coefficient in a 10% span range around midspan. 145

Figure 6.19 Axial trends in peak KE loss coefficient, $\widehat{\zeta'}$, at three spanwise locations, for experiment and two CFD methods. 146

Figure 6.20 Spanwise profiles of streamwise path length, *d*, between the local TE and each of planes 1, 2, and 3. 146
Figure 6.21 Trends in peak KE loss coefficient, $\widehat{\zeta'}$, at three spanwise locations, with local streamwise path length. 146
Figure 6.22 Trends in wake width, *w*, at three spanwise locations, as a function of local streamwise path length. 147
Figure 6.23 Trends in mass-flux-averaged KE loss coefficient, ζ'', at three spanwise locations as a function of local streamwise path length. 147
Figure 6.24 Axial trends of plane-average KE loss coefficient, ζ'', and mixed-out KE loss coefficient, ζ'''', for experiment and cooled URANS. 148
Figure 6.25 Circumferential profiles of ζ' at midspan in plane 1, at five different vane exit Mach number conditions. 149
Figure 6.26 Midspan trends in peak loss coefficient and wake width, with exit Mach number. 150
Figure 6.27 Circumferentially-mass-averaged KE loss coefficient, ζ'', at midspan in plane 3, as a function of M_2. 150
Figure 6.28 *h-s* charts showing the expansion process for: (a) uniform exit static pressure; (b) radial profile of exit static pressure. 154
Figure 6.29 Sensitivity of ζ to both p_2/p_{01} and p_{02}/p_{01} in typical ranges. 155
Figure 6.30 Illustrations of methods for defining profile and endwall integration regions: (a) tight boundaries around specific features; (b) remaining plane area included in the profile-loss integral region; (c) simple radial limits. 157
Figure 6.31 Axial trends of profile and endwall components of KE loss coefficient, evaluated using each of methods (a)–(c). 157

7 Impact of Trailing Edge Overhang Length on the Loss Characteristics of Fully Cooled Transonic Nozzle Guide Vanes

Figure 7.1 Schematic of the NGV ring and measurement planes. 163
Figure 7.2 Diagram showing the vane (top left), and a magnified view of the four TE geometries. The SS-overhang length for Geometry 1 is marked *l*. 164
Figure 7.3 (a) CFD geometry; (b) midspan mesh cross-section for Geometry 1; (c) near-TE mesh detail for all geometries. 165
Figure 7.4 Wake pressure fluctuations for each of the four geometries at three span locations characterised by: (a) normalised RMS magnitude; and (b) Strouhal number. 166
Figure 7.5 Midspan URANS CFD snapshots for Geometries 1 and 4 showing: (a–b) contours of local KE loss coefficient, ζ', in the wake region; (c–d) contours of

λ_2-criterion in the wake region; (e–f) schematic diagrams of vortex street layouts. 166
Figure 7.6 Experimental distributions of local KE loss coefficient, ζ', in plane 1 ($x/C_x = 0.25$) for each TE geometry. 167
Figure 7.7 CFD distributions of local KE loss coefficient, ζ', in plane 1 ($x/C_x = 0.25$) for each TE geometry. 167
Figure 7.8 The wake-endwall junction regions at hub and case for all four TE geometries in experiment (a–h) and CFD (i–p). 169
Figure 7.9 Radial profiles of circumferentially-mass-flux-averaged KE loss coefficient, $\zeta''(r)$, in plane 2. 170
Figure 7.10 Radial profiles of circumferentially-mass-flux-averaged whirl angle, β, in plane 2. 170
Figure 7.11 Circumferential profiles of local loss coefficient, ζ', compared between the four TE geometries at 25%, 50%, and 75% span in plane 1: (a–c) experiment; (d–f) URANS CFD. 171
Figure 7.12 Circumferential profiles of whirl angle at midspan in plane 1 from: (a) experiment; (b) URANS CFD. 172
Figure 7.13 Peak KE loss coefficient, $\widehat{\zeta'}$, at midspan as a function of true axial distance. 173
Figure 7.14 Wake width, w, at midspan as a function of true axial distance. 173
Figure 7.15 Circumferentially-mass-flow-averaged KE loss coefficient, ζ'', at midspan as a function of true axial distance. 173
Figure 7.16 Plane-average and mixed-out average KE loss coefficients in the profile loss region, normalised with respect to ζ_1'''' (data from plane 3). 174
Figure 7.17 Midspan base pressure distributions. 176
Figure 7.18 (a) Normalised average base region pressures; (b) base pressure coefficients. 176
Figure 7.19 (a) Control volume for the wake mixing process occurring downstream of a staggered cascade with a solid TE; (b) control volume for the wake mixing process occurring downstream of a staggered cascade with a TE slot; (c) inset diagram of the TE geometry for the control volume in (b). 181
Figure 7.20 Normalised KE loss coefficient as a function of t_{SS}, for each TE geometry. 183

1 Introduction and Thesis Outline

The high pressure (HP) turbine operates at the most extreme conditions of high total pressure and total temperature in the gas turbine engine. This presents unique challenges in the design of the first stage nozzle guide vanes (NGVs). In modern engines, the flow temperature at entry to the HP NGV row is significantly above the melting temperature of the NGV base material. This means that cooling of the vanes is essential for them to survive to an acceptable lifetime. Cooling is inevitably accompanied by an efficiency penalty because coolant air is generally taken from the HP compressor—it does not pass through the combustor and HP turbine main gas path (reducing the potential work output), and must be reintroduced into the main flow with associated mixing loss. The wakes generated at this point in the engine proceed to pass through the subsequent downstream blade rows, having additional impacts on the efficiency of the expansion processes. In this work, the performance of cooled HP NGV engine parts is studied in terms of both *capacity*, and *efficiency* (expressed as a loss coefficient). Each of these two aspects is introduced shortly.

A lot of the previous research into turbine blade row performance has been conducted in relatively simple cascade experiments, particularly in academic studies focussed on developing fundamental understanding of specific flow features. They often: use simplified vane geometries (not engine components, often lacking endwall fillets or other 3D vane shaping typical of modern engine parts); use linear or annular sector cascade geometries containing a small number of blades; omit surface film cooling and trailing edge cooling features; and may not operate at representative conditions of Mach number, Reynolds number or inlet turbulence parameters. Simple experiments of this kind offer advantages including a low cost of operation and allowing much denser and more specialised instrumentation for closer examination of specific flow features of interest. However, they of course have the trade-off of being less representative of the engine environment. In contrast, high technology readiness level (TRL) experiments (for example testing actual engine parts with representative operating conditions and boundary conditions) capture a multitude of complex flow features and interactions which are not present in simpler

experimental setups. On the other hand, they come with significant associated operating expense and often have limited scope for instrumentation—making them less suitable for visualising and understanding fundamental flow structures. Performing high-TRL experiments is an important part of the research process, both for testing conclusions drawn from much simpler experiments in a more representative environment, and for calibrating and validating numerical prediction models.

All of the work presented in this thesis originates from an experimental test programme conducted using the Engine Component Aerothermal (ECAT) facility at the University of Oxford, and complimentary CFD simulations. The ECAT facility is a high-TRL blowdown facility containing a full-annular cascade of engine parts (in this case fully cooled HP NGVs) operated at non-dimensionally engine-representative conditions of Mach number, Reynolds number and coolant-to-mainstream total pressure ratio. It has capabilities for making capacity, aerodynamic loss, and metal effectiveness measurements of the vane cascade. The first two of these capabilities are utilised in the present research. The ECAT facility has a unique modular construction, which allows for rapid interchange of the NGV cascade working section. This feature lends the capability to perform back-to-back tests of engine parts with small geometrical differences, and identify and analyse the changes in performance. In the present research this capability is used to compare the performance of a series of incrementally-varying trailing edge overhang lengths on a single set of HP NGV engine components.

1.1 Cooled trailing edge design and trailing edge overhang length

Trailing edge overhang length (describing the distance which the suction side trailing edge extends downstream of the pressure side trailing edge, also often referred to as pressure side cutback length) is a key aspect of the HP NGV passage geometry. It affects the flow separation at the trailing edge, the formation of free shear layers, the interaction between the mainstream flows on either side of the trailing edge and the trailing edge coolant flow, and the unsteady nature of the wake region. We can therefore see that both NGV capacity and aerodynamic performance will be sensitive to trailing edge overhang length.

Most early cooled trailing edge designs tended to have a centred-ejection design (a slot located centrally within the trailing edge with no overhanging material on either side). More recent engine designs have favoured trailing edge geometries with a suction side overhang, as they are generally thought to offer aerodynamic advantages by presenting a thinner ultimate separated trailing edge region (or base region). However, the literature is not in consensus on this point (as will be shown in the following literature review). To further confuse matters, there is more recent evidence suggesting that shorter overhangs may offer both aerodynamic and thermal advantages at low-transonic Mach numbers. This has become more relevant as designers consider the possibility of twin-HP turbines, with HP NGV exit Mach numbers in the range 0.8 to 0.9 (compared to the typical value of 0.95). The lack of consensus in the existing literature is the primary motivation for more carefully re-examining and understanding the sensitivity of NGV aerodynamic loss to trailing edge overhang length. In addition, the trailing edge is highly susceptible to deterioration during the service lifetime of the NGV component. Impacts from foreign body particles passing through the engine core, for example, can result in damage to the trailing edge material. Damaged sections of trailing edge material are commonly removed deliberately across the whole of the vane span as part of the repair process of damaged in-service components, in order to mitigate the effects of such deterioration. A secondary motivation for the present work is to clarify the penalty (or otherwise) associated with this repair process.

The main themes of the five papers included in this integrated thesis are split broadly into two sections. The first two papers focus on NGV capacity: firstly, a review and discussion of improvements made to the experimental capacity measurement technique; and secondly a study of the sensitivity of capacity to changes in trailing edge overhang length. The last three papers focus on aerodynamic loss measurements of the NGV cascade: firstly, a comparison of different averaging methods for representing aerodynamic performance parameters in non-uniform, transonic flow-fields; secondly a detailed analysis of aerodynamic measurements downstream of the NGV cascade and comparison between experimental and numerical data; and thirdly a study of the sensitivity of aerodynamic loss measurements to changes in trailing edge overhang length.

1.2 Introduction to nozzle guide vane capacity

Capacity provides a non-dimensional measure of the mass flow rate passing through a nozzle. At its most simple, capacity can be defined as:

$$\Gamma = \frac{\dot{m}\sqrt{T_0}}{p_0} \tag{1}$$

where $\dot{m}$ is the mass flow rate, and p_0 and T_0 are the upstream total pressure and temperature, respectively. Although this is not a non-dimensional quantity, it is a useful formulation because it removes the primary sensitivities of mass flow rate to total pressure and temperature, and gives a parameter which at choked conditions can be thought of as a crude proxy for the effective area of the nozzle. Accurate assessment of NGV capacity (typically within 1%) is essential at an early stage in the engine design process, as it has a strong influence on turbine aerodynamic performance (incorrect assessment of NGV capacity can lead to mismatched turbine stages) and overall engine power output (incorrect prediction of the core mass flow rate).

Although high-fidelity numerical methods—using fully featured component geometries with finely resolved meshes—have improved rapidly in capability over recent years and are now routinely deployed for predicting NGV capacity, their accuracy for absolute capacity prediction remains considerably worse than experimental techniques, struggling to get within 1–2%. Thus, experimental measurement of NGV capacity is still regarded as an essential part of many engine programmes. The inaccuracy of numerical capacity predictions is due to the strong aerodynamic sensitivity to geometric features which are at the limit of the resolving capability of the CFD process, and also due to inadequacies in the numerical methods. It is perhaps unsurprising that, even with rapid advances in computational capabilities in recent years, first-time prediction of capacity to high accuracy is extremely challenging.

The purpose of experimentally measuring NGV capacity to ultra-high accuracy is therefore two-fold. Firstly, such experiments provide direct capacity evaluation of a particular vane, important for engine optimisation during the development programme. Secondly, building up a

bank of ultra-high accuracy experimental data provides a reference source for continual development and calibration of numerical capacity prediction methods.

A minimum requirement for ultra-high accuracy experimental evaluation of vane capacity is a fully annular cascade of real engine NGVs, operated at appropriate non-dimensional conditions of Mach and Reynolds numbers. Experimental capacity measurement has therefore generally been the domain of engine manufacturers (rather than academic researchers) due to the prohibitive expense of operating high-TRL (technology readiness level) facilities. Much of the effort on the part of engine manufacturers has naturally been aimed at direct validation of capacity for engine design optimisation, whilst studies designed to understand sensitivities to specific features (e.g. film cooling configuration, trailing edge shape and cooling, platform gaps and leakages, etc.), as well as efforts to minimise experimental uncertainty, have been rather limited.

Attempts to evaluate and understand the effects of secondary influences on capacity only add to the challenge of capacity measurement. The computational cost required to achieve accurate numerical absolute capacity prediction inevitably rises, due to the very fine mesh required to resolve small-scale geometric features which can disproportionately impact the aerodynamics (particularly around the critical trailing edge area), and the increased importance of capturing unsteady flow phenomena downstream of the trailing edge. When attempting to detect small capacity changes between different experiments, two additional considerations arise. First, the precision uncertainty of the experiment must be sufficiently low that the capacity change to be measured can be distinguished from the general run-to-run variation. Secondly, we must be confident that the detected capacity change is caused by the intended geometric or condition change, as opposed to another unintended difference in the cascade between the experiments. This requires very careful planning of the experimental test process.

In the first paper, the current state-of-the-art in experimental gas turbine capacity measurement is reviewed and analysed. Improvements to the semi-transient method of

experimental capacity measurement (first described by Povey et al.[1]) are detailed, including: the capability for rapid interchange of test vane modules; separate metering of the mainstream and coolant mass flow rates; and optimised cascade inlet and exit flow instrumentation. A comprehensive uncertainty analysis for capacity measurement is presented. The combination of ultra-low uncertainty vane capacity measurement and the ability to rapidly interchange test sections is an important development as it enables very small capacity changes between NGV cascades to be detected, and thus opens the way for studies of the sensitivity of vane capacity to secondary influences with much greater flexibility than has previously been possible. Consideration is also given to the most useful definition of vane capacity for the case of a cooled NGV (with mainstream and coolant flows at different inlet total pressure and temperature conditions).

In the second paper, the capability developed and analysed in the first paper is employed to study the sensitivity of NGV capacity to changing trailing edge geometry. A machining process is described which allows the trailing edge overhang length to be incrementally varied on a single set of engine HP NGV components, without removing the vanes from the test module or otherwise disturbing the geometry of the annular cascade. This unique experimental method enabled the changes in vane capacity between a series of four different trailing edge designs to be evaluated, in a parametric study bridging the gap between centred-ejection and overhang geometries. This represents a significant step in the understanding of capacity sensitivity to secondary geometric influences in the controlling region of the passage. The results presented in this paper provide validation of the numerical method for both absolute capacity prediction, and for the assessment of capacity changes with small geometric changes. Close examination of the results develops understanding of the fundamental mechanisms responsible for the observed shift in vane capacity with changing trailing edge overhang length. The capacity trend is primarily analysed by examining the local flow-field distributions through the controlling region of the vane passage. A

[1] Povey, T., Sharpe, M., Rawlinson, A.; 2011; Experimental Measurements of Gas Turbine Flow Capacity Using a Novel Transient Technique; ASME J. Turbomach., Vol. 133: 011005, DOI: 10.1115/1.4000481

pair of models of the controlling region are proposed which represent the two extremes of the trailing edge geometry variation (long overhang and centred-ejection). These models provide a framework which demonstrates a key aspect of the system dynamics. This is used to explain the change in flow behaviour as trailing edge overhang becomes short.

1.3 Introduction to nozzle guide vane efficiency and aerodynamic loss

In addition to capacity evaluation, experimental measurements of aerodynamic loss are made using a multi-hole pressure probe to traverse full-area-surveys in several axial planes downstream of the cascade trailing edge. Over many decades since the invention of the gas turbine engine, one of the major objectives in its continued development has been to drive up cycle efficiency, and in so doing drive down specific fuel consumption. This over-arching goal (increased overall engine efficiency) is contributed to by improvements in the efficiency of individual components (compressor and turbine stages and the combustion process), for example the HP NGV row.

Simple thermodynamics tells us that turbine efficiency can be increased by raising the gas inlet temperature. Turbine entry temperature has therefore continually increased over time, and in modern engines reaches approximately 2,000 K. This is well above the melting temperature of the NGV base material, making cooling of the vanes essential. In the engine, coolant air is drawn from the HP compressor just upstream of the combustor. It is removed from the mainstream gas flow, does not pass through the combustor, and therefore slightly reduces the potential work output from the turbine. In addition, mixing loss is generated as the coolant is re-introduced into the flow. Both of these effects are deleterious to efficiency.

The HP turbine has almost the most extreme conditions of total pressure and temperature in the entire engine, and the HP NGV row in particular has the highest cooling requirement of all blade rows. The HP rotor row has significantly lower cooling requirement due to the thermal time constant being sufficiently large that the blades cannot respond to the incident circumferential temperature variation, and the peak in the radial temperature traverse has been reduced in passing through the NGV row, with higher temperatures biased towards higher radii where stresses are lower. Hence the research interest in measuring aerodynamic performance of cooled HP NGVs

in particular. The aerodynamic performance of a vane row is commonly expressed using a loss coefficient. At a typical turbine stage efficiency of 95%, a 1% change in NGV total pressure loss (as a % of the loss) is equivalent to a 0.05% change in HP stage efficiency.

Trailing edge loss is one part of the total loss of the NGV row, arising due to the relatively blunt trailing edges of finite thickness, and the mixing process of the suction side and pressure side mainstream flows and the coolant flow downstream of the trailing edges. Further detail on this is included in the following literature review. Trailing edge loss typically accounts for around one third of total profile loss[2], and therefore represents a significant proportion of the aerodynamic performance of the NGV row. It is clear that the change in trailing edge geometry studied in the experimental and numerical test programmes in the present work will significantly impact the aerodynamics around the trailing edge region of the vane passage—including the relationship between the base pressures on each side of the trailing edge slot, and the mixing of the mainstream and trailing edge coolant flows—and consequently will significantly impact trailing edge loss and row efficiency.

In the third paper, various representations of aerodynamic performance parameter for the NGV cascade are considered. This study was an interesting and useful by-product of the detailed processing and analysis of the large dataset of non-uniform flow-field measurements obtained from the experimental test programme comparing different trailing edge geometries in an NGV cascade. The objective of this work was to demonstrate the sensitivity of the key data points presented elsewhere to processing steps and parameter definitions, and to analyse the impact of such sensitivities, which can often be overlooked in papers, on the conclusions drawn from aerodynamic performance measurements. The performance representations examined are line-average and plane-average loss coefficients based on different weighting functions for total pressure; and mixed-out loss coefficients using different mixing methods. The weighting method (e.g. area, volume flow or mass-flow-weighting) can sometimes be seen as a relatively minor

[2] Denton, J., Xu, L.; 1990; The Trailing Edge Loss of Transonic Turbine Blades; ASME J. Turbomach., Vol. 112(2): 277–285, DOI: 10.1115/1.2927648

concern, with many authors neglecting to even state which weighting method they used. In certain low-speed cases, or where measurements are made far downstream of the component, the flow will be relatively uniform and the practical difference between different weighting methods may be negligible. However, in high-speed applications or for measurements close to the trailing edge, this becomes increasingly unlikely. The different averaging methods are compared in terms of their sensitivities to: axial location of the measurement plane; radial averaging range; and exit Mach number. The observed sensitivities are explained through discussion of the underlying physical mechanisms which arise from the non-uniform exit flow-field.

In the fourth paper, detailed analysis of aerodynamic loss measurements for a single vane geometry are presented. These data address a gap in the literature for detailed aerodynamic traverse measurements downstream of actual engine parts, complete with film and trailing edge cooling flows. They also provide an important benchmark for high technology readiness level numerical predictions of high pressure NGV aerodynamic performance. The data are presented as: full-area surveys in three axial planes downstream of the NGV cascade; circumferential profiles of local loss coefficient at several radial heights; radial profiles of circumferentially-averaged loss coefficient and whirl angle; and fully mixed-out loss coefficient values. The level of agreement between experimental and numerical data for each loss coefficient representation, at a range of levels of fidelity in the numerical method (inclusion of cooling flows and unsteadiness) is considered. This aids in assessing the contribution of specific features of the CFD calculation to the disagreement with experiment. The impact of the engine-component NGV cascade geometry (profiles of lean, sweep and turning profile; and flow migration caused by the radial pressure gradient) on local loss coefficient distributions is carefully examined. The development of the wake flow characteristics (wake depth and width) with distance downstream of the cascade trailing edge is also analysed. This analysis provides a framework for studying wake mixing rates and determining the level of non-uniformity remaining in the flow at a specific downstream location.

In the fifth paper, the sensitivity of aerodynamic loss measurements to trailing edge geometry is examined by comparing experimental measurements and unsteady CFD predictions between the four trailing edge geometries (a range of SS-overhang lengths right up to a centred-ejection design). As noted above, this study aims to reconsider the evidence presented in the previously published literature (reviewed in the following section) regarding the impact of trailing edge geometry (and specifically overhang length) on aerodynamic performance. The performance of the four trailing edge geometries is compared in terms of average profile loss coefficient, local loss coefficient distributions, and wake mixing rates, and fundamental mechanisms responsible for the observed effects are discussed. This essentially brings together the performance analysis set out in the fourth paper, and the changes in cascade geometry and underlying flow-field examined in the second paper.

1.4 Research objectives

The primary objectives of the work presented in this integrated thesis were as follows:

1. Optimise the semi-transient method for experimental capacity measurement to drive down further the absolute uncertainty achieved. Consider and present a clear opinion on the most useful definition of vane capacity for a cooled NGV.
2. Develop an experimental process to incrementally vary the trailing edge overhang length of an annular cascade of engine component NGVs, without disassembling and rebuilding the cascade between back-to-back tests.
3. Present ultra-low uncertainty experimental capacity measurements for a series of different trailing edge overhang lengths on the same set of vanes. Compare the experimental data against CFD results to validate the numerical method for both absolute capacity prediction, and prediction of the capacity trend with varying trailing edge overhang length.
4. Examine and develop understanding of the fundamental aerodynamic changes in the controlling region of the vane passage which cause the changes in NGV capacity between different trailing edge geometries.
5. Compare the use of different averaging methods for representing aerodynamic performance parameters. Examine and understand the differing sensitivities of these averaging methods to the axial location of the measurement plane, radial averaging range, and exit Mach number.
6. Evaluate the agreement between experimental data and CFD predictions with various levels of fidelity (inclusion of cooling flows and unsteadiness) for aerodynamic performance measures of an engine-component HP NGV cascade (both local distributions and averaged values).
7. Analyse and understand the impact of engine-component NGV cascade geometry (combination of an annular cascade and 3D vane shaping) on the aerodynamic flow-field measured in a specific axial plane, and the development of the wake flow characteristics downstream of the NGV cascade.

8. Compare aerodynamic loss measurements (both local distributions and averaged values) between different trailing edge overhang lengths. Analyse and understand the fundamental mechanisms which give rise to the sensitivity of loss coefficient to overhang length.

2 Review of Related Literature

This section gives an overview of the previous literature which provided the foundation for the work presented in this thesis. It is split into two main areas: firstly NGV capacity measurement techniques and primary influencing factors on capacity; and secondly a general overview of the basics of NGV aerodynamic performance leading into a review of the effects of cooled trailing edge geometry on aerodynamic loss.

2.1 Nozzle guide vane capacity measurement techniques and influencing factors

Capacity is a non-dimensional parameter commonly defined for a particular nozzle as:

$$\Gamma = \frac{\dot{m}\sqrt{c_p T_{01}}}{p_{01} A} \tag{2}$$

where $\dot{m}$ is the mass flow rate of gas passing through the nozzle, A is the limiting flow area of the nozzle, p_{01} and T_{01} are the stagnation pressure and temperature conditions upstream of the nozzle, and c_p is the specific heat at constant pressure for the gas. Capacity is also commonly defined as:

$$\Gamma = \frac{\dot{m}\sqrt{T_{01}}}{p_{01}} \tag{3}$$

Although this is not a non-dimensional quantity, it is a useful formulation because it removes the primary sensitivities of nozzle mass flow rate to total pressure and temperature. This gives a parameter which, at choked conditions, can be thought of as a crude proxy for the effective area of the nozzle. In this formulation, capacity is a function of the gas properties, γ and R, and the total-to-static pressure ratio across the vane row, p_2 / p_{01}.

Despite the importance of HP NGV capacity at an early stage in the engine design process (due to its role in setting overall engine performance and turbine stage matching), there have been very few studies of capacity in the open literature. Investigations into both high-accuracy methods of experimental capacity measurement and key secondary influences have only begun in recent years.

In 1984, Fielding [1] considered the influence of frictional losses in the passage on vane capacity. He defined a parameter which he called *restriction factor*, φ, to describe the reduction

in nozzle effective flow area due to momentum deficit in the boundary layer regions. The restriction factor can be thought of as providing an estimate of the ratio of actual (in as far as it represents the real vane) flow capacity to the 1D isentropic capacity. For relatively low aspect ratio vanes with profile total pressure loss coefficients in the range $0.0 \leq Y_p \leq 0.1$, restriction factor was shown to be closely estimated by the simple relationship $\varphi = 1 - 0.56Y_p$. For a typical vane row with $Y_p = 0.04$, capacity values evaluated using this relationship and from a 1D isentropic calculation differed by 2.44%. This study was a useful contribution to the literature in highlighting the impact of frictional losses in the passage on flow capacity and providing a relatively simple method to account for their non-uniform distribution. However, from the point of view of evaluating the capacity of modern, complex NGV rows it is of limited use because of its reliance on simplistic ideas of 1D choked throats. The results presented in the more recent literature demonstrate that the impact of frictional losses on capacity is very small in relation to the impact of fundamentally 2D aerodynamic effects which were entirely overlooked in this study.

In 2004, Afanasiev et al. [2] showed computationally that vanes with identical minimum *geometric* area but different loading distributions can have differences between their capacity characteristics of up to 10%. Capacity characteristics (as functions of exit Mach number, M_2) from each of the two vanes are shown in Figure 1a. The peak value of both characteristics fell below that of the 1D isentropic characteristic, due to frictional losses incurred in the vane passage (in accord with [1]). The Mach number at which the maximum, or choked, capacity was reached differed between the two vanes, due to a shift in position of the *controlling* minimum area in relation to the passage. This is illustrated in the Mach number contours shown in Figure 1b and c, where the sonic condition is marked by a thick black line. The position of the sonic line shifted significantly downstream in the more aft-loaded case, and for vane 2 was fully downstream of the covered region of the passage and the geometric throat area (stretching between the wake region and a point on the SS of the adjacent vane). This demonstrates the disconnect between the geometric throat and the controlling area—the first time this had been clearly shown in the literature.

Although retrospectively unsurprising, the importance of this result is highlighted by the persistence, even today, of overly simplistic attempts to reconcile capacity differences between different vanes by ultra-high accuracy measurement of geometric throat area alone. As our understanding of the sensitivity of modern HP NGV aerodynamic performance to small design features develops, it rapidly becomes apparent that such attempts are highly unlikely to be successful. Even defining a geometric throat for a highly 3D modern part presents its own challenges. We can clearly see from Figure 1c that the sonic line is very far from a 1D plane across the passage, and when it extends into the wake region it becomes almost impossible to define a meaningful area at all.

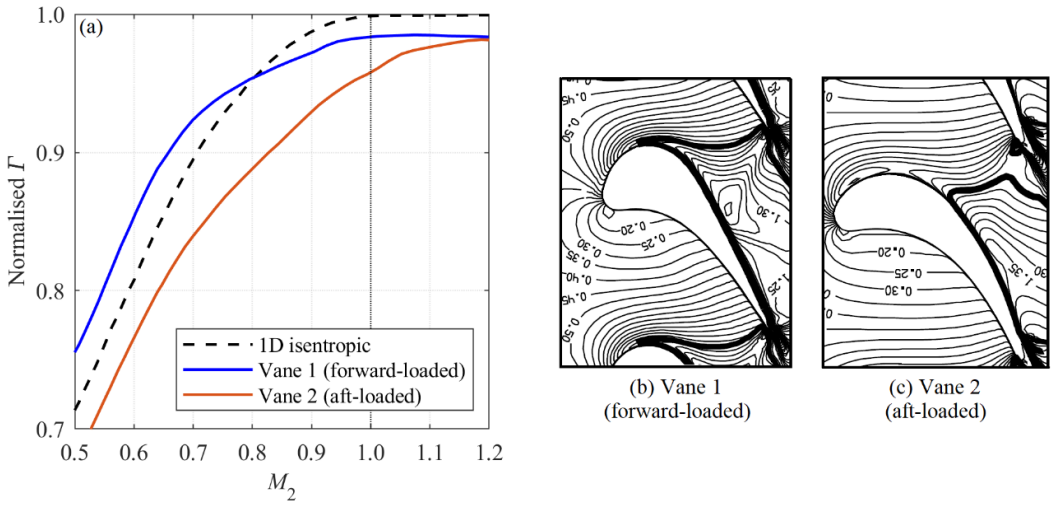


Figure 1: (a) Predicted capacity characteristics for two vanes of different loading distributions, compared against the 1D isentropic characteristic; contours of Mach number in the controlling region of the vane passage for (b) forward-loaded vane; and (c) aft-loaded vane. All modified from [2].

In 2010, Povey [3] presented an analytical model for estimating the impact of film cooling on capacity based on fundamental cooling performance parameters. A control volume mixing approach was employed, in which, importantly, the free-stream static pressure was allowed to vary in the flow direction, in line with the models of, for example, Kollen and Koschel [4]. Mainstream and coolant flows were partially mixed (to a defined film cooling effectiveness) at a defined 'throat' Mach number. The model was used to estimate a *correction parameter* between the capacity at typical experimental rig conditions and at engine conditions (for typical boundary conditions). It was concluded that there are unacceptable (of order 1.88%) sensitivities

(differences between rig and engine conditions) when capacity was calculated on the basis of uniform hot gas conditions being prevalent over the entire flow (that is, an overall vane capacity definition similar to equation (2) in which the total (mainstream plus coolant) mass flow is normalised by the prevailing mainstream inlet total pressure and temperature). Alternatively, when capacity was calculated based on a fully-mixed-out total pressure and temperature, capacity differences between rig and engine conditions reduced to approximately 0.20%, were proportional to the total coolant mass flow, and were amenable to analytical modelling.

In 2012, Hambidge and Povey [5] investigated the impact of a typical film cooling arrangement on HP NGV capacity using a 2D numerical method (with multiple coolant films resolved in the numerical mesh from small internal plena). This can be thought of as a computational extension of the analytical theory of Povey [3]. The capacity characteristic predicted by CFD for an uncooled vane is shown in Figure 2a. This had a similar form to the aft-loaded characteristic observed by Afanasiev et al. [2] (see Figure 1), with the maximum capacity not being reached until significantly above the nominal choked condition. Mach number fields through the passage at midspan are shown in Figure 2b and c for uncooled and cooled vanes, respectively. These results show the sonic line (indicated by a thick black line) crossing the geometric 'throat' plane (marked by a dashed black line) almost perpendicularly, and forming a very complex and irregular shape extending downstream of the covered region of the vane passage into the wake region. This supports the observations made in [2]. The shape of the sonic line was actually largely insensitive to the introduction of film cooling (compare Figure 2b and c).

For a typical 2D vane section operating at unit exit Mach number, introducing film cooling was found to cause a 0.125% fall in capacity. This was compared against the analytical model of [3], which predicted a corresponding capacity drop of 0.144%. It was demonstrated that the effect on vane capacity of multiple rows blowing simultaneously could be closely approximated by superposition of the effects of each row blowing in isolation. The errors incurred in making this simplification were of order 0.01% of overall vane capacity. It was therefore concluded that the

impact of film cooling on capacity is only weakly sensitive to the actual distribution of film cooling holes over the vane surfaces, and is primarily determined by the overall coolant mass flow rate. The impact can likely be adequately accounted for using analytical methods, correlations based on single-row experiments or simulations, or simple 2D CFD.

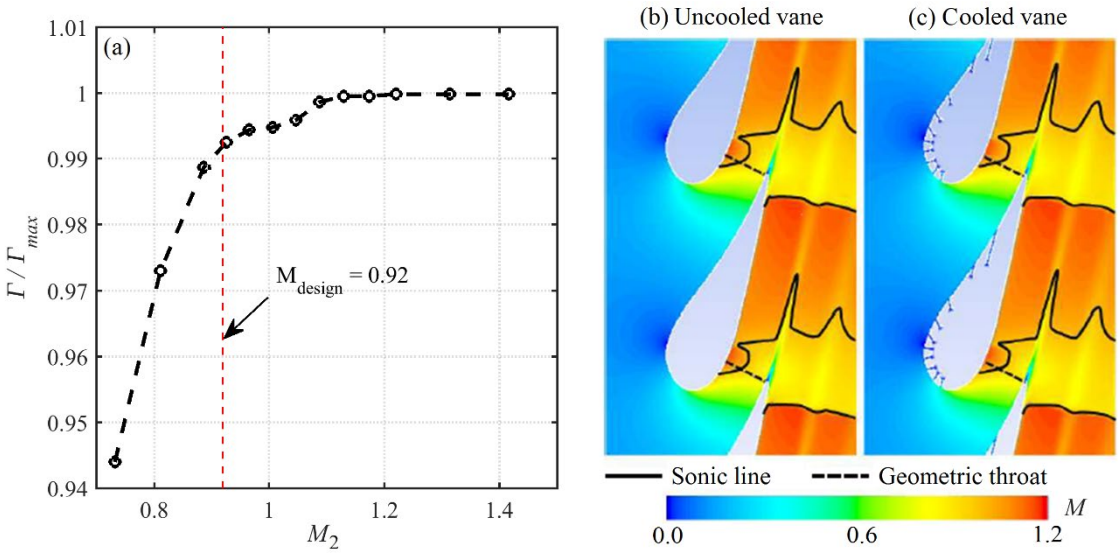


Figure 2: (a) CFD-predicted capacity characteristic for an uncooled vane; predicted Mach number contours through the vane passage for (b) uncooled and (c) cooled vanes. All modified from [5].

In 2011, Povey et al. [6] described for the first time a novel semi-transient experimental technique for NGV capacity measurement. By careful experimental design, the semi-transient technique offered a shorter test duration (approximately 60 s), reduced operating cost, and improved precision and bias uncertainty relative to the conventional (continuously running) industrial method. A fully-annular cascade of engine components was operated at non-dimensionally engine representative conditions of Mach number, Reynolds number and coolant-to-mainstream pressure ratio. Precision and bias uncertainties in vane capacity of ±0.028% and ±0.546% respectively were achieved (to 95% confidence). Of the ±0.546% bias uncertainty, ±0.500% was inherited from the primary mass flow metering nozzle. This was the bias error in the nozzle calibration, traceable to an international standard. The experimental method was designed to minimise the small additional bias uncertainty (+0.046%) arising from the experimental measurement process. This paper represents the first description in the literature of an academic effort towards low

uncertainty experimental measurement of NGV capacity, and is an effective starting point for developing understanding of secondary influences on capacity.

In the same paper, the impact of the definition of vane exit static pressure on the capacity characteristic was considered. Isentropic capacity predictions based on 1D, 2D (radial pressure profile) and 3D (radial and circumferential pressure profiles) models of static pressure distribution were compared to experimental data for a modern HP NGV. All of these models produced a poor match to the *shape* of the experimental capacity characteristic—in particular the degree to which capacity at the nominal choked pressure ratio fell below the maximum capacity. The agreement with the experimental data improved slightly moving from the 1D to the 2D to the 3D models, due to an improved approximation of the pressure boundary condition in the real passage. The poor agreement demonstrates the complexity of the flow environment and highlights the pitfalls of applying simplified logic based on isentropic equations (e.g. the simplistic—in this context—concept of a *throat*). The disagreement (between models and experiment) was taken to be partly due to total pressure loss (in accordance with the ideas of [1]—a similar model was used in the paper to remove the effects of assuming zero loss, and the difference was shown to be small and even in the wrong direction to account for the disagreement), but primarily due to the difficulty of establishing a pressure measurement at a point of well-defined area.

In 2016, Högner et al. [7] numerically quantified the impacts on NGV capacity of a range of typical geometric variations in the vicinity of the trailing edge region which may arise due to manufacturing scatter. These included the thickness and position of the trailing edge slot, SS and PS trailing edge overhang lengths, and pressure and suction surface offsets. The effects of typical variation in each aspect of geometry were estimated both in isolation and in parallel (via a Monte Carlo simulation), in order to study the interactions between them. The pressure surface offset and the position of the trailing edge slot were identified as the strongest influencing factors on capacity. Simple linear superposition of these two parameters acting in isolation gave a comparable result to the parallel study, demonstrating a high degree of linearity and a relative lack of cross-dependence.

In 2017, Kirollos et al. [8] presented a novel experimental method, and an associated analysis technique, for evaluating the flow capacity characteristics of individual film cooling rows of NGV components and scaling capacities between experimental rig conditions (with all rows blowing to atmospheric pressure) and engine conditions (rows blowing to different pressures determined by the vane aerodynamics). The method is applicable to both *uncoupled* (film rows have minimal interaction and therefore the sum of individual row capacities blowing in isolation is approximately equal to the total coolant capacity with all rows blowing together) and *coupled* (row capacities have interdependencies due to internal losses and therefore the sum of individual row capacities blowing in isolation differs significantly from the total coolant capacity with all rows blowing together) film cooling systems. The latter is particularly relevant to modern additive-manufactured parts which can have very complex internal cooling networks. For the purpose of scaling capacities between different conditions, the row interactions were represented using an experimentally-calibrated network model. The method utilised a differential mass-flow measurement technique. That is, two experiments were conducted to measure the capacity of a specific film row: firstly measuring the capacity of all rows blowing together; and secondly measuring the capacity with only the row of interest blocked and all other rows blowing. The difference between these two results was then a function of the capacity of the row of interest. This method minimised the need to block rows and therefore the potential for leaks. The method was demonstrated for both an uncoupled and a coupled example, and it was shown to achieve bias and precision uncertainties in individual row capacities of ±0.6% and ±0.5%, respectively.

2.2 NGV aerodynamic performance and sensitivity to trailing edge cooling

2.2.1 Introduction to nozzle guide vane efficiency and loss

The basic purpose of a nozzle guide vane (NGV) row is to supply angular momentum flux to the rotor blade row following immediately downstream. The local momentum flux is proportional to the local kinetic energy (KE) per unit volume. It is usual to describe the performance of an NGV row by defining an *efficiency*, η—the ratio of the actual useful output from the vane row to the output from an ideal, isentropic case. That is, for an NGV row:

$$\eta = \frac{\text{Actual exit KE}}{\text{Ideal exit KE}} \tag{4}$$

The relationship between efficiency and *loss* coefficient, ζ, is most commonly given by $\zeta = 1 - \eta$ (although not exclusively: some authors prefer to define loss coefficient as $\zeta = (1 - \eta) / \eta$). The assessment of efficiency and loss in terms of KE (and thus enthalpy) is far from universal. The use of a total pressure loss coefficient, Y, is very common. Y is typically defined as

$$Y = \frac{p_{01} - p_{02}}{p_{01} - p_2} \tag{5}$$

where the subscripts 1 and 2 represent inlet and fully-mixed exit stations, respectively. The total pressure loss coefficient is attractive due to its simplicity and ease of evaluation from experimental measurements. However, whilst it is a useful means of presenting the change of average stagnation pressure across a vane row, it is a weaker measure of the loss generated across the vane row. Denton [9] strongly advocated for the use of an entropy loss coefficient to describe turbomachine stage losses, based on the fact that it is the production of irreversible entropy increase in viscous and turbulent dissipative processes within and downstream of the vane passage which determine the loss of efficiency. In practice, the difference between absolute values of KE and entropy loss coefficients is very small, and the use of KE loss coefficients is far more common due to the difficulty in directly measuring changes in entropy.

Figure 3a shows the expansion process in an NGV row on an *h-s* chart (process 1–2). For a completely uniform exit flow (uniform p_2), the ideal process is defined as the KE obtained in an isentropic expansion from the inlet total pressure to the exit static pressure (process 1–2s). The KE loss coefficient is then given by

$$\zeta = 1 - \frac{v_2^2}{v_{2\mathrm{s}}^2} = 1 - \frac{h_0 - h_2}{h_0 - h_{2\mathrm{s}}} = 1 - \frac{\left(1 - \frac{h_2}{h_0}\right)}{\left(1 - \frac{h_{2s}}{h_0}\right)} \tag{6}$$

where v_2 is the measured flow velocity at vane exit, $v_{2\mathrm{s}}$ is the *isentropic velocity* at vane exit, and, for an adiabatic nozzle, $h_{01} = h_{02} = h_0$. For constant c_p, and recalling the isentropic relation $T_2 / T_1 = (p_2 / p_1)^{\chi}$, where $\chi = (\gamma - 1) / \gamma$, this can be cast as

$$\zeta = 1 - \frac{1 - \left(\frac{p_2}{p_{02}}\right)^{\chi}}{1 - \left(\frac{p_2}{p_{01}}\right)^{\chi}} \tag{7}$$

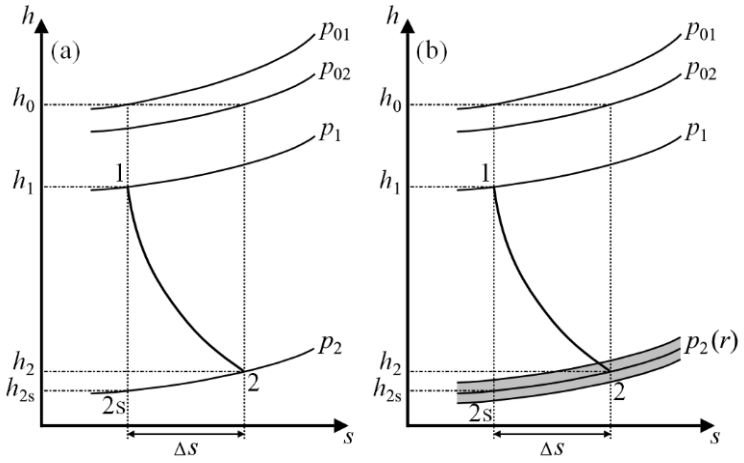


Figure 3: *h-s* charts showing the expansion process across an NGV row for: (a) uniform exit static pressure (linear cascade situation); (b) radial profile of exit static pressure (annular cascade situation).

2.2.2 Representation and evaluation of loss coefficient

The simple definition of KE loss coefficient in equation (6) requires single values of downstream total pressure, p02, and static pressure, p2. However, the flow downstream of a turbomachine blade row does not have uniform total and static pressure—certainly not at a typical experimental traverse plane which may be only a short distance downstream of the cascade. Therefore, it is necessary to decide how to represent the real, non-uniform flow distribution in the evaluation of a loss coefficient.

Most commonly, downstream conditions of total and static pressure are computed at a hypothetical plane far downstream at which the flow is fully mixed-out. That is, the non-uniform flow in the measurement plane is artificially mixed-out to a uniform (or partly uniform) condition, using one of several potential methods which are described shortly. Whilst for a turbomachine blade row the following row is typically located long before the exit flow has been fully mixed out, in most cases the downstream machinery is not able to usefully recover the residual secondary KE of the non-uniform flow. Evaluating a loss coefficient based on mixed-out conditions is also useful for comparing measurements of different components which may have been made in different planes, and therefore have differing degrees of residual non-uniformity.

An alternative is to calculate a loss coefficient based on averaged representations of the total and static pressure fields in the measurement plane (either 1D line-averages at a particular radial height or circumferential position, or a 2D plane-average). This produces representations of total and static pressure, and thus a loss coefficient, which are unique to the plane they are based on. This is useful in certain applications, for example if we wish to evaluate wake mixing rate.

Additionally, in an annular cascade there must be a radial gradient of static pressure (to satisfy radial equilibrium). This is true regardless of the distance downstream of the cascade (assuming that the mixing takes place in a constant-area annular duct). That is, there must be a range of static pressures in both the measured and mixed-out exit flows, $p_2(r)$. This situation is illustrated in the *h*-*s* chart in Figure 3b.

Pianko and Wazelt [10] presented a comprehensive review of the methods in common use for averaging non-uniform internal flows in turbomachines. They concluded that it is not possible to replace a real, non-uniform flow with an equivalent uniform (i.e. averaged) flow matching all significant fluxes and parameters.

Cumpsty and Horlock [11] proposed that the 'correct' method for averaging a non-uniform total pressure field is that which ensures that the properties of the averaged flow which are most relevant to a particular application are equal to their values in the actual, non-uniform flow at the same location (i.e. along the same line or in the same plane). In particular, they discussed some common applications in turbomachinery flows: non-uniform flow entering a compressor or turbine (in which the work input or output is the important parameter); non-uniform flow entering a propelling nozzle (in which the gross thrust is the important parameter); and non-uniform flow entering a choked nozzle row (in which the flow capacity is the important parameter). They also noted that, whilst there is no good physical basis for mass-averaging total pressure (flux-based averages such as the mass-flow-weighted average have no physical meaning when applied to intensive rather than extensive quantities), in many typical experimental situations the absolute variation in total pressure is sufficiently small that the difference between these methods is small.

Four mixing methods are presented in the literature. All four of these methods proceed by applying conservation of mass, momentum and energy between the non-uniform flow measured in the traverse plane, and the hypothetical fully mixed flow in a plane far downstream. They differ in the additional constraints and/or assumptions which they use to close the system of equations. An example non-uniform traverse plane, with measured total pressure $p_{02A}(\theta)$, and the hypothetical fully mixed plane, with total pressure p_{02}, are illustrated schematically in Figure 4.

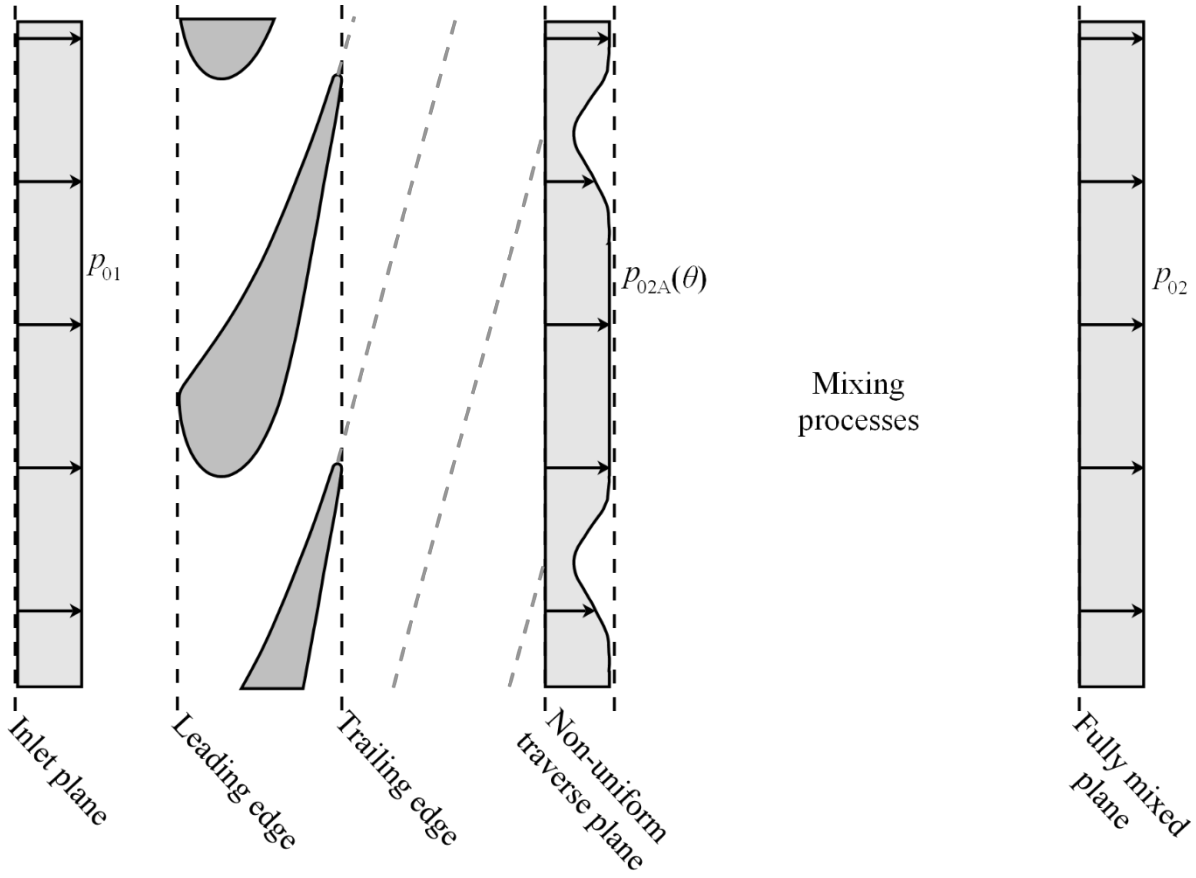


Figure 4: Diagram of key planes in the process of determining mixed-out loss coefficients for a turbine cascade.

Amecke [12] described a mixing method for 2D and/or radially uniform cascades, in which a circumferentially non-uniform flow is mixed to a uniform total and static pressure. The conservation equations are applied to the measured circumferentially non-uniform flow, and a Taylor series expansion in the critical downstream Mach number provides a solution for the mixed-out total and static pressures. This solution is only valid in the loosely transonic range of Mach numbers (0.8–1.2). The annular geometry of the NGV row in an engine adds further

complication, as the exit flow-field must have a radial pressure gradient in order to satisfy radial equilibrium (that is, as the flow mixes out in an annular duct, the static pressure field will not tend to a single, radially-uniform value of static pressure regardless of the length of the duct), and also the cascade aerodynamics are unlikely to be radially uniform. Dominy and Harding [13] proposed a way to apply the method of Amecke to an annular cascade featuring significant radial variation. They conceptually split the measured non-uniform flow into a series of thin, radial layers of 2D flow. Each layer is individually mixed out without interaction with its neighbours. Putting all of the solved layers together gives a radial distribution of mixed-out flow parameters (including p_{02} and p_2). Single values of p_{02} and p_2 are obtained by integrating the radial distributions, and these are then used to evaluate the loss coefficient. Due to the complete absence of radial mixing, this method is considered to be unsuitable for highly 3D vane geometries or measurements with radially-localised features such as film cooling flows. The radial static pressure distribution also does not necessarily satisfy radial equilibrium.

Dzung [14] proposed to mix out the measured flow at a single, swirl-averaged radius (that is, a nominal radius at which the measured swirl velocity profile has the average value). This takes the flow-field measured in a 2D plane and determines the mixed-out properties at a single representative radial height, yielding single values of mixed-out total and static pressure. This is a significant simplification of the real mixed-out flow, but is in many applications mathematically convenient. This method is very commonly used for annular cascade flows due to its ease of application and close agreement with the results of the more sophisticated method of Main et al. (see below).

Main et al. [15] proposed to mix the measured flow to a free-vortex condition. That is, the circumferential velocity component is constrained to be inversely proportional to radius. The resultant mixed-out flow therefore has zero vorticity, radially-uniform total pressure, p_{02}, and a radial static pressure distribution, $p_2(r)$, which, unlike the methods of Amecke and Dzung, does satisfy radial equilibrium. This method has the drawback that in experiments it is slightly

problematic to include coolant flows in the definition of the ideal exit flow (for the purpose of defining a loss coefficient) unless the radial distribution of coolant input is known.

Prasad [16] conducted a similar analysis to Main et al. but enforced a *forced vortex* (rather than free vortex) at the mixed-out plane. The choice of mixed-out condition (free or forced vortex) comes with advantages and drawbacks. A forced vortex is the only possible swirling, annular flow that can be in complete kinematic (all elements of the strain rate tensor are zero) and thermal (flow supports no temperature gradients) equilibrium. However, the resulting mixed-out flow has a radial gradient of total pressure, p_{02} (r), as well as a radial static pressure distribution, with higher total pressure at larger radii. This causes issues in defining a reference isentropic condition, and therefore loss coefficient, when the inlet total pressure, p_{01}, is uniform. In contrast, a free-vortex has a non-zero component of the strain rate tensor and hence is not entirely self-sustaining; but mixes the flow to a uniform total pressure, p_{02}.

In equation (6), the ideal reference process is an isentropic expansion from p_{01} to p_2. Strictly speaking, this is only appropriate for the case of a linear cascade with uniform exit static pressure. Of course, in an annular cascade there must be a radial distribution of static pressure on account of the radial pressure gradient. The true definition of the ideal reference flow then ought to be more complex, although it is very common in practice to simply use an averaged value of static pressure. The free vortex mixing method of Main et al. [15] allows for the calculation of a unique isentropic reference flow, also defined by a free vortex condition, in which the ideal exit total pressure is equal to p_{01} and the ideal exit static pressure at the average radius (generally taken to be the midspan radius) is equal to the mixed-out static pressure at the average radius. This is a major advantage of the free vortex mixing method which makes it, for an uncooled (uniform inlet state) annular cascade, the most physically sound mixing method. Day [17] considered the determination of isentropic reference processes for a cooled annular cascade, using the mixing methods of Dzung [14] and Main et al. (free vortex) [15]. In this case the inlet total pressure condition is no longer uniform. Whilst the Dzung method requires no changes to deal with a cooled cascade because the exit flow is represented using a single value of p_2 (and thus the ideal

exit KE is simply expressed as the sum of separate mainstream and coolant terms, with each stream expanding isentropically from its inlet total pressure condition to p_2), the free vortex method cannot define a unique isentropic process (the local distributions of the mainstream and coolant flows in the mixed-out plane, and hence the static pressures to which each should be mixed out, will be unknown), and therefore the primary advantage of the method is lost. Day therefore concluded that the method of Dzung is the most suitable for a cooled annular cascade.

2.2.3 Relationship between trailing edge loss and total loss

Denton [9] provided a comprehensive review of a range of relevant loss mechanisms in turbomachine flows. Total loss is very commonly categorised into contributions from *profile* loss, *endwall* (or *secondary*) loss, and *leakage* losses. This apparently well-defined breakdown of contributions to total loss is in reality rather arbitrary. In a real NGV row there are a multitude of cross-overs and interactions between these contributions. Nevertheless, it is a very widely used framework which aids in understanding performance differences between different experiments and between experiment and CFD.

Leakage loss is generally relevant to unshrouded rotors. The pressure differential between the SS and PS of the blade drives flow near the blade tip to leak through any gap between the tip and the outer casing. There is both a loss of potential work associated with this leakage flow, and a mixing loss as the leakage jet re-enters the mainstream. This loss contribution is not relevant to the NGV cascades studied in the present work.

Endwall (or secondary) loss is the loss associated with the interaction between the mainstream flow around the blade section, and the boundary layer flow at the endwalls, which causes vortical structures to form and propagate through the blade row. HP NGVs in particular tend to have thick, blunt leading edges and a high degree of turning through the blade row, and thus generate strong secondary flows. Langston et al. [18] presented the first detailed measurements of turbine secondary flows. Models of the general secondary flow pattern in turbine cascades were put forward by Langston [19], and Sharma and Butler [20]. Figure 5 shows a diagram of the standard secondary flow structures through an NGV row, taken from [20]. The

endwall boundary layer at inlet to the blade row rolls up to form a contra-rotating vortex pair as it approaches the leading edge stagnation point. These two vortices 'wrap around' the leading edge and form a characteristically-shaped 'horseshoe vortex' structure. The PS leg of the horseshoe vortex is stimulated to migrate across the passage from the PS to the adjacent SS by the cross-passage pressure gradient, becoming the passage vortex. When it reaches the SS, it interacts with the counter-rotating SS leg of the horseshoe vortex which wraps around the PS leg. This combined structure, generally referred to as the passage vortex system, gradually expands further away from the endwall as it progresses through the passage. Wang et al. [21] used experimental visualisation techniques in a linear turbine cascade to develop understanding of the secondary flow structures. The SS leg of the horseshoe vortex was shown to move above the passage vortex before wrapping around it; and several smaller wall and corner vortices were identified as part of the overall passage vortex system.

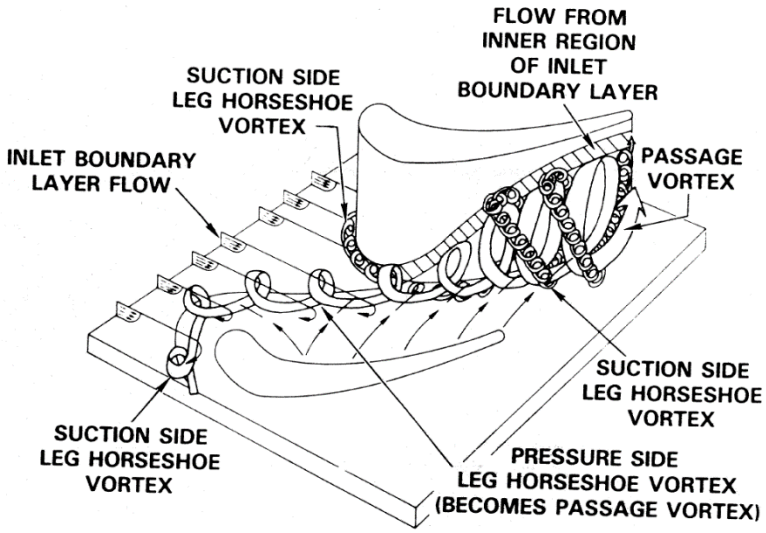


Figure 5: Diagram of the secondary flow structure of a turbine NGV cascade. Taken from [20].

Profile loss describes the loss which arises from flow around the aerofoil section, with no interaction from the cascade endwalls. Profile loss can be further broken down into contributions from: (i) vane surface boundary layers; (ii) shockwaves; and (iii) trailing edge flow and mixing processes. Mee et al. [22] made detailed experimental measurements of a turbine cascade operating at exit Mach numbers ranging from 0.6 to 1.2, and evaluated the relative contributions of each of the three sources listed above to the total profile loss coefficient. Boundary layer loss

coefficient was estimated from surface boundary layer traverse measurements by calculating the integrated KE deficit (with respect to the adjacent free-stream) through the boundary layer profiles at the TE. Boundary layer loss in a turbine cascade is generally dominated by the SS boundary layer due to its higher surface velocity compared to the PS (local rate of entropy generation in boundary layers scales with the cube of local surface velocity). Boundary layer loss is highly sensitive to the location of transition on the SS, as the rate of entropy generation per unit volume rises rapidly as the flow transitions from laminar to turbulent. Whilst loss generation in both laminar and turbulent boundary layers is well understood, predicting the onset of transition is challenging and remains a prominent source of inaccurate loss prediction in numerical methods.

Shock loss coefficient was estimated by examining the decrement of total pressure in free-stream regions in the traverse plane with respect to the measured inlet total pressure. This process was designed to detect the drop in total pressure which occurred across the discontinuity of the shockwave. The method relies on a low noise content in the experimental traverse signal, and is also sensitive to the definition of the boundaries between the 'wake' and 'free-stream' regions. However, the shocks that appear in transonic turbine stages tend to be oblique, and the resulting total pressure discontinuities (and thus direct shock losses) rather small. The influence of the trailing edge shock structure in transonic turbines on loss tends to be more indirect. Flow expands around the trailing edge to a very low base pressure (associated with high trailing edge loss) and is recompressed by shockwaves originating from the confluence region of the SS and PS flows. Loss generation occurs in the viscous dissipation processes in the shear layers bounding the base region (often included in the trailing edge loss) and across the shocks themselves [9]. Loss is also generated through shock-boundary layer interaction. The trailing edge shock on the PS of the wake propagates towards and impinges upon the SS of the adjacent vane. This usually causes boundary layer separation at the impingement point (and in the case of a laminar boundary layer is highly likely to cause transition), producing a rise in boundary layer loss. Hence the effects of shocks are difficult to isolate from the other contributions to profile loss, particularly from traverse data alone.

Mee et al. [22] attributed the remainder of the total profile loss coefficient (subtracting boundary layer and shock contributions) to TE and mixing losses. This includes both loss due to the finite thickness and blunt geometry of the TE, and the mixing out of secondary KE downstream of the cascade. Trailing edge loss is considered in more detail below. Figure 6, adapted from [22], shows the three contributions to total profile KE loss coefficient plotted as functions of exit Mach number. In the subsonic range, profile loss coefficient is relatively evenly split between boundary layer and TE / mixing losses. As Mach number approaches unity, shock losses rise rapidly, and in the transonic and supersonic range all three components are significant contributors to total profile loss coefficient with TE / mixing loss being the largest by some margin. These data are of course specific to a particular vane geometry. More generally, the relative sizes of the loss contributions will depend on many factors including: the vane surface pressure distribution; the states of the surface boundary layers at the TE; the TE shock structure and consequent shock-boundary layer interactions; the TE thickness and shape; the presence of TE coolant ejection; and the unsteady flow behaviour downstream of the TE. Some of these factors are now considered in more detail.

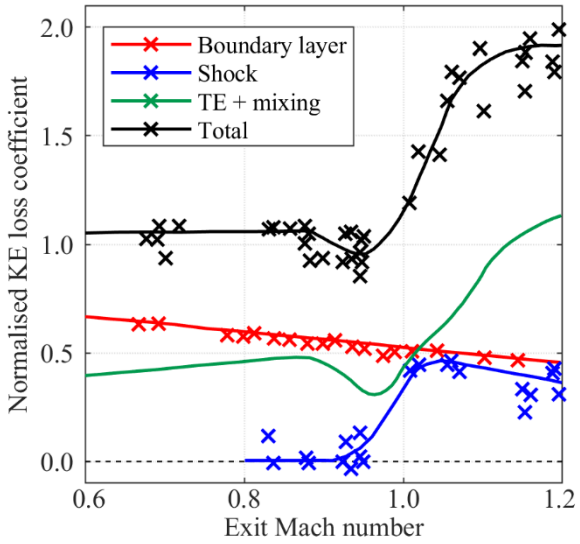


Figure 6: Contributions to total profile loss coefficient as functions of exit Mach number, for a Reynolds number of 10^6. Adapted from [22].

2.2.4 Influence of trailing edge coolant ejection on trailing edge loss

From a purely aerodynamic viewpoint, the trailing edge should be thin and sharp, thereby producing a clean separation at the TE and a very thin, steady wake region. Thicker TEs provide

greater blockage to the flow, producing a wider and deeper wake and therefore higher TE loss. However, in practice compromise is required to meet the mechanical and thermal constraints of the engine environment. Very thin, sharp TEs are highly susceptible to structural damage due to the large forces acting on the vanes, and the presence of foreign particles passing through the vane row. Furthermore, the operating conditions at the first turbine stage NGV are at their most extreme in the entire engine. Over recent decades, the turbine entry temperature has continuously risen to facilitate higher thermal efficiency and lower specific fuel consumption. The NGV inlet total temperature in a modern gas turbine engine is typically of order 2,000 K. This is well beyond the melting temperature of the NGV base material, and thus cooling the vanes is essential to preserve the mechanical integrity of the components and achieve an acceptable service lifetime.

Sufficient cooling is commonly achieved through a combination of internal cooling (coolant passes through a labyrinthine network of channels inside the vanes including features such as rib and pin-fin arrays, pedestal banks and impingement plates, allowing heat transfer from the external flow to the coolant by conduction through the blade material and convection to the coolant), and ejecting coolant into the external flow-field through cooling holes distributed over the vane surfaces (typically around the leading edge stagnation region and over the pressure surface) and through a TE slot. Cooling the material near the TE is particularly important due to the small scale of the geometry. Early studies (e.g. [52]) considered cooling the TE using rows of film cooling holes located just upstream, but such 'discretised' methods (discrete holes) struggle to offer uniform coverage across the vane span, causing 'hot spots' and potential localised deterioration. Ejecting coolant from a continuous TE slot also provides an efficient method for removing spent coolant air from the vane internal cavity, due to the low pressure in the TE base region.

The presence of a slot within the TE naturally requires a thicker TE than an equivalent uncooled vane. There is a compromise to be struck between achieving sufficient cooling to maintain component lifetime, and minimising the aerodynamic penalty. Early studies of the sensitivity of TE loss to TE geometry focussed on the impacts of TE thickness in vanes with solid

TEs. Johnston et al. [27] studied the impact of varying TE thickness on loss and efficiency with experiments conducted on representative turbine blade cascades. The data were used as a validation case for existing theoretical models ([25],[24]) (note that these models are in principle the same as the theoretical solutions for profile / TE loss presented in [9] and [44], and the basis for the model implemented for estimating the impact of changing TE thickness on loss coefficient in part of the current work). The sensitivity of TE loss to TE thickness was found to be in close agreement with theoretical predictions for a family of stator vanes, but rotor blades were found to be much less sensitive to TE thickness (less than predicted). Full turbine stage experiments suggested that the effect of increasing stator TE thickness on the effective loss coefficient was significantly greater than predicted by simple theory. This was attributed to a change in incidence angle to the downstream rotor.

2.2.5 Relationship between base pressure and trailing edge loss

Rather than directly measuring the wake flow, several previous studies have used base pressure measurements to provide an insight into cascade aerodynamic performance. Base pressure scales with the 'form drag' of the component and therefore can be used as a proxy for TE loss. Denton [9] gives a simplified expression for the profile total pressure loss coefficient of a vane cascade, obtained from a control volume analysis:

$$\frac{\Delta p_0}{\frac{1}{2}\rho v^2} = \frac{2\theta^*}{w} + \left(\frac{t+\delta^*}{w}\right)^2 - \frac{tC_{\mathrm{pb}}}{w} \qquad \text{where} \quad C_{\mathrm{pb}} = \frac{p_{\mathrm{b}} - p_{\mathrm{ref}}}{\frac{1}{2}\rho_{\mathrm{ref}} v_{\mathrm{ref}}^2}$$

t and w are the nominal TE thickness and passage width respectively, p_{b} is the base pressure, δ^* and θ^* are the total (SS + PS) boundary layer displacement and momentum thicknesses respectively, and p_{ref}, v_{ref} and ρ_{ref} are the static pressure, velocity and density at a reference location (typically either at the downstream system boundary or on the vane surfaces just upstream of the TE) [9]. The first right-hand side term represents the loss contained in the surface boundary layers just upstream of the TE (including associated mixing losses). The second right-hand side term represents the loss arising from the combined blockage of the TE and the boundary layers, and the abrupt expansion which occurs downstream of them. The third right-hand side term represents

the form drag arising from the low base pressure acting on the TE. Therefore, if changes in boundary layer thickness and TE thickness between different experiments are measured, or assumed, to be small then changes in base pressure provide a useful indication of changes in TE loss. For cooled TEs, the situation is more complex and the base pressure proxy is less straightforward since it does not account for mixing losses between the mainstream and TE coolant flows or the KE introduced by the coolant flow.

Sieverding et al. [28] originally studied the problem of predicting base pressure in turbine cascades in 1979. They presented detailed base pressure distributions for a simplified, enlarged-scale test section designed to represent the uncovered region of a turbine passage and reproduce the flow-field in the vicinity of the TE. This experimental setup enabled a greater density and resolution of pressure measurements around the TE base than would be possible in 1:1 scale cascade tests. They proposed a correlation for base pressure in terms of downstream static pressure, TE wedge angle, and post-throat SS curvature, based on experimental measurements taken from 16 different cascades operating over a range of exit Mach numbers from 0.65 to 1.40. The correlation predicted 80% of the base pressure measurements to within ±5%.

Detailed measurements of base pressure distributions around the TE at a range of Mach number conditions were presented in [29], [30]. Whilst at low-subsonic Mach numbers the base pressure was approximately isobaric, at high-subsonic and transonic Mach numbers (around 0.7–1.0) a characteristic minimum pressure was observed in the TE centre. The pressure variation around the TE was shown to be as much as ±11.6% of the mean value at a Mach number of 0.97 [30]. The central pressure minimum was caused by the unsteady wake flow: the shear layers shed from the TE rolled up into vortices at a location which gradually shifted closer to the TE as Mach number increased. It was clear that the resulting non-uniform base pressure distribution at transonic Mach number would not be accurately measured by a single pressure tapping in the TE. This casts doubt on some of the data presented in the literature. At supersonic Mach numbers, the site of vortex formation moved downstream of the oblique shockwaves formed at the confluence

point (see below)—i.e. further downstream of the TE, and the base pressure distribution was again approximately isobaric.

In 1982, Sieverding [31] extended the study of turbine cascade base pressures by studying the influence of coolant ejection from a central TE slot on the base pressure distribution. He presented data from both simplified, large-scale highly instrumented geometries and more representative but less heavily instrumented cascade tests. Tests without coolant ejection showed that the base pressure was constant over approximately 70% of the TE circumference, and at an almost identical level between the two sides of the central slot.

Introducing coolant flow generated a rise in average base pressure of up to 15% of exit dynamic head at high-subsonic and transonic exit Mach numbers. However, the pressure variation around the TE circumference remained almost flat on each side of the slot. It was therefore concluded that a single pressure tapping in each half-base is sufficient to measure base pressure. Coolant ejection also produced a notable asymmetry in the average base pressures between the two sides of the slot. The degree of asymmetry was dependent on both the coolant-to-mainstream total pressure ratio and the coolant ejection angle relative to the wake. Average base pressure on both SS and PS sides of the slot first increased with coolant-to-mainstream total pressure ratio up to a maximum, before falling as the pressure ratio continued to rise. This finding is supported by a significant body of experimental literature, which is reviewed in the following section.

The influence of coolant-to-mainstream density-ratio on base pressure was also investigated by ejecting foreign gases from the TE slot. Increasing the density-ratio from close to unity to around the typical engine range of 1.5–2.0 had almost no impact on the measured average base pressures prior to the maximum point (at low coolant-to-mainstream mass flow ratios). However, at higher mass flow ratios an increased density-ratio reduced the gradient of the base pressure drop beyond the peak. This is an important result in setting appropriate combinations of slot width and coolant-to-mainstream pressure ratio.

2.2.6 Trailing edge flow in transonic turbine cascades

The flow behaviour and shock structure around a turbine blade trailing edge in supersonic flow is fairly well understood. The flow pattern is illustrated in Figure 7a (taken from [23]). Immediately downstream of the trailing edge is the triangular base region, containing relatively low velocity fluid at a low, approximately uniform base pressure. The base region is bounded by shear layers (velocity varies rapidly from the high free-stream velocity to the low velocity in the base region) spanning from the flow separation points on the vane surfaces, to the confluence point at which the suction and pressure side flows meet. As the flow separates from the vane surfaces at the trailing edge, the change in direction generates expansion waves which propagate out into the free-stream. At the confluence point, the meeting flows are turned outwards again as they find a common exit flow direction. In doing so they are compressed, generating shockwaves which also propagate out into the free-stream flow (the trailing edge shocks). The shock on the pressure side of the trailing edge propagates towards the suction surface of the adjacent vane in the cascade, and significantly influences its surface pressure distribution. As a consequence, there is a shock-boundary layer interaction at this location: the boundary layer rapidly thickens and may temporarily (or even permanently) separate from the surface, with an associated increase in entropy generation. Downstream of the confluence point is a turbulent, unsteady wake [23].

Denton and Xu [23] present a theoretical model (a development of the model first described by Stewart [24] and Lieblein and Roudebush [25]) for predicting the fully mixed-out total pressure loss coefficient produced in a transonic turbine cascade. The model is based on the application of the conservation of mass, momentum and energy in a control volume spanning from the cascade trailing edge to a hypothetical fully mixed plane far downstream. This method is demonstrated to predict the mixing losses downstream of the trailing edge exactly, without requiring any knowledge of the complex viscous processes occurring within the control volume. *If* the boundary conditions for the problem—and particularly the static pressure distribution on the uncovered part of the SS—are specified correctly, the method should be able to accurately assess profile loss coefficients. However, predicting or knowing the correct relationship between the uncovered SS pressure distribution and the base pressure or downstream pressure is very difficult, especially so

in transonic cases involving impingement of a trailing edge shock on the SS. Predicted base pressures and loss coefficients are highly sensitive to this relationship. The effects of surface boundary layers at the trailing edge (effectively increase total trailing edge blockage by the displacement thickness), trailing edge coolant ejection (effectively reduce trailing edge blockage and therefore loss), and SS curvature (increased SS curvature in the aft-chord region reduced loss coefficient relative to a straight surface) on the model predictions were also discussed.

2.2.7 Unsteady behaviour of turbine wakes

The unsteady phenomenon of vortex shedding from a blunt trailing edge was first observed in the early 20th century ([32],[33]). A mechanism for vortex formation and shedding was first proposed by Gerrard [34] in 1966. This is illustrated in Figure 7b. The lines originating from the top and bottom of the circular body (marked (1a) and (1b) in the diagram) represent fluid filaments in the shear layers separating from each side (analogous to the separated suction and pressure side shear layers in the case of a turbine trailing edge). The shear filaments alternately roll up and entrain flow from the free-stream (marked (2)). Entrainment is driven by a combination of the vorticity of the previously shed vortex just downstream, and the vorticity of the separated shear layer. Entrainment causes the vortex to grow, until at a certain point it starts to entrain flow from the shear layer separated from the opposite side of the body. This flow has an opposing sense of vorticity and thus acts to 'cancel out' the vorticity of the growing vortex. Eventually this process prevents further growth of the vortex, and it is shed from the body (marked (3)). The next vortex then begins to roll up from the opposite shear layer.

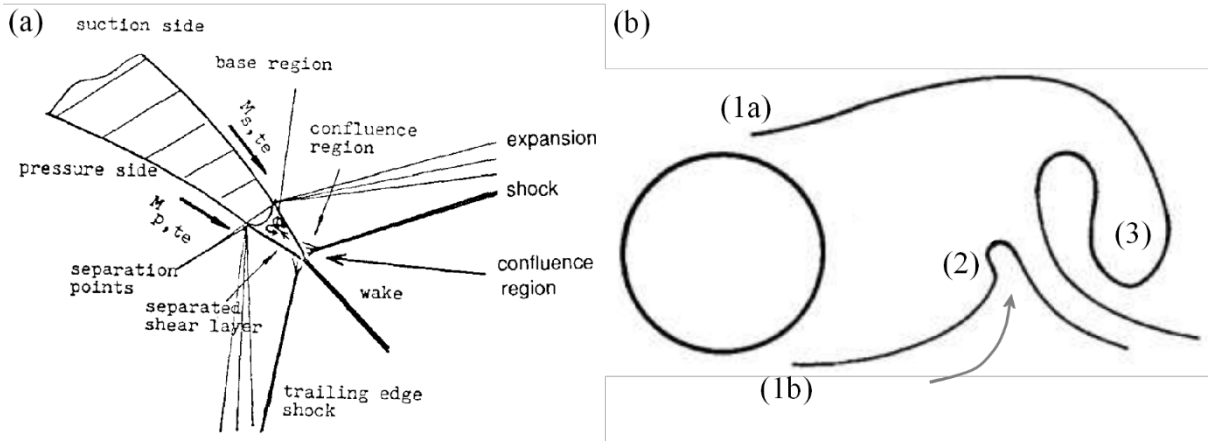


Figure 7: (a) Turbine trailing edge shock structure in supersonic flow (from [23]); (b) schematic illustration of vortex formation and shedding in the wake of a bluff body (from [34]).

Sieverding et al. [35] experimentally characterised the unsteady wake flow downstream of a turbine blade cascade operating at high-subsonic exit Mach number. They measured a significant non-uniformity in base pressure around the TE circle (as opposed to the almost constant base pressure level observed at lower Mach number) with a minimum base pressure in the centre, and also periodic temporal fluctuation in average base pressure following the shedding of vortices. The local Mach number measured in the shear layers expanding around the curvature of the TE reached as high as 1.25 at the apex of the inward sweep of the vortex roll-up, at a nominal exit Mach number of 0.79. This demonstrates how local pockets of supersonic flow, and hence shockwaves, can be formed in otherwise subsonic flow.

More recently, Melzer and Pullan ([37],[38]) extensively compared the performance of round, square and elliptical TE shapes in both simple flat plate tests and in cascade tests. They demonstrated the critical role of *transonic vortex shedding* in determining TE loss, and showed that TE shapes that were capable of partially or fully suppressing transonic shedding yielded a very significant loss coefficient reduction at certain operating conditions. Transonic vortex shedding is a specific unsteady wake flow behaviour in which, as the SS and PS shear layers alternately expand around the TE into the base region, the flow becomes locally supersonic. When the vortices formed from the rolled-up shear layers are shed from the TE, the shear layer is pushed back outwards, generating a pressure wave which propagates upstream. In the case where the expanded flow has become locally supersonic, the pressure wave will form a shockwave which

propagates out into the free-stream. The unsteady shocks generate total pressure loss and interfere with the surface boundary layers. TE shapes with very small radii of curvature can therefore generate supersonic flow and unsteady shockwaves even when the nominal exit Mach number condition is safely subsonic (as low as $M_2 = 0.6$ depending on the boundary layer states). A Schlieren photograph illustrating the mechanism of transonic vortex shedding is shown in Figure 8.

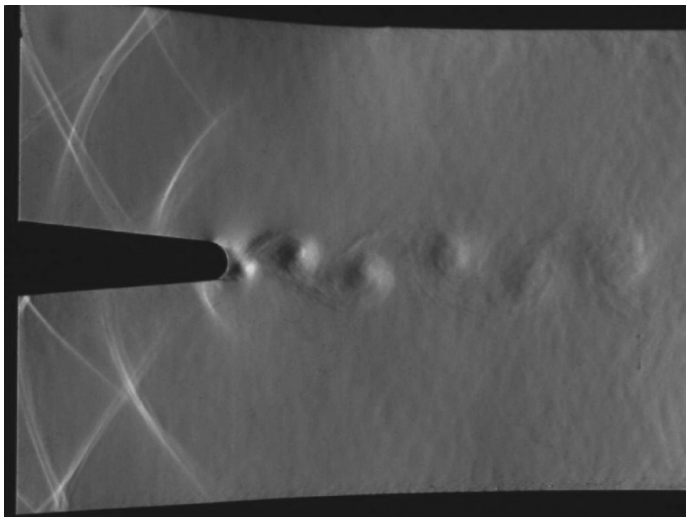


Figure 8: Schlieren image of a vortex sheet shed from a solid, round TE at a nominal exit Mach number of 0.65. Taken from [38].

At low exit Mach number (with no transonic shedding for any TE shape), all three shapes produced similar loss coefficients (differences of no more than 10%), with the ranking $\zeta_{\text{square}} > \zeta_{\text{round}} > \zeta_{\text{elliptical}}$. This is in accord with many previous studies. However, the onset of transonic shedding occurred at lower Mach number for square TEs than for round, as the shear layers expanded around much sharper corners (producing a higher maximum-to-nominal Mach number ratio). At high Mach numbers, when transonic shedding was present in both square and round TEs, loss coefficient was approximately 8% *lower* for square TEs compared to round. The square geometry limited the extent of the shedding cycle and the quantity of free-stream flow entrained into the vortices. Elliptical TEs suppressed transonic shedding—with vortices only rolling up around one TE diameter downstream—at all conditions.

Using results from simple flat plate experiments, Melzer proposed a criterion to predict the onset of transonic vortex shedding based on measured boundary layer thicknesses. When the ratio

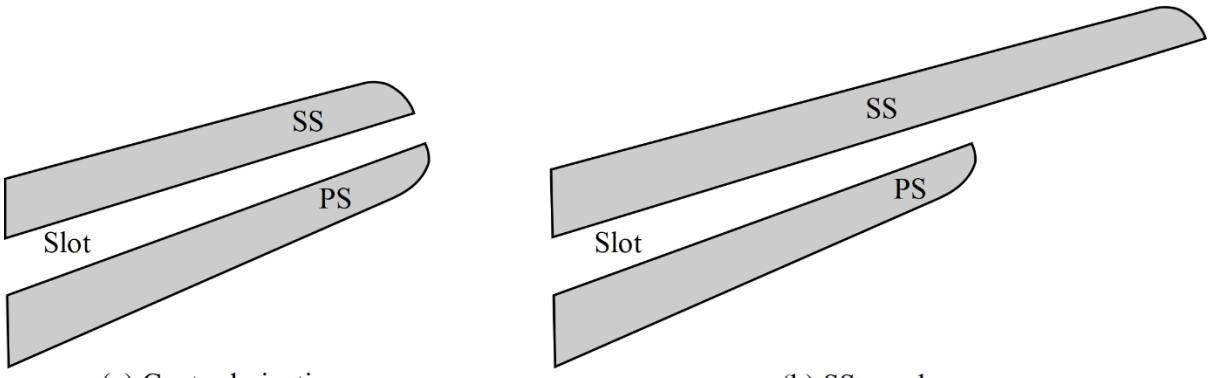
of TE thickness to total (SS + PS) boundary layer momentum thickness was less than approximately 7, the boundary layers were sufficiently thick to suppress transonic shedding (low energy boundary layer flow entrained by vortices instead of higher energy free-stream). However, this criterion broke down when applied in a realistic cascade environment due to the different SS and PS boundary layer states (SS likely fully turbulent, PS likely laminar or transitional). This generally delayed the onset of transonic vortex shedding to higher values of TE to total momentum thickness ratio, but with strong sensitivity to the exact boundary layer states. A simple, universal criterion could not be determined from the data.

The work of Sieverding et al. ([31],[35]) and Melzer et al. ([37],[38]), among others, clearly demonstrates the importance of unsteady flow phenomena in determining NGV aerodynamic performance. Therefore, running unsteady CFD calculations is generally seen as a minimum requirement for predictions of NGV efficiency and loss, particularly in the transonic and supersonic Mach number ranges. Léonard et al. [36] compared steady Reynolds-Averaged Navier-Stokes (RANS), unsteady RANS (URANS) and Large Eddy Simulation (LES) calculation methods as applied to a typical HP turbine blade row operating at high-subsonic exit Mach number. Note that the fundamental history of these three well-known numerical methods is not covered in this literature review. Unsurprisingly, a clear hierarchy of prediction accuracy was demonstrated amongst the three methods. Although steady RANS offered good estimates of the mean exit flow and surface boundary layer properties, an unsteady method (URANS or LES) was required to reproduce the trailing edge flow structures observed in experiments. Both URANS and LES produced reasonably accurate predictions of the time-averaged wake profile, but only LES was able to correctly recreate unsteady flow features such as the shedding and propagation of pressure waves from the shear layer separation points in phase with shed vortices. We can deduce from the work of Melzer [37] that less sophisticated CFD methods may struggle to predict the onset of transonic vortex shedding and hence its significant impact on loss and efficiency. Examination of instantaneous snapshots of the unsteady flow-field produced by URANS and LES showed that whilst URANS had largely the same unsteady features, they were much weaker and

dispersed far more rapidly than in LES, and hence their influence is partially masked. The dissipation of large-scale eddies was over-estimated by URANS due to them being modelled in the same way as much smaller structures instead of directly resolved in LES. Large-scale eddies tend to be quite different in nature and highly anisotropic.

2.3 Cooled trailing edge geometries

Earlier-generation engines tended to feature *centred-ejection* type TE designs, in which the slot is set centrally in the TE base. The SS and PS half-bases on either side of the slot are located flush in the direction of slot ejection (see Figure 9a). More recent engines have favoured TE designs with a *SS-overhang*, in which the SS half-base extends further downstream (in the direction of slot ejection) than the PS half-base (see Figure 9b). Such designs are generally (although not conclusively) considered to be advantageous from an aerodynamic perspective by presenting a thinner base region. There are a small number of direct comparisons of the performance of these two main types of cooled TE geometry in the open literature which are reviewed in the following section.



(a) Centred-ejection (b) SS-overhang

Figure 9: Diagrams of basic cooled trailing edge geometries.

The earliest studies of TE coolant ejection slot geometry and performance of which I am aware are those reported by Whitney et al. (1969) [39], Prust et al. (1974) [40] and Prust (1975) [41]. They tested centred-ejection TE geometries with a range of TE thicknesses, slot widths, and coolant mass flow rates, in a simple 2D cascade experiment. The introduction of TE coolant flow was reported to cause a reduction in mainstream mass flow rate of up to −1% (due to displacement by the added coolant flow), a reduction in mean exit flow angle of up to −2°, and an increase in

turbine work output of up to +8%. It should be noted that efficiency changes between different TE geometries were reported in terms of primary efficiency—that is, taking no account of the kinetic energy input of the added coolant flow. In most cases, efficiency was found to rise significantly with coolant-to-mainstream mass flow ratio, except for very narrow slots with mass flow ratios below 1.0% where a minimum loss coefficient was seen. The change in efficiency arose due to a combination of the KE of the coolant jet in relation to that of the mainstream, and also the impact of the coolant flow on TE loss (affecting the base pressure distribution and the effective TE blockage). At mass flow ratios below approximately 2.0%, the KE of the coolant jet was low and the latter effect was relatively strong, producing higher efficiency from wider slot designs. In contrast for mass flow ratios above 2.0% the former effect was dominant and narrower slots performed better. The positive impact of high coolant KE on efficiency was conflated by the fact that the efficiency definition took no account of the coolant flow in the ideal reference flow. This problem was addressed in more recent studies by including the coolant energy input in the definitions of efficiency and loss coefficient.

2.3.1 Analysis of trailing edge cooled nozzle guide vane performance and sensitivity of loss coefficient to trailing edge blowing rate

A number of authors have studied the performance of single cooled vane geometries, commonly focussing on the impact of varying TE blowing rate on TE loss. These are now reviewed in chronological order.

In 1995, Bohn et al. [42] experimentally and numerically investigated the flow downstream of an annular NGV cascade with coolant ejection from a central TE slot. They used Laser Doppler Anemometry (LDA) to measure velocity and turbulence distributions immediately downstream of the slot exit. The radial pressure gradient in the annular cascade strongly influenced the effects of TE coolant flow on the external flow-field. The induced radial migration of coolant flow towards the hub gave rise to significantly higher coolant concentration at lower radii. Note that these traverse measurements were made extremely close to the TE (approximately one slot thickness downstream—well within one TE thickness), and therefore detect the mainstream and coolant jet flows at a very early stage of their interaction. This is generally not possible using

conventional traverse measurement techniques. Turbulence measurements revealed a pronounced anisotropy in regions of high velocity gradient in the wake. The numerical model was reasonably successful in reproducing the experimental velocity field, but was unable to replicate the anisotropic turbulence and thus some of the complex mixing mechanisms, due to the limitations of the turbulence model. This highlights the difficulty of predicting the wake profile development immediately downstream of the TE.

In 1997, Deckers and Denton [43] experimentally tested a cooled TE with a central slot in a transonic test facility, using both a flat plate model and a 2D turbine cascade. They confirmed that the effect of changing coolant-to-mainstream temperature ratio on both the base pressure and the associated TE loss coefficient was negligible. The aerodynamic effect of TE coolant ejection can therefore be satisfactorily studied in low temperature experiments. The mere presence of the TE slot, with no coolant flow, significantly raised the base pressure (cavity effect).

The cascade test data in [43] showed a rise in base pressure with increasing coolant flow rate at low coolant-to-mainstream mass flow ratio, and the opposite trend at higher flow rates. There was therefore a maximum base pressure condition at intermediate flow rate. A small degree of asymmetry was observed between the base pressures on either side of the TE slot, in agreement with [31]. The asymmetry was small for the symmetric slot tested in this study, but would likely be larger for more complex, asymmetric TE designs. The trend in KE loss coefficient largely mirrored that in base pressure, falling to a minimum at a coolant-to-mainstream mass flow ratio of approximately 1% before rising at higher flow rates. However, the minimum loss coefficient and maximum base pressure conditions did not exactly coincide. This point is expanded on in [45] which breaks down individual contributions to TE loss coefficient, see below. Measuring base pressure alone is therefore not sufficient to assess aerodynamic performance. They also considered the trend in loss coefficient with exit Mach number. Loss coefficient grew rapidly as exit Mach number approached unity (due to additional mixing loss, shock loss and boundary layer loss caused by stronger shock-boundary layer interaction) and somewhat surprisingly, fell equally

rapidly above Mach 1. This was primarily attributed to changes in the TE shock system, which influence the SS shock-boundary layer interaction.

Deckers and Denton also analysed theoretical predictions of base pressure and loss for TE-cooled NGV cascades [44]. The theoretical method applied a control volume analysis (conserving mass, momentum, and energy) between the exit plane of a choked cascade and a hypothetical fully mixed-out plane far downstream (mixing taking place in an adiabatic, constant area duct). This was an extension of the analytical methods first developed by Stewart [24] in the 1950s, and refined and presented by Denton and Xu [23], adapted to the case of a TE-cooled transonic cascade. It is also theoretically similar to the 2D mixing method of Amecke [12], replacing the non-uniform traverse plane with the cascade exit plane where flow is assumed to be uniform across the free-stream. To the extent that it captures the boundary conditions of the real cascade, such a model was shown to predict the base pressure and TE loss exactly. That is, trends in base pressure and TE loss (excluding changes occurring upstream of the TE, for example in the surface boundary layers) could be predicted without knowing details of the complex viscous dissipation processes occurring inside the control volume: changes in TE loss can be explained through inviscid effects alone. The analysis is only valid for cases which can reasonably be represented given the necessary simplifications. Chief among these is the assumption that the flow chokes at a well-defined 1D throat (flat sonic line), which is virtually guaranteed to be a poor approximation to a real NGV row. In reality the sonic surface (such that one can be defined) is expected to be highly curved due to streamline curvature (intersecting the minimum physical area plane at a high angle) and may extend into the wake region downstream of the passage. Results obtained from the model showed that for a given coolant-to-mainstream pressure ratio, the TE slot should ideally be as wide as possible. This indicates an aerodynamic effect dominated by the coolant jet reducing the effective TE blockage.

In 1998, Raffel and Kost [45] tested a central-ejection TE slot on a flat plate working section in a high-speed tunnel (exit Mach number approximately 1.1–1.3) with contoured endwalls. This setup generated representative flow structures around the TE. Schlieren imaging

and PIV experimental visualisation techniques were used to examine wake and shock structures in the vicinity of the TE. Detailed analysis was provided of the practical challenges of using PIV in this application: seeding the whole of the flow, including the TE coolant flow, with tracer particles; the need to use sufficiently small seed particles to avoid the effect of velocity lag in such high-speed flow; and accurately recording the movement of such small seed particles between successive frames.

Exit flow-fields were compared between different coolant-to-mainstream mass flow ratios. The introduction of moderate TE coolant flow significantly weakened the oblique shockwaves formed on either side of the TE. The single shock observed on each side of the TE in the uncooled case was replaced by a pair of weaker oblique shocks. This configuration had a lower associated total loss, and hence coincided with a minimum in the mixed-out loss coefficient trend. The change in TE shock structure was reversed at higher coolant-to-mainstream mass flow ratios.

The impact of TE coolant ejection on mixed-out loss coefficient was split into two distinct (but interconnected) effects: change in TE loss caused by change in base pressure; and coolant mixing loss. These two contributions had opposing trends with coolant-to-mainstream mass flow ratio. As coolant flow rate rose, TE loss coefficient first dropped to a minimum at moderate coolant-to-mainstream mass-flow-rate, before increasing at higher flow rates. This trend was driven by an opposite change in base pressure (maximum base pressure coinciding with minimum TE loss coefficient). Coolant mixing loss coefficient rose with coolant flow rate at low to moderate mass flow ratios, before falling as the coolant-to-mainstream velocity ratio approached unity. At very high flow rates, the effect of coolant mixing on total loss coefficient actually became negative.

In 1999, Pappu and Schobeiri [46] presented experimental measurements from two different vane cascades with centred-ejection TE geometries operated at high-subsonic condition and a range of coolant-to-mainstream mass flow ratios (0–4%). The data were compared with predictions from the theoretical model of Schobeiri [47]. This was a control volume mixing model (similar to the model in [44]) which expressed TE mixing loss as a function of the key influencing

parameters: slot-to-TE thickness ratio; coolant-to-mainstream mass-flow ratio, velocity ratio, and temperature ratio; and slot ejection angle. Experimental data and theoretical predictions agreed strongly in terms of the relative sensitivities of loss coefficient to variations in coolant-to-mainstream mass flow ratio and slot-to-TE thickness ratio.

'Mixing total pressure loss coefficients' were plotted as functions of coolant-to-mainstream velocity ratio (rather than mass flow ratio, as in most of the literature). The somewhat obscure loss coefficient definition refers to the total pressure loss in the mixing process downstream of the cascade (excluding all other sources of loss). This is equivalent to the coolant mixing term in [45] in isolation. Three distinct regions of behaviour were observed as velocity ratio gradually increased. Mixing total pressure loss initially rose with respect to the uncooled case for velocity ratios up to 0.26. The momentum of the coolant jet was so low that it was rapidly entrained by the mainstream flow and completely dissipated. For higher velocity ratios, the momentum of the coolant jet was sufficient to prevent it from being completely dissipated. The mixing total pressure loss coefficient therefore reduced, reaching a minimum at a velocity ratio of 1.01. At this condition the shear layers between the coolant and mainstream flows were at their smallest. Beyond this, further increases in velocity ratio led to the mixing total pressure loss coefficient rising again. The additional momentum of the coolant jet (above the specific momentum of the mainstream flow) was simply dissipated and contributed to increased mixing loss. This function shape was largely in accord with the results in [45], but over a wider range of coolant flow rates. The neutral effect on mixing loss coefficient with respect to uncooled at a velocity ratio of approximately 0.50 was replicated between the two sources.

Selecting an inappropriate slot-to-TE thickness ratio was shown to potentially yield a mixing loss coefficient much worse than for the solid, uncooled vane. The range of slot thicknesses over which TE cooling could provide an advantage was small. The higher the coolant-to-mainstream mass flow ratio, the higher the optimum slot-to-TE thickness ratio, the greater the mixing loss coefficient advantage it provided with respect to the solid vane, and also the wider the range of

slot thicknesses that gave some benefit. These conclusions would need to be considered in terms of the total loss coefficient.

In 2007, Brundage et al. [48] experimentally investigated the aerodynamic and thermal performance of a cooled TE at a range of coolant-to-mainstream mass flow ratios from 0–4% and at high-subsonic exit Mach number. The experimental setup again used a flat plate test model in a tunnel with contoured walls (similar to the experiments in [45]), designed to simulate the pressure distribution of a turbine cascade. Heat transfer from the mainstream to the coolant flow increased with increasing coolant-to-mainstream mass-flow-rate, but with diminishing returns at higher coolant flow rates. The impact of varying coolant flow rate on aerodynamic performance was quantified using base pressure measurements. In accord with the previous literature ([31],[45],[46]), base pressure increased as TE coolant mass flow rate was steadily increased from zero, reaching a maximum at a coolant-to-mainstream mass flow ratio of 2.1%. This of course corresponds with a minimum in the TE loss contribution to total loss coefficient. Further increase in coolant flow rate produced a stronger coolant jet, influencing the separation points on the SS and PS surfaces and broadening the wake region, with an associated drop in base pressure.

In 2009, Montis et al. [49] compared experimental and numerical assessments of the aerodynamic performance of a TE cooled NGV cascade for a range of coolant-to-mainstream mass flow ratios from zero (uncooled) to 1.5%, at an exit Mach number of 0.8. The vane geometry used in this study had a SS-overhang, but one significantly shorter than those in many other studies in the literature. The numerical method over-estimated absolute loss coefficient by around 10% but matched closely the measured trends in average loss coefficient with coolant-to-mainstream mass flow ratio. Average loss coefficients were presented using both ‘primary’ and ‘thermal’ coefficient definitions. The former benchmarks the measured exit flow against an ideal expansion from the inlet conditions of the mainstream flow only. The latter additionally includes the energy input of coolant flow in the ideal expansion process. These two representations showed opposite trends with coolant-to-mainstream mass flow ratio. ‘Primary’ loss coefficient rose to a maximum at a mass flow ratio of 0.7% (additional mixing loss in shear layers between the

mainstream and coolant flows of differing exit velocities) before dropping sharply at higher coolant flow rates (significant energy added to the system in the coolant flow, effectively seen as 'free' energy, due to not being 'counted' in the inlet flow energy). In contrast, 'thermal' loss coefficient fell to a minimum at a mass flow ratio of 0.3% (Small coolant flow 'filled in' the low energy wake region, increasing base pressure) before rising monotonically with further increases in mass flow ratio (Higher energy coolant flow was unable to accelerate wake flow—extra energy was rapidly dissipated and base pressure fell). This demonstrates the importance of accounting for the input energy of the coolant flow when evaluating accurate absolute loss coefficient values, or when comparing between different coolant flow rates.

In 2014, Saha et al. [51] tested an annular sector NGV cascade with centred-ejection TE geometry. Detailed traverse measurements showed that the impact of TE cooling on the secondary flow structures was minimal. Introducing coolant flow produced a rise in total pressure loss, and a reduction in turning (up to −0.4°). At the nominal coolant-to-mainstream mass flow ratio of 1.35%, profile loss coefficient rose by approximately 31% with respect to the uncooled vane. Increasing coolant flow rate gave a monotonic rise in KE loss coefficient (accounting for the KE input of the coolant flow in the isentropic reference condition) across the whole profile region. However, primary KE loss coefficient (in which the isentropic reference condition includes the KE input of the mainstream flow only) was remarkably insensitive to coolant flow rate, with an approximately equal increase with respect to the uncooled vane for all tested coolant-to-mainstream mass-flow ratios. These results are at odds with most of the prior literature, which observed stationary points in the trend of loss coefficient with coolant flow rate using both definitions. It should be noted that the range of coolant-to-mainstream mass flow ratios tested in this study was small in comparison to others (0.8–1.5%, compared to a typical range of at least 0.0–4.0%). A different result might be revealed if a wider range of mass-flow-rates were tested.

Saha et al. [51] also proposed a novel hybrid definition of local KE loss coefficient for cooled turbine blade rows. This effectively approximated the local distribution of coolant flow by setting the coolant-to-mainstream mass flow ratio equal to the overall ratio in the wake regions,

and equal to zero in the free-stream. When used to evaluate circumferential-average loss coefficient values, the method was in excellent agreement with the primary loss coefficient (i.e. local loss coefficient defined in the form of equation (6)).

2.3.2 Comparisons of different trailing edge geometries

Studies in the open literature which have directly compared the performance of two or more cooled TE geometries are now reviewed, in chronological order.

In 1985, Kost and Holmes [52] compared the performance of turbine blades with a central TE slot and with film cooling rows close to the TE on both the PS and SS, at an exit Mach number of 1.15. The latter design provided a thinner ultimate TE (akin to a modern SS-overhang design), as well as film coverage near the TE. With no coolant flow, the central slot blade gave 76.2% higher KE loss coefficient (expressed as a % of the film-cooled loss coefficient) than the film cooled blade. The introduction of moderate coolant flow yielded a reduction in loss coefficient for both TE geometries, but a larger reduction for the slotted blade. When coolant-to-mainstream mass flow ratio reached 3.5%, the difference in loss coefficient dropped to 11.2%. The large difference in loss coefficient between the two designs is unsurprising since the ultimate TE thickness of the slotted blade was approximately 2.7 times greater to accommodate the slot. This result is a valid comparison, however, since the minimum metal thickness (of the entire TE in the film-cooled case and of the individual tips on either side of the slot in the slotted case), which would be set by the thermal and mechanical constraints on the blade, was approximately equal in both cases. This highlights the challenge of making fair and relevant comparisons between different TE geometries, which is faced by many studies in this review and also in the present work.

In 1994, Kapteijn et al. [53] compared the performance of centred-ejection and SS-overhang TE geometries over a range of exit Mach numbers 0.7–1.2. Precise details of the two geometries were not stated explicitly, but inspection of the diagrams shown in the paper suggests that the minimum metal thickness for the SS-overhang design was around 25% higher than that for the centred-ejection design. It should also be noted that the energy contribution of the coolant

flow was not accounted for in defining loss coefficients, which is an issue when comparing results for different coolant-to-mainstream mass flow ratios. At subsonic conditions, the SS-overhang geometry gave approximately 24% higher KE loss coefficient than the centred-ejection design. This difference is likely to be exaggerated by the difference in minimum metal thickness noted above. As the exit Mach number passed unity, both geometries exhibited a rapid rise in loss coefficient. The rise in loss coefficient was roughly 50% larger for the SS-overhang, such that the difference between them grew to 36%. At zero coolant flow rate and Mach number 1.1, schlieren images showed a distinct shockwave originating at the backward-facing step of the PS TE lip. This shock impinged on the adjacent vane SS and induced boundary layer separation, which explains the larger rise in loss coefficient in supersonic flow. The shock was suppressed by coolant-to-mainstream mass flow ratios above 2%, as the effective step height was reduced. The SS-overhang geometry was also shown to have a slightly faster wake mixing rate, although this was partially explained by the location of the slot exit moving slightly further upstream.

In 2001, Uzol and Camcı [50] experimentally compared the performance of vanes with centred-ejection and SS-overhang style TE designs (with equal minimum metal thicknesses), at four different coolant-to-mainstream mass flow ratios at subsonic conditions. Particle Image Velocimetry (PIV) was used to visualise the time-mean velocity field in the near-TE wake, and showed that, with respect to the centred-ejection design, the SS-overhang geometry produced both a shallower (reduced peak velocity-deficit in the wake centre) and more asymmetrical wake (more gradual velocity profile decay on the PS than the SS). These changes in the wake profile produced a lower average total pressure loss coefficient for the SS-overhang design by –15.9%. Losses were presented only in terms of total pressure loss coefficient, so the quantitative results should be treated with some caution. With increasing coolant-to-mainstream mass flow ratio, average total pressure loss coefficient first rose to a maximum before falling at high mass flow ratios for both TE geometries. This matched the trend in primary KE loss coefficient reported in the previous literature, although the sensitivity of average total pressure loss to mass flow ratio was significantly higher for the SS-overhang geometry. The gradient of the trend before the

maximum point was roughly five times greater than for the central slot design. This difference was attributed to the influence of changing mass flow ratio on the effective height of the surface discontinuity at the PS lip and consequently on the deviation of the PS mainstream flow.

In 2009, Johnson et al. [54] examined the aerodynamic performance of a vane with a 'gill slot' TE geometry—effectively a slot with a SS-overhang. In a follow-up paper, Fiala et al. [55] compared the gill slot data with a 'letterbox' design. This was very similar to the gill slot, but with the slot split up by a series of internal partitions along the vane span. Their tests were performed in a low-speed cascade, and thus are less applicable to the engine environment. These papers had a different focus to the rest of the literature in this section, in particular considering the impacts of TE cooling on secondary flow structures, and sensitivity to incident turbulence intensity.

The gill slot and letterbox geometries produced very similar local total pressure distributions, including secondary flow structures. The main difference was the introduction of pronounced radial total pressure fluctuations over the profile region of span for the letterbox TE, corresponding with the internal partitions. With respect to a reference solid TE, the letterbox geometry produced a slightly smaller (−0.2%) increase in mass-averaged total pressure loss than the gill slot design. That is, the internal partitions gave a small reduction in total pressure loss (note that, based on the evidence from the studies in the previous sub-section, local coolant flow deficits could generate either an increase or decrease in loss coefficient depending on the coolant flow rate and the exact coefficient definition). An increase in inlet turbulence intensity from a very low level up to a high intensity representative of a combustor exit flow produced a rise in average total pressure loss. This was attributed to an increase in free-stream turbulent mixing loss, and a thickening of the inlet boundary layers. The relative performance of the different TE geometries was found to be virtually insensitive to the level of inlet turbulence intensity.

In 2012, Rehder [56] tested three cooled TE geometries in an enlarged scale linear cascade: a central slot; an SS-overhang; and a row of film cooling holes close to the TE on the pressure surface. He compared their performance over a range of coolant-to-mainstream mass flow ratios

(0–2%), and at exit Mach numbers 0.9 and 1.2. The observed trend with varying coolant-to-mainstream mass flow ratio was in accord with the literature in the previous section, with a maximum base pressure (closely associated to a minimum loss coefficient) occurring at 1% mass flow ratio. Rehder used Schlieren imaging to visualise the difference in TE flow-fields between the geometries. For the SS-overhang design, PS mainstream flow inevitably separated at the upstream lip of the cutback region. The separated flow rolled up into a vortex and turned mainstream flow into the cutback area, contributing to a lower base pressure with respect to the central slot geometry at the same condition. At high-subsonic exit Mach number, the SS-overhang geometry exhibited very strong vortex shedding in the wake for low coolant blowing rates, as well as pressure waves shed in phase with the vortices. These propagated out into the flow and reflected from the adjacent vane SS. Such strong unsteady behaviour was not observed for the central slot design, and was largely suppressed at supersonic exit Mach number for both geometries. Higher TE blowing rate from the SS-overhang vane was also successful in partly suppressing vortex and pressure wave shedding, as the coolant flow 'filled in' the dead air within the overhang region.

Total mixed-out loss coefficient was broken down into separate contributions using an adaptation of the control volume mixing method of Amecke [12]. Boundary layer loss and shock loss components—whilst being major contributors to total loss coefficient—were almost independent of coolant-to-mainstream mass flow ratio, whereas coolant mixing loss and TE loss were highly sensitive to coolant-to-mainstream mass flow ratio. This result fits with expectations. The central slot geometry gave the lowest total loss coefficient at both high-subsonic and supersonic Mach number, and for all coolant flow rates. The SS-overhang produced approximately 50% higher total loss coefficient at moderate coolant flow rate, rising to as much as 200% higher at high flow rates. Rehder concluded that a central slot is always superior in terms of total loss coefficient. The additional loss generated in the SS-overhang case was attributed to interaction between mainstream and coolant flow in the cavity downstream of the PS lip. However, inspection of the tested geometries casts some doubt on these conclusions. Firstly, the

SS tip of the SS-overhang geometry was as thick as the entire centred-ejection TE (including the slot). It therefore had significantly higher minimum metal thickness causing an inevitable increase in total loss. Secondly, the SS-overhang design also had an extended rib array inside the TE slot, which reduced coolant exit velocity for a given coolant-to-mainstream mass flow ratio, thereby increasing the mixing loss. Both of these factors unfairly penalise the SS-overhang geometry.

In 2016, Wang et al. [57] presented perhaps the most comprehensive computational study of the impact of SS overhang length on turbine blade aerodynamic performance in the literature to date. They used 2D RANS CFD, validated against linear cascade experimental data, to study a typical HP rotor geometry with an SS-overhang TE design, at an exit Mach number of 1.2. They compared five different overhang lengths ranging from 6–14% of tangential chord at a range of coolant-to-mainstream mass flow ratios 0–6%. This is the first known parametric study of SS TE overhang length in the literature. The SS TE tip was fixed between all geometries, with changes in overhang length realised by moving the PS lip. This means that the SS TE thickness (and therefore the ultimate TE thickness) was fixed between all of the geometries, although there may have been some change in the PS TE thickness which could have a small influence on the results. Figure 10 shows KE loss coefficient (accounting for coolant energy input in the isentropic reference) data as a function of coolant-to-mainstream mass flow ratio, and it is clear that the sensitivity of loss coefficient to mass flow ratio depends on the overhang length. Short overhang lengths (up to about 10% of tangential chord) have a minimum loss coefficient condition at a moderate mass flow ratio (up to 3%). This trend is by now very familiar from the literature in the previous section. In contrast, overhangs of 12% of tangential chord or longer show a monotonic rise in loss coefficient with mass flow ratio. The shorter the overhang, the greater the coolant flow rate required to achieve the minimum loss coefficient (and the higher the minimum achievable loss coefficient). At moderate mass flow ratios relevant to the HP turbine (typically 2–3%), short and mid-length overhangs perform best. At higher mass flow ratios, short overhangs appear strongly beneficial. No clear reasoning was given for the worse performance of longer overhang geometries at higher mass flow ratios.

The fundamental effect of changing overhang length on the TE flow and shock structure was also examined. Shockwaves were observed originating at the point of confluence of the SS and PS flows downstream of the TE on both the SS and PS of the vane. In longer overhang geometries, a second PS shock was visible, originating from the PS lip as mainstream flow passing over the backward-facing step was compressed by the inner surface of the SS TE. The presence and intensity of this shock was determined by both overhang length and coolant-to-mainstream mass flow ratio. Increasing overhang length and/or increasing the coolant flow rate reduced the effective height of the backward-facing step, and therefore reduced the intensity of the shock. It may be that the single stronger shock was a higher loss configuration than the pair of weaker shocks, contributing to the higher loss coefficient for long overhangs at higher mass flow rates.

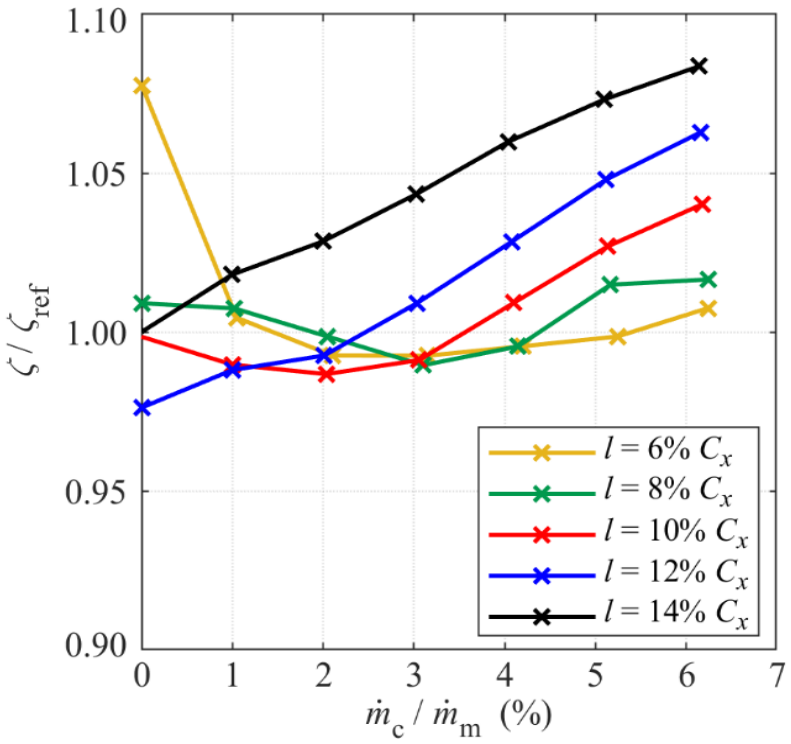


Figure 10: Normalised trends in KE loss coefficient with TE coolant-to-mainstream mass-flux ratio, for different TE overhang lengths. Adapted from [57].

Melzer [37] experimentally compared different SS-overhang lengths at a range of Mach numbers 0.4–1.0 and TE blowing ratios 0.0–1.0 in both an isolated TE (on a flat plate) and a cascade setting. He used Schlieren imaging to visualise the unsteady wake flows produced by each geometry, and showed that detecting transonic vortex shedding (involving vortex formation very close to the TE and periodic shedding of shocks) is central to understanding TE flow behaviour.

Transonic shedding was responsible for large increases in TE loss coefficient. Suppressing transonic shedding, (moving the site of vortex formation at least one TE thickness downstream) was a key factor in minimising TE loss coefficient.

Three distinct cases of flow behaviour were observed at different ranges of TE blowing ratio. At low blowing ratios (0.0–0.2), transonic vortex shedding was observed from the entire (SS + PS) TE base region, unless suppressed by a sufficiently long SS overhang (at least approximately 6% of tangential chord). The long overhang acted like a splitter plate to prevent vortex roll-up. In this case, longer overhang designs offered advantages in TE loss coefficient of up to 43%. At moderate blowing rates (in the range 0.3–0.7), all geometries successfully suppressed transonic shedding. In this case the differences in KE loss coefficient between geometries were comparatively small (within ±22%). At high blowing rates (above approximately 0.7), the high energy coolant jet split the base region in two with distinct vortex sheets shed from each of the SS and PS TE tips. Transonic shedding was observed only for a specific short overhang length (approximately 1.5% of tangential chord), when vortices shed from the two separate TE tips were synchronised and were able to combine to form a single vortex sheet structure. This had an associated TE loss coefficient increase of up to 43%. These results illustrate the scale of the challenge of accurately predicting TE losses of transonic turbine cascades using numerical methods: without an unsteady method able to predict the presence of transonic vortex shedding, TE losses will likely be significantly under-predicted.

Using the data presented by Wang et al. [57] and Melzer [37], we can estimate the sensitivity of TE loss to SS overhang length at an engine-representative exit Mach number. Figures 10 and 11 show normalised KE loss coefficient as a function of TE blowing ratio for a range of SS overhang lengths, using data from [57] and [37] respectively. Whilst these two datasets were obtained from different vane geometries at different exit Mach numbers (1.20 for Figure 10 compared to 0.97 for Figure 11), and use different normalisations, we can compare the indicated sensitivities to overhang length.

Both figures show a change in the ranking of the different overhang lengths with blowing ratio. The overhang length giving the lowest loss coefficient gradually falls with increasing blowing ratio. In Figure 10, at low blowing ratios the lowest loss coefficient is provided by mid-length overhangs (10–12% of tangential chord). At higher blowing ratios, loss coefficient rises sharply for the longer overhangs whilst remaining flatter for shorter overhangs, and the lowest loss coefficient is given by overhangs of 6–8% of tangential chord. In Figure 11, the long overhang gave the lowest loss coefficient at very low blowing ratio, whilst the short overhang gave the lowest at a blowing ratio of approximately 0.5. At blowing ratios above around 0.7, the loss coefficient of the short overhang design rose rapidly as vortices shed from the two separate bases combined to form a single von Kárman vortex sheet. At these conditions, the centred-ejection geometry actually narrowly gave the lowest loss coefficient.

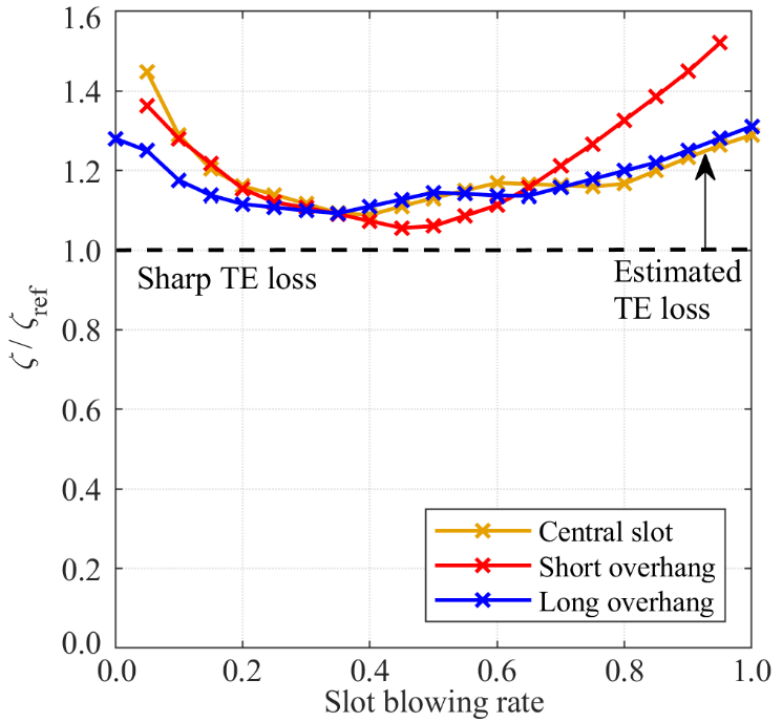


Figure 11: Normalised trends in KE loss coefficient with TE slot blowing rate for different TE designs, at an exit Mach number of 0.97. Adapted from [37].

2.3.3 Summary of cooled trailing edge literature

There is a very solid consensus in the literature in terms of the trend in trailing edge loss coefficient with coolant-to-mainstream mass flow ratio. When the energy input of the coolant flow is accounted for in the loss coefficient definition, loss coefficient first falls to a minimum

value at a moderate mass flow ratio (typically around 1%), before rising as mass flow ratio becomes high. The corresponding trend in base pressure is broadly the reverse, with a maximum base pressure value occurring at moderate mass flow ratio. The minimum loss coefficient and maximum base pressure do not exactly coincide, as changes in base pressure are directly related to only one part of the trailing edge loss. Coolant mixing loss has a different variation, scaling with the velocity gradients in the shear layers between the mainstream and coolant flows.

The literature does not present a convincing consensus regarding the relative aerodynamic performance of different cooled trailing edge geometries. Some sources (e.g. [53], [56]) recorded *greater* loss coefficients for geometries with trailing edge overhang than for centred-ejection geometries at equivalent operating conditions, and by very large margins. On the other hand, other sources (e.g. [50]) recorded significantly *lower* loss coefficients for geometries with trailing edge overhang.

The few published parametric studies of trailing edge overhang length show that the loss coefficient ranking of different overhang lengths is strongly sensitive to coolant-to-mainstream mass flow ratio (longer overhangs appear more advantageous at low mass flow ratios, whilst centred-ejection style geometries tend to perform better at high mass flow ratios). The relative performance of different overhang lengths is also highly influenced by changes in unsteady flow behaviour.

2.3.4 Other recent developments in cooled trailing edge geometry

Finally, some recent developments related to cooled trailing edge geometries are highlighted.

In 2013, Aminossadati and Mee [58] tested a low-speed turbine cascade with coolant ejected from a series of holes set in the TE. The study focussed on the impact of radially inclining the channels feeding the TE ejection holes, which was thought to offer potential benefits in vane thermal performance. Only one vane in the cascade was actually cooled, so there is some concern regarding the periodicity and boundary conditions. For fixed coolant channel geometry, the trend of KE loss coefficient with TE blowing rate matched the previous literature. The inclination angle of the coolant channels had almost no impact on loss coefficient for low blowing rates (whilst

coolant-to-mainstream velocity ratio was less than unity). For velocity ratios greater than unity, an inclination angle of just 15° produced a rise in loss coefficient of up to 80%.

Parbat et al. [59] presented a novel cooled-TE design featuring a TE section with a pitchwise-sinusoidal profile along the span. This design was intended to distribute coolant over both the PS and SS TE surfaces (as opposed to PS only in an SS-overhang design) with associated thermal advantages, whilst also minimising aerodynamic losses. Indeed, the novel design provided film coverage of both TE surfaces over the full span. Whilst it exhibited spanwise oscillations in cooling effectiveness on both surfaces corresponding with the sinusoidal geometry, these were notably smaller than a conventional SS-overhang (which barely cooled the SS TE at all) and therefore gave a significant improvement in thermal performance. On the other hand, the novel design gave approximately 25% higher wake total pressure deficit with respect to conventional SS-overhang and centred-ejection designs. This demonstrates that a lot of development and optimisation of the new design would be required to achieve satisfactory aerodynamic performance. Such a design would also present manufacturing challenges, and would likely suffer severely from in-service deterioration effects, due to its complex 3D geometry.

2.4 Studies of nozzle guide vane aerodynamic performance in high-TRL experimental environments

Simplified experiments designed to isolate the impact of particular design features (e.g. film and TE cooling configurations; TE design; fillets at the vane surface-endwall junctions; 3D shaping; inlet flow conditions at the combustor-turbine interface) are well-suited to developing understanding of fundamental aspects of design, but poorly-suited to characterising engine parts in a realistic operating environment. This is important both for early-stage design and also for CFD calibration. Doing so requires the use of actual engine components operating at scaled engine conditions (Mach and Reynolds numbers, and coolant-to-mainstream pressure ratio), ideally (because of periodicity effects) in a fully-annular cascade.

A handful of studies in the open literature meet some of these requirements, presenting aerodynamic traverse data from either annular sector or fully-annular cascades which are, to

varying degrees, representative of typical engine geometries. These studies generally focus on one or two specific aspects of the turbine flow-field, and examine how they develop in a more realistic environment (for example under the influence of the radial pressure gradient in annular cascades), or their interactions with features of realistic engine component geometries such as endwall fillets and realistic secondary flow structures.

In 1982, Binder and Romey [60] presented experimental traverse measurements (annular area surveys of total pressure loss and flow angles) made in four different axial planes downstream of an annular turbine NGV cascade (up to 3.3 chord lengths downstream), at an exit Mach number of 0.74. These data were primarily used to study the wake mixing process and the secondary flow structures, whilst estimates of mixing loss coefficient were also assessed. Secondary vortex cores were identified in the traverse data on the basis of the velocity and flow angle distributions. Secondary cores at the hub were located very close to the hub endwall, whilst at the case they were located further from the wall. This was driven by the radial pressure gradient in the annular swirling flow, which causes radially-inward flow migration—and particularly strongly for lower momentum flow in wake and secondary regions. Development of the local flow-field continued throughout the entirety of the traversed axial range, accompanied by a gradual increase in average loss coefficient with distance downstream of the TE due to the rise in mixing loss.

In 1984, Sieverding et al. [61] studied the 3D flow-field downstream of an annular NGV cascade at low-speed condition. The vane geometry was radially-uniform so not particularly representative of a modern NGV design, but for the time was a step forward in the TRL of experiments in the literature. They presented area-surveys of total pressure, static pressure, and secondary velocity components in a series of axial planes. The significant influence of the radial pressure gradient on the development of the flow-field was observed, generating very different passage vortex strengths between hub and case and hence different endwall effects for total pressure loss and flow angles. Sieverding et al. [62] in 1996 also studied the flow-field downstream of an annular cascade of TE-cooled NGVs operating at transonic conditions (Mach number 1.05). The vane geometry was very similar to that used in [61], with an SS-overhang TE

design. They made the same observations regarding the radial distribution of secondary losses as the other authors in this section. By one axial chord length downstream of the TE, the wakes had spread circumferentially to cover the entire passage, whilst the secondary loss cores combined with the endwall boundary layers. The impact of TE coolant flow on the wake profiles was minimal, indicating a rapid mixing with the mainstream. A fast-response pressure probe was used to measure turbulent velocity fluctuations across the wake profile. Higher magnitude of fluctuations was found in the wakes as expected, with a small secondary peak thought to show the impact of the TE coolant jet. Interestingly, the magnitude of turbulence in the free-stream was slightly lower than the nominal level of inlet turbulence intensity, possibly attributable to unsteady shedding processes.

In 1986, Williamson and Moustapha [63] presented full-area surveys of total pressure loss downstream of a full-annular cascade of a quite different (from the other studies listed in this section) vane geometry with most of the flow turning completed near the leading edge and a long, almost straight tail-section. Tests were conducted at a range of exit Mach numbers from subsonic up to 1.15. The three-dimensionality of the flow-field increased markedly as exit Mach number approached and exceeded the transonic region, accompanied by a significant increase in average values of mean total pressure loss coefficient and mean flow whirl angle.

In 1999, Day et al. [64] presented experimental data from a full-annular NGV cascade operating at transonic exit Mach number (0.96) and with a high inlet turbulence level typical of the combustor-turbine interface. They examined the impact of a typical surface film cooling configuration on mixed-out row efficiency, based on full-area surveys of total pressure, Mach number, and flow angles. The primary effect of moderate film blowing rate was to significantly widen the wake regions, but with little change in wake depth. Higher film blowing rates produced a slight further widening of the wakes as well as an increase in wake depth. The use of different coolant gas species was also tested, to assess the influence of coolant-to-mainstream density-ratio. It was confirmed that momentum-flux-ratio (rather than blowing rate) is the appropriate parameter to match to remove sensitivity to density-ratio. Mixed-out average loss coefficients evaluated

from 2D traverse measurements showed increases of +9.0% and +10.5% with respect to the uncooled case for two different density-ratios.

In 2002, Trieber et al. [65] performed tests with a full-annular cascade of vanes with a geometry typical of a reaction-type steam turbine. Local distributions of total pressure loss were produced from traverse measurements in multiple axial planes up to one axial chord downstream. The data were used to analyse the evolution of secondary vortex structures and their relationships with the loss generation mechanisms. Components of vorticity were also evaluated from the traverse measurements and used to identify secondary loss core locations and senses of rotation. Two different cascade geometries were compared: a prismatic geometry and a similar cascade with compound lean. The wake profiles downstream of both cascades were skewed circumferentially around the annulus with increasing distance downstream, due to the radial gradient of flow whirl angle. The flow-field behind the vanes with compound lean naturally had much greater curvature with a distinctive bowed shape, and greater variation in the wake thickness over the span. The two legs of the leading edge horseshoe vortex were observed to be the dominant feature of the secondary flow system, and generated further interaction with the endwall boundary layers, dependent on the 3D cascade geometry. Quite different axial developments of total pressure loss and average vorticities were found between the prismatic and leaned cascades, potentially offering a minimum loss condition at a specific axial location, which could be coincided with the following blade row. However, the cause of this effect was not fully explained.

In 2010, Yasa et al. [66] studied an annular sector of cooled engine parts at exit Mach numbers 0.60 and 0.95. Experimental data were compared with complimentary CFD simulations, achieving reasonable agreement in terms of total pressure loss, particularly at the subsonic condition. At the higher Mach number, there was a noticeable over-prediction of profile loss coefficient in CFD. Given that the CFD model had no cooling, this suggests that the level of agreement may not be as good as is indicated. Traverse measurements of the downstream flow-field were used to examine wake characteristics (depth, breadth, and decay rates), radial profiles of flow angles, and secondary flow structures. Fast-response probe measurements were used to

characterise the unsteady vortex shedding in the wake and secondary flow regions. An increase in frequency of unsteady fluctuations was detected moving to the transonic Mach number condition, whilst a drop in frequency was achieved through moderate TE coolant ejection.

2.5 Reference list for literature review

[1] Fielding, L.; 1981; The Effect of Irreversibility on the Capacity of a Turbine Blade Row; Proc. Inst. Mech. Eng., Vol. 195, pp. 127–137

[2] Afanasiev, I.V., Granovskiy, A.V., Karelin, A.M., Kostege, M.K.; 2004; Effect of 3D Vane Shape on the Vane Capacity; Proceedings of ASME Turbo Expo 2004, Vienna, Austria, 14–17 June 2004, Paper No. GT2004-53095, DOI: 10.1115/GT2004-53095

[3] Povey, T.; 2010; Effect of Film Cooling on Turbine Capacity; ASME J. Eng. Gas Turbines Power, Vol. 132(1), DOI: 10.1115/1.3026564

[4] Kollen, O., Koschel, W.; 1985; Effect of Film Cooling on the Aerodynamic Performance of a Turbine Cascade; Paper No. AGARD CP-390

[5] Hambidge, C., Povey, T.; 2012; Numerical and Analytical Study of the Effect of Film Cooling on HP NGV Capacity; Proceedings of ASME Turbo Expo 2012, Copenhagen, Denmark, 11–15 June 2012, Paper No. GT2012-69066, DOI: 10.1115/GT2012-69066

[6] Povey, T., Sharpe, M., Rawlinson, A,; 2011; Experimental Measurements of Gas Turbine Flow Capacity Using a Novel Transient Technique; ASME J. Turbomach., Vol. 133:011005, DOI: 10.1115/1.4000481

[7] Högner, L., Nasuf, A., Voigt, P., Voigt, M., Vogeler, K., Meyer, M., Berridge, C., Goenaga, F.; 2016; Analysis of High Pressure Turbine Nozzle Guide Vanes Considering Geometric Variations; Proceedings of ASME Turbo Expo 2016, Seoul, Korea, 13–17 June 2016, Paper No. GT2016-57502

[8] Kirollos, B., Povey, T.; 2017; Method for Accurately Evaluating Flow Capacity of Individual Film-Cooling Rows of Engine Components; ASME J. Turbomach., Vol. 139(11): 111004, DOI: 10.1115/1.4037028

[9] Denton, J.D.; 1993; Loss Mechanisms in Turbomachines; Proceedings of ASME 1993 International Gas Turbine and Aeroengine Congress and Exposition; Cincinnati, OH, USA, 24–27 May 1993, Paper No. 93-GT-435, V002T14A001, DOI: 10.1115/93-GT-435

[10] Pianko, M., Wazelt, F.; 1982; Propulsion and Energetics Panel Working Group 14 on Suitable Averaging Techniques in Non-Uniform Internal Flows; AGARD Advisory Report No. 182

[11] Cumpsty, N.A., Horlock, J.H.; 2005; Averaging Non-Uniform Flow for a Porpoise; Proceedings of ASME Turbo Expo 2005, 6–9 June 2005, Reno-Tahoe, NV, USA, Paper No. GT2005-68081

[12] Amecke, J.; 1970; Anwendung der Transsonischen Ähnlichkeitsregel auf die Strömung durch ebene Schaufelgitter; VDI Forschungsheft, Vol. 540, pp. 16–28

[13] Dominy, R.G., Harding, S.C.; 1989; An Investigation of Secondary Flows in Nozzle Guide Vanes; AGARD-CP-469, Paper No. 7

[14] Dzung, L.S.; 1971; Konsistente Mittlewerte in der Theorie der Turbomaschinen für Kompressible Medien; BBC-Mitt., Vol. 58: 485–492

[15] Main, A.J., Oldfield, M.L.G., Lock, G.D., Jones, T.V.; 1997; Free Vortex Theory for Efficiency Calculations from Annular Cascade Data; ASME J. Turbomach., Vol. 119(2): 247–255, DOI: 10.1115/1.2841107

[16] Prasad, A.; 2005; Calculation of the Mixed-Out State in Turbomachine Flows; ASME J.Turbomach., Vol. 127(3): 564–572, DOI: 10.1115/1.1928289

[17] Day, C. R.B, 1997; Aerodynamics of an Annular Film-Cooled Turbine Cascade; D.Phil thesis, University of Oxford

[18] Langston, L.S., Nice, M.L., Hooper, R.M.; 1977; Three-Dimensional Flow Within a Turbine Cascade Passage; ASME J. Eng. Power; Vol. 99(1): 21–28, DOI: 10.1115/1.3446247

[19] Langston, L.S.; 1980; Crossflows in a Turbine Cascade Passage; ASME J. Eng. Power, Vol. 102(4): 866–874, DOI: 10.1115/1.3230352

[20] Sharma, O.P., Butler, T.L.; 1987; Predictions of Endwall Losses and Secondary Flows in Axial Flow Turbine Cascades; ASME J. Turbomach., Vol. 109(2): 229–236, DOI: 10.1115/1.3262089

[21] Wang, H.P., Olson, S.J., Goldstein, R.J., Eckert, E.R.G.; 1997; Flow Visualization in a Linear Turbine Cascade of High Performance Turbine Blades; ASME J. Turbomach., Vol. 119(1): 1–8, DOI: 10.1115/1.2841006

[22] Mee, D.J., Baines, N.C., Oldfield, M.L.G., Dickens, T.E.; 1990; An Examination of the Contributions to Loss on a Transonic Turbine Blade in Cascade; ASME J. Turbomach., Vol. 114(1): 155–162, DOI: 10.1115/1.2927979

[23] Denton, J., Xu, L.; 1990; The Trailing Edge Loss of Transonic Turbine Blades; ASME J. Turbomach., Vol. 112(2): 277–285, DOI: 10.1115/1.2927648

[24] Stewart, W.L.; 1955; Analysis of Two-Dimensional Compressible-Flow Loss Characteristics Downstream of Turbomachine Blade Rows in terms of Basic Boundary-Layer Characteristics; NACA Technical Note 3515.1955.

[25] Lieblein, S., Roudebush, W.H.; 1956; Theoretical Loss Relations for Low-Speed Two-Dimensional Cascade Flow; NACA Technical Note 3662.1956

[26] Reeman, J., Simonis, E.A.; 1943; The Effect of Trailing Edge Thickness on Blade Loss; RAE Technical Note Eng. 116

[27] Johnston, I.H., Dransfield, D.C., Fullbrook, D.J.; 1967; Experiments Concerning the Effect of Trailing Edge Thickness on Blade Loss and Turbine Stage Efficiency; Ministry of Aviation Aeronautical Research Council Reports and Memoranda No. 3459

[28] Sieverding, C.H., Stanislas, M., Snoek, J.; 1979; The Base Pressure Problem in Transonic Turbine Cascades; Proceedings of ASME 1979 International Gas Turbine Conference and Exhibit and Solar Energy Conference, Vol. 1B: Gas Turbines, San Diego, CA, USA, 12–15 March 1979, Paper No. 79-GT-120, DOI: 10.1115/79-GT-120

[29] Sieverding, C.H., Richard, H., Desse, J.M.; 2003; Turbine Blade Trailing Edge Flows Characteristics at High Subsonic Outlet Mach Number; ASME J. Turbomach., Vol. 125(2), 298–309, DOI: 10.1115/1.1539057

[30] Vagnoli, S., Verstraete, T., Mateos, B., Sieverding, C.H.; 2015; Prediction of the Unsteady Turbine Trailing Edge Wake Flow Characteristics and Comparison with Experimental Data; Proc. IMechE Part A: J. Power Energy, Vol. 229(5), 487–497, DOI:10.1177/0957650915592074

[31] Sieverding, C.H.; 1982; The Influence of Trailing Edge Ejection on the Base Pressure in Transonic Turbine Cascades; Proceedings of ASME 1982 International Gas Turbine Conference and Exhibit; London, UK, 18–22 April 1982, 82-GT-50, DOI: 10.1115/82-GT-50

[32] Mallock, H.R.A.; 1907; On the Resistance of Air; Proc. R. Soc. London A 79: 262–273, DOI: 10.1098/rspa.1907.0038

[33] Bénard, H.; 1908, Formation de Centres de Giration à l'Arrière d'un Obstacle en Movement; Comptes Rendus Academie des Sciences, 147: 839–842

[34] Gerrard, J.H.; 1966; The Three-Dimensional Structure of the Wake of a Circular Cylinder; Journal of Fluid Mechanics, Vol. 25(1): 143–164, DOI: 10.1017/S0022112066000090

[35] Sieverding, C.H., Richard, H., Desse, J.M.; 2003; Turbine Blade Trailing Edge Flow Characteristics at High Subsonic Outlet Mach Number; ASME J. Turbomach., Vol. 125(2): 298–309, DOI: 10.1115/1.1539057

[36] Léonard, T., Gicquel, L.Y.M., Gourdain, N., Duchaine, F.; 2015; Steady/Unsteady Reynolds-Averaged Navier-Stokes and Large Eddy Simulations of a Turbine Blade at High Subsonic Outlet Mach Number; ASME J. Turbomach., Vol. 137(4): 041001, DOI: 10.1115/1.4028493

[37] Melzer, A.; 2018; Aerodynamics of Transonic Turbine Trailing Edges; PhD thesis, University of Cambridge

[38] Melzer, A.P, Pullan, G.; 2019; The Role of Vortex Shedding in the Trailing Edge Loss of Transonic Turbine Blades; ASME J. Turbomach., Vol. 141(4): 041001, DOI: 10.1115/1.4041307

[39] Whitney, W.J., Szanca, E.M., Behning, F.P.; 1969; Cold-Air Investigation of a Turbine with Stator-Blade Trailing-Edge Coolant Ejection: Part I–Overall Stator Performance; NASA Technical Memorandum X-1901

[40] Prust, H.W., Bartlett, W.M.; 1974; Cold-Air Study of the Effect on Turbine Stator Blade Aerodynamic Performance of Coolant Ejection from Various Trailing-Edge Slot Geometries: Part I–Experimental Results; NASA Technical Memorandum X-3000

[41] Prust, H.W.; 1975; Cold-Air Study of the Effect on Turbine Stator Blade Aerodynamic Performance of Coolant Ejection from Various Trailing-Edge Slot Geometries: Part II–Comparison of Experimental and Analytical Results; NASA Technical Memorandum X-3190

[42] Bohn, D.E., Becker, V.J., Behnke, K.D., Bonhoff, B.F.; 1995; Experimental and Numerical Investigations of the Aerodynamical Effects of Coolant Injection Through the Trailing Edge of a Guide Vane; Proceedings of ASME 1995 International Gas Turbine and Aeroengine Congress and Exposition, Houston, TX, USA, 5–8 June 1995, Paper No. 95-GT-026, DOI: 10.1115/95-GT-026

[43] Deckers, M., Denton, J.D.; 1997; The Aerodynamics of Trailing-Edge-Cooled Transonic Turbine Blades: Part 1—Experimental Approach; Proceedings of ASME International Gas Turbine and Aeroengine Congress and Exhibition 1997, Orlando, FL, USA, 2–5 June 1997, Paper No. 97-GT-518, DOI: 10.1115/97-GT-518

[44] Deckers, M., Denton, J.D.; 1997; The Aerodynamics of Trailing-Edge-Cooled Transonic Turbine Blades: Part 2—Theoretical and Computational Approach; Proceedings of ASME International Gas Turbine and Aeroengine Congress and Exhibition 1997, Orlando, FL, USA, 2–5 June 1997, Paper No. 97-GT-519, DOI: 10.1115/97-GT-519

[45] Raffel, M., Kost, F.; 1998; Investigation of Aerodynamic Effects of Coolant Ejection at the Trailing Edge of a Turbine Blade Model by PIV and Pressure Measurements; Experiments in Fluids, 24(5–6), 447–461

[46] Pappu, K.R., Schobeiri, M.T.; 1999; Optimization of Trailing Edge Ejection Mixing Losses: A Theoretical and Experimental Study; ASME J. Fluids Eng., 121(1): 118–125, DOI: 10.1115/1.2821991

[47] Schobeiri, M.T.; 1989; Optimum Trailing Edge Ejection for Cooled Gas Turbine Blades; ASME J. Turbomach., Vol. 111(4): 510–514, DOI: 10.1115/1.3262301

[48] Brundage, A.L., Plesniak, M.W., Lawless, P.B., Ramadhyani, S.; 2007; Experimental Investigation of Airfoil Trailing Edge Heat Transfer and Aerodynamic Losses; Experimental Thermal and Fluid Science, Vol. 31(3): 249–260, DOI: 10.1016/j.expthermflusci.2006.04.004

[49] Montis, M., Niehuis, R., Guidi, M., Salvadori, S., Martelli, F., Stephan, B.; 2009; Experimental and Numerical Investigation on the Influence of Trailing Edge Bleeding on the Aerodynamics of a NGV Cascade; Proceedings of ASME Turbo Expo 2009, Orlando, FL, USA, 8–12 June 2009, Paper No. GT2009-59910, DOI: 10.1115/GT2009-59910

[50] Uzol, O., Camcı, C.; 2001; Aerodynamic Loss Characteristics of a Turbine Blade with Trailing Edge Coolant Ejection: Part II—External Aerodynamics, Total Pressure Losses and Predictions; ASME J. Turbomach., Vol. 123(2): 249–257, DOI: 10.1115/1.1351817

[51] Saha, R., Fridh, J., Fransson, T.H., Mamaev, B.I., Annerfeldt, M., Utrainen, E.; 2014; Shower Head and Trailing Edge Cooling Influence on Transonic Vane Aero Performance; ASME J. Turbomach. 136(11): 111001, DOI: 10.1115/1.4028024

[52] Kost, F.; Holmes, A.; 1985; Aerodynamic Effect of Coolant Ejection in the Rear Part of Transonic Rotor Blades; AGARD-CP-390, Heat Transfer and Cooling in Gas Turbine Blades, Paper 41

[53] Kapteijn, C., Amecke, J., Michelassi, V.; 1994; Aerodynamic Performance of a Transonic Turbine Guide Vane with Trailing Edge Coolant Ejection: Part I—Experimental Approach; Proceedings of ASME 1994 International Gas Turbine and Aeroengine Congress and Exposition, Den Haag, Netherlands, 13–16 June 1994, Paper No. 94-GT-288, V001T01A099, DOI: 10.1115/94-GT-288

[54] Johnson, J.D., Fiala, N.J., Ames, F.E.; 2009; Gill Slot Trailing Edge Aerodynamics: Effects of Blowing Rate, Reynolds Number, and External Turbulence on Aerodynamic Losses and Pressure Distribution; ASME J. Turbomach., Vol. 131(1): 011016, DOI: 10.1115/1.2813002

[55] Fiala, N.J., Johnson, J.D., Ames, F.E.; 2010; Aerodynamics of a Letterbox Trailing Edge: Effects of Blowing Rate, Reynolds Number, and External Turbulence on Aerodynamic Losses and Pressure Distribution; ASME J. Turbomach., Vol. 132(4): 041011, DOI: 10.1115/1.3195035

[56] Rehder, H.J.; 2012; Investigation of Trailing Edge Cooling Concepts in a High Pressure Turbine Cascade: Aerodynamic Experiments and Loss Analysis; ASME J. Turbomach., Vol. 134(5): 051029, DOI: 10.1115/1.4004748

[57] Wang, Y., Zhou, X., Liu, X., Wang, S.; 2016; Influence of Trailing Edge Coolant Ejection Rate and Cut-back Length on Energy Loss and Shockwave Intensity of a Transonic Turbine Blade; Proceedings of ASME Turbo Expo 2016, Seoul, Korea, 13–17 June 2016, Paper No, GT2016-56859, DOI: 10.1115/GT2016-56859

[58] Aminossadati, S.M., Mee, D.J.; 2013; An Experimental Study on Aerodynamic Performance of Turbine Nozzle Guide Vanes with Trailing-Edge Span-Wise Ejection; ASME J. Turbomach., Vol. 135(3): 031002, DOI: 10.1115/1.4006663

[59] Parbat, S.N., Yang, L., Chyu, M.K., Siw, S.C., Lee, C.P.; 2019; Numerical Study of Heat Transfer in Novel Wavy Trailing Edge Design for Gas Turbine Airfoils; Proceedings of ASME Turbo Expo 2019, Phoenix, AZ, USA, 17–21 June 2019, Paper No. GT2019-91123, DOI: 10.1115/GT2019-91123

[60] Binder, A., Romey, R.; 1983; Secondary Flow Effects and Mixing of the Wake Behind a Turbine Stator; ASME J. Eng. Power, Vol. 105(1): 40–46, DOI: 10.1115/1.3227396

[61] Sieverding, C.H., van Hove, W., Boletis, E.; 1984; Experimental Study of the Three-Dimensional Flow Field in an Annular Turbine Nozzle Guidevane; ASME J. Eng. Gas Turbines Power, Vol. 106(2): 437–444, DOI: 10.1115/1.3239585

[62] Sieverding, C.H., Arts, T., Dénos, R., Martelli, F.; 1996; Investigation of the Flow Field Downstream of a Turbine Trailing Edge Cooled Nozzle Guide Vane; ASME J. Turbomach., Vol. 118(2): 291–300, DOI: 10.1115/1.2836639

[63] Williamson, R.G., Moustapha, S.H.; 1986; Annular Cascade Testing of Turbine Nozzles at High Exit Mach Numbers; ASME J. Fluids Eng., Vol. 108(3): 313–320, DOI: 10.1115/1.3242579

[64] Day, C.R.B., Oldfield, M.L.G., Lock, G.D.; 1999; The Influence of Film Cooling on the Efficiency of an Annular Nozzle Guide Vane Cascade; ASME J. Turbomach., Vol. 121(1): 145–151, DOI: 10.1115/1.2841223

[65] Treiber, M., Abhari, R.S., Sell, M.; 2002; Flow Physics and Vortex Evolution in Annular Cascades; Proceedings of ASME Turbo Expo 2002, Amsterdam, Netherlands, 3–6 June 2002, Paper No. GT2002-30540, DOI: 10.1115/GT2002-30540

[66] Yasa, T., Paniagua, G., Fridh, J., Vogt, D.; 2010; Performance of a Nozzle Guide Vane in Subsonic and Transonic Regimes Tested in an Annular Sector; Proceedings of ASME Turbo Expo 2010, Glasgow, UK, 14–18 June 2010, Paper No. GT2010-22901, DOI: 10.1115/GT2010-22901

Check for updates

Original Article

Institution of MECHANICAL ENGINEERS
Journal of POWER AND ENERGY

Proc IMechE Part A:
J Power and Energy
0(0) 1–27
© IMechE 2020



Article reuse guidelines:
sagepub.com/journals-permissions
DOI: 10.1177/0957650920909718
journals.sagepub.com/home/pia



Analysis of ultra-low uncertainty gas turbine flow capacity measurement techniques

Daniel Burdett, Chris Hambidge and Thomas Povey

Abstract

Accurate assessment of nozzle guide vane (NGV) capacity is essential for understanding engine performance data, and to achieve accurate turbine stage matching. In accelerated engine development programmes in particular, accurate and early assessment of NGV capacity is a significant advantage. Whilst the capabilities of computational methods have improved rapidly in recent years, the accuracy of absolute capacity prediction capability is lower than experimental techniques by some margin. Thus, experimental measurement of NGV capacity is still regarded as an essential part of many engine programmes. The semi-transient capacity measurement technique, developed and refined at the University of Oxford over the last 10 years, allows rapid and accurate measurement of engine component (typically fully cooled NGVs) capacity at engine-representative conditions of Mach and Reynolds numbers and coolant-to-mainstream pressure ratio. The technique has been demonstrated to offer considerable advantages over traditional (industrial steady-state) techniques in terms of accuracy, time and operating cost. Since the original facility was constructed, the facility has been modularised to allow for rapid interchange of test vane modules, and the instrumentation has been optimised to drive down the uncertainty in NGV capacity. In this paper, these improvements are described in detail, and a detailed uncertainty analysis is presented of the original facility, the current facility, and a proposed future facility in which the uncertainty of the measurement has been driven down to a practical limit. The bias errors of the three facilities are determined to be $\pm 0.535\%$, $\pm 0.495\%$ and $\pm 0.301\%$, respectively (to 95% confidence). The corresponding precision uncertainties are $\pm 0.028\%$, $\pm 0.025\%$ and $\pm 0.025\%$, respectively. The extremely low precision uncertainty in particular allows very small changes in capacity to be resolved. This, combined with rapid interchangeability of test modules, allows studies of the sensitivity of capacity to secondary influences with much greater flexibility than was previously possible. Consideration is also given to the definition of vane capacity in systems with several streams at different conditions of inlet total pressure and temperature. A typical high pressure (HP) NGV has three distinct streams: a mainstream flow; coolant flow ejected from film cooling holes (distributed over the vane surface); and trailing edge coolant ejection. Whilst it is helpful for the coolant mass flow rates and inlet temperatures to be included in the definition, only a relatively small difference arises from the way in which this is achieved. Several definitions appear to share similar usefulness in terms of their robustness to changing inlet conditions of individual streams, but the favoured definition offers the possibility of isolating sensitivities to key effects such as trailing edge coolant ejection. This is achieved by explicitly expressing vane capacity as a function of two controlling pressure ratios. The overall purpose of this paper is to review and analyse in detail the current state-of-the-art in gas turbine flow capacity measurement.

Keywords

Turbomachinery aerodynamics, turbomachinery flow, turbine heat transfer, turbine design, gas turbine cycles, gas turbine performance, gas turbines, gas turbine aerodynamics, engine performance, engine testing, capacity, experimental methods

Date received: 15 August 2019; accepted: 7 January 2019

Department of Engineering Science, University of Oxford, Oxford, UK

Corresponding author:
Thomas Povey, Department of Engineering Science, University of Oxford, Oxford OX2 0ES, UK.
Email: thomas.povey@eng.ox.ac.uk

Introduction

Capacity is commonly defined as

$$\Gamma = \frac{\dot{m}\sqrt{T_0}}{p_0} \tag{1}$$

Although this is not a non-dimensional quantity, the formulation is useful because it removes the primary sensitivities of mass flow rate to total pressure and temperature, and gives a parameter which at choked conditions can be thought of as a crude proxy for effective area. In this formulation, capacity is a function of gas properties, γ and R, and the pressure ratio across the vane, p_{exit}/p_{01}. We can write $\Gamma = f(\gamma, R, p_{\text{exit}}/p_{01})$. The definition of capacity for a fully cooled HP nozzle guide vane (NGV)—and its sensitivity to key operating parameters—is discussed later in this paper.

Accurate assessment of NGV capacity (here we refer loosely to the capacity characteristic of the part, but note that most engines operate on the relatively flat part of the curve at near-choked conditions) is important for both performance (stage matching implications) and power (overall core mass flow rate). The *exchange rate* between capacity and efficiency can be as high as 0.2. Likewise the exchange rate between capacity and engine power is close to unity.

Although high fidelity numerical methods are now deployed routinely for capacity evaluation (fully featured NGV part geometries, with finely resolved meshes), it remains difficult to evaluate vane capacity numerically to high accuracy (better than 1–2%). This is due to the strong dependence of the aerodynamics on features which are at the limit of the process capability to geometrically resolve, and due to inadequacies in the numerical methods.

Errors in the CFD geometry can arise either due to manufacturing variation (real part differs from the casting definition), where the CFD geometry is based on the design CAD, or due to limitations of the scanning process (e.g. by structured light scanning techniques, for example), where the CFD geometry is based on cast parts. Even for processes which use scans of real parts, questions arise regarding how best to clean the geometry (to take it from a cloud of scan points to a clean CAD geometry) and how best to create a part (or parts) from a statistical distribution of geometries. In a high accuracy process, this becomes significant.

Regardless of the method of geometry and mesh generation, elimination of deviations from the real part geometry at a relevant scale for high accuracy capacity evaluation is difficult. To justify this, consider two specific cases. First, the width of the slot formed near the region of minimum area in a modern civil engine is typically of order 10 mm. Hence a 0.1 mm deviation of the numerical mesh from the real part geometry will equate to a capacity discrepancy of order 1%.

Second, consider coolant ejection from a trailing edge slot—either a centred slot, or a slot with a suction side trailing edge overhang. Both configurations are common, with coolant flows up to 2.50% of the mainstream flow.[1] HP NGVs generally operate transonically in this region of the flow path (local Mach number typically in the range 0.8–1.1). The aerodynamic flow field is therefore strongly influenced by the introduction of coolant flow. In particular, the computational method must establish appropriate boundary conditions for the trailing edge coolant slot, and reproduce the geometry with sufficient accuracy. For example, the radius of the trailing edge lands—often dressed by hand—and internal geometry features which define the distribution of coolant flow within the slot. Further, the numerical solver is required to establish the base pressure correctly in a region with three converging high momentum streams (pressure surface, suction surface and trailing edge-coolant jet) separated by four shear layers, in a situation where the underlying flow field is transonic and highly unsteady. Numerical prediction of unsteady flow phenomena considerably increases the computational cost and requires accurate modelling of turbulent dissipation effects.

It is perhaps unsurprising that, even with rapid advances in computational capabilities in recent years, first-time prediction of capacity to high accuracy is extremely challenging. The purpose of ultra-high accuracy experiments is therefore twofold. First, such experiments can be used for direct capacity evaluation of a particular vane, for engine optimisation during a development programme. Second, building up a bank of ultra-high accuracy experimental measurements provides a reference source for continual development and calibration of numerical capacity prediction processes (both the generation of input geometry, and the CFD solution method).

A minimum requirement for ultra-high accuracy experimental evaluation of vane capacity is a fully annular facility with real engine NGVs, operated at appropriate non-dimensional conditions of Mach and Reynolds numbers. For this reason, capacity measurement has generally been the domain of the OEM due to the prohibitive expense of high-TRL (technology readiness level) facility operation. Much of the effort on the part of the OEM has been aimed at direct validation of capacity for engine design optimisation. Experiments to understand particular sensitivities (e.g. film cooling configuration, trailing edge coolant ejection, coolant-to-mainstream pressure ratio, platform gaps and leakages, etc.) have therefore been rather limited, as have efforts to minimise uncertainty—by whatever means—in the experimental method. Indeed, other than two early papers (referenced below) the only sustained effort towards low-uncertainty capacity measurement and understanding is from the group involved in this paper.

In 1984, Fielding[2] examined the relationship between downstream energy loss coefficients and

boundary layer characteristics at the trailing edge, and defined a parameter which he called *restriction factor*, to account for viscous effects in the vane passage. It can be thought of as a fraction of passage area 'lost' due to momentum deficit in the boundary layer regions. Accounting for losses in this way, as opposed to a basic irreversible 1D estimation, was found to give a change in the estimated capacity value for a typical turbine vane of around 2.4%. In 2004, Afanasiev et al.[3] showed computationally that vanes with identical minimum *geometric* area but different loading distributions can have differences between their capacity characteristics of up to 10%. The difference arises due to a shift in position of the controlling minimum area in relation to the passage. Although retrospectively unsurprising, the importance of this result is highlighted by the persistence, even today, of over-simplistic attempts to reconcile capacity differences between different vanes by ultra-high accuracy measurement of geometric throat area. With improved understanding of the aerodynamic sensitivities (to small design features) of typical HP NGVs, it rapidly becomes apparent that such attempts are unlikely to be successful. Even defining a geometric throat for a highly 3D modern part presents its own challenges.

So far as the published work from the current group is concerned, in 2010, Povey[4] presented an analytical model for estimating the impact of film cooling on capacity based on fundamental cooling performance parameters. This work can be thought of as an extension of Fielding[2] to include film cooling. A control volume mixing approach was employed, in which, importantly, the free-stream static pressure was allowed to vary in the flow direction, in line with the models of, for example, Kollen and Koschel.[5] The conclusions from this work are summarised later in this paper.

In a related 2011 paper, Povey et al.[6] described for the first time a novel semi-transient experimental technique for NGV capacity measurement. By careful experimental design, the semi-transient technique offered a shorter test duration (approximately 60 s), reduced operating cost, and improved precision and bias uncertainty relative to the conventional (continuously running) industrial method. A fully annular cascade of engine components was operated at non-dimensionally engine representative conditions of Mach number, Reynolds number and coolant-to-mainstream pressure ratio. Precision and bias uncertainties in vane capacity of $\pm 0.028\%$ and $\pm 0.546\%$, respectively, were achieved (to 95% confidence). Of the $\pm 0.546\%$, $\pm 0.500\%$ was inherited from the primary mass flow metering nozzle. This is the bias error in the nozzle calibration, traceable to an international standard. The method was designed to minimise the small additional uncertainty ($+0.046\%$) arising from the experimental measurement process. In the same paper, the impact of the definition of the vane exit static pressure on the capacity characteristic was considered. Simplified 1D, 2D (radial pressure profile) and 3D (radial and circumferential pressure profiles) analytical models were compared to experimental data for a modern HP NGV. A poor match between the *shape* of the experimental characteristic and any of the analytical models demonstrated the complexity of the flow environment. This highlights the pitfalls of applying simplified logic based on 1D isentropic equations (e.g. the simplistic—in this context—concept of a *throat*). The disagreement (between models and experiment) in both shape and absolute level were taken to be partly due to total pressure loss, but primarily due to the difficulty in establishing a pressure measurement at a point of well-defined area. This latter point is interesting: the most robust measurement location for static pressure (see later discussion) is on the vane downstream platform, but this is reasonably far from the controlling region where the area is smallest (however defined). In contrast, at locations of well-defined area it would be hard to measure pressure boundary conditions adequately with any practical instrumentation (indeed, an *integration* across a plane would be required to measure capacity directly).

In 2012, Hambidge and Povey[7] investigated the impact of a typical film cooling arrangement on HP NGV capacity using a 2D numerical method. This is can be thought of as a computational extension of Povey.[4] For a typical vane operating at unit Mach number, introducing film cooling was found to cause a 0.125% fall in capacity. This was compared against the analytical model of Povey,[4] which predicted a corresponding capacity drop of 0.144%. It was demonstrated that the effects of multiple rows blowing simultaneously can be closely approximated by superposition of each row blowing in isolation. The errors incurred in making this simplification were of order 0.01% of overall vane capacity. It was therefore concluded that the impact of film cooling typically depends primarily on coolant mass flow, and to a much lesser degree on the actual film cooling arrangement. The impact can likely be adequately accounted for via analytical methods, correlations based on single-row experiments or simulations, or simple 2D CFD.

Since 2011, the semi-transient technique reported by Povey et al.[6] has been used to support a number of engine programmes, and has been the subject of continuous validation and improvement over a series of more than 10 major test campaigns. This facility (Povey et al.[6]) is referred to as the *original facility*. The semi-transient method has been demonstrated to have equivalent or higher accuracy (made possible by more accurate control of experimental conditions) than continuous running facilities, but offers very significant savings in both time and cost. In 2014, the Oxford capacity facility was upgraded to become part of the Oxford Engine Component Aerothermal (ECAT) test bed, offering significantly enhanced capability including metal effectiveness

and downstream traverse measurements.[8] This facility (Kirollos et al.[8]) is referred to as the *current facility*.

With the maturation of the test technique, and the desire for ever-greater accuracy in capacity evaluation, there has been a drive to further optimise the accuracy of the technique, to allow for ultra-low uncertainty (primarily bias error) measurements. This has become particularly relevant in recent years, as the calibration uncertainty of primary nozzles can now be as low as ±0.250% (half the typical lowest uncertainty possible when the original facility was built). This paper concerns key improvements to the test methodology which lower the overall uncertainty of the measurement technique. In particular, improvements in experimental hardware and instrumentation, test methodology, and processing. The impact of each improvement on the additional bias uncertainty in the final capacity measurement is evaluated, and the precision error in the mean is evaluated from a series of repeat experiments. The improvements to the test technique and working section are:

1. Modular construction of the working section and NGV cascade module. This offers improved test efficiency, rapid interchanging of NGV modules, and reduced bias error between repeat test campaigns using the same cascade.
2. Reduced uncertainty in cascade inlet conditions of stagnation pressure and temperature due to increased quantity of measurements.
3. Reduced uncertainty in cascade exit conditions of static pressure distribution due to increased quantity and density of measurements.
4. Independently metered coolant supply streams, allowing for improved benchmarking of coolant mass flow rates. This allows studies of, for example, sensitivity of capacity to coolant-to-mainstream pressure ratio and mass flow rate. Because the bias uncertainty in the measurement of coolant stream mass flow rates is uncorrelated to that in the mainstream mass flow rate, independent metering offers a small reduction in overall bias error.

Each of these aspects—and the associated impacts on the measurement process uncertainty—will be discussed and analysed in turn. The overall uncertainty in the measurement of vane capacity is discussed in detail and compared between the current[8] and original[6] facilities. A *proposed upgraded facility* is also considered. This would take advantage of improvements in nozzle calibration to reduce the primary nozzle calibration uncertainty from ±0.500% to ±0.250%. This improvement derives from advances in the accuracy of the techniques employed at the primary calibration station (a gravimetric method is used, and instrumentation has improved in recent years.). The facility would then represent state-of-the-art in every respect, and defines a practical limit for uncertainty in such facilities. The paper concludes with a detailed comparison of bias, precision, and overall uncertainty in vane capacity measurement in each of the original, current, and proposed upgraded facilities.

Achieving ultra-low uncertainty in the measurement technique makes it possible to examine and understand the impact on capacity of secondary influences such as film cooling, trailing edge coolant ejection, surface deterioration, vane inlet conditions of swirl and turbulence, and small geometry features such as discontinuities and irregularities from casting and installation.

Experimental facility

The Oxford ECAT facility is an engine-scale, semi-transient blowdown facility. Air is stored at 400 psi (27.6 bar) in 60 m^3 tanks, allowing tests at very high energy density for sustained periods (up to 100 s) at relatively low installed plant cost. During a test, the air is discharged through an annular cascade of HP NGVs. The facility is typically used to investigate engine parts from current civil engines. Thus the parts typically have heavy film cooling and coolant ejection from a trailing edge slot. A high degree of non-dimensional similarity (to engine operating conditions) is achieved in the facility, with Mach number, Reynolds number and coolant-to-mainstream pressure ratio being matched. A schematic diagram of the test bed layout is shown in Figure 1.

The facility can be built with a variety of working sections dedicated to metal effectiveness, downstream loss, capacity measurements, or any combination of these. The facility has the capability to replicate both rich-burn and lean-burn inlet conditions, including swirl and temperature profiles. Further details of the ECAT facility capabilities for aerodynamic and heat transfer measurements can be found in Kirollos et al.[8] The facility has a unique modular construction which allows different vane modules to be rapidly interchanged without compromising the sealing integrity. The vane module is built as a stand-alone assembly. Because of the variability in engine parts, wet-seals are required to make up gaps at the platform interfaces. Module components are held in place by a steel fixture during the sealing process to ensure precise alignment of the built module, with gaps to accommodate sealant and allow for slight part variability. Cassettes around the annulus allow easy insertion and reconfiguration of upstream instrumentation. The construction, sealing and testing of the vane module is described in the following section.

The ECAT facility can operate in two modes: *blowdown mode* or *regulated mode*. Blowdown mode is used for measuring capacity over a wide range of operating conditions. In this mode, total temperature and pressure at the cascade inlet steadily drop over

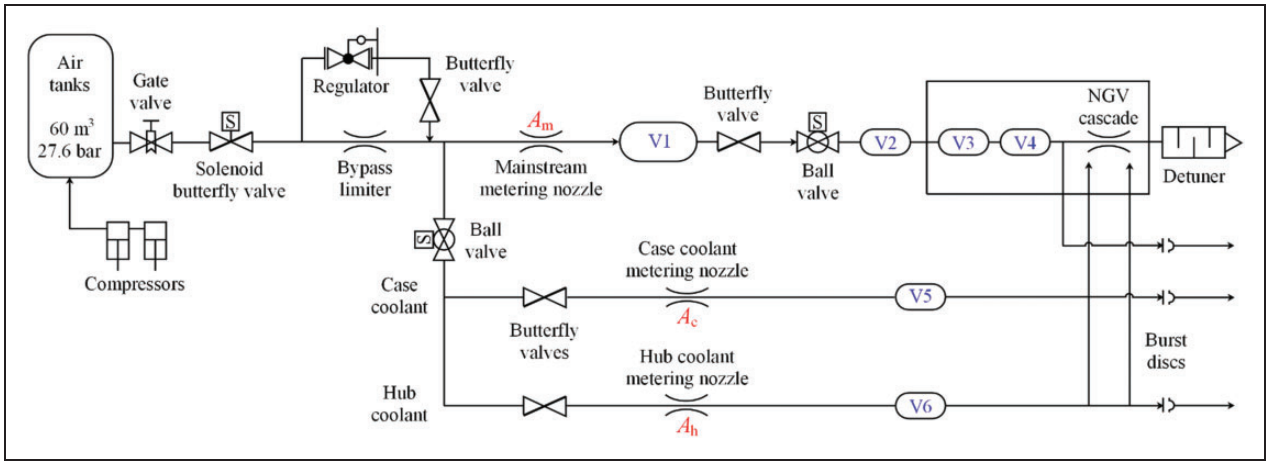


Figure 1. Schematic diagram of the capacity test core installed in the Oxford ECAT test bed.

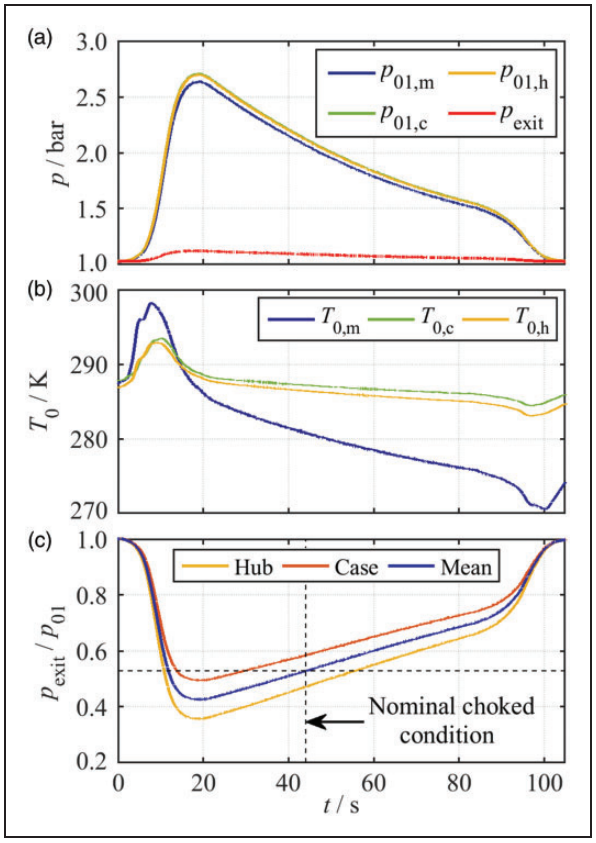


Figure 2. Pressure (a), temperature (b) and vane pressure ratio (c) characteristics during a typical blowdown run.

the course of a test as the supply air tanks are slowly depleted. Pressure and temperature characteristics from a typical run (blowdown mode) are shown in Figure 2. The blue line represents the inlet total pressure of the mainstream feed. After an initial transient of approximately 15 s, the pressure settles to a stable characteristic (between 20 and 85 s) during which time the capacity measurement is performed. The yellow and green lines (which overlay almost exactly) represent coolant total pressures measured in the hub and case feed plena respectively. The ratio of hub and case coolant-to-mainstream mass flow rates are carefully set to match the coolant-to-mainstream total pressure ratios to the engine design condition during the period of stable operation.

During the period of quasi-steady operation, the vane pressure ratio (and Mach number) passes slowly down a characteristic, traversing a range through the design value. The vane pressure ratio trend from a typical run is shown in Figure 2(c). The mean vane pressure ratio varies between $0.43 < p_{exit}/p_{01} < 0.72$, corresponding to a Mach number range $0.70 < M < 1.17$. Thus, a full characteristic can (in principle) be determined from a single test. There are two advantages of operating in this mode. First, a full capacity characteristic, $\Gamma(p_{exit}/p_{01})$, can be determined from a single run of the facility. Second, the facility is naturally quasi-steady, eliminating the need to stabilise an operating point (e.g. stable compressor conditions) as would be necessary in a traditional continuous measurement approach.

Regulated mode is used for measuring capacity at a fixed condition and for cross-checks against the semi-transient blowdown measurement technique, as well as performing traverse measurements of the flow field downstream of the NGV cascade at steady-state condition. An inline high-flow pressure regulator is installed in the upstream pipework (with bypass loop, see Figure 1), allowing the cascade inlet conditions to be held at steady-state for a period of up to 60 s.

Vane module construction and sealing

The vane module has a clamshell-style design, shown schematically in Figure 3. The four principal components—(1) to (4)—and the five potential leak paths—A to E—are marked in the figure.

To ensure precise alignment of the components, the vane pairs (typically 20) are located with dowels on

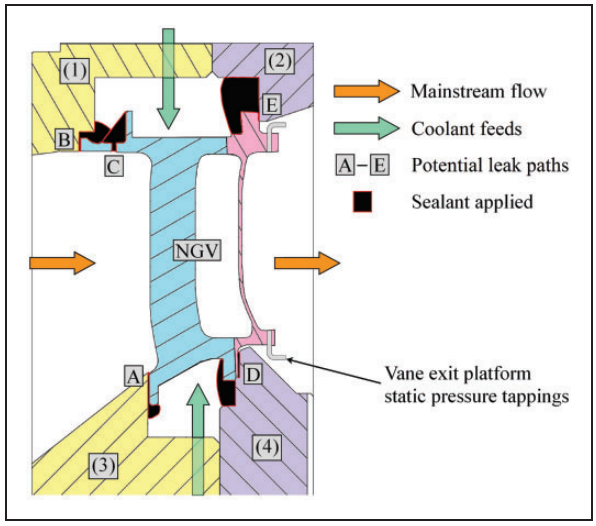


Figure 3. De-featured section schematic of the vane module assembly showing potential leak paths and associated wet seal locations. The main components are: (1) case front support ring; (2) case rear mount ring; (3) hub front support ring; (4) hub rear mount plate.

the hub rear mounting plate, and sealed with a wet seal (aerospace grade silicone sealant) to avoid leaks. The location of the seal is marked 'D' in the figure. At the same stage, seal E is made with the case rear mount ring, and the components are bolted to the hub rear mount plate. During this process, the case rear mount ring and hub rear mount plate are held in place with respect to each other using a ground steel fixture. This ensures precise concentricity and axial alignment while the seals are wet.

Upstream hub and case support rings are then fitted over the vane front platforms and bolted to the hub rear mount plate and case rear mount ring respectively. The components are doweled to ensure precise alignment, and clearance spaces are allowed at locations A and B, designed to account for variability in the cast engine components, and sealed with wet sealant during assembly. The upstream hub and case support rings also form part of the annulus line of the working section.

After assembly, the module dimensions are carefully checked. All mating surfaces are machined (as opposed to cast) to achieve high build accuracy. The vane module seals to the working section components using O-rings, allowing rapid interchange of vane modules without disturbing the wet seals. The ground steel fixture remains attached to the components during assembly (and bolting) into the working section, after which it is removed. This ensures that the components remain in a fixed position during assembly, and therefore that no stress can be imparted to the wet seals during the process.

There are two further advantages of the clam-shell module design. First, a vane module can be stored separate from the main working section, and in a particular build configuration, and re-tested at a future date. For studies of vane capacity targeting deltas of order 0.1%, this capability is extremely useful as it removes an additional source of uncertainty between repeat tests (variability in the precise installation of the vanes in the module). Second, the removable vane module opens the way for back-to-back testing of NGVs with small geometric changes introduced sequentially to the module—e.g. studies of damage to leading or trailing edges, which can be simulated by sequential machining of the components. The ability to make such changes without dismantling the vane module or disturbing the wet seals makes it possible to detect very small shifts in vane capacity.

It is important to distinguish between primary and secondary leak paths through the vane module. Primary leak paths (D and E in Figure 3) allow air from the coolant cavities to bypass the vane and flow directly into the downstream system. Incomplete sealing at these locations would cause error in the capacity measurement and must be avoided. Secondary leak paths (A, B and C in Figure 3) allow coolant flow into the mainstream channel upstream of the cascade. This would affect the cascade inlet flow condition, and consequently have a secondary influence on capacity. Table 1 summarises the leak paths.

Prior to an experimental test campaign, a series of tests are conducted to check the integrity of the working section seals. This is required to ensure that leaks do not influence the measured capacity result. The process is now described.

The tests involve feeding only the two coolant streams (not the mainstream feed) and accurately measuring the total coolant flow capacity characteristic (up to approximately ten times a typical design coolant-to-mainstream pressure ratio) in the *ex-situ* environment (no aerodynamic field due to the main flow). The measured capacity characteristic is then compared to a second set of measurements performed on a statistically large sample of vanes (10–20 vane pairs from the cascade) in individual bench-test experiments. In the bench-test experiment, coolant is supplied from both hub and case feeds (pressure balanced), and coolant flow capacity is measured at a number of coolant-to-downstream pressure ratios. Agreement between the two coolant capacity data (good overlap of the uncertainty bounds) is taken as indication of good build integrity. These tests are referred to as *dynamic leak tests*. As the coolant capacity is only a small fraction of the overall capacity (typically $< 10\%$), and because high accuracy can be achieved in the dynamic leak tests, they provide an accurate method of diagnosing unintended leak paths.

Figure 4(a) shows typical coolant capacity characteristics (solid lines) from four separate sets of tests of the same parts, taken at intervals during a 12-month period. Between each set of tests, the vane module was removed from the facility working section and reinstalled. In this particular example, an external machining operation was performed on the vane ring between each test, to study the effect of trailing edge cut-back on

Table 1. Summary of working section leak paths.

Leak path	Primary/secondary	Description
A	Secondary	Hub coolant cavity into mainstream through annular gap between vane hub front platform and hub support ring
B	Secondary	Case coolant cavity into mainstream through annular gap between vane case front platform and case support ring
C	Secondary	Case coolant cavity into mainstream through vane case platform cooling holes
D	Primary	Hub coolant cavity into downstream through annular gap between vane hub rear platform and hub mounting plate
E	Primary	Case coolant cavity into downstream through annular gap between vane case rear platform and case mounting plate

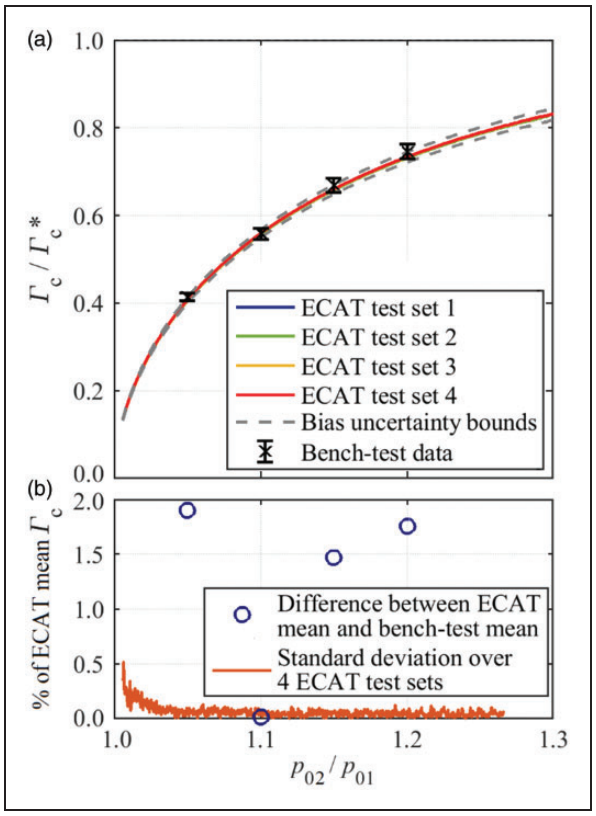


Figure 4. (a) Coolant capacity characteristics measured in dynamic leak tests in four ECAT test campaigns over a 12-month period, compared against bench-test data; (b) percentage standard deviation between different ECAT test sets, and percentage difference between ECAT and bench-test data.

capacity. This operation was external to the trailing edge slot, and not expected to affect the coolant capacity in the absence of mainstream flow.

A typical test set is composed of six runs, allowing both the mean characteristic and the precision error in the mean to be calculated. We see that the four data sets overlay so closely that the individual lines are indistinguishable. The average standard deviations *within* each of the four data sets, averaged over the range $1.01 < p_{02}/p_{01} < 1.27$, were 0.11%, 0.10%, 0.11% and 0.09%. These very low values confirm the high degree of stability and repeatability in the measurements.

The standard deviation *between* the four data sets is shown in Figure 4(b) (orange line). Over the pressure ratio range $1.05 < p_{02}/p_{01} < 1.27$, the standard deviation was 0.05%. The standard deviation between the four trends is therefore lower than that between individual runs comprising a trend. This confirms the extremely high repeatability of the coolant capacity measurements over four separate builds of the facility in a 12-month period. It is concluded that no unintended leaks were introduced during this time. The bias error in coolant capacity measurements in the ECAT facility was calculated as ±1.62% to 95% confidence (indicated by dotted lines on the plot). This bias uncertainty was calculated following the method presented in the later section on uncertainty analysis. Inputs included the measured coolant cavity total pressures and temperatures, coolant stream mass flow rates and vane external static pressure in the *ex-situ* (no external aerodynamic field) situation.

The black crosses in Figure 4(a) represent the average from bench test capacity measurements (i.e. individual vane pairs measured in a separate facility) of 14 vanes, conducted at four discrete pressure ratios. The error bars on the bench-test data points (Figure 4(a)) represent two standard deviations for the distribution of coolant capacity values for the set of 14 vane pairs tested. The average (across four operating conditions) standard deviation was 4.58% of the mean capacity value, corresponding to a standard error in the mean (of 14 vanes) of ±2.45% to 95% confidence. The bias uncertainty was evaluated (in separate uncertainty analysis) as ±0.40% (95% confidence). Mass flow rate measurements in the bench test were made using a sonic Venturi nozzle calibrated by CEESI, with calibration traceable to a national standard. The difference between the mean ECAT data (across four test sets) and the bench-test data, taken at the four discrete pressure ratios is marked in Figure 4(b) (blue circles). The average across these four points was 1.28%. The two data have overlapping uncertainty bands indicating this is a likely result for a build with no leaks.

Coolant capacity data (dynamic leak tests) are typically collected over a range of coolant-to-mainstream pressure ratio $1.0 < p_{02}/p_{01} < 1.3$, where $p_{01} \approx p_{exit}$. In

this *ex-situ* situation (no mainstream flow), the maximum pressure difference across the wet seals is approximately $p_{02} - p_{exit} = p_{02} - p_{atm} = 0.3$ bar. This is considerably lower than at typical *in-situ* operating conditions, where the pressure difference $p_{02} - p_{exit}$ can be as large as 1.5 bar (see Figure 2), being greatest across the wet seals of *primary* leak paths (D and E in Figure 3). Thus the coolant capacity check poses no additional risk to the seals over that experienced in a typical run. It is considered good practice to repeat the check at the end of a test campaign, to confirm there has been no damage to any seals.

The coolant capacity characteristic in Figure 4(a) can be extrapolated to a choked condition by fitting an isentropic capacity curve. This allows the ratio of the estimated choked coolant capacity, Γ_c^*, to the choked vane capacity, Γ_{vane}^*, to be estimated. This gives $\Gamma_c^*/\Gamma_{vane}^* = 0.152$. In the worst-case scenario in which a leak in an incompletely sealed vane module was entirely a primary flow leak, a leak with a capacity equivalent to the difference between the mean of the four ECAT datasets and the bench-test data (1.29% of Γ_c^*) would equate to 0.20% of Γ_{vane}^*. The dynamic leak check is a robust way of reducing the risk of leaks affecting NGV capacity measurement.

Mass flow rate measurement

Flow into the facility is split into three separate streams: mainstream flow, and hub and case coolant supply flows. Each stream is controlled and metered by an independent choked nozzle. The mainstream flow is fed by a 3″ diameter sonic Venturi nozzle (labelled A2 in Figure 1). The nozzle was calibrated to a National Institute of Standards and Technology (NIST) traceable standard at Colorado Engineering Experiment Station Inc. (CEESI) and installed according to ISO 9300.[9] The bias uncertainty associated with the measurement is ±0.500% (to 95% confidence).

The NGV coolant feeds are supplied with air via separate hub and case supply streams. The coolant stream mass flows are controlled and metered using sonic Venturi nozzles. These are labelled A3 and A4 in Figure 1. The air feeds are drawn off downstream of the regulator and bypass line, but upstream of the main nozzle. This ensures (instantaneously) essentially identical feed pressure to all three nozzles (mainstream, hub and case coolant) giving ratiometric mass flow rates, even during blowdown mode operation in which the facility passes down a characteristic. The coolant metering nozzles are interchangeable, allowing precise adjustment of coolant-to-mainstream mass flow rates and pressure ratios at the NGV. The overall NGV capacity accounts for both mainstream and coolant flows. This is discussed in a later section.

Mass flow rate unsteady correction

During a blowdown test, the pressure and temperature in the main tank decay as the tank is emptied, following an approximately isentropic expansion. Likewise, the pipework system and working section pass down a pressure characteristic as seen in Figure 2. During this process, the mass stored in each of the pipework volumes reduces over time. This effect causes a small discrepancy between the mass flow rates passing through the metering nozzles, and those delivered at the test vane. The rate at which the mass stored in the *intermediate plena* (those volumes located between the metering nozzles and points of delivery to the vane) is depleted must be accounted for. This correction is considered now.

The intermediate plena are indicated schematically in Figure 1, and labelled V1–V6. V1–V4 are intermediate plena on the mainstream flow path. V5 and V6 are the intermediate plena on the case and hub coolant flow paths, respectively. Assuming ideal gas behaviour, the rate of change of stored mass in an individual plenum is given by

$$\dot{m} = \frac{\mathrm{d}}{\mathrm{d}t}\left(\frac{pV}{RT}\right) = \frac{V}{RT}\left(\frac{\mathrm{d}p}{\mathrm{d}t} - \frac{p}{T}\frac{\mathrm{d}T}{\mathrm{d}t}\right) \tag{2}$$

The total *mainstream* unsteady correction mass flow is therefore given by the sum

$$\dot{m}''_m = \sum_{i=1}^{4} \dot{m}_i = \sum_{i=1}^{4} \frac{V_i}{RT_i}\left(\frac{\mathrm{d}p_i}{\mathrm{d}t} - \frac{p_i}{T_i}\frac{\mathrm{d}T_i}{\mathrm{d}t}\right) \tag{3}$$

Corrections for the coolant stream plena, V5 and V6, follow the same form.

Overall mass flow rate for a typical blowdown run (same run as Figure 2) is plotted in Figure 5(a). The mass flow rate characteristics are truncated at the beginning and end of the test when the pressure ratio across the metering nozzle fails to reach the critical choked condition. Outside of this range, the nozzle is out of its calibration range, and mass flow rate is not computed. During the pressurisation of the working section, the total mass flow rate through the vane lags behind the combined mass flow rate measured through the three feed nozzles. This effect results from mass accumulation in the intermediate plena. Positive mass accumulation is associated with the increase in pressure during pressurisation of the facility. For completeness, it is noted that the increase in pressure is accompanied by an increase in temperature (below the isentropic compression rate, due to heat transfer), which reduces the accumulation rate due to a density decrease with temperature.

The overall mass accumulation rate is plotted in Figure 5(b). The rate of mass accumulation has a maximum value of around 2 kg s^{-1} (at approximately $t = 10$ s) during the initial pressurisation of the facility

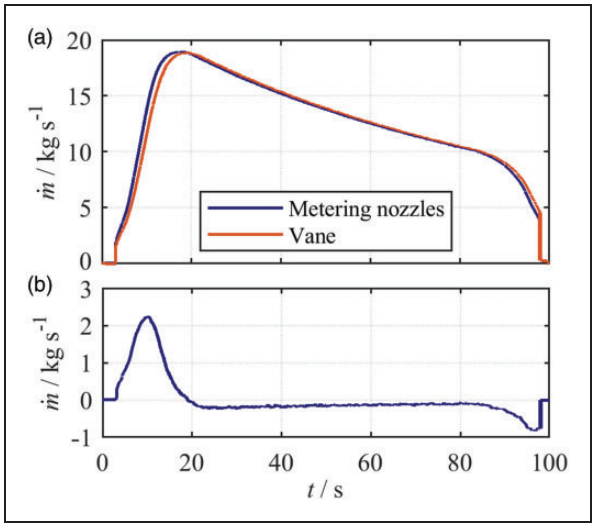


Figure 5. (a) Overall mass flow rate characteristics for a typical blowdown test (rescaled to an arbitrary maximum of 19.0 kg s^{-1}); (b) overall mass accumulation rate in intermediate plena.

working section. During the period of quasi-steady operation (20–80 s), the quantity of mass stored in the plena reduces as the pressure falls. The maximum depletion rate (at $t \approx 20$ s) is 0.26 kg s^{-1} and steadily decays over the course of the test period. The vane mass flow rate at the same time is 19.0 kg s^{-1}, giving a maximum correction during the quasi-steady period of approximately 1.37%.

As will be discussed in detail later, the bias uncertainty in the correction mass flow rate is approximately ±13.1% (to 95% confidence), leading to an increase in the bias uncertainty in the vane mass flow rate measurement (over that at the main metering nozzle) of approximately 0.015%. Performing the unsteady correction therefore contributes only a small amount to the overall uncertainty.

Inlet total pressure and temperature measurement

Measurements of total pressure and temperature at vane inlet are performed with cassette-mounted probes just upstream of the vane module in the mainstream flow, and in the coolant supply plena for the hub and case coolant flows. Measurement locations are shown in the section diagram of Figure 6.

Inlet total pressure and temperature to the cascade were each measured at 32 locations, each using four probes at separate circumferential locations. On each probe, the measurement locations were distributed evenly across the span. The measurement plane was located four axial chords upstream of the cascade leading edge. The cassettes are interchangeable and reconfigurable, allowing optimisation of the instrumentation according to the test requirements. There are four cassette locations around the annulus, and each cassette can accommodate up to six probes.

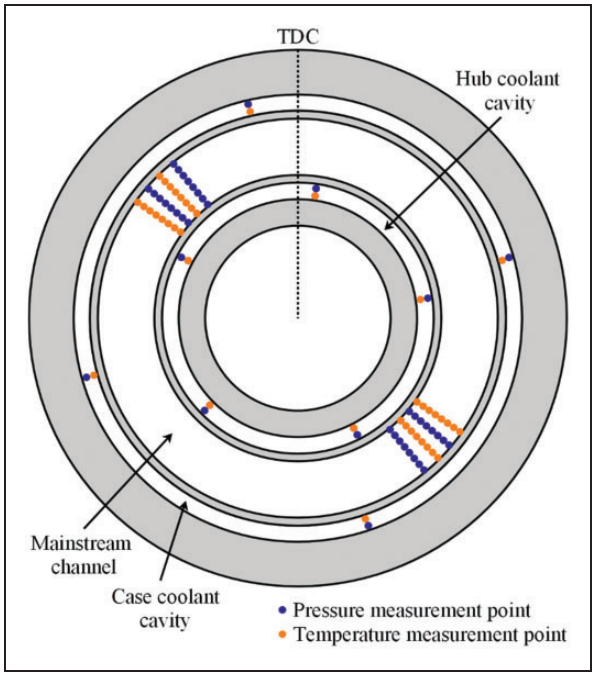


Figure 6. Locations of inlet condition measurements for mainstream and coolant flows, viewed from downstream.

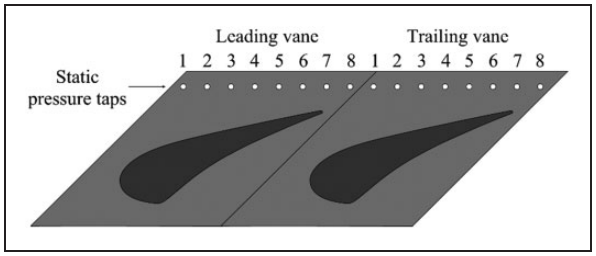


Figure 7. Simplified view of a vane pair exit platform instrumented with eight static pressure tappings per passage.

Hub and case coolant inlet total pressure and temperature were each measured at five and four evenly spaced locations around the annulus, respectively. These measurement points are located in the hub and case coolant cavities of the vane module, which feed coolant flow into the vane internal cooling systems.

Exit static pressure measurement

Static pressure at vane exit is measured on the hub and case downstream platforms of three instrumented vane pairs (six vanes from a typical total of 40). Figure 7 shows a simplified diagram of the locations of static pressure tappings on a typical instrumented vane pair platform. The location of a tapping on the vane platforms is illustrated in Figure 3. The three instrumented vane pairs are spaced 120° apart around the annulus. A typical test campaign uses eight tappings per vane pitch at hub and case. For a total of 12 instrumented platforms (six at the hub and

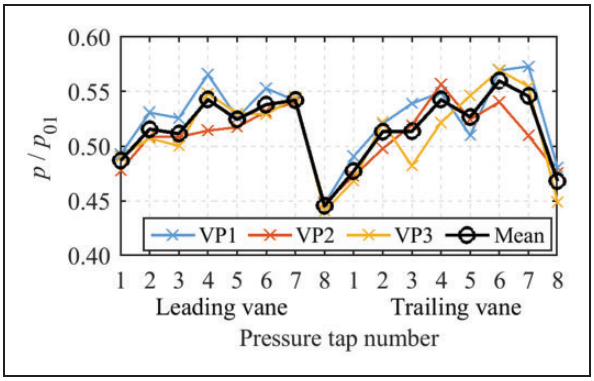


Figure 8. Example of a typical measured circumferential static pressure profile on three instrumented vane pair platforms. The x-axis represents the tapping locations shown in Figure 7.

six at the case), this gives 96 tappings. The significance of the number of tappings to the bias uncertainty in the vane exit static pressure condition is discussed later in this paper.

Example circumferential static pressure profiles measured on three vane pair platforms from a typical experiment are plotted in Figure 8 for an arbitrary mean operating pressure ratio of 0.46 (note the measured static pressures are offset from the nominal mean value due to the radial pressure gradient). The three instrumented vane pairs are distinguished as VP1, VP2 and VP3. The three vane pairs give very similar trends, with average standard deviation between measurements of 3.5%. Small differences arise due to repeatability in the cast part geometry. Run-to-run repeatability was excellent, with an average standard deviation of 0.10% between data (at the same measurement location and *mean* pressure ratio) from 17 repeat tests. In a later section, the sensitivity of vane capacity measurement to tapping number, axial location, and positional accuracy is analysed.

Capacity definition for fully cooled NGVS

Consideration is now given to the definition of capacity in a system with several streams at different conditions of inlet total pressure and temperature. This is relevant to an HP NGV because a typical vane has a mainstream flow, coolant flow ejected from film cooling holes (often distributed over the vane surface) and coolant ejection from the trailing edge.

A schematic representation of a typical HP vane cooling system is presented in Figure 9. The flow system can be characterised by a mainstream flow (subscripted 1), a film cooling system (subscripted 2), simplified to a single stream for the purpose of this analysis, and a trailing edge coolant outlet (subscripted 3). At engine conditions the two coolant flows generally enter at significantly lower total temperature than the mainstream, and marginally higher total pressure. Comparisons between systems therefore depend on the particular definition of capacity used. In this system, film cooling flow (2) enters the

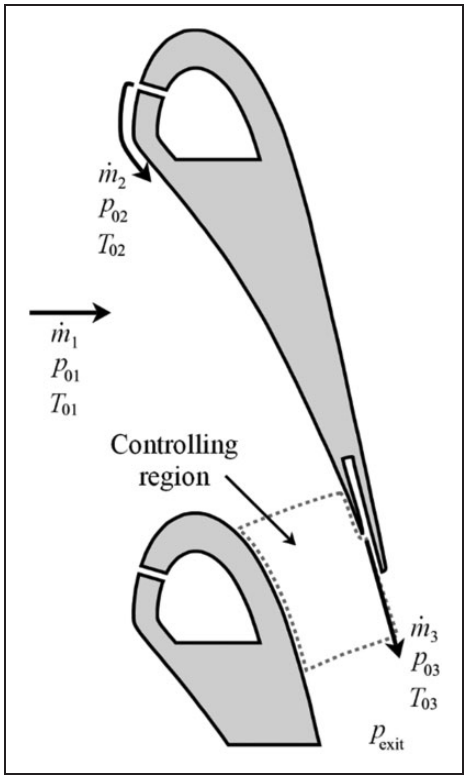


Figure 9. Schematic of a typical HP vane cooling system showing mainstream flow (1), film cooling flow (2), and trailing edge coolant flow (3).

mainstream in a low Mach number region and partially mixes before passing through the *controlling region* (this terminology is discussed below) of the passage. Trailing edge coolant (3) enters the domain within the (loosely defined) controlling region.

In the description above, the traditional terminology of a *vane throat* was avoided, as it gives rise to misleading notions which are only applicable to 1D systems. The minimum *geometric* passage area can be determined by reference to CAD drawings of the part or by using techniques such as structured light scanning to directly measure the part geometry. The complex 3D geometry of some parts further complicates even the practical definition of a minimum physical area. Should the definition be restricted to a flat plane or should the area be defined as that integrated across projections normal to the local streamlines? However, this alone gives poor insight into the vane capacity.

It is well established that NGVs with the same geometric minimum area can have capacity characteristics that differ by 10% or more.[3] Indeed, a typical HP vane has a large region of fairly complex flow in the transonic Mach number range. At the point of minimal physical area (defined either by a plane or a more complex surface), the flow is generally found to be either sub-or super-critical over most of this 'throat', often by a significant margin. Indeed, for a vane operating at a nominally choked (based on 1D assumptions) pressure ratio, the sonic surface can pass through the minimum physical area with quite a

high angle of intersection (i.e. the sonic surface and the surface of minimum physical area are poorly aligned). In some cases, the sonic surface is not bounded by the vane passage, but extends out into the wake region downstream. This rather fundamental observation brings into question the usefulness of concepts of minimum geometric area.

The question therefore arises as to the most appropriate way to define vane capacity in a multi-stream system. The simplest definition might be to base the capacity definition on the overall mass flow, and the mainstream total temperature and pressure:

$$\Gamma_{\text{vane}} = \frac{\dot{m}_{\text{total}}\sqrt{T_{01}}}{p_{01}} \tag{4}$$

One objective in evaluating the suitability of a capacity definition, however, might be that it be as independent as possible of the individual stream flow properties (in the simplest case this means the inlet total pressure and temperature for each stream)—i.e. the capacity should change as little as possible when the individual stream properties change. Three simplified representations of the system in Figure 9 are now considered.

Model 1

In the first model, three initially independent streams fully mix at low Mach number before being accelerated to uniform exit conditions at a single controlling area. This model is referred to as the *fully mixed, multi-stream, single controlling area model*. It is illustrated schematically in Figure 10.

In this system, the mass flow rate through the controlling area depends only on the flow conditions of the fully mixed flow stream and the downstream static pressure (p_{exit}). The average total temperature (assuming constant c_p) at this location is

$$\overline{T_0} = \frac{\dot{m}_1 T_{01} + \dot{m}_2 T_{02} + \dot{m}_3 T_{03}}{\dot{m}_{\text{total}}} \tag{5}$$

where the total mass flow rate, $\dot{m}_{\text{total}}$, is the sum of the three individual stream mass flow rates. Total pressure averaging should properly be done using a control volume mixing model, but this strays towards analytical prediction of capacity which is inherently problematic for reasons discussed (strong dependence on the aerodynamic state of the controlling region). For the purpose of this simple model, and considering that cooling mass flow rates are typically relatively small (up to 10% of the total flow) and with only a small difference in total pressure condition between mainstream and coolant (typically within 3%), it is considered adequate to adopt the following mass-flow averaged definition

$$\overline{p_0} = \frac{\dot{m}_1 p_{01} + \dot{m}_2 p_{02} + \dot{m}_3 p_{03}}{\dot{m}_{\text{total}}} \tag{6}$$

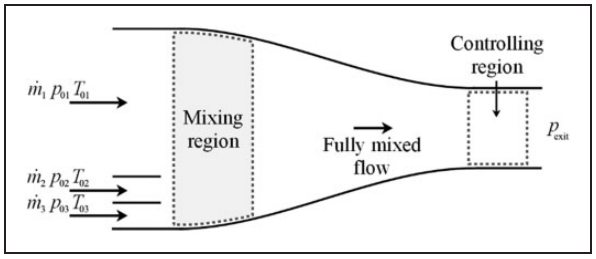


Figure 10. Schematic diagram of the fully mixed, multi-stream, single controlling area model.

This leads directly to the following definition of capacity

$$\Gamma_{\text{vane}} = \frac{\dot{m}_{\text{total}}\sqrt{\overline{T_0}}}{\overline{p_0}} \tag{7}$$

For completeness, it should be noted that a difference in c_p between the streams (e.g. that seen between mainstream and coolant flows in the engine situation) would require equation (5) to be adapted. It may also be necessary to consider the variation in gas properties (γ and R) between the streams.

In systems which can be approximated by the model of Figure 10, the definition in equation (7) should be relatively insensitive to the individual stream properties. Recalling the caveats regarding the evaluation of the average flow properties passing through the controlling area, effects leading to incorrect averaging would cause capacity differences between systems that, in the framework of this model, would be considered nominally identical (same controlling area). That is, whilst definition (7) is to some extent insensitive to individual stream properties, simplifications in the model mean it is not entirely so.

Model 2

In the second model, the streams are considered to be entirely independent of one other. That is, they each have independent controlling areas which do not interact. This model is illustrated in Figure 11. This system is referred to as the *unmixed, multi-stream, multiple controlling area model*, and represents the opposing extreme to Model 1. The capacity of this system is represented by the sum of the three individual stream capacities

$$\begin{aligned}\Gamma_{\text{vane}}\left(\frac{p_{\text{exit}}}{p_{01}}, \frac{p_{\text{exit}}}{p_{02}}, \frac{p_{\text{exit}}}{p_{03}}\right) = {} & \frac{\dot{m}_1\sqrt{T_{01}}}{p_{01}}\left(\frac{p_{\text{exit}}}{p_{01}}\right) \\ & + \frac{\dot{m}_2\sqrt{T_{02}}}{p_{02}}\left(\frac{p_{\text{exit}}}{p_{02}}\right) \\ & + \frac{\dot{m}_3\sqrt{T_{03}}}{p_{03}}\left(\frac{p_{\text{exit}}}{p_{03}}\right)\end{aligned} \tag{8}$$

where the three right hand side terms are functions of the pressure ratios given in parentheses.

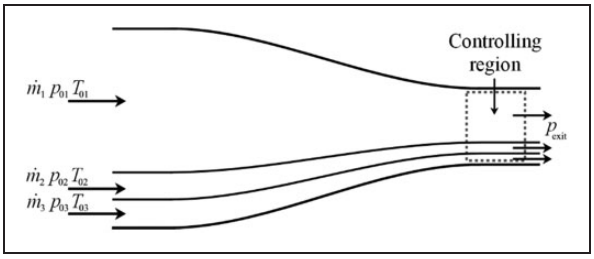


Figure 11. Schematic diagram of the unmixed, multi-stream, multiple controlling area model.

In a typical cooling system (represented in Figure 9), the ratios of the downstream pressure to the coolant stream pressures, p_{exit}/p_{02} and p_{exit}/p_{03}, are generally functions of the vane pressure ratio, p_{exit}/p_{01}, and the coolant-to-mainstream total pressure ratio, p_{02}/p_{01}. The former sets the mainstream aerodynamics and the latter, for a given mainstream flow, sets the coolant flow. Note we make the assumption that the film coolant and trailing edge coolant flows share a common inlet total pressure condition (i.e. $p_{02} = p_{03}$). Equation (8) can therefore be simplified to the following form

$$\Gamma_{vane}\left(\frac{p_{exit}}{p_{01}}, \frac{p_{02}}{p_{01}}\right) = \frac{\dot{m}_1\sqrt{T_{01}}}{p_{01}}\left(\frac{p_{exit}}{p_{01}}, \frac{p_{02}}{p_{01}}\right) + \frac{\dot{m}_2\sqrt{T_{02}}}{p_{02}}\left(\frac{p_{exit}}{p_{01}}, \frac{p_{02}}{p_{01}}\right) + \frac{\dot{m}_3\sqrt{T_{03}}}{p_{03}}\left(\frac{p_{exit}}{p_{01}}, \frac{p_{02}}{p_{01}}\right) \quad (9)$$

Each of the three terms on the right hand side of equation (9) are *surfaces* of capacity. The term on the left-hand side, total capacity, is a surface which is simply the summation of those three terms. Two variables are sufficient to define a position on the surface: the vane pressure ratio (p_{exit}/p_{01}) and the coolant-to-mainstream pressure ratio (p_{02}/p_{01}). A typical capacity surface in (p_{exit}/p_{01}, p_{02}/p_{01})-space is shown in Figure 12. Here the gradient of capacity in the p_{02}/p_{01}-axis has been exaggerated by an order of magnitude from a typical trend to more clearly illustrate the sensitivity in both axes. The negative trend arises because, while the coolant stream capacity terms (second and third terms on the right hand side of equation (9)) increase in magnitude with increasing p_{02}/p_{01}, for many NGVs the effect of mainstream 'displacement' by increased coolant flow is more significant. Surprisingly perhaps, the gradient of Γ_{vane} with p_{02}/p_{01} can be negative even where the coolant flow is a single stream issuing from a trailing edge slot in a cut-back pressure side of the vane.

It is well established that one of the prime sensitivities in setting HP NGV capacity (at the design or manufacture stage) is the interaction of trailing edge coolant flow with the mainstream. The effect is typically greater by at least an order of magnitude than the

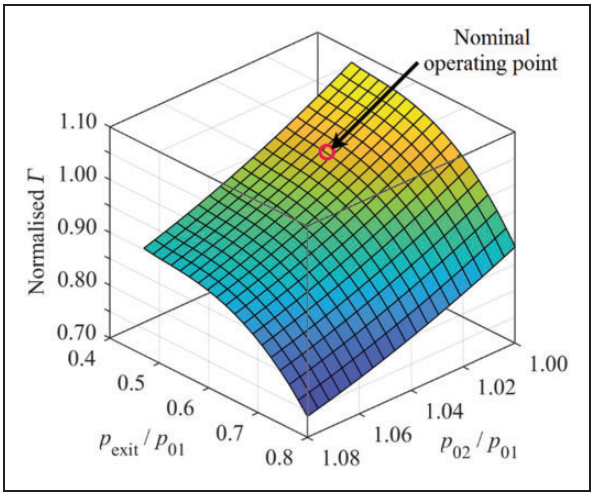


Figure 12. Surface of capacity, as a function of both vane pressure ratio, p_{exit}/p_{01}, and coolant-to-mainstream pressure ratio, p_{02}/p_{01}. The sensitivity to p_{02}/p_{01} has been exaggerated by a factor of 10.

sensitivity to particular film cooling arrangements. The trailing edge sensitivity is a function of both the detailed shape of the part in this region, and coolant-to-mainstream pressure ratio. An advantage of definition (9) is that the sensitivity to p_{02}/p_{01} is inherently built into the definition. This comes at the cost, in this simple formulation, that streams 1 and 2 are considered to be entirely non-interacting. This is a poor representation of most film cooling systems, which are typically fairly well mixed out as they pass through the controlling area.

Model 3

It is possible to construct a hybrid model in which the mainstream and film cooling flows mix fully before passing through a single controlling area, and in which there is an independent controlling area for the trailing edge cooling flow. This model is shown schematically in Figure 13.

A related system to this hybrid model was studied analytically by Povey.[4] Although this study[4] was restricted to only two streams (mainstream and film coolant), a more sophisticated treatment of mixing was developed (by means of a full control-volume approach, accounting for pressure losses in the partially mixed layer and changes in gas properties) allowing for both partial mixing (to a defined film cooling effectiveness) and a particular acceleration (to a defined 'throat' Mach number). In Povey,[4] the difference in capacity between experimental rig and engine conditions for typical boundary conditions was evaluated as a correction parameter. It was concluded[4] that there are unacceptable (of order 1.88%) sensitivities (differences between rig and engine situations) when definition (4) is used. This is because the entire flow is referenced to the mainstream flow properties. The definitions arising from Model 1 are

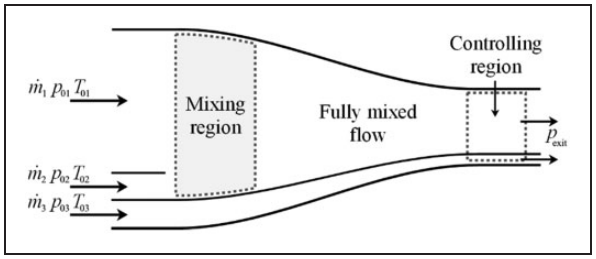


Figure 13. Schematic diagram of a hybrid model involving fully mixed mainstream and film cooling flows (1, 2) and unmixed trailing edge coolant (3).

therefore of little use in translating between systems with different T_{02}/T_{01}. It was also shown[4] that when capacity is based on a fully-mixed-out total pressure and temperature (similar to equation (7)), capacity differences between rig and engine reduce to approximately 0.20%, are proportional to the coolant mass flow (a later study,[7] showed also that this result was surprisingly independent of the specific arrangement of film cooling holes), and are amenable to analytical modelling.[7]

Attention is now turned to the difference between definitions (4), (7) and (9). Here we are concerned with the temperature averaging method alone, and do not consider more sophisticated aspects of the mixing and loss (the latter is treated in Povey[4]). To illustrate the sensitivity to temperature averaging, we simplify typical cold rig (A), warm rig (B), and engine conditions (C) to the values in Table 2.

The current experiments in the ECAT facility are closest to the cold rig situation (A). In all situations, the system has been simplified to a single cooling feed (i.e. $\dot{m}_3 = 0$). This is equivalent to the film cooling and trailing edge cooling flows sharing common inlet conditions p_{02} and T_{02}, with $\dot{m}_2$ representing the total coolant mass flow input to the system.

The sensitivity of capacity—according to these definitions—to variations in the coolant mass flows is also considered. Conditions A′ and A″ are defined to represent variations of −10% and +10% of $\dot{m}_2/\dot{m}_{\text{total}}$ respectively, with respect to the design point condition A. Likewise, pairs of ±10% cooling conditions are defined for situations B and C. The differences between equations (9) and (4) and between equations (9) and (7) are plotted in Figures 14 and 15 respectively, as functions of $\dot{m}_2/\dot{m}_{\text{total}}$ and T_{01}/T_{02}.

Consider first Figure 14 which shows the difference between equations (9) and (4). At cold rig conditions (A), there is no discrepancy between definitions due to temperature averaging alone, as the streams share a common temperature. At warm rig (B) and engine (C) conditions, there are 0.679% and 3.018% differences in capacity (respectively) between these definitions. Perhaps more importantly, consider the sensitivity to coolant mass flow rate variation. Assuming that total mass flow rate, $\dot{m}_{\text{total}}$, remains constant, equation (4) is unaffected by variation in $\dot{m}_2/\dot{m}_{\text{total}}$ (i.e. between

Table 2. Summary of simplified rig and engine conditions.

Situation	p_{02}/p_{01}	$\dot{m}_2/\dot{m}_{\text{total}}$	T_{01}/T_{02}
Cold rig (A)	1.00	0.070	1.0
Warm rig (B)	1.00	0.076	1.2
Engine (C)	1.00	0.100	2.0

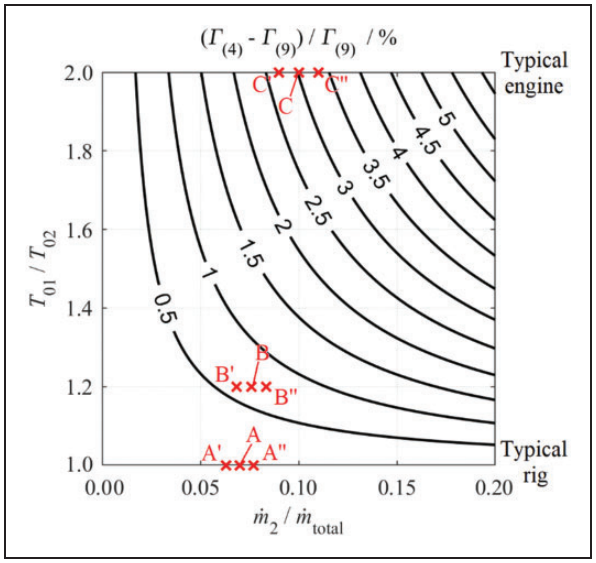


Figure 14. Contours of percentage difference in capacity defined according to equations (4) and (9), as a function of coolant-to-mainstream mass flow ratio and temperature ratio.

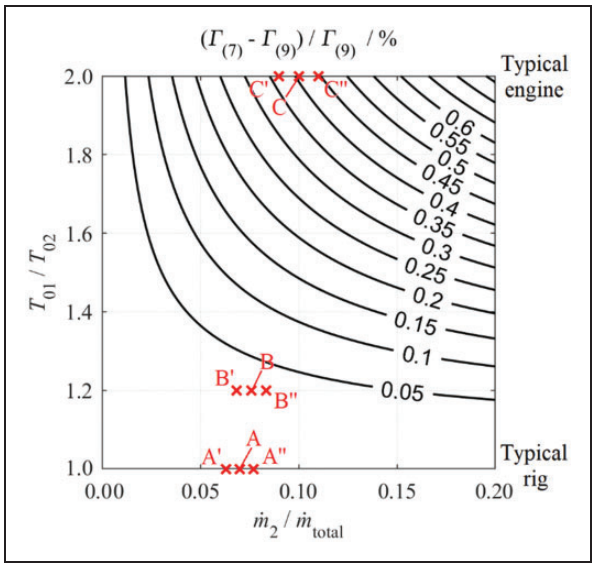


Figure 15. Contours of percentage difference in capacity defined according to equations (7) and (9), as a function of coolant-to-mainstream mass-flow ratio and mainstream-to-coolant temperature ratio.

A′ and A″). Equation (9) changes by 0.133% between B′ and B″, and by 0.603% between C′ and C″. Of course, when performing comparisons across conditions, correct scaling must be performed to ensure

Table 3. Summary of differences in sensitivity of different capacity definitions from Figures 14 and 15.

	$\Gamma_{(4)}$	$\Gamma_{(7)}$	$\Gamma_{(9)}$	Δ between $\Gamma_{(4)}$ and $\Gamma_{(9)}$	Δ between $\Gamma_{(7)}$ and $\Gamma_{(9)}$
$\Delta\Gamma$ at A / %	–	–	–	0.000	0.000
$\Delta\Gamma$ at B / %	–	–	–	0.679	0.028
$\Delta\Gamma$ at C / %	–	–	–	3.018	0.409
$\Delta\Gamma$ from A′ to A″ / %	0.000	0.000	0.000	0.000	0.000
$\Delta\Gamma$ from B′ to B″ / %	0.000	0.128	0.133	0.133	0.005
$\Delta\Gamma$ from C′ to C″ / %	0.000	0.526	0.603	0.603	0.077

these effects (and many others) are accounted for. Nonetheless, this illustrates the points that the exact definition of capacity matters, and that there are relatively high exchange rates between capacity (according to more rational definitions, e.g. equation (9)) and coolant mass flow rate at both warm rig and engine conditions. These results are summarised in Table 3.

Consider now Figure 15, which shows the difference between equations (9) and (7). Again, at cold rig conditions (A) there is no difference in capacity due to temperature averaging alone, as the streams share a common temperature.

At warm rig (B) and engine (C) conditions, there are 0.028% and 0.409% differences in capacity (respectively) between these definitions. These differences are considerably smaller (by an order of magnitude at warm rig conditions) than between equations (9) and (4), showing that the difference between these methods of temperature averaging—i.e. implied by equations (9) and (7)—is relatively subtle.

As coolant mass flow rate is varied at cold rig conditions (A′ to A″), there is no difference in the capacity change between definitions (9) and (7), because the capacity value is insensitive at a temperature ratio of unity. At warm rig conditions (B), ±10% variation in cooling mass flow rate (B′ to B″) gives a capacity change of 0.128% according to definition (7) and 0.133% according to definition (9). The difference in sensitivity between the two definitions is therefore 0.005%. Likewise, at engine conditions (C), the capacity changes with ± 10% variation in cooling flow (C′ to C″) according to definitions (7) and (9) are 0.526% and 0.603%, respectively, giving a difference in sensitivity between the definitions of 0.077%. These differences in sensitivity to cooling mass flow rate are very small indeed.

We conclude that whilst it is helpful (for the purpose of translating between different environments; see also studies[4,7]) for the mass flow rate and inlet temperature of coolant flows to be included in the capacity definition (as in equations (7) and (9), but not in equation (4)), the difference arising from the way in which this is achieved is relatively small. That is, using the square root of the mass-flow-weighted temperature with the total mass flow rate (equation (7)), or using the mass-flow-weighted sum of individual $\sqrt{T_0}$ terms for each stream (equation (9)). As corrections between different conditions (e.g. $\dot{m}_2/\dot{m}_{\text{total}}$ and T_{01}/T_{02}) are reasonably involved, and include many considerations in addition to temperature averaging, equations (7) and (9) appear to share similar usefulness in terms of their robustness (to first order) to changing inlet total conditions of individual streams between systems.

However, the definition in equation (9) has one significant advantage: in the correct experiment, it is possible (by virtue of the form of the equation) to isolate sensitivities to key effects such as trailing edge coolant ejection. That is, where the mass flow rates of the individual streams are independently metered, it becomes possible to identify the change in the mainstream mass flow ($\dot{m}_1$) caused by a change in the flow structure initiated by a change in one of the cooling mass flows ($\dot{m}_2$ or $\dot{m}_3$). This is possible because in equation (9), Γ_{vane} is a function of both p_{exit}/p_{01} *and*—crucially—p_{02}/p_{01}. The advantage of equation (9) lies primarily in the fact that it is explicitly expressed as a function of these two pressure ratios.

We feel that this justifies, for most purposes, defining NGV capacity in the form of equation (9)—it is sufficiently complete (on account of Γ_{vane} being a function of both p_{exit}/p_{01} and p_{02}/p_{01}) to allow sensitivities to, for example, trailing edge coolant flow to be included inherently in the definition. It is noted that there is weak physical justification for the complete lack of mixing of streams 1 and 2, but it is felt that this is sufficiently compensated for by the explicit inclusion of the sensitivity to p_{02}/p_{01}. Recall that the purpose here is to select, from a range of apparently arbitrary possibilities, a capacity definition that is as robust and transportable between different environments as possible. The objective is not to develop a quasi-analytical model,[4] as there is, of course, no physical description of the flow within this framework.

Evaluation of vane capacity characteristic

A capacity characteristic for a test vane can be generated, in principle, from a single test in blowdown mode operation. In practice, a number of repeat tests are performed, both to reduce the precision error in the mean of the characteristic and to allow

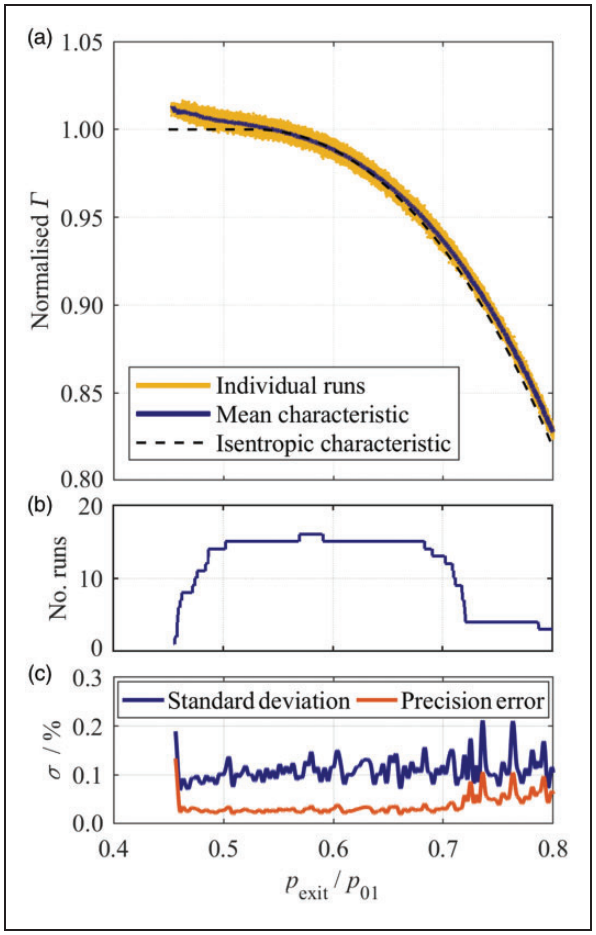


Figure 16. (a) Capacity characteristics from a typical HP NGV showing 17 repeat runs, and the mean-line trend; (b) number of repeat tests conducted as a function of p_{exit}/p_{01}; (c) standard deviation and precision uncertainty in the mean capacity trend.

this precision error to be evaluated. In this section, data from a typical set of experiments is presented and the method of generating a mean characteristic is demonstrated.

In this particular set, a total of 17 individual tests were conducted, shown by yellow lines in Figure 16(a). The mean capacity characteristic is overlaid in blue. Capacity is defined as in equation (9). Mass flow rates and vane inlet conditions of total pressure and temperature for each of the three constituent streams (mainstream, hub and case coolant) are measured as described in the preceding sections. The data are normalised with respect to the value at the nominal choked condition ($p_{exit}/p_{01} = 0.5283$).

To produce the mean characteristic, the data from all of the individual runs were resampled onto a uniform pressure ratio grid, allowing an unbiased mean to be computed. Individual runs had different ranges of p_{exit}/p_{01}. The number of individual runs covering each value of pressure ratio is plotted in Figure 16(b). The standard deviation of individual capacity characteristics from the mean characteristic, and the corresponding standard error in the mean are plotted in Figure 16(c) as functions of the mean vane pressure ratio, p_{exit}/p_{01}. Over the engine range of pressure ratio (typically $0.53 < p_{exit}/p_{01} < 0.65$), the standard deviation of individual capacity runs was 0.109% and the standard error in the mean ±0.025%. This is a low value, and is a small contributor to the overall uncertainty in capacity.

The capacity characteristic is, to first order, that of the classical isentropic trend (shown by the dashed curve in Figure 16a). In contrast to the isentropic trend, however, after reaching a near-plateau at around the critical vane pressure ratio ($p_{exit}/p_{01} \approx 0.5283$), when p_{exit}/p_{01} is further reduced the value of capacity continues to rise relatively steeply. By a pressure ratio of $p_{exit}/p_{01} = 0.45$, capacity has risen by 0.84% relative to the critical pressure ratio (similar effect seen in Povey et al.,[3,6,7]). In this transonic region of the characteristic, the flow field through the controlling region of the passage is complex, with relatively strong trailing edge shocks, and unsteady effects due to vortex shedding from the trailing edge.

Evaluation of bias uncertainty in capacity measurement

The bias uncertainty in a typical vane (or overall) capacity measurement (defined as in equation (9)) is now considered. Capacity is a derived (as opposed to directly measured) variable. Evaluating its bias uncertainty therefore follows several stages. Before the bias uncertainty in capacity can be evaluated, the bias uncertainty in the following quantities must be determined:

i. The mass flow metering nozzle effective areas;
ii. The measured inlet feed mass flow rates;
iii. The unsteady mass flow correction term for each individual mass flow rate;
iv. The vane inlet total pressure for each individual stream;
v. The vane inlet total temperature for each individual stream.

Error propagation techniques are then used to calculate the bias uncertainty in:

vi. The individual stream capacity terms (three terms on the right hand side of equation (9);
vii. The total vane capacity (left hand side of equation (9)).

Once the bias uncertainty in the total vane capacity has been obtained, the additional contributions to bias uncertainty arising from the following sources are considered:

viii. Uncertainty in the evaluation of the mean vane operating pressure ratio, p_{exit}/p_{01};
ix. Uncertainty in the evaluation of the coolant-to-mainstream pressure ratio, p_{02}/p_{01}.

The analysis is now progressed through the preceding nine stages. All bias uncertainty figures are given to 95% confidence. To frame the discussion around a particular example, a typical cold-rig test case is considered with the conditions listed in Table 4. The values of bias, precision, and overall uncertainties in vane capacity obtained from this analysis are then summarised and compared against those achieved in the original facility (the uncertainty analysis for which can be found in Povey et al.[6]), and a proposed upgraded facility. The latter differs from the current facility only in that the mainstream mass flow metering nozzle will be calibrated to ±0.250% bias uncertainty in effective area. All other parts of the measurement chain remain unchanged.

(i) Bias uncertainty in mass flow metering nozzle effective areas

The mainstream is fed with a sonic Venturi nozzle, operated at choked pressure ratios. The nozzle was calibrated to a bias uncertainty in the effective area, A_m, of ±0.500% (95% confidence). That is, $\sigma^{\%}_{A_m} = \pm 0.500\%$.

The hub and case coolant streams are fed from separate choked Venturi nozzles. The nozzle diameters used were approximately 16.0 mm and 15.3 mm for the hub and case, respectively. The estimated bias uncertainty in the coolant nozzle diameters is ±0.05 mm, or $\sigma^{\%}_{D_h} = \pm 0.313\%$ for the hub nozzle and $\sigma^{\%}_{D_c} = \pm 0.327\%$ for the case nozzle. The discharge coefficient in both cases was taken from ISO 9300[9] to be $C_d = 0.993$. The uncertainty in C_d was established to be negligible in relation to that in the nozzle diameters (less than ±0.001%). The estimated bias uncertainties in the coolant nozzle effective areas are therefore given by: $\sigma^{\%}_{A_h} = \pm 0.626\%$, and $\sigma^{\%}_{A_c} = \pm 0.654\%$.

(ii) Bias uncertainty in mass flow measurements

The mass flow rate through a choked Venturi nozzle is a function of the nozzle effective area and the upstream total pressure and temperature. First, consider the mainstream nozzle. The relationship is given by

$$\dot{m}_{\mathrm{m}} \propto A_{\mathrm{m}}\, p_{0,\mathrm{m}} \sqrt{T_{0,\mathrm{m}}} \tag{10}$$

where $p_{0,\mathrm{m}}$ and $T_{0,\mathrm{m}}$ are the total pressure and temperature upstream of the nozzle, respectively. For completeness, note there is also a weak dependence on gas properties, γ and R. This is estimated to be small (bias uncertainty below 0.01%) in the typical cold-rig situation and is ignored in this analysis.

The general equation for propagation of percentage uncertainty from directly measured to derived quantities is given in equation (21) in Appendix 1. For this case we get

$$\sigma^{\%}_{\dot{m}_{\mathrm{m}}} = \left[\sigma^{\%\,2}_{A_m} + \sigma^{\%\,2}_{p_{0\mathrm{m}}} + \tfrac{1}{4}\sigma^{\%\,2}_{T_{0\mathrm{m}}} \right]^{1/2} \tag{11}$$

The total pressure upstream of the main nozzle (nominal value 12.0 bar) was measured by two 30 bar transducers with quoted bias uncertainty (combined non-linearity and hysteresis) of ±0.04% of the transducer range. The uncertainty in the average measurement was therefore given by $0.04\% \times (30.0/12.0)/\sqrt{2} = \pm 0.071\%$.

The total temperature upstream of the main nozzle (nominal value 268 K) was measured using eight 0.025 mm K-type bare-bead thermocouples, with a quoted measurement accuracy of ±1.5 K, or ±0.560%. The percentage uncertainty in the average temperature measurement was therefore $0.56\%/\sqrt{8} = \pm 0.198\%$. The additional uncertainty associated with the thermal dissimilarity (to the calibration experiment) of the nozzle boundary layer due to the nonisothermal nature of the blowdown test can be shown to be very small and is ignored. The bias uncertainty in the primary nozzle mass flow rate measurement is then obtained by substituting the computed uncertainties into equation (9). This gives $\sigma^{\%}_{\dot{m}_{\mathrm{m}}} = \pm 0.515\%$.

$\sigma^{\%}_{\dot{m}_{\mathrm{m}}}$ is dominated by the uncertainty in the primary nozzle calibration. It is now possible (with state-of-the-art calibration techniques) to improve the calibration accuracy from ±0.500% to ±0.250%. The implications of this for experimental capacity measurement are discussed at the end of this paper. The corresponding bias uncertainties in the hub and case coolant nozzle mass flow rates are calculated in the same way. The uncertainties are summarised in Table 5.

(iii) Bias uncertainty arising from unsteady mass flow correction terms

Mass accumulation in the intermediate plena between the metering nozzles and the vane (due to changing pressure and temperature) creates a small difference between the mass flow rates delivered to the vane by each of the three streams, and the mass flow rates

Table 4. Summary of conditions for example capacity test case.

p_{exit}/p_{01}	T_{01}/T_{02}	p_{01}/p_{02}	$\dot{m}'_h/\dot{m}'_{\mathrm{total}}$	$\dot{m}'_c/\dot{m}'_{\mathrm{total}}$
0.55	1.0	1.025	0.039	0.036

Table 5. Summary of bias uncertainties in coolant stream pressures, temperatures and mass flow rates.

Stream	$\sigma^{\%}_{p_0}$	$\sigma^{\%}_{T_0}$	$\sigma^{\%}_{\dot{m}}$
Hub coolant	±0.292%	±0.270%	±0.703%
Case coolant	±0.292%	±0.270%	±0.728%

measured at the corresponding metering nozzles. The measured mass flow rates are corrected for this effect, as discussed in the earlier section.

Again taking the mainstream feed as an example, the mass flow rate delivered to the vane, $\dot{m}'_{\mathrm{m}}$, is given by

$$\dot{m}'_{\mathrm{m}} = \dot{m}_{\mathrm{m}} + \dot{m}''_{\mathrm{m}} = \dot{m}_{\mathrm{m}} + \sum_{i=1}^{4} \dot{m}''_{\mathrm{i}} \tag{12}$$

where $\dot{m}_{\mathrm{m}}$ is the mass flow rate measured at the mainstream nozzle and $\dot{m}''_{\mathrm{m}}$ is the correction term. $\dot{m}''_{\mathrm{m}}$ can be expressed as a summation over the intervening plena—in this case the sum over $i = 1$–4 of the correction terms, for the arbitrarily segmented description of the mainstream feed system (see Figure 1).

The unsteady mass flow correction term for each of the intermediate plena V1–V6 is computed based on equation (2): $\dot{m}'' = f\,(V_i,\ p_i,\ T_i,\ \mathrm{d}p_i/\mathrm{d}t,\ \mathrm{d}T_i/\mathrm{d}t)$, where the subscript i denotes an individual plenum. The volumes of the intermediate plena were measured to an estimated accuracy of ±5%. Uncertainties in the rates of change of plenum pressures and temperatures ($\mathrm{d}p_i/\mathrm{d}t$, $\mathrm{d}T_i/\mathrm{d}t$) were estimated conservatively to be of order ±15%. This is a high degree of uncertainty compared to the directly measured quantities and therefore dominates the estimated uncertainties in the correction mass flow rates.

Applying the general equation for uncertainty propagation (equation (21) in Appendix 1) to the expression for the plenum mass flow correction term (equation (2)), an expression is derived for the estimated bias uncertainty in the mass flow correction term for a single plenum

$$\sigma^{\%}_{\dot{m}''_i} = \left[\begin{array}{l} \left(\frac{V_i}{\dot{m}''_i RT_i}\right)^2 \left(\frac{\mathrm{d}p_i}{\mathrm{d}t} - \frac{p_i}{T_i}\frac{\mathrm{d}T_i}{\mathrm{d}t}\right)^2 \sigma^{\%2}_{V_i} \\ \quad + \left(\frac{p_i V_i}{\dot{m}''_i RT_i^2}\frac{\mathrm{d}T_i}{\mathrm{d}t}\right)^2 \sigma^{\%2}_{p_i} \\ \quad + \left(\frac{V_i}{\dot{m}''_i RT_i}\right)^2 \left(\frac{2p_i}{T_i}\frac{\mathrm{d}T_i}{\mathrm{d}t} - \frac{\mathrm{d}p_i}{\mathrm{d}t}\right)^2 \sigma^{\%2}_{T_i} \\ + \left(\frac{V_i}{\dot{m}''_i RT_i}\frac{\mathrm{d}p_i}{\mathrm{d}t}\right)^2 \sigma^{\%2}_{\frac{\mathrm{d}p_i}{\mathrm{d}t}} + \left(\frac{p_i V_i}{\dot{m}''_i RT_i^2}\frac{\mathrm{d}T_i}{\mathrm{d}t}\right)^2 \sigma^{\%2}_{\frac{\mathrm{d}T_i}{\mathrm{d}t}} \end{array} \right]^{1/2} \tag{13}$$

The individual plenum correction terms are estimated and then the uncertainty in the total mainstream correction mass flow rate is determined by summing the terms for plena V1–V4

$$\sigma^{\%}_{\dot{m}''_{\mathrm{m}}} = \left[\sum_{i=1}^{4} \left(\frac{\dot{m}''_i}{\dot{m}''_{\mathrm{m}}}\right)^2 \sigma^{\%2}_{\dot{m}_i} \right]^{1/2} \tag{14}$$

The correction flow rates for the hub and case coolant streams require terms for plena V6 and V5 respectively. Results for a typical test are summarised in Table 6. The result of applying the unsteady correction is to marginally increase the uncertainty in mainstream mass flow rate (from ±0.515% to ±0.530%). The coolant stream mass flow rates are only marginally affected. Curiously, the uncertainty of the corrected hub coolant flow rate is very slightly smaller than the corresponding uncertainty for the uncorrected flow rate. This surprising result arises from the statistical process of combining uncertainties, and is discussed in detail in Appendix 1.

Table 6. Summary of typical mainstream, hub and case coolant correction mass flow rates and estimated bias uncertainties.

Flow stream Plena	Mainstream V1–V4	Case coolant V5	Hub coolant V6
$\dot{m}$ / kg s^{-1}	13.120	0.519	0.561
$\dot{m}''$ / kg s^{-1}	0.149	0.003	0.002
$\dot{m}'$ / kg s^{-1}	13.269	0.521	0.563
$\sigma^{\%}_{\dot{m}}$	±0.515%	±0.728%	±0.703%
$\sigma^{\%}_{\dot{m}''}$	±13.09%	±11.42%	±16.03%
$\sigma^{\%}_{\dot{m}'}$	±0.531%	±0.729%	±0.702%

(iv) Bias uncertainty in inlet total pressure measurements

The mainstream total pressure at vane inlet (nominal value 2.0 bar) is measured using 32 transducers of range 5 bar, with quoted bias uncertainty of ±0.1% of full-scale range. The bias uncertainty in a single measurement was therefore 0.1 (5.0/2.00) = ±0.250%. The bias uncertainty in the mean of all 32 measurements was therefore $\sigma^{\%}_{p_{0\mathrm{m}}} = 0.250\%/\sqrt{32} = \pm 0.044\%$.

The standard deviation of the 32 individual measurements at a representative single point during a test was ±0.187%. This is within the ±0.250% bias uncertainty expected in an individual measurement due to the transducer specification. Hence, the spatial non-uniformity in inlet total pressure is extremely small.

Hub and case coolant total pressures are measured in the coolant cavities within the vane module in the form of differential measurements relative to the mainstream vane inlet total pressure. The nominal coolant-to-mainstream pressure differential was 0.050 bar. The differentials at hub and case were measured by five and four ±0.350 bar differential transducers, respectively, with quoted bias uncertainty due to non-linearity and hysteresis of ±0.2% of the full-scale range. The estimated percentage bias uncertainties in total pressure are calculated as $\sigma^{\%}_{p_{0,\mathrm{h}}} = \pm 0.626\%$ and $\sigma^{\%}_{p_{0,\mathrm{c}}} = \pm 0.700\%$ for the hub and case, respectively. Here Δp_0 refers to the coolant-to-mainstream pressure *differential*.

The bias uncertainty in the *absolute* values of coolant inlet total pressure is dominated by the mainstream total pressure measurement due to the small

relative size of the pressure differential. Bias uncertainty is computed as $\sigma^{\%}_{p_{0\mathrm{hc}}} = \sigma^{\%}_{p_{0\mathrm{cc}}} = \pm 0.046\%$ for both the hub and case streams.

(v) Bias uncertainty in inlet total temperature measurements

Mainstream total temperature at vane inlet (nominal value 277 K) is measured by 32 K-type thermocouples, each with a quoted measurement accuracy of ±1.5 K or ±0.540% bias uncertainty. The bias uncertainty in the mean of all 32 measurements was therefore $\sigma^{\%}_{T_{0\mathrm{m}}} = 0.540\%/\sqrt{32} = \pm 0.096\%$.

The standard deviation of the 32 individual measurements at a representative single point during a test was ±0.074%. This is small in comparison to the ±0.540% bias uncertainty in the individual measurements, indicating that the spatial non-uniformity in inlet total temperature is negligible. For completeness, note that the assumption that all of the individual measurements are entirely independent is unlikely to be true in practice, as the instruments come from a common batch and thus their bias uncertainties will be partially correlated.

Hub and case coolant stream total temperatures are measured in the coolant cavities within the vane module, by five and four K-type thermocouples, respectively. The bias uncertainties are therefore determined as $\sigma^{\%}_{T_{0\mathrm{h}}} = \pm 0.241\%$ and $\sigma^{\%}_{T_{0\mathrm{c}}} = \pm 0.270\%$.

(vi) Bias uncertainty in individual stream capacity terms

The bias uncertainties in mass flow rate, inlet total pressure and total temperature are now combined to calculate the bias uncertainty in capacity. This is done for each of the mainstream, hub and case coolant streams, represented by the three terms on the right-hand side of equation (9). As an example, the bias uncertainty in the mainstream capacity term, Γ_{m}, is given by

$$\sigma^{\%}_{\Gamma_{\mathrm{m}}} = \left[\sigma^{\%\ 2}_{\dot{m}'_{\mathrm{m}}} + \sigma^{\%\ 2}_{p_{0\mathrm{m}}} + \frac{1}{4}\sigma^{\%\ 2}_{T_{0\mathrm{m}}} \right]^{1/2} \tag{15}$$

Substituting in numbers gives $\sigma^{\%}_{\Gamma_{\mathrm{m}}} = \pm 0.534\%$. Comparing the uncertainty in the mainstream capacity term to the uncertainty in the corresponding mass flow term, $\sigma^{\%}_{\dot{m}'_m} = \pm 0.530\%$, shows that the difference arising from the measurement of mainstream cascade inlet flow conditions is only 0.004%—a very small value. This indicates that instrumentation of the mainstream vane inlet flow conditions is optimised. The bias uncertainty of the hub and case coolant capacity terms are determined in the same way, giving $\sigma^{\%}_{\Gamma_{\mathrm{h}}} = \pm 0.714\%$ and $\sigma^{\%}_{\Gamma_{\mathrm{c}}} = \pm 0.743\%$, respectively.

The difference in uncertainty between the individual coolant stream mass flow rate and capacity terms is therefore ±0.012% for the hub and ±0.014% for the case. This is driven primarily by the bias uncertainty in coolant feed total temperature measurements. There is little to gain from further optimisation of stream inlet total pressure instrumentation.

(vii) Bias uncertainty in overall capacity measurement

The bias uncertainties associated with the individual capacity terms are now combined to calculate the uncertainty in the overall capacity (definition of equation (9)), as follows

$$\sigma^{\%}_{\Gamma_{\mathrm{vane}}} = \left[\left(\frac{\Gamma_{\mathrm{m}}}{\Gamma_{\mathrm{vane}}}\right)^2 \sigma^{\%^2}_{\Gamma_{\mathrm{m}}} + \left(\frac{\Gamma_{\mathrm{h}}}{\Gamma_{\mathrm{vane}}}\right)^2 \sigma^{\%^2}_{\Gamma_{\mathrm{h}}} + \left(\frac{\Gamma_{\mathrm{c}}}{\Gamma_{\mathrm{vane}}}\right)^2 \sigma^{\%^2}_{\Gamma_{\mathrm{c}}} \right]^{1/2} \tag{16}$$

Substituting in the previously computed values gives $\sigma^{\%}_{\Gamma_{\mathrm{vane}}} = \pm 0.494\%$. The *percentage* uncertainty (but not the absolute uncertainty) in the sum is lower than that in any of the constituent measurements. The small reduction arises because the measurements are assumed to be entirely independent. The mathematical basis for this effect is discussed in Appendix 1.

(viii) Bias uncertainty in capacity due to uncertainty in exit static pressure and vane pressure ratio

The overall capacity defined in equation (9) is a function of two controlling pressure ratios: p_{exit}/p_{01} and p_{02}/p_{01}. This can be visualised as a surface in the pressure ratio space (Figure 12). Measurement error in either p_{exit}/p_{01} or p_{02}/p_{01} leads to error in the evaluation of vane capacity. The magnitude of this error is proportional to the local gradient of the function $\Gamma_{\mathrm{vane}}(p_{\mathrm{exit}}/p_{01}, p_{02}/p_{01})$ in the relevant axis (i.e. the partial derivative in a particular direction). Each of these pressure ratio axes is now considered in turn.

Uncertainty in the measurement of mean static pressure at vane exit, p_{exit}, leads to error in the evaluation of the pressure ratio p_{exit}/p_{01}. This can be thought of as a movement over the capacity surface in the $(p_{\mathrm{exit}}/p_{01})$-direction (see Figure 12). Recall that static pressure at vane exit is measured experimentally by a total of 96 tappings located on the vane platforms at hub and case, a short distance downstream of the vane trailing edges (Figure 7). The definition of vane exit static pressure is somewhat arbitrary. In principle, one could determine an accurate area-average or mass-flow-average static pressure by traversing, but this would be impractical and possibly subject to probe interference effects. Even if it were desired, it would only be possible at a downstream plane—defining a unique *controlling area* here that was related to the measurement would not be possible. In short, it

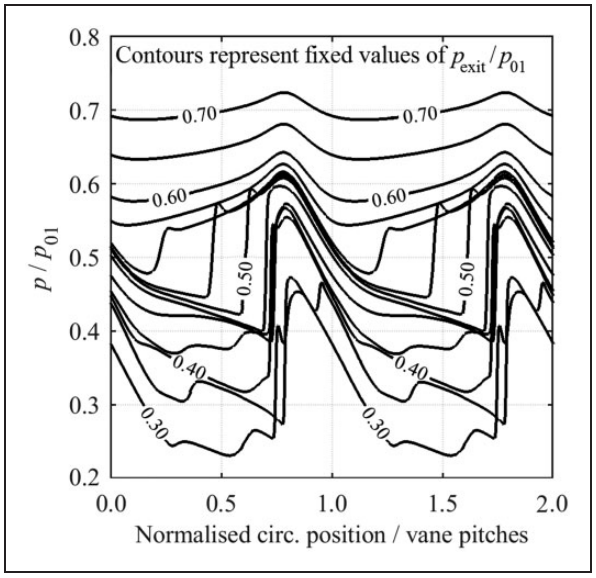


Figure 17. CFD-predicted circumferential static pressure profiles at vane exit (single axial position) for a range of operating pressure ratios.

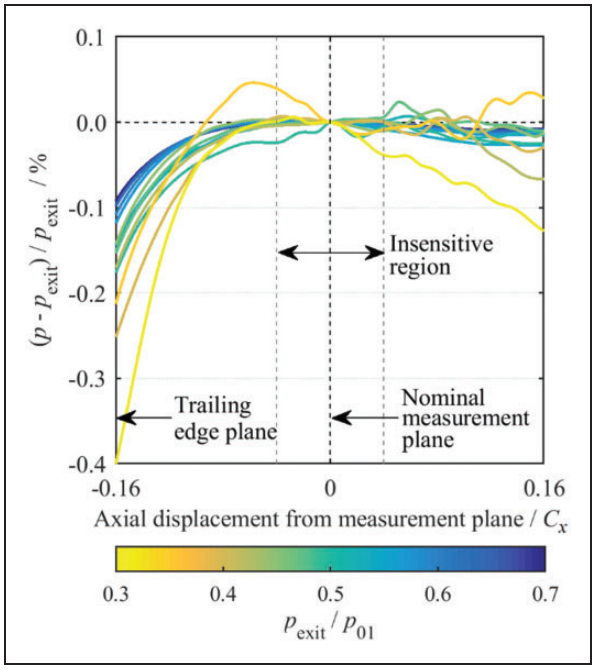


Figure 18. CFD-predicted variation in circumferentially averaged pressure ratio as a function of axial interrogation plane for a range of p_{exit}/p_{01}.

is hard to see any advantage in measuring static pressure by traversing, and there are a number of possible disadvantages that would need to be considered.

Likewise, in principle a vane exit static pressure could be defined based on a single tapping measurement. This would likely lead to an unusual capacity characteristic, as the flow structure (exact location and strength of shocks etc.) close to the tapping location would change with vane pressure ratio, thus distorting the x-axis of the characteristic. A more significant problem would be the sensitivity to the exact tapping location, and the difficulty of replicating the precise position in a corresponding CFD study or repeat experiment. The aim—as far as capacity measurement is concerned—is to define a static pressure measurement protocol which is robust between repeat experiments, different builds of the same experiment, and in comparisons against computational simulations.

The sensitivity of capacity to the vane exit static pressure measurement is now examined using 2D Reynolds-Averaged Navier-Stokes (RANS) simulations. The profile is based on a section of the vane at midspan. Results of the simulation are presented in Figures 17 and 18.

Circumferential static pressure distributions at vane exit are plotted in Figure 17 for 13 values of mean vane pressure ratio in the range $0.30 \leqslant p_{exit}/p_{01} \leqslant 0.70$. The data were extracted (from CFD) at the same axial location as the experimental measurement points, 0.17 axial chords downstream of the vane trailing edge. Corresponding experimental data for a single pressure ratio were shown in Figure 8. As p_{exit}/p_{01} is decreased, the circumferential non-uniformity in the profile increases. For $p_{exit}/p_{01} \leqslant 0.55$, a shock crosses the measurement plane, marked by a high gradient of static pressure. As p_{exit}/p_{01} decreases, the shock strengthens and moves rightwards. This profile is characteristic of forward loaded HP NGVs.

At each value of p_{exit}/p_{01} (representing an individual CFD solution), the static pressure distributions in the underlying data (Figure 17) are circumferentially averaged *at each axial location* to give a single value. The trends in the axial direction of this circumferential average are presented in Figure 18 as functions of pressure ratio (p_{exit}/p_{01}). A range of axial positon $|x/C_x| < 0.16$ has been considered, centred on the nominal measurement plane ($x/C_x = 0$). At a particular value of p_{exit}/p_{01} based on the nominal measurement plane, the circumferentially averaged values of p_{exit}/p_{01} at each axial location (in the range $|x/C_x| < 0.16$) are expressed as a percentage difference from the value at the nominal measurement plane ($x/C_x = 0$).

With the exception of very low pressure ratios ($p_{exit}/p_{01} < 0.4$), the axial gradient of average static pressure close to the measurement plane ($|x/C_x| < 0.05$) is extremely small (variation of less than 0.03%), showing very low sensitivity to small axial deviations in tapping location. Further downstream ($x/C_x > 0.05$), a complex shock system develops in the flow field, causing an increase in the sensitivity to the choice of axial measurement plane. This will be returned to in the context of defining an optimum distribution of tappings (axial and circumferential locations) for capacity measurement.

Before determining an optimum practicable distribution of pressure tappings, three principal sources of bias uncertainty affecting the evaluation of a robust mean vane exit static pressure are examined. These are:

(a) Discrete sampling (limited number of tappings) of the time-varying, spatially non-uniform static pressure field at vane exit, which features complex flow features with high gradients. This is referred to as *uncertainty due to tapping pattern*.
(b) Uncertainty in the location of tappings, arising due to variation in the vane manufacture and/or inaccuracies in the positioning of the tappings. This is referred to as *uncertainty due to variation in tapping location*.
(c) Uncertainty in the measurement of static pressure at each tapping due to pressure transducer bias uncertainty. This is referred to as *transducer measurement uncertainty*.

Each of these sources of error is now dealt with in turn.

Uncertainty due to tapping pattern arises due to the sensitivity of the mean vane exit static pressure measurement to the tapping pattern. The error is defined as the difference between the arithmetic mean of the static pressure values at the finite set of tapping locations, and the underlying circumferential average pressure. Taking this definition, the uncertainty due to tapping pattern depends on both the number of measurement points, and on their circumferential locations relative to the underlying flow field. Certain measurement points will sit in particularly high pressure gradients in the flow—for example a tapping sitting in the path of a shock which moves across the tapping location with changing vane pressure ratio. Other tappings will be located in less sensitive regions of the flow, closer to mid-passage, for example, or in regions which (over a normal operating pressure range) remain on one side or another of a shock. By increasing the number of tappings, these sensitivities are averaged out.

Using the data of Figure 17, the uncertainty due to tapping pattern is estimated by considering the difference between the average pressure measured by a *particular number* of evenly spaced circumferential sample points and the underlying circumferentially averaged pressure. For a given number of tappings, the maximum difference is found by considering every possible circumferential positioning. This is referred to as the *worst-case* error. In Figure 19, the worst-case error, normalised by $p_{01} - p_{exit}$ (y-axis), is plotted as a function of vane pressure ratio over the range $0.30 \leqslant p_{exit}/p_{01} \leqslant 0.70$ (x-axis), for a number of sample points between two and eight.

The worst-case error is approximately inversely proportional to the number of sample points. This result is expected as the average of an increasing number of discrete samples converges on the continuous average.

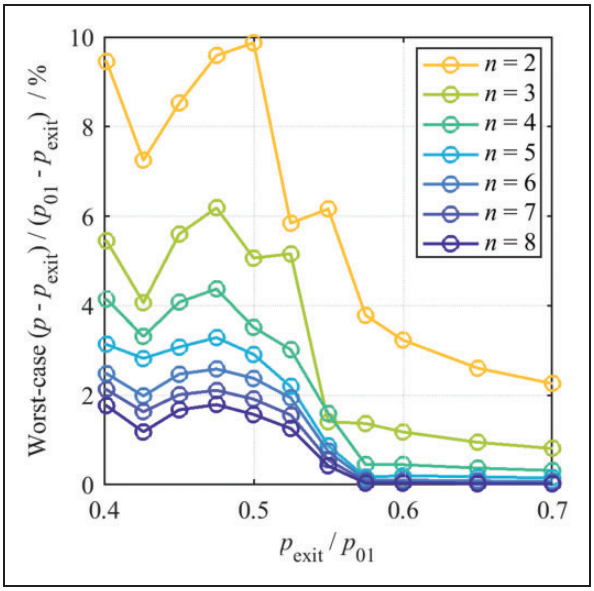


Figure 19. Normalised maximum difference between the underlying circumferentially-averaged pressure, and the average pressure as measured by a particular number of evenly spaced circumferential sample points. Each line represents a different number of sample points.

The trend with decreasing pressure ratio (p_{exit}/p_{01}) shows a sharp rise in the maximum pressure difference as the flow enters the transonic region. This is due to the presence of shocks, which cause high gradients in static pressure (see Figure 17). A typical experimental campaign has eight tappings per vane pitch (see Figure 7). From Figure 19, for $n = 8$, at a nominal vane pressure ratio of $p_{exit}/p_{01} = 0.55$, the normalised worst case error is approximately $\pm 0.417\%$. This gives a (non-normalised) worst case bias uncertainty in p_{exit} due to tapping pattern of $\pm 0.327\%$.

Uncertainty due to tapping location variation arises due to the sensitivity of the mean vane exit static pressure measurement to deviations of individual static tappings from their intended locations on the vane platforms. To estimate the uncertainty arising from this effect, the location of each sample point in the CFD model is allowed to move both circumferentially and axially. The range of possible deviations was estimated very pessimistically to be ± 1.5 mm in both directions. The position of a given tapping is then represented by a 2D normal distribution in space, with 95% of samples lying within ± 1.5 mm of the nominal location. At each vane pressure ratio, the distribution of each pressure measurement corresponding to the 2D normal distribution for the tapping was then evaluated by interpolating the underlying predicted 2D flow field (visualised in 1D in Figures 17 and 18). Thus, a probability density function (PDF) is determined to describe the expected static pressure measured at a given tapping. These functions vary greatly from tapping to tapping, in some cases being similar to skewed normal distributions, and in others being bimodal (in the vicinity of a

shock, for example). Uncertainty bounds on the value at each tapping are determined to the 95% *credible interval* (the interval within which 95% of samples are expected to fall, given that the true, underlying PDF is known) at each value of p_{exit}/p_{01}. Sample points located close to shocks have a larger credible interval due to high spatial pressure gradients within the region in which the sample could lie.

For each particular tapping distribution (particular number of tappings and circumferential positioning), the PDF and associated credible interval for the pitch-wise-average static pressure are calculated by considering the PDF and associated credible interval for each individual tapping location. In each case, the maximum credible interval is taken from all possible circumferential locations of the sample points (similar analysis to that used to evaluate the pattern location uncertainty). The size of the credible interval for p_{exit} defines the uncertainty in p_{exit} due to tapping location uncertainty.

The worst-case (across all possible circumferential positions of a given number of samples) credible interval for the inferred value of p_{exit} is plotted in Figure 20 as a function of both p_{exit}/p_{01} and the number of sample points. For a given value of p_{exit}/p_{01}, increasing the number of samples significantly reduces the size of the credible interval, as the averaging effect causes the inferred average pressure to become increasingly insensitive to particularly high gradients in the flow field. The worst-case credible interval grows substantially as p_{exit}/p_{01} passes through the transonic range into the mildly supersonic range. This is due to the presence of strong pressure gradients across shockwaves. At low p_{exit}/p_{01}, the uncertainty due to tapping location variation is reduced significantly by increasing the number of sample points. At high p_{exit}/p_{01}, a larger number of tappings is less important as the flow field is more uniform.

A typical experimental campaign has eight tappings per vane pitch (see Figure 7). From Figure 20, at a nominal vane pressure ratio of $p_{exit}/p_{01} = 0.55$, the normalised credible interval for the inferred average pressure value is therefore approximately 0.864%. This gives a (non-normalised) worst case error in p_{exit} due to tapping location variation of ±0.407%. This uncertainty is mitigated by the use of several instrumented vanes (three vane pairs or twelve instrumented platforms in a typical experiment in the current facility). Assuming the positioning of tappings on each platform to be independent, the bias uncertainty in p_{exit} based on 12 platforms is given by $0.407/\sqrt{12} = \pm 0.118\%$.

Finally, the contribution to the bias uncertainty in p_{exit} of *transducer measurement uncertainty* is considered. In a typical experiment in the current facility, the vane exit static pressure is measured using a total of 96 transducers (2 bar range) distributed over the 12 instrumented vane platforms. The quoted bias uncertainty was ±0.1% of transducer range, and the nominal operating pressure was 1.09 bar. The bias uncertainty in an individual measurement was

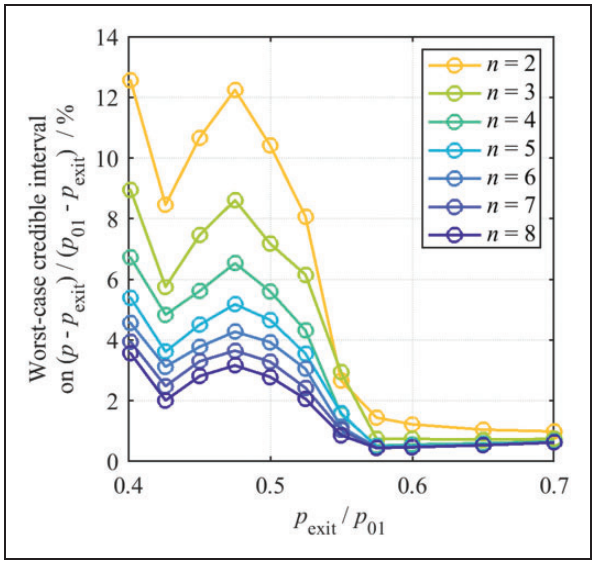


Figure 20. Normalised credible interval for average pressure measured by a particular number of—nominally—evenly spaced circumferential sample points subject to random spatial variation of ±1.5 mm both axially and circumferentially. Results are for a single instrumented platform. Each line represents a different number of samples.

therefore $0.1 \times (2.00/1.09) = \pm 0.184\%$. This gives a bias uncertainty in the mean pressure measured on a single vane platform (mean of eight measurements) of ±0.065%. The uncertainty in the mean pressure measured across all 12 platforms (mean of 96 measurements) was therefore 0.019%.

The overall bias uncertainty in the vane exit static pressure measurement is determined by combining the uncertainties arising from each of the three sources of uncertainty. The overall bias uncertainty is plotted as a function of p_{exit}/p_{01} in Figure 21. The contribution to the bias uncertainty of each of the three underlying sources of uncertainty is also shown. Dashed lines represent the result for an individual platform (eight tappings). Solid lines represent a typical experiment with 12 instrumented platforms. Note only one line is shown for tapping pattern uncertainty, which is independent of the number of platforms considered.

At the nominal pressure ratio ($p_{exit}/p_{01} = 0.55$), the overall bias uncertainty in p_{exit} associated with a single vane platform measurement is ±0.633%. The uncertainty associated with a measurement over 12 instrumented platforms is ±0.362%. This bias uncertainty is then combined with the previously evaluated bias uncertainty in vane inlet total pressure, p_{01}, to obtain the bias uncertainty in vane pressure ratio, p_{exit}/p_{01}. This gives $\sigma^{\%}_{\frac{p_{exit}}{p_{01}}} = \pm 0.365\%$.

The bias uncertainty in p_{exit}/p_{01} can be translated into a bias uncertainty in vane capacity by reference to the surface of capacity in pressure–ratio space, $\Gamma_{vane}(p_{exit}/p_{01}, p_{02}/p_{01})$. This was presented in Figure 12. In the figure the sensitivity to p_{02}/p_{01} was exaggerated for visualisation purposes. The underlying

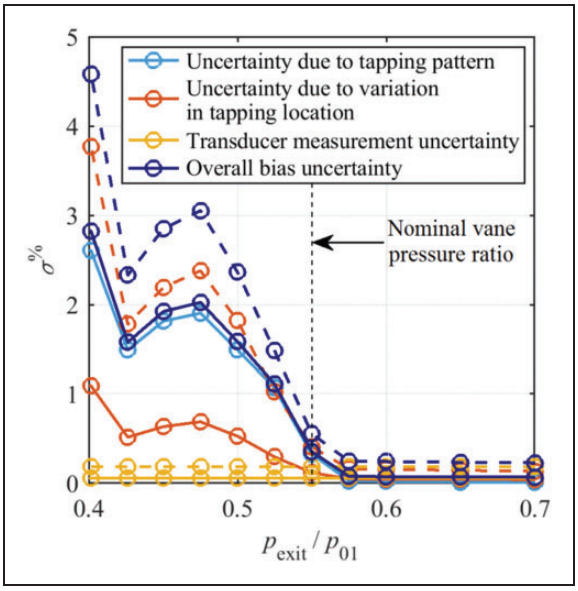


Figure 21. Bias uncertainty in p_{exit} from each of the three principal sources, along with the overall bias uncertainty, as functions of p_{exit}/p_{01}. Dashed and solid lines represent the uncertainties associated with single platform and 12 platform measurements, respectively.

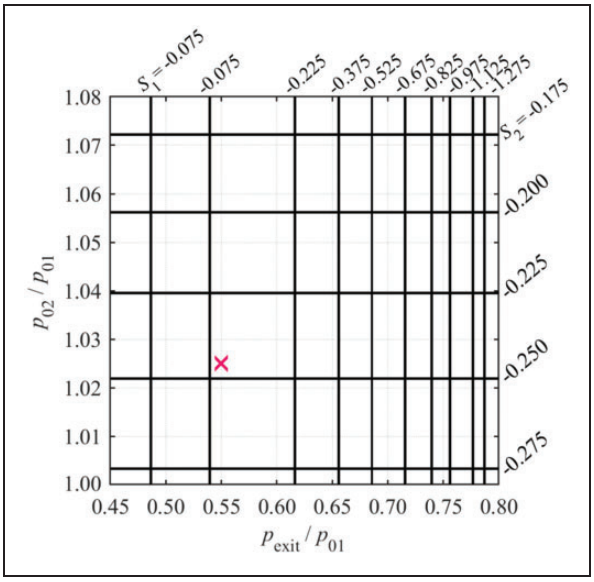


Figure 22. Contours of the sensitivity coefficients S_1 (defined in equation (17)) and S_2 (defined in equation (20)) as functions of p_{exit}/p_{01} and p_{02}/p_{01}.

(unexaggerated) data is now used to evaluate typical sensitivities in both axes. The sensitivity of $\Gamma_{vane}(p_{exit}/p_{01}, p_{02}/p_{01})$ to p_{exit}/p_{01}, which we call S_1, is defined in terms of the normalised partial derivative, as follows

$$S_1 = \frac{\partial \Gamma_{vane}\left(\frac{p_{exit}}{p_{01}}, \frac{p_{02}}{p_{01}}\right)}{\partial\left(\frac{p_{exit}}{p_{01}}\right)} \times \frac{\left(\frac{p_{exit}}{p_{01}}\right)}{\Gamma_{vane}} \tag{17}$$

Contours of S_1, along with a second sensitivity coefficient, S_2, which describes the sensitivity of capacity to p_{02}/p_{01}, are plotted in Figure 22. This will be returned to in the following section. The nominal operating point is marked by a red cross.

At the operating point, S_1 takes a value of approximately -0.092. This shows that the uncertainty in vane capacity is an order of magnitude lower than the uncertainty in p_{exit}/p_{01}. For a bias uncertainty in p_{exit}/p_{01} of $\pm 0.365\%$, the corresponding uncertainty in vane capacity is $\pm 0.034\%$. To calculate the impact on overall uncertainty in vane capacity, this is combined with the uncertainty in vane capacity arising from steps (i) to (vii)—above—to obtain

$$\sigma^{\%}_{\Gamma_{vane}} = \left(0.494^2 + 0.034^2\right)^{1/2} = \pm 0.495\% \tag{18}$$

That is, the additional impact of uncertainty in exit static pressure and vane pressure ratio increases the overall bias uncertainty in vane capacity from $\pm 0.494\%$ to $\pm 0.495\%$.

(ix) Bias uncertainty in capacity due to uncertainty in coolant-to-mainstream pressure ratio

The additional uncertainty in capacity due to uncertainty in coolant-to-mainstream pressure ratio, p_{02}/p_{01}, is now considered. Here p_{02} is defined as the mean of the hub and case coolant total pressures—these are similar in most engine scenarios.

The bias uncertainties in mainstream and coolant inlet total pressures have been calculated as $\pm 0.044\%$ and $\pm 0.046\%$, respectively. These quantities share a large common element, as the coolant pressure is measured as a differential relative to the mainstream—that is, $p_{02}/p_{01} = 1 + \Delta p_{0,c}/p_{01}$, where $\Delta p_{0,c}$ is the coolant-to-mainstream pressure differential. The resulting bias uncertainty in coolant-to-mainstream pressure ratio is determined according to equation (21)

$$\sigma^{\%}_{\frac{p_{02}}{p_{01}}} = \left(\frac{\Delta p_{0,h} + \Delta p_{0,c}}{p_{0,h} + p_{0,c}}\right)\left(\begin{array}{c}\sigma^{\%\ 2}_{p_{0m}} + \frac{1}{4} \times \sigma^{\%\ 2}_{\Delta p_{0,h}} \\ + \frac{1}{4} \times \sigma^{\%\ 2}_{\Delta p_{0,c}}\end{array}\right)^{1/2} \tag{19}$$

Substituting in values gives $\sigma^{\%}_{\frac{p_{02}}{p_{01}}} = \pm 0.012\%$.

In the same manner as the prior analysis, the bias uncertainty in p_{02}/p_{01} can be translated into a bias uncertainty in vane capacity by defining a sensitivity coefficient, S_2, which represents the sensitivity of $\Gamma_{vane}(p_{exit}/p_{01}, p_{02}/p_{01})$ to p_{02}/p_{01}, as follows

$$S_2 = \frac{\partial \Gamma_{vane}\left(\frac{p_{exit}}{p_{01}}, \frac{p_{02}}{p_{01}}\right)}{\partial\left(\frac{p_{02}}{p_{01}}\right)} \times \frac{\left(\frac{p_{02}}{p_{01}}\right)}{\Gamma_{vane}} \tag{20}$$

This sensitivity coefficient is plotted in Figure 22. At the operating point, the value of S_2 is approximately −0.246. That is, the uncertainty in vane capacity is reduced by a factor of around four relative to the uncertainty in p_{02}/p_{01}. For a bias uncertainty in p_{02}/p_{01} of ±0.012%, the corresponding uncertainty in vane capacity is of order ±0.003%.

To calculate the impact on overall uncertainty in vane capacity, this is combined with the uncertainty arising from steps (i) to (viii)—above—to obtain $\sigma^{\%}_{\Gamma_{\text{vane}}} = \pm 0.495\%$. That is, the uncertainty in p_{02}/p_{01} increases the overall uncertainty in vane capacity by a negligibly small amount.

Summary of uncertainties and comparison to original and proposed upgraded facilities

The bias uncertainties in mass flow rate and capacity measurements are now summarised and compared with the results both from the original facility (Povey et al.[6]), and a proposed upgraded facility.

Recall that—to a large extent—the overall uncertainty in mass flow rate and capacity measurements is driven by the bias uncertainty in the effective area of the primary (mainstream) metering nozzle. This is inherited from a calibration process (which gives a result traceable to an international standard) and cannot be improved by experimental technique. The uncertainty values for this term are given in the first row of Table 7. The other rows of the table should be referenced to these values.

The remaining rows of the table present the bias uncertainty in the mass flow rate measurements and capacity measurements of the three individual streams (mainstream, hub and case), and the bias uncertainty in the overall capacity measurement. The last is presented both excluding and including the errors associated with uncertainty in p_{exit}/p_{01} and p_{02}/p_{01}—parameters Γ_{vane} and Γ'_{vane}, respectively.

To calculate the overall uncertainty in capacity, the bias error must be combined with the precision uncertainty in the mean of the capacity characteristic. The latter is evaluated experimentally and has been discussed in the context of Figure 16. For the original facility, the standard deviation of individual capacity runs was ±0.040%. This gave a standard error in the mean (based on a typical campaign of approximately 20 runs) of ±0.028%. The corresponding values for the current facility are ±0.109% and ±0.025%, respectively. For the proposed upgraded facility, the same values are assumed. The values of overall uncertainty are summarised in Table 8.

Figure 23 provides visualisation of the propagation of bias uncertainty through the measurement and analysis chain, following the nine stages of analysis, i–ix, previously described. The original facility (described in detail by Povey et al.[6]) is shown by a blue line. The final bias uncertainty in capacity for this facility is ±0.536%.

The current facility is represented by red lines, with dotted lines indicating the coolant streams, and the solid line indicating the mainstream. The lines combine when the overall vane capacity is calculated (analysis stage vii.). The final bias uncertainty in capacity for this facility is ±0.495%. The primary improvements over the original facility come in steps vii and viii, leading to an improvement of ±0.040% in the final bias uncertainty in capacity. The yellow lines represent a proposed upgraded facility, differing from the current one only in that the calibration of the primary mass flow metering nozzle will be improved from ±0.500% bias uncertainty to ±0.250%. This results in a final bias uncertainty of ±0.301%.

The following conclusions regarding the uncertainty analysis are drawn:

- In the original facility, the entire measurement and analysis chain led to an *overall* uncertainty in capacity of ±0.536%, only ±0.036% greater than the ±0.500% bias uncertainty inherited from the primary nozzle. This was achieved by careful

Table 7. Comparison of *bias* uncertainties in mass flow rate and capacity measurements between: the original facility,[1] the current facility, and a proposed upgraded facility.

	Bias uncertainty (95%) / %		
Parameter	Original facility (Povey et al.[6])	Current facility	Proposed upgraded facility
A1	±0.500	±0.500	±0.250
$\dot{m}_m'$	±0.518	±0.530	±0.312
$\dot{m}_h'$	–	±0.702	±0.702
$\dot{m}_c'$	–	±0.729	±0.729
Γ_m	–	±0.534	±0.320
Γ_h	–	±0.714	±0.714
Γ_c	–	±0.743	±0.743
Γ_{vane}	±0.531	±0.494	±0.299
Γ'_{vane}	±0.535	±0.495	±0.301

Table 8. Comparison of *overall* uncertainties in capacity measurements between: the original facility,[6] the current facility, and a proposed upgraded facility.

	Original facility[1]	Current facility	Proposed upgraded facility
Γ'_{vane} bias	±0.535%	±0.495%	±0.301%
Γ'_{vane} precision (20 runs)	±0.028%	±0.025%	±0.025%
Γ'_{vane} overall	±0.536%	±0.496%	±0.302%

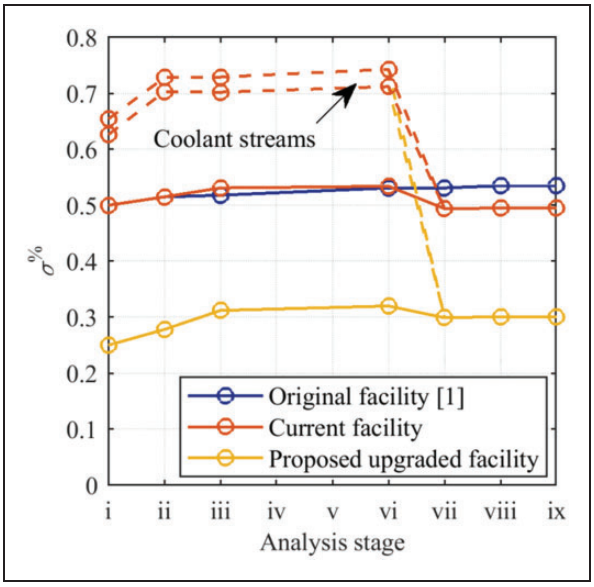


Figure 23. Visualisation of the propagation of bias uncertainty through to the final capacity measurement, for each of the three considered facilities.

experimental design in terms of hardware, instrumentation and experimental technique. Note that these values differ slightly from Povey et al.[6] as the bias uncertainty due to error in vane exit static pressure measurement is more comprehensively considered.

- In the current facility, a combination of small improvements in the measurement of inlet and exit flow conditions, and small refinements to the experimental technique have led to an *overall* uncertainty in capacity of ±0.496%, or ±0.004% *lower* than the ±0.500% bias uncertainty of the primary (mainstream) nozzle. This is possible because mainstream and coolant streams are independently metered. Figure 23 shows that the reduction in overall uncertainty relative to the original facility has two significant drivers: the independent measurement of coolant streams (approximately 8% of total flow), which has the curious effect of driving down the overall uncertainty (see Appendix 1); and a reduced uncertainty in p_{exit}/p_{01} due to increased number of vane exit static pressure measurements. These are analysis stages vii and viii. The improvement achieved is modest but noteworthy, and is justified by the importance of accurate capacity evaluation in the engine design and optimisation process.
- A proposed upgraded facility has been analysed which differs from the current facility only in the implementation of an improved calibration for the primary nozzle. This will reduce the *inherited* bias uncertainty from ±0.500% to ±0.250%. The *overall* uncertainty in capacity for this proposed upgraded facility will be ±0.302%, or ±0.052% greater than the bias uncertainty inherited from the primary nozzle. With a reduction in baseline uncertainty, the relative impact of the measurement and analysis chain (as described in stages ii–ix) will naturally be more significant. In particular, the measurement of flow conditions upstream of the primary nozzle (stage ii) and the application of the unsteady mass flow correction (stage iii) become significant contributors to overall uncertainty. It is felt that this facility would represent as optimal a system as practicable within realistic constraints.

Conclusions

In this paper, the current state-of-the-art in ultra-low uncertainty semi-transient techniques for experimental capacity measurement in gas turbines has been reviewed. A number of improvements to the technique, relative to previously published work, have been discussed. These improvements include: modularisation of the working section of such facilities to allow for rapid interchange of test vane modules; a move to independent metering of mainstream and coolant mass flow rates; and optimisation of instrumentation to minimise the measurement error in vane inlet and exit flow conditions.

A detailed uncertainty analysis has been presented which references the facility in which the technique was originally developed, the current facility, and a proposed future facility in which the uncertainty in capacity has been driven down to a practical limit using state-of-the-art nozzle calibration technology. The bias errors in vane capacity achieved by each of these three facilities are determined to be ±0.535%, ±0.495% and ±0.301%, respectively (to 95% confidence). The corresponding precision uncertainties are ±0.028%, ±0.025% and ±0.025%, respectively. The reduction in bias uncertainty between the original and current facilities was therefore ±0.040%. This is a small improvement but important in the context of the engine design and optimisation process. The combination of the extremely low precision uncertainty offered by the technique and the capability for rapid interchanging of test modules allows very small changes in capacity to be resolved. This facilitates studies of capacity sensitivity to secondary influences with much greater flexibility than was previously possible. In particular, studies of the effect of trailing edge coolant ejection, platform leakage flows, vane surface deterioration, and inlet flow disturbances (lean-burn combustor profiles) are topics of current interest.

The definition of vane capacity in systems with several streams at different inlet conditions of total pressure and temperature has been discussed. It is shown that whilst it is helpful for coolant stream mass flow rates and temperatures to be included in the capacity definition, the difference arising from the exact way in which this is achieved is minor. Whilst several definitions are similarly useful in terms of their robustness

to changes in the inlet conditions of individual streams, it is felt that the favoured definition offers the possibility—in the correct experiment—to isolate sensitivities to key effects such as trailing edge coolant ejection. This is achieved by explicitly expressing vane capacity as a function of the two key controlling pressure ratios. It is argued that this definition may be of more practical use when comparing results from different sources.

It is hoped that this paper will serve as a reference point for the current state-of-the-art in experimental gas turbine flow capacity measurement, and also as a manual for best practice in the development and analysis of experiments in this area.

Acknowledgment

The support of Rolls-Royce plc is gratefully acknowledged.

Declaration of Conflicting Interests

The author(s) declared no potential conflicts of interest with respect to the research, authorship, and/or publication of this article.

Funding

The author(s) received no financial support for the research, authorship, and/or publication of this article.

ORCID iD

Thomas Povey http://orcid.org/0000-0001-8977-9644

References

1. Raffel M and Kost F. Investigation of aerodynamic effects of coolant ejection at the trailing edge of a turbine blade model by PIV and pressure measurements. *Experiments Fluid* 1998; 24: 447–461.
2. Fielding L. The effect of irreversibility on the capacity of a turbine blade row. *Proc Inst Mech Eng* 1981; 195: 127–137.
3. Afanasiev IV, Granovskiy AV, Karelin AM, et al. Effect of 3D vane shape on the vane capacity. In: *Proceedings of ASME turbo expo 2004*, Vienna, Austria, 14–17 June 2004, Paper No. GT2004-53095.
4. Povey T. Effect of film cooling on turbine capacity. *ASME J Eng Gas Turbines Power* 2010; 132: 011901.
5. Kollen O and Koschel W. Effect of film cooling on the aerodynamic performance of a turbine cascade. Paper No. AGARD CP-390, 1985.
6. Povey T, Sharpe M and Rawlinson A. Experimental measurements of gas turbine flow capacity using a novel transient technique. *ASME J Turbomach* 2011; 133: 011005.
7. Hambidge C and Povey T. Numerical and analytical study of the effect of film cooling on HP NGV capacity. In: *Proceedings of ASME turbo expo 2012*, Copenhagen, Denmark, 11–15 June 2012, Paper No. GT2012-69066.
8. Kirollos B, Lubbock R, Beard P, et al. ECAT: an engine component aerothermal facility at the University of Oxford. In: *Proceedings of ASME Turbo Expo 2017*, Charlotte, NC, USA, 26–30 June 2017, Paper No. GT2017-64736.
9. British Standards Institution. *BS EN ISO 9300:2005 Measurement of gas flow by means of critical flow venturi nozzles*. London, UK: British Standards Institution, 2005.
10. Moffat RJ. Contributions to the theory of single-sample uncertainty analysis. *J Fluids Eng* 1982; 104: 250–258.

Appendix

Notation

A	area
A_{m}	effective area of mainstream Venturi nozzle
A_{h}	effective area of hub Venturi nozzle
A_{c}	effective area of case Venturi nozzle
C_d	discharge coefficient
C_x	axial chord length
c_p	specific heat capacity at constant pressure
D	diameter
F	arbitrary function used in Appendix
i	summation variable
K	arbitrary ratio used in Appendix
M	Mach number
$\dot{m}$	mass flow rate
$\dot{m}'$	mass flow rate delivered to NGV (corrected)
$\dot{m}''$	correction mass flow rate
$\dot{m}_{\mathrm{m}}$	mass flow rate measured at mainstream nozzle
$\dot{m}_{\mathrm{c}}$	mass flow rate measured at case coolant nozzle
$\dot{m}_{\mathrm{h}}$	mass flow rate measured at hub coolant nozzle
$\dot{m}_{\mathrm{total}}$	total mass flow rate (sum of $\dot{m}_m$, $\dot{m}_c$ and $\dot{m}_h$)
n	number of sample points per vane passage
p	pressure
$\overline{p_0}$	mass-flow averaged total pressure
p_{atm}	atmospheric pressure
p_{exit}	mean static pressure at vane exit
R	gas constant
S_1	sensitivity coefficient between capacity and vane pressure ratio
S_2	sensitivity coefficient between capacity and coolant-to-mainstream pressure ratio
T	temperature
$\overline{T_0}$	mass-flow averaged total temperature
t	time
V	plenum volume
x	arbitrary variable used in Appendix
y	arbitrary variable used in Appendix

Greeks

α	arbitrary uncertainty
Γ	capacity
Γ_{m}	mainstream capacity (component of Γ_{vane})
Γ_{h}	hub coolant stream capacity (component of Γ_{vane})
Γ_{c}	case coolant stream capacity (component of Γ_{vane})
Γ_{vane}	vane (or overall) capacity
γ	ratio of specific heat capacities
σ	uncertainty
$\sigma^{\%}$	percentage uncertainty
$\sigma^{\%}_{\Gamma_{\mathrm{vane}}}$	percentage uncertainty in vane capacity
$\sigma^{\%}_{\Gamma'_{\mathrm{vane}}}$	percentage uncertainty in vane capacity, including due to measurement of p_{exit}/p_{01} and p_{02}/p_{01}

Subscripts

0	stagnation condition
1	mainstream flow at cascade inlet
2	Film cooling flow at cascade inlet
3	trailing edge cooling flow at cascade inlet
c	case coolant stream
h	hub coolant stream
m	mainstream

Superscript

*	choked condition

Appendix 1. Propagation of uncertainty in a simple summation

For an arbitrary function of a set of entirely independent variables, for example $F=f(x, y,\ldots)$, the percentage bias uncertainty in the value of the function can be estimated from

$$\sigma_F^{\%} = \left[\left(\frac{\partial F}{\partial x}\right)^2 \frac{x^2}{F^2}\sigma_x^{\%2} + \left(\frac{\partial F}{\partial y}\right)^2 \frac{y^2}{F^2}\sigma_y^{\%2} + \ldots\right]^{1/2} \quad (21)$$

Let F be a simple summation of independent variables

$$F(x, y, \ldots) = x + y + \ldots \quad (22)$$

The partial derivative of F with respect to each of the variables x, y etc. is equal to unity, and the propagation equation for percentage uncertainty in F (equation (21)) simplifies to

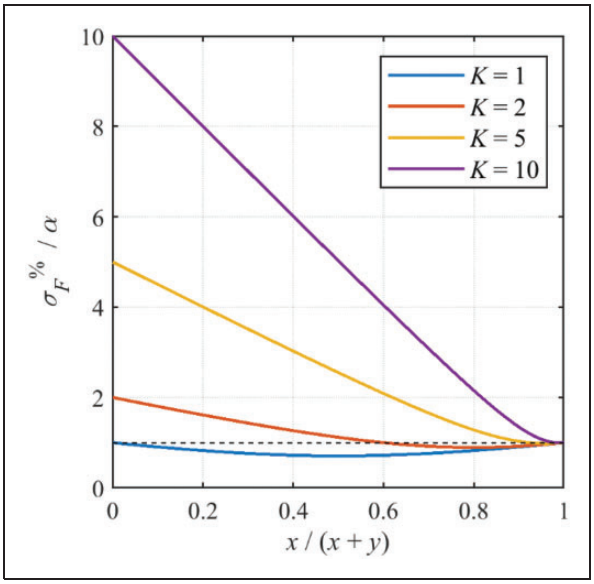


Figure 24. Percentage uncertainty in the sum of two variables, *x* and *y*, as a function of the relative sizes and relative percentage uncertainties of *x* and *y*.

$$\sigma_F^{\%} = \left[\frac{x^2}{F^2}\sigma_x^{\%2} + \frac{y^2}{F^2}\sigma_y^{\%2} + \ldots\right]^{1/2} \quad (23)$$

This has some surprising results. To illustrate this, consider a simple example where F is a sum of just two variables, x and y. The percentage uncertainty in x is defined to be $\sigma_x^{\%} = \alpha$, and the percentage uncertainty in y, $\sigma_y^{\%} = K\alpha$, where K is the uncertainty ratio between the two variables. Equation (23) then becomes

$$\sigma_F^{\%} = \frac{\alpha}{F}\left(x^2 + K^2y^2\right)^{1/2} \quad (24)$$

Figure 24 shows $\sigma_F^{\%}$ (y-axis), normalised by α, as a function of the relative size of the two variables (x-axis), for a range of values of K (individual lines). The limits of the x-axis at 0 and 1 correspond to $x=0$ and $y=0$. At these limits the uncertainty $\sigma_F^{\%}$ tends towards the uncertainty in the dominant variable—$\sigma_y^{\%}$ and $\sigma_x^{\%}$ respectively. This is a logical result.

In the case where $K=1$ ($\sigma_x^{\%} = \sigma_y^{\%} = \alpha$), the uncertainty in F is lower than that in the input variables, for any relative size $x/(x+y)$. That is, $\sigma_F^{\%} < \alpha$. For $x/(x+y)=0.5$, $\sigma_F^{\%} = 0.7\alpha$, a 30% reduction compared to the underlying uncertainties. This effect is explained by the fact that the measurement errors in the two variables are assumed uncorrelated. As K is increased, the range of $x/(x+y)$ over which the uncertainty in the summation is less than α is reduced but does not entirely disappear. This leads to the counter-intuitive result that adding a very small proportion of

a comparatively high uncertainty component, y, to a dominant and lower uncertainty component, x, has the effect of *reducing* the uncertainty in the summed quantity.

In this paper, the application of the unsteady mass flow rate correction and the combination of the individual stream capacity terms to determine the overall vane capacity are practical examples of this effect. Consider the unsteady correction for the hub coolant stream. Here, x is the uncorrected mass flow, $x = \dot{m}_{\mathrm{h}} = 0.561\,\mathrm{kg\ s^{-1}}$, and y is the correction term, $y = \dot{m}''_{\mathrm{h}} = 0.002\,\mathrm{kg\ s^{-1}}$. Therefore, $x/(x+y) = 0.996$. The uncertainties in x and y are $\pm 0.703\%$ and $\pm 16.03\%$, respectively, giving $K \approx 22$. Applying equation (24), the resulting uncertainty in the summation value (corrected mass flow) is 0.9997α—that is, a reduction of 0.027%. This drop is very marginal, but illustrates how a counter-intuitive result can arise.

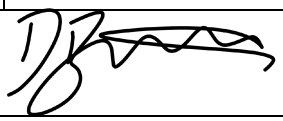
Statement of Authorship for joint/multi-authored papers for PGR thesis

To appear at the end of each thesis chapter submitted as an article/paper

The statement shall describe the candidate's and co-authors' independent research contributions in the thesis publications. For each publication there should exist a complete statement that is to be filled out and signed by the candidate and supervisor **(only required where there isn't already a statement of contribution within the paper itself).**

Title of Paper	Analysis of ultra-low uncertainty gas turbine flow capacity measurement techniques
Publication Status	□Published
Publication Details	Burdett, D., Hambidge, C., Povey, T.; 2020; Analysis of Ultra-low Uncertainty Gas Turbine Flow Capacity Measurement Techniques; Proc. Inst. Mech. Eng., Part A: J. Power and Energy, DOI: 10.1177/0957650920909718

Student Confirmation

Student Name:	D Burdett		
Contribution to the Paper	Performed experimental testing to collect data, analysed and interpreted experimental data, performed uncertainty analysis, and wrote manuscript.		
Signature		Date	13/02/2021

Supervisor Confirmation

By signing the Statement of Authorship, you are certifying that the candidate made a substantial contribution to the publication, and that the description described above is accurate.

Supervisor name and title: Professor Thomas Povey		
Supervisor comments: Dan substantially conducted the research himself (some plots were contributed by another PhD student who is second author on this paper) and entirely wrote the paper himself, with technical contributions from the co-authors. It is substantially his own work.		
Signature: Thomas Povey	Date	19/02/2021

This completed form should be included in the thesis, at the end of the relevant chapter.

Check for updates

Understanding Capacity Sensitivity of Cooled Transonic Nozzle Guide Vanes: A Parametric Experimental and Computational Study of the Impact of Trailing Edge Geometry

Daniel Burdett
Department of Engineer Science,
University of Oxford,
Oxford OX2 0ES, UK
e-mail: daniel.burdett@univ.ox.ac.uk

Frédéric Goenaga
Rolls-Royce plc,
WH88, P.O. Box 3,
Filton BS34 7QE, UK
e-mail: Frederic.Goenaga@rolls-royce.com

Thomas Povey[1]
Department of Engineering Science,
University of Oxford,
Oxford OX2 0ES, UK
e-mail: thomas.povey@eng.ox.ac.uk

High-pressure (HP) nozzle guide vane (NGV) capacity is one of the most important parameters for setting overall turbine power output, for stage matching, and for understanding turbine performance. Accurate capacity prediction early in the engine design process reduces the cost and risk of late-stage changes in the overall turbine design. High accuracy predictions rely on calibrated computational fluid dynamics (CFD) methods. Because of the numerous sensitivities in the methods, they are generally restricted to certain classes of design for which there is experimental validation. This paper considers the effect of changes in trailing edge (TE) geometry—particularly suction side (SS) TE overhang length—on the flow capacity of a modern HP NGV. Ultra-low uncertainty experimental measurements and complementary numerical predictions of capacity are presented for four TE geometries, in a parametric study bridging the gap between a classical centered-ejection design and a SS overhang TE design. This study discusses the absolute and relative (differences between designs) accuracies of the numerical method and develops understanding of the sensitivity of capacity to TE geometry. Fundamental mechanisms responsible for the observed capacity changes are elaborated. The impacts on capacity of both changes in the coolant flows and the boundary layers in the controlling region of the vane passage are considered. These effects are found to be very small. A simple total pressure loss model was also developed but was found to be a poor predictor of the observed capacity changes across the entire range of overhang lengths. To understand the observed changes, two more sophisticated models of the vane passage are proposed. In the first model—for relatively long TE overhangs—the mainstream and TE flows (and a wake) pass through a common minimum area. In the second model—for relatively short TE overhangs—the two flows are considered to pass through independent, non-interacting minimum areas. This framework reconciles the experimental and numerical data with the models but illustrates the complexity of the problem. In particular, it demonstrates the arbitrariness of considering a single minimum area. Contrary to some received industrial wisdom, it is argued that deemphasising this construct, and explaining capacity changes by examining aerodynamic changes in the entire controlling region of the passage, is more helpful in attempting to understand design sensitivities. [DOI: 10.1115/1.4050068]

Keywords: computational fluid dynamics (CFD), fan, compressor, and turbine aerodynamic design, fluid dynamics and heat transfer phenomena in compressor and turbine components of gas turbine engines, measurement techniques, turbomachinery blading design

Downloaded from http://asmedigitalcollection.asme.org/turbomachinery/article-pdf/143/5/051001/6672930/turbo_143_5_051001.pdf by guest on 05 July 2021

Introduction

Capacity provides a quasi-non-dimensional measure of the mass flowrate passing through a turbomachine row or stage. Accurate evaluation of high-pressure (HP) nozzle guide vane (NGV) capacity, in particular, is important to ensure well-matched turbine stages, correct compressor operating point, and accurate understanding of turbine performance parameters (efficiency, specific work, etc.). Capacity can be defined by

$$\Gamma = \frac{\dot{m}\sqrt{T_0}}{p_0} \tag{1}$$

While Eq. (1) is *not* strictly non-dimensional, it does remove the dependence of mass flowrate on the total pressure and temperature conditions at inlet to the nozzle. Designers typically require estimations of NGV capacity accurate to within 1% even at an early design stage. Evaluation at this accuracy level necessitates consideration of not just primary influencing factors such as vane loading

[1]Corresponding author.

Contributed by the Heat Transfer Division of ASME for publication in the Journal of Turbomachinery. Manuscript received July 21, 2020; final manuscript received January 4, 2021; published online March 30, 2021. Assoc. Editor: James L. Rutledge.

 Copyright © 2021 by Rolls-Royce plc

distribution [1] and the development of energy loss in the vane surface boundary layers [2] but also secondary design features including 3D vane geometry (sweep, lean, endwall contouring, etc.), surface film cooling, trailing edge (TE) shape, TE coolant ejection, inlet conditions of swirl and turbulence intensity, platform steps, platform leakage, and so forth. Significant advances made in both experimental and numerical methods for low uncertainty capacity evaluation in recent years have made it possible to understand the impact of these secondary factors on NGV capacity.

High accuracy evaluation of NGV capacity requires a high technology readiness level (TRL) experimental setup. The use of a fully annular cascade of engine component NGV parts is necessary to ensure correct boundary conditions are supplied to the vane. The cascade must further be operated at appropriate non-dimensional conditions of Mach and Reynolds numbers. Traditionally, the operation of such high-TRL facilities has been limited to original equipment manufacturers due to the great expense which they entail. For this reason, there are very few studies of NGV capacity in the open literature—in contrast to its importance in the engine design process. To date, the work of the group involved in this paper is the only major program targeting low uncertainty experimental capacity measurement in an academic environment.

In 2011, Povey et al. [3] presented a novel experimental technique for capacity measurement in a semi-transient blowdown facility. This technique offered significant improvement in accuracy over conventional continuous-running techniques, with significant reductions in operating cost and test runtime. In 2017, the installation of a second-generation facility [4] extended the capability to include high-fidelity aerodynamic traverse measurements of the downstream flow field and overall cooling effectiveness measurements using infrared thermography, as well as a modular working section uniquely suited to measuring very small capacity changes arising from small vane geometry changes. Around the same time, Burdett et al. [5] implemented a number of small improvements to the hardware and experimental technique to allow ultra-low uncertainty capacity evaluation. This facility was used for the experimental work in this paper. Burdett et al. [5] provide a comprehensive uncertainty analysis. The development of these techniques and facilities has paved the way for sensitivity studies in which very small changes in flow capacity (of order 0.1% or lower) are to be studied.

In this paper, we consider the impact of suction side (SS) TE overhang on capacity. This type of design has evolved to afford a thinner TE (improved aerodynamic performance) with acceptable thermal life (controlled coolant ejection over the thin SS overhang). Because the overhang feature occurs in the *controlling region* (defined more fully later) of the vane passage, the vane capacity and loss are expected to be highly sensitive to the overhang design. Centered-ejection-type TE designs were common in earlier-generation engines because of the ease of cooling. More modern engine designs have favored TE designs with a SS overhang, as they are generally found to yield lower loss than equivalently optimized centered-ejection designs on account of their thinner *base region* [6,7]. However, recent evidence suggests that at lower exit Mach number conditions, the centered-ejection design may offer benefits from both aerodynamic and thermal perspectives. This is of particular interest to the development of current twin-HP engine designs and was the primary motivation for the present study.

In addition, deterioration of the TE overhang geometry can occur during the service lifetime of the NGV component. Impacts from foreign body particles passing through the engine core can result in significant removal of material from the TE tip. Attempts are commonly made to mitigate the effects of such deterioration by periodically removing damaged sections of the TE material across the whole vane span.

Accurate evaluation of capacity (to within approximately 1%) by numerical means is also challenging. It is first required to replicate faithfully the 3D geometry of the physical part. The geometry is commonly obtained either from a computer aided design (CAD) casting drawing of the nominal part (and therefore subject to deviation from a specific manufactured component due to tolerances in the casting process) or by employing optical scanning techniques (which encounter errors relating to the process of converting from a set of scanned points to a clean geometry which will then be meshed) to measure a physical part directly. The width of the passage in a typical HP NGV close to the region of minimum physical area is of order 10 mm. Therefore, a discrepancy in passage width in this area between the physical part geometry and the numerical mesh of just 0.1 mm would result in a capacity shift of order 1%. This demonstrates the small margin for error in the process of geometry and mesh generation.

Attempts to investigate and understand the effects of secondary geometry features only add to the difficulty. A fine mesh is required to resolve small-scale geometric features which can disproportionately impact the aerodynamic flow field. This naturally brings increased computational cost. At typical operating conditions, the flow field in the immediate vicinity of the controlling region is transonic (flow Mach number largely in the range $0.8 \leq M \leq 1.1$) and highly unsteady, generally featuring vortex shedding from the TE. Running unsteady simulations is therefore greatly advantageous and is usually considered a requirement for correctly determining the vane TE loss.

At the TE, there is a strong interaction between coolant flow ejecting from the TE slot and the external flow field around the TE. A mass flowrate boundary condition is typically imposed at inlet to the TE slot, varied between operating conditions (e.g., pressure ratio) and geometry to take account of the time mean pressure field in the so-called *base region*. The mass flow might be predicted using a low-order model of the system. In addition to boundary conditions, coolant ejection will also be influenced by internal cooling geometry features within the TE slot. Typically, these include ribs, pin-fins, and impingement plates which cause the TE ejection profile to be non-uniform over the vane span. It is therefore important that these features should be included in the numerical geometry, adding further complexity.

A small number of studies have employed numerical or theoretical methods to consider the influence of secondary factors on NGV capacity. These will now be summarized.

Afanasiev et al. [1] compared vanes with common minimum area but different loading distributions. A typical change in loading was found to alter capacity by up to 10%. Aft-loading can move the *controlling* minimum area well downstream of the *geometric* minimum area, where a simplistic 1D analysis would expect the flow to choke. This demonstrates the folly of attempting to understand small capacity discrepancies between vanes by considering their geometric throat areas alone—however accurately they are measured.

Povey [8] introduced a novel analytical model designed to predict the impact of film cooling on NGV capacity, using a control volume mixing model. The model was used to estimate a correction parameter between capacity at typical experimental test conditions and at engine conditions. Capacity differences between the conditions of order 1.88% are suffered when the mainstream properties are assumed for the whole flow. Alternatively, defining capacity using fully mixed out properties, the capacity difference could be reduced by an order of magnitude to approximately 0.20%.

Hambidge and Povey [9] developed this further by comparing theoretical and numerical predictions of the impact of film cooling on NGV capacity. The introduction of a typical film cooling system was estimated to reduce capacity by 0.125% or 0.144% using numerical and theoretical methods, respectively. They also showed that the impact on capacity is only weakly sensitive to the actual distribution of film cooling holes and is primarily determined by the overall coolant mass flowrate.

Högner et al. [10] numerically quantified the impacts on NGV capacity of a range of typical geometric variations which may arise due to manufacturing scatter. These included thickness and position of the TE slot, SS and pressure side (PS) TE overhang lengths, and pressure and suction surface offsets. The effects of typical variation in each aspect of geometry were estimated both

Downloaded from http://asmedigitalcollection.asme.org/turbomachinery/article-pdf/143/5/051001/6672930/turbo_143_5_051001.pdf by guest on 05 July 2021

in isolation and in parallel (via a Monte Carlo simulation). The pressure surface offset and the position of the TE slot were identified as the primary influences on capacity. Simple linear superposition of these two parameters acting in isolation gave a comparable result to the parallel study, demonstrating a high degree of linearity and relative lack of cross-dependence.

In this paper, the impact of TE slot geometry on NGV capacity is examined using both experimental and numerical techniques. Specifically, we attempt to understand the effect of varying the overhang length of the SS TE tip (with respect to the PS TE tip). A series of four different TE geometries have been tested. These are presented along with the method by which they were manufactured in the experimental test cascade. The NGV capacity trend is quantitatively analyzed from the experimental and numerical results. Experimental measurements are used to validate the numerical method. Numerical results are then used to enhance understanding of the fundamental changes to the underlying flow field which give rise to the measured change in capacity.

Experimental Capacity Measurement

Experimental measurements were conducted in the Oxford Engine Component Aerothermal (ECAT) facility [4]. This facility utilizes the semi-transient method of experimental capacity measurement, first presented by Povey et al. in 2011 [3]. Burdett et al. [5] provide a comprehensive explanation of the application of the method in the ECAT facility and analyze the bias uncertainty in capacity measurements achieved. Bias uncertainty is evaluated as ±0.495% to 95% confidence.

Air, supplied from a HP reservoir, is discharged through a full-annular cascade of test vanes. The cascade was made up of 20 vane pairs (40 vanes in total) from a modern civil turbofan engine. Figure 1 shows a simplified cross section through the axisymmetric working section. Mainstream air flows from left to right in the figure. The test vanes feature distributed surface film cooling and coolant ejection from a TE slot. Coolant air is supplied from independent feeds at the hub and case.

The mainstream mass flowrate delivered to the cascade is accurately measured using a choked sonic Venturi nozzle calibrated to a National Institute of Standards and Technology (NIST) traceable standard at Colorado Engineering Experiment Station, Inc. (CEESI) and installed according to ISO 9300 [11]. Coolant mass flowrates are measured using independent sonic Venturi nozzles. The coolant metering nozzle area sets the coolant-to-mainstream inlet total pressure ratio. Figure 2(*a*) shows the mainstream, coolant, and overall (mainstream + coolant) mass flow trends from a typical test. The mainstream trend is truncated at the start and end of the test, where the pressure ratio across the metering nozzle is

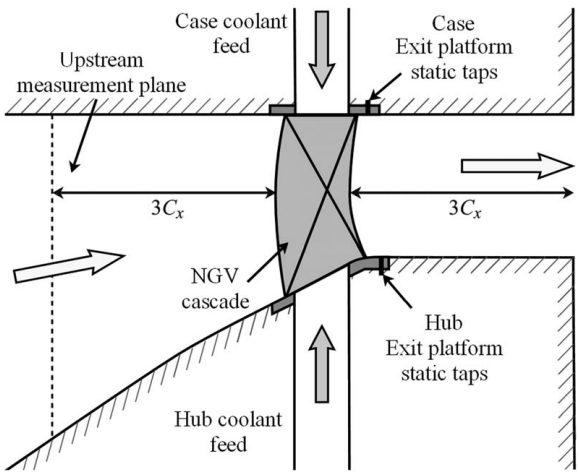


Fig. 1 Simplified diagram of a meridional cross section through the ECAT facility working section

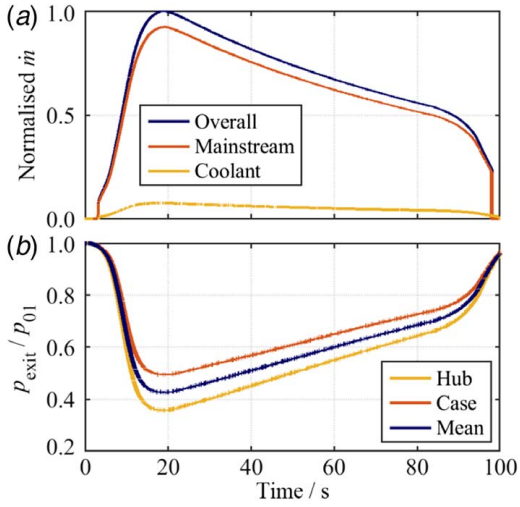


Fig. 2 Trends from a typical experiment of (*a*) mass flowrates and (*b*) vane exit-static to inlet-total pressure ratio

insufficient for the nozzle to choke. The nozzle is then outside of its calibrated range. The data are normalized with respect to the maximum overall mass flowrate. The mass flowrates gradually decay during the test. The coolant-to-mainstream mass flow ratio is held constant during the quasi-steady period ($t = 20$–85 s) at approximately 7.50%.

The facility matches the non-dimensional parameters Mach number, Reynolds number, and coolant-to-mainstream pressure ratio to typical values at engine operating conditions.

Vane inlet total pressure and temperature are each measured at 32 points, distributed circumferentially around the annulus and radially across the vane span, in rakes located three axial chord lengths upstream of the cascade leading edge (see Fig. 1). Vane exit static pressure is measured at 84 tappings located on the hub and case exit platforms of six instrumented vanes distributed around the annulus. The tappings are approximately 5 mm (17% of axial chord length) axially downstream of the midspan TE position. A detailed analysis of these measurements, and their impact on the bias uncertainty in the vane capacity measurement, can be found in Ref. [5]. Vane pressure ratio, p_{exit}/p_{01}, is defined as the ratio of the mean of the 84 exit static pressures to the mean of the 32 inlet total pressure measurements.

During a test, the total pressure and temperature supplied to the test cascade drop as the supply reservoir is depleted. Figure 2(*b*) shows the resulting operating pressure ratio trends across the cascade from a typical test. The mean pressure ratio traverses smoothly through a continuous range $0.42 < p_{exit}/p_{01} < 0.72$ during the quasi-steady period.

The capacity of the fully cooled vane cascade is defined as

$$\Gamma_{vane}\left(\frac{p_{exit}}{p_{01}}, \frac{p_{02}}{p_{01}}\right) = \frac{\dot{m}_1\sqrt{T_{01}}}{p_{01}}\left(\frac{p_{exit}}{p_{01}}, \frac{p_{02}}{p_{01}}\right) + \frac{\dot{m}_2\sqrt{T_{02}}}{p_{02}}\left(\frac{p_{exit}}{p_{01}}, \frac{p_{02}}{p_{01}}\right) + \frac{\dot{m}_3\sqrt{T_{03}}}{p_{03}}\left(\frac{p_{exit}}{p_{01}}, \frac{p_{02}}{p_{01}}\right) \quad (2)$$

where the subscripts 1, 2, and 3 represent mainstream, film cooling (total for all film cooling holes), and TE coolant flows, respectively. Each term is a *surface* of capacity—i.e., a 2D function of the two controlling pressure ratios given in parentheses. This definition allows—in an appropriate experiment—the sensitivity of capacity to changes in individual constituent cooling flows (e.g., TE coolant ejection) to be isolated and examined. It also achieves a level of robustness to changing inlet stream conditions (e.g., T_0) comparable to alternative definitions. The choice of capacity definition is discussed in more detail in Ref. [5]. The three right-hand side terms can be considered as contributions to the overall (or vane)

Downloaded from http://asmedigitalcollection.asme.org/turbomachinery/article-pdf/143/5/051001/6672930/turbo_143_5_051001.pdf by guest on 05 July 2021

capacity from each flow. In this case, we take $p_{02} = p_{03}$, since both streams are fed from the same two (hub and case) plena, which are at a common pressure. The capacity definition was consistent between experiments and computational fluid dynamics (CFD).

A capacity *characteristic*—i.e., capacity expressed as a function of the vane pressure ratio, p_{exit}/p_{01}—is generated from a single test. Coolant-to-mainstream pressure ratio, p_{02}/p_{01}, is held at a fixed value. Typically, 20 repeat tests are conducted to reduce the precision uncertainty in the mean capacity measurement. A typical test campaign achieves a precision uncertainty of 0.025% to 95% confidence [5]. Low precision uncertainty is particularly important when considering small capacity changes induced by, for example, a change in TE geometry.

Variation of Trailing Edge Geometry

Four different TE geometries were tested experimentally, with four different SS TE overhang lengths. The four geometries are illustrated in Fig. 3 and are referred to as follows:

Geometry 1: Baseline SS overhang length (approximately 13.4% of the axial chord length)
Geometry 2: Two-thirds of the baseline SS overhang length (approximately 9.0% of the axial chord length)
Geometry 3: One-third of the baseline SS overhang length (approximately 4.5% of the axial chord length)
Geometry 4: No SS overhang (PS and SS TE tips flush in the plane normal to the cascade circumferential direction)—centered-ejection design

NGV capacity is highly sensitive to the precise geometry around the controlling region of the vane passage. As demonstrated previously, a deviation of just 0.1 mm in the passage width close to the plane of minimum physical area, for example, due to a slight shift in the seating of one vane in the cascade relative to its neighbor, would be expected to cause a capacity change of order 1%. Therefore, in order to confidently isolate and assess the impact of varying, for example, TE overhang length, it is critical to ensure geometry remains otherwise identical.

This objective was achieved by generating all four tested TE geometries on the *same set of vane parts*, without disassembling the cascade throughout the duration of testing. The cascade assembly (Fig. 4) was constructed prior to the first set of tests, with the vanes having TE Geometry 1. After the first set of tests, the cascade assembly was removed from the ECAT facility as a single component. At all times when not installed in the facility, a set of five ground steel fixtures each covering 72 deg of the annulus (labeled in Fig. 4) was bolted to the assembly. This ensured that the vanes remained fixed in position throughout the process and prevented stress being imparted to the wet seals. Only one of the five fixtures was removed at any one time to allow the vane TEs located beneath it to be addressed and operated

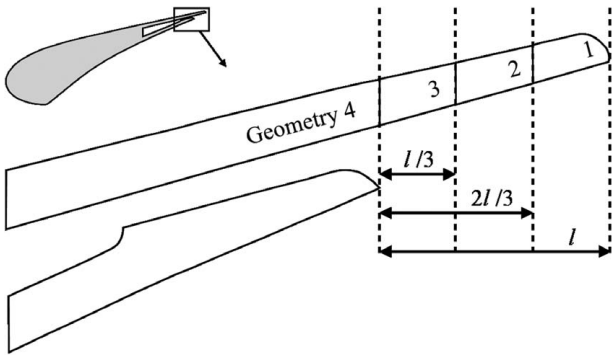


Fig. 3 Diagram showing the four tested TE geometries. The inset in the top-left shows the context of the full vane. *l* is the baseline SS overhang length.

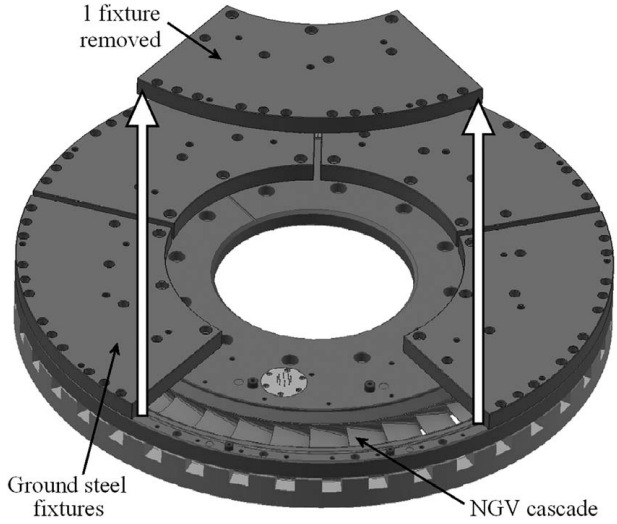


Fig. 4 Diagram of the NGV cascade assembly with ground steel fixtures

on. This is illustrated in Fig. 4. An operation was then performed to cut back the SS TE tip of every vane in the cascade from Geometries 1 to 2 *without* removing any vanes from the assembly. The cascade was then reinstalled in the ECAT facility and tests performed for Geometry 2. This process was repeated to test Geometries 3 and 4 in turn.

The operations performed on the vane TEs are now described. The assembly was placed on a rotating stage on a three-axis computer numerically controlled (CNC) milling machine. The entire assembly could then be finely rotated to accurately address the TE of each vane in turn. For each TE, three separate points along the span were located with an edge-finding tool and compared against a CAD drawing of the nominal part. The nominal TE profile was thus adjusted on a vane-by-vane basis to account for small manufacturing deviations from the nominal geometry. Thus, as far as practically possible, an identical operation was applied to every TE around the annulus. The profile was offset circumferentially by $l/3$ (the increment of material to be removed in each operation—see Fig. 3) to define the path of the cutting tool. The operation was performed using a carbide endmill tool. The NGVs were made of an Inconel alloy with a thermal barrier coating. Care was taken to ensure no debris entered film cooling holes.

The machining process left the SS TE tip in Geometries 2–4 with a squared-off face, as shown in Fig. 3, in contrast to the small radius on the same corner in Geometry 1. The effect of TE shape was examined in detail by Melzer and Pullan [12]. They concluded that the sharp corners of squared-off TEs fix the location of the TE flow separation points, and thus fix the strength of vortex shedding in the transonic regime. This effect can cause squared-off TEs, in some cases, to generate less loss than a rounded TE of equal thickness (when both exhibit transonic vortex shedding). Elliptical TEs were found to suppress transonic vortex shedding, yielding a significant reduction in loss in conditions where it occurs.

The SS TE tip thickness, t, for each geometry is reported in Table 1, normalized with respect to Geometry 1. The thickness of the tip, t, is measured normal to the SS exit metal angle as indicated

Table 1 Passage widths and TE thicknesses for each geometry

Geometry	$w_{PS}/w_{PS,1}$	$w_{SS}/w_{PS,1}$	$w_{SS}/w_{SS,1}$	t/t_1
1	1.000	1.015	1.000	1.000
2	1.000	1.030	1.015	1.085
3	1.000	1.051	1.035	1.204
4	1.000	1.069	1.053	1.310

Downloaded from http://asmedigitalcollection.asme.org/turbomachinery/article-pdf/143/5/051001/6672930/turbo_143_5_051001.pdf by guest on 05 July 2021

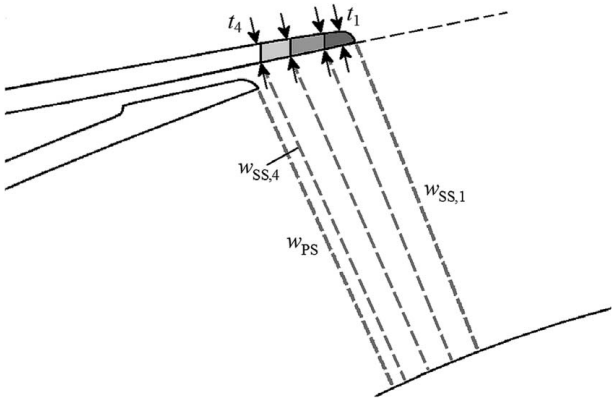


Fig. 5 TE thickness and passage width parameters

in Fig. 5. For Geometry 1, t_1 is measured just upstream of the SS corner radius. Between Geometries 1 and 4, t increases by 31.0%. The minimum physical passage area (marked w_{PS} in Fig. 5) occurs between the PS TE tip and the adjacent vane suction surface. This value is the same for all four geometries. Another measure of passage width is the minimum distance between the SS TE tip and the adjacent vane suction surface (marked w_{SS} in Fig. 5). The values for each geometry, normalized with respect to that for Geometry 1, are reported in Table 1. Between Geometries 1 and 4, w_{SS} increases by 5.3%.

All four TE geometries were tested at the same coolant-to-mainstream total pressure ratio, p_{02}/p_{01}.

Prior to each phase of testing, the coolant capacity characteristic (in the absence of mainstream flow) was measured to ensure that no damage had been sustained to the wet-applied seals. A leak would result in a change in coolant capacity, allowing an imperfect seal to be identified. This method is extremely precise, allowing very small leaks (of order 0.05% of overall capacity at the nominal choked condition) to be detected. The process for measuring the coolant capacity characteristic is described in detail in Ref. [3] (see also Ref. [5]).

Numerical Method

Numerical capacity predictions were made using 3D steady Reynolds-averaged Navier–Stokes (RANS) simulations. The geometry was the rotationally periodic annular sector of two complete NGV passages. This is shown in Fig. 6. The NGV geometry was based on the nominal casting intent (some even more advanced

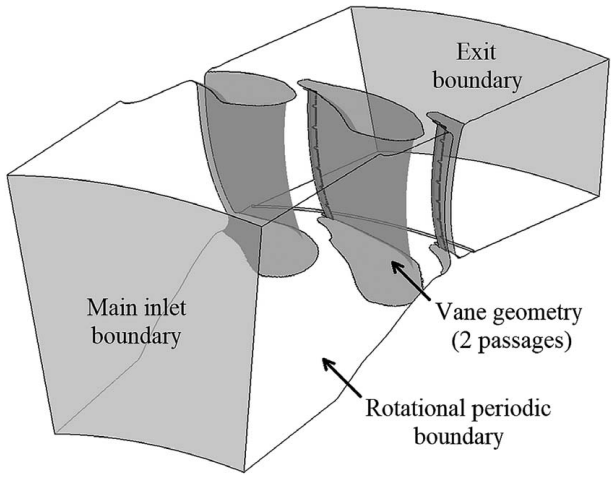


Fig. 6 Geometry for 3D numerical simulations

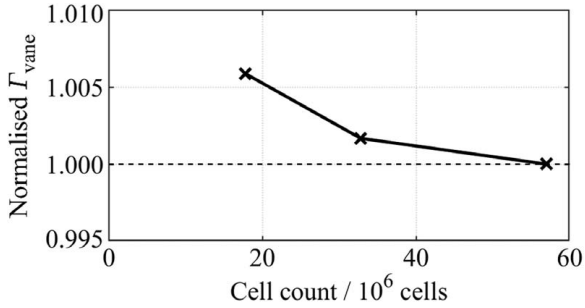


Fig. 7 Normalized vane capacities for CFD solutions with 18 M, 33 M, and 57 M cells

methods use individually scanned parts). The annulus line matches the ECAT facility (see Fig. 1). The TE geometry was modified to match the four tested geometries. *BOXERmesh* was used to generate an octree-based mesh.

A grid independence study was performed with cell counts 18 M, 33 M, and 57 M cells. The predicted capacity values for each grid are summarized in Fig. 7, normalized with respect to the 57 M cell mesh capacity. The change between the 33 M and 53 M cell solutions was 0.17%. The 57 M cell mesh was therefore taken to have sufficiently mesh-independent solutions for comparisons between geometries. Figure 8 shows a midspan section through the mesh for Geometry 1. The left and right edges of the figure are periodic boundaries. The grid was refined around the vane surfaces, in the wake region, and in a region close to the vane TEs. Significant grid refinement was applied across the entire passage width in the controlling region.

A detail of the TE region meshes for all geometries is shown in Fig. 9. Emphasis was placed on minimizing differences in the meshes away from immediate vicinity of the SS of the TE. The value of $y+$ over the PS was in the range 1–5, and over the SS in the range 3–6. Here, we are concerned with aerodynamics and not heat transfer, and these values were considered adequate for the purpose. Uniform inlet conditions of total pressure, total temperature, and turbulence intensity were set on the main inlet boundary plane, matched to the corresponding experimental values. These values are summarized in Table 2. An area-average static pressure condition was specified at the exit boundary, with radial profile arising from radial equilibrium (unconstrained). Extreme care was taken to ensure that the vane pressure ratio condition was defined in the same way in CFD as in the experiment. The CFD mean exit static pressure was taken as the mean of 84 locations matched to the experimental tapping locations, and the CFD inlet total pressure was uniform. A detailed uncertainty study is presented in Ref. [5].

Film cooling flows were modeled using source-terms: mass flowrates and direction vectors were specified on a per-hole basis.

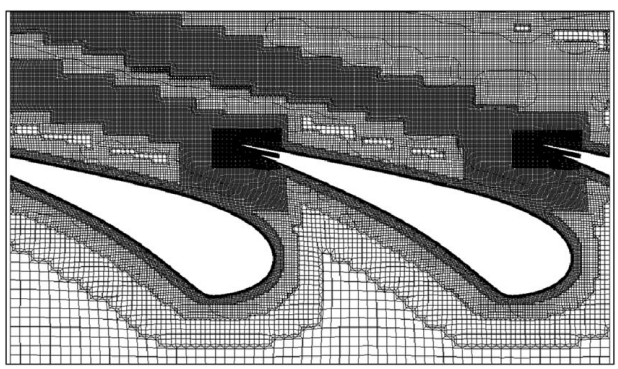


Fig. 8 Midspan section through the mesh for Geometry 1

Downloaded from http://asmedigitalcollection.asme.org/turbomachinery/article-pdf/143/5/051001/6672930/turbo_143_5_051001.pdf by guest on 05 July 2021

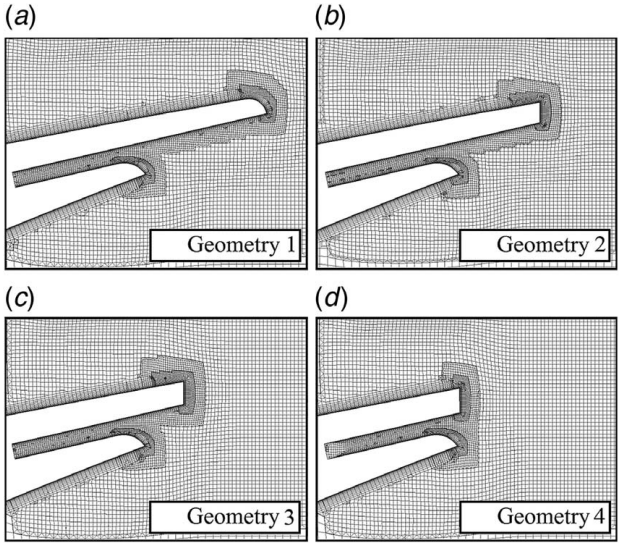


Fig. 9 Detail of midspan sections through TE region meshes

Table 2 Experimental and CFD boundary conditions

Variable	Experiment	CFD
p_{01} (bar)	2.00	2.00
T_{01} (K)	286	286
Tu	~10%	10%
p_{exit}/p_{01}	0.542	0.542
p_{02}/p_{01}	1.025	1.025

The capacity characteristics for individual cooling rows (including the TE slot) were taken from the nominal cooling design for the vane, allowing expected mass flows at experimental conditions (of total pressure and temperature, etc.) to be calculated. *Per-hole* mass flowrates were calculated based on the variation in hole-exit static pressure, evaluated from preliminary uncooled simulations. A common scaling factor (close to unity) was applied to all rows to match the overall coolant stream capacity measured experimentally at the same pressure ratio. Boundary conditions of inlet mass flowrate and total temperature are specified at the TE slot inlet boundaries (total pressure calculated by the solver).

Simulations were performed using a density-based RANS solver in ANSYS CFX with second order discretisation. The shear stress transport (SST) k–ω model was employed for turbulence closure. This is a common choice for studies of this type due to its hybrid nature combining the strengths of standard k–ε and k–ω models which perform well in the freestream and inner regions of the boundary layer, respectively.

A single experimental test produces a capacity characteristic covering a range of pressure ratio, which is compared to the CFD-predicted capacity value at a single vane pressure ratio. The nominal operating point of $p_{exit}/p_{01} = 0.54$ was used for the comparison.

Experimental and Numerical Capacity Characteristics

Experimental measurements and numerical predictions of vane capacity are now presented for TE Geometries 1–4.

Figure 10 compares the measured capacity characteristics (functions of p_{exit}/p_{01}) for all four TE geometries with CFD-predicted results at a single operating point. All data are normalized with respect to the experimental capacity for Geometry 1 at the design pressure ratio ($p_{exit}/p_{01} = 0.542$).

Consider first the experimental characteristic for Geometry 1. In the subsonic range ($p_{exit}/p_{01} > 0.5283$), the capacity characteristic is within $\pm 0.50\%$ of the isentropic trend. The isentropic curve (dashed line) is matched to the experimental measurement for Geometry 1 at the design pressure ratio. As p_{exit}/p_{01} falls below 0.5283, the characteristic increasingly diverges from the isentropic trend. That is, rather than plateauing at the nominal choked condition, the gradient of the curve increases with reducing pressure ratio. At $p_{exit}/p_{01} = 0.46$, the measured capacity is higher than the isentropic value by 1.1%. The flow in the controlling region is complex, featuring TE shocks, unsteady vortex shedding effects, and an interaction between the two wakes (SS and PS *lands* of the vane), the mainstream and the cooling flow. For this reason, there should be no expectation of 1D isentropic behavior.

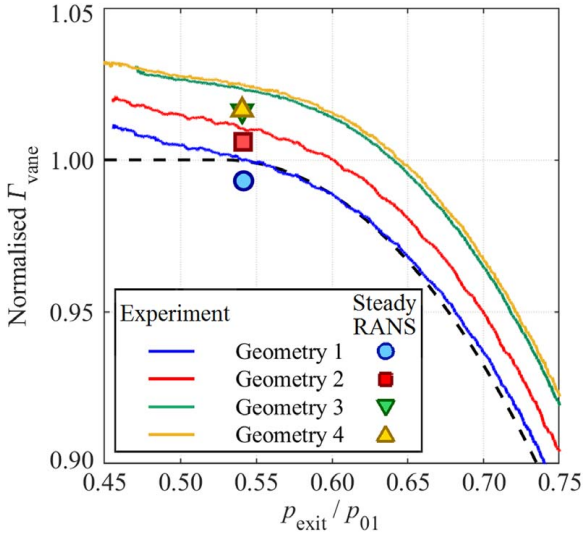


Fig. 10 Experimental capacity characteristics (solid lines) and CFD-predicted capacity (single points) for each TE geometry, normalized with respect to Geometry 1 at the design condition ($p_{exit}/p_{01} = 0.542$)

Comparing the experimental characteristics for Geometries 1–4 in Fig. 10, the trends with changing overhang length are extremely similar. Figure 11 shows the difference between the characteristics as a function of vane pressure ratio. At the design point ($p_{exit}/p_{01} = 0.54$), the differences 1–2, 1–3, and 1–4 are +0.968%, +2.306%, and +2.516%, respectively. As the TE is cut back (i.e., overhang gets shorter), capacity increases monotonically, but with little

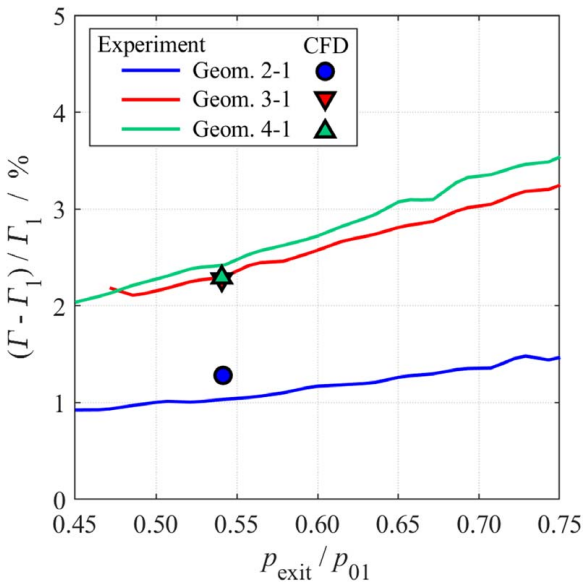


Fig. 11 Percentage capacity changes between Geometries 1–2, 1–3, and 1–4 as functions of vane pressure ratio

Downloaded from http://asmedigitalcollection.asme.org/turbomachinery/article-pdf/143/5/051001/6672930/turbo_143_5_051001.pdf by guest on 05 July 2021

Table 3 Summary of percentage capacity changes relative to Geometry 1 from experiment and CFD at $p_{exit}/p_{01} = 0.542$

Geometry	SS overhang length, l	$\Delta\Gamma$ from Geometry 1 (%)	
		Experiment	CFD
1	1.000	–	–
2	0.667	+0.968	+1.298
3	0.333	+2.306	+2.272
4	0.000	+2.516	+2.291

change for the final cutback (moving from Geometry 3 to 4). The mechanisms underlying this will be examined in greater detail later. Looking at the trends with pressure ratio in Fig. 11, the capacity increase (between geometries) with overhang length rises as pressure ratio is reduced. This is a consistent trend for all of the geometries tested.

We see from Fig. 10 that the absolute accuracy of the CFD predictions is extremely good. At the design point, CFD-predicted vane capacity deviated from the absolute experimental capacity measurements by −0.691%, −0.417%, −0.705%, and −0.812% for TE Geometries 1–4, respectively. The average under-prediction was therefore −0.656%. This is well within the typical range of accuracy for well-calibrated numerical methods (indeed ±2% might be considered more typical). Finally, looking at the predictions for the capacity change with overhang length, differences between CFD simulations 1–2, 1–3, and 1–4 are +1.298%, +2.272%, and +2.291%, respectively. These differ in absolute terms from the experimental differences between cases by +0.330%, −0.033%, and −0.225%. This is taken to be extremely good agreement in terms of absolute level of difference.

The experimental and computationally predicted capacity changes are tabulated in Table 3 (for a pressure ratio of $p_{exit}/p_{01} = 0.542$) and plotted in Fig. 12. Overall, the experimental trends seem well behaved, and there is a close match between CFD results and experiment, both in terms of absolute levels and trend with overhang.

Analysis

In this section, we attempt to understand the underlying mechanisms for the change in capacity with changing overhang length. The analysis is progressed under the following five headings:

(1) Analysis of coolant stream capacity changes
(2) Analysis of changes in surface boundary layer profiles due to aerodynamic changes
(3) Simplistic analysis of vane total pressure loss
(4) Incomplete model of the controlling region
(5) Analysis of the aerodynamic flow field in the controlling region

Analysis of Coolant Stream Capacity Changes. In this section, we consider the impact on overall capacity of changes (between geometries) in coolant capacity. This has the potential to affect the overall capacity through changes in the total pressure deficit (or surplus) in the mixing layer [6] on the vane surfaces (which passes through the controlling region of the vane) or through changes in the TE slot flow.

In the experiment, the coolant-to-mainstream total pressure ratio was set to a nominal value of 1.025 with high precision (root-mean-square (RMS) variation of within 0.5% of the coolant-to-mainstream total pressure differential), and the total coolant mass flowrate (sum of film and TE coolant) was measured to precision and bias uncertainties of ±0.08% and ±1.62%, respectively. Thus, the *in situ coolant capacity characteristic* can be accurately determined in each experiment [3,5]. The process for setting the row-by-row mass flowrates in the CFD model has been described,

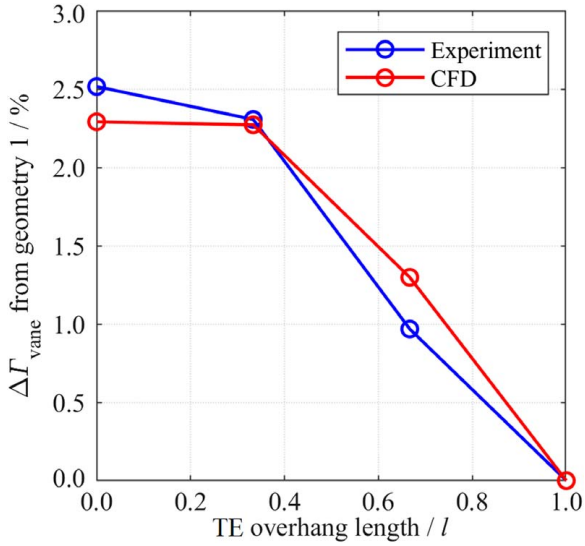


Fig. 12 Change in vane capacity relative to Geometry 1 as a function of TE overhang length for $p_{exit}/p_{01} = 0.542$

and these are accurately matched to the experimental condition at the relevant pressure ratio.

To understand the impact on overall capacity of changes in film cooling and TE slot flows, it is necessary first to deconstruct the in situ cooling capacity characteristic into film and TE slot flow characteristics. These two flows were not independently measured in the experiment, and the method of deconstruction, while accurate, is somewhat involved. The method is described in detail in Appendix A. We now consider the impact of changes in film and TE capacity in turn.

We find that the largest inferred (from measurement) change in *film* capacity between any two TE geometries (Geometries 1–4) was +0.18% of Γ_{vane}. Using a method developed by Povey [8], we estimate the resultant impact on overall capacity as a reduction of −0.005% of Γ_{vane} (i.e., the loss developed in the mixing layer outweighs the effect of enhanced total pressure at the ejection point). This is negligible in comparison to the observed changes in overall capacity, and we therefore conclude that the effects due to changes in film cooling flows alone are relatively insignificant.

The largest inferred (from measurement) change in TE coolant capacity between geometries (Geometries 1–4) was +0.037% of Γ_{vane}. Although we will later show that there is a moderate change in base pressure between geometries, the fact that the TE slot flow operates at large overall pressure ratio means that the impact of base pressure changes on the TE flow capacity is relatively small. In a later section, we present models of interaction between mainstream and TE slot flows with different TE overhang lengths. It is argued that there is some interaction between these flows that is model-dependent (and, therefore, geometry-dependent), but always with an *exchange rate* between TE slot flow and overall flow in the range 0–1 (see the models in Fig. 13 and the associated arguments). That is, the absolute maximum overall capacity change that might be expected from the model would be +0.037% of Γ_{vane}. This is more than an order of magnitude smaller than the measured overall vane capacity change. We conclude that the change in TE slot capacity is not, in isolation, responsible for the observed vane capacity change with changing overhang length.

In summary, we conclude that neither the changes in film cooling nor TE coolant flows are significant contributors to the observed changes in vane capacity between TE geometries.

Analysis of Changes in Surface Boundary Layer Profiles Due to Aerodynamic Changes. This section considers how aerodynamic changes arising from changes in TE geometry impact the boundary layer profiles in the controlling region of the passage,

Downloaded from http://asmedigitalcollection.asme.org/turbomachinery/article-pdf/143/5/051001/6672930/turbo_143_5_051001.pdf by guest on 05 July 2021

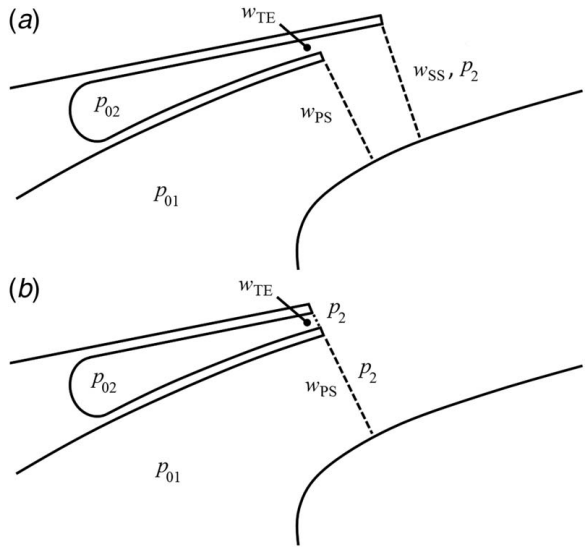


Fig. 13 Schematic diagrams representing model (*a*), a model with common controlling area, model (*b*), a model with independent controlling areas

and consequently the overall capacity. The fundamental mechanism is that mass flow *deficit* within the boundary layer—measured, e.g., with respect to the ideal, inviscid (non-zero slip at the wall) case—reduces the passage mass flowrate. This can be represented by the displacement thickness, δ^*. Changes in δ^* between geometries would affect the overall capacity. This analysis is related to that of Fielding [2,13], in that it considers the capacity change due to effective blockage caused by passage frictional losses.

Boundary layer velocity profiles predicted by CFD at both the SS and PS limits of the plane of minimum physical area (w_{PS}) at midspan are presented in Appendix B for all four TE geometries. Displacement thicknesses, δ^*, and corresponding passage mass flow deficits (estimated as $\dot{m} = \rho U \delta^* h$, where ρ and U are the flow density and velocity at the boundary layer edge and h is the vane span) were evaluated for each profile and summarized in Table 6 in Appendix B.

For each of Geometries 2–4, there was a small (of order −10%) reduction in boundary layer displacement thickness with respect to Geometry 1 and a corresponding negligible rise (of order +0.04%) in passage mass flowrate. These changes are an order of magnitude smaller than the observed capacity changes. We therefore conclude that the difference in passage mass flowrate between geometries arising due to changes in boundary layer velocity deficit cannot alone be a significant mechanism responsible for the observed changes in measured vane capacity.

Simplistic Analysis of Vane Total Pressure Loss. In this section, we consider the impact on overall capacity of changes (between geometries) in the row efficiency or total pressure loss, of the vane, due to aerodynamic changes caused by changes in TE geometry.

So far as capacity is concerned, a typical NGV is a fundamentally 2D (or higher, if radial pressure gradients are considered) system. The sonic line is often far from aligned with the plane of minimum area for example and instead crosses obliquely. One-dimensional analogies are therefore at best incomplete and at worst highly misleading. By this, we mean that the 1D model in which the vane is represented by a unique area (or *throat*), with associated upstream total pressure and temperature conditions, and a corresponding downstream static pressure, is not an adequate description of the system. The problem of reducing our particular system to a 1D system can be illustrated with reference to Fig. 5. Here, as we change from Geometry 1 to Geometry 4, the area w_{PS} is fixed while w_{SS} changes. The entire flow also passes through a common downstream area (e.g., a fixed area axial plane) but at an angle which has a complex dependence on the vane aerodynamics. This determines the *true area* in the streamwise direction. The distributions of total pressure, Mach number, and flow angle have complex relationships with each other and differ between the four geometries. The concept of a unique area for our 1D model is thus problematic.

Notwithstanding this rather fundamental problem, it is worth noting that there were some serious early attempts to develop models based on 1D analogies. To the extent that these partially capture the true overall system, they can be considered useful. One such model is that of Fielding [2,13] who, in what might be considered a quasi-2D framework, defined a *restriction factor*, which described the degree to which passage frictional losses reduced the nozzle effective flow area with respect to the ideal, frictionless case. This model accounted for the fact that the loss was concentrated within the boundary layers, not distributed uniformly across the passage.

In Appendix C, we explore the extent to which a relatively simple quasi-2D analysis of this type can provide any insight into our system. We adapt the Fielding [2] model (consideration of total pressure loss) to include information about passage area for our particular system, in an attempt to predict capacity changes with TE geometry changes. A somewhat arbitrary choice must be made about the definition of total pressure loss, and with this choice comes an associated definition of passage area. We argue the case for representing total pressure loss using downstream total pressure characteristics (experimental traverse measurements or CFD-predicted distributions) and passage area with a new concept that we refer to as a *repeating area unit*. The repeating area unit is a physical area in the guided part of the vane, aligned as normal as possible to the assumed flow direction. It is chosen to provide the most direct possible analogy to a 1D system, which is necessary for the quasi-2D approach that is developed. The arguments around these choices are elaborated in Appendix C. We use the adapted model to attempt to reproduce the experimentally measured and CFD-predicted changes in vane capacity.

We conclude (see Fig. 27 in Appendix C) that a simple area-loss model in the spirit of Fielding [2] does not meaningfully reproduce the observed capacity changes between all geometries. For small changes in overhang length, the model performance was reasonably good: the modeled capacity change for Geometry change 1–2 agreed to within 0.32% of Γ_{vane} for experiment and to within 0.20% of Γ_{vane} for CFD. Good agreement was expected because the primary changes in the flow field could be approximated by a 1D model. The model performance was poor for Geometry change 1–3 and very poor for Geometry change 1–4. In the latter case, the model over-predicted the changes in experimentally measured and CFD-predicted capacities by 2.71% and 3.79% of Γ_{vane}, respectively. The poor agreement was to some extent expected due to the more significant (2D) aerodynamic changes which cannot be represented within the framework of the quasi-2D model.

The conclusion is that simple area-loss models of this kind are inadequate for analyzing even relatively small capacity changes when there is any significant change in the 2D aerodynamics.

Incomplete Models of the Controlling Region. In this section, the flow field through the controlling region of the vane passage is examined more holistically in an attempt to explain the observed changes in vane capacity.

We first introduce two *incomplete* models of the vane passage. By incomplete we mean that while the models convey one important interactive effect in the flow (between the TE slot flow and the mainstream) they do not, in isolation, explain the capacity trends observed in experiments when TE overhang length is reduced. The two models (a) and (b) are represented in Fig. 13. In these models, the mainstream and TE flows have uniform total pressures p_{01} and p_{02}, respectively, and exhaust to a common static pressure p_2.

In model (a), the two *controlling areas* w_{PS} and w_{TE} (for the mainstream and TE flows, respectively) pass through a common third

Downloaded from http://asmedigitalcollection.asme.org/turbomachinery/article-pdf/143/5/051001/6672930/turbo_143_5_051001.pdf by guest on 05 July 2021

controlling area, w_{SS}, which marks the exit static pressure boundary for the system. In this model, the three controlling areas are highly interacting, as the TE slot mass flow (and associated total pressure profile, including loss from separation off the SS overhang) partially mixes with the mainstream flow before passing through the controlling area w_{SS}. The interaction is complex, but we highlight one important aspect of the dynamics. For fixed w_{PS} and w_{TE}, and fixed p_2 at the controlling area w_{SS}, the static pressure achieved at the exits w_{PS} and w_{TE} is affected by the area-ratios w_{PS}/w_{SS} and w_{TE}/w_{SS}. That is, if the TE overhang length is changed such that w_{SS} changes, the static pressures and mass flowrates at exits w_{PS} and w_{TE} would also be expected to change. Thus, we would expect small changes in overhang length (and w_{SS}) to affect the overall system mass flowrate and hence capacity.

With reference to Fig. 5, it is possible to argue that model (a) is relevant to the incremental changes between Geometries 1 and 2 and between Geometries 2 and 3, but less relevant to the change between Geometries 3 and 4. Examining the TE geometries, we find that $w_{SS} < (w_{PS} + w_{TE})$ for Geometries 1 and 2, but $w_{SS} > (w_{PS} + w_{TE})$ for Geometries 3 and 4. That is, the minimum area, in this simplified model, switches from the downstream area w_{SS} to the combination of the individual areas $w_{PS} + w_{TE}$ between Geometries 2 and 3. The model would seem to go some way to explaining the observed capacity changes between Geometries 1–2 and 2–3. The mechanism underlying this in the model is the reducing back-pressure at w_{PS} and w_{TE} as w_{SS} is increased, for the same pressure p_2 at w_{SS} (within the framework of the model).

In model (b), the TE overhang is entirely removed so that the PS and SS lands are flush. Here, there are effectively two *independent controlling areas*, w_{PS} and w_{TE}, for the mainstream and TE flows, which exhaust to a common exit static pressure. The absence of the third controlling area w_{SS} reduces the complexity of the interplay between the mass flowrates associated with w_{PS} and w_{TE}. In this model, small changes in overhang length are not expected to significantly affect the overall system capacity characteristic, in line with the very small capacity change between Geometries 3 and 4 (Fig. 10), in a region in which $w_{SS} > w_{PS} + w_{TE}$.

We have already noted that these models are incomplete, but they do provide some insight into one important mechanism. We have used the term *controlling area* to describe a *series* of interacting areas. Even in these simplistic and incomplete models (Fig. 13), the controlling areas are identified to be somewhat arbitrary (identified only as easily identifiable and measurable minima) planes within a looser *controlling region*. We explicitly distinguish these concepts from well-defined *throats* (with their associated and extremely unhelpful connotations of 1D flow) because of the fundamental 2D nature of the pressure field in typical vane passages.

While their simplicity makes 1D analogies attractive, in a typical vane passage, the pressure contours pass through the point of minimum area at a high angle (often up to 45 deg). This alone is sufficient to demonstrate the weakness of the 1D analogy. To conclude, none of the controlling areas *choke* in a conventional sense, and it would be hard to say that any one were more important than any other. It is the *general* pressure field developed in the controlling region (i.e., the loosely defined transonic region around the vane minimum area) that is responsible for setting vane capacity.

Analysis of the Aerodynamic Flow Field in the Controlling Region. In this section, changes in the aerodynamic flow field as the TE overhang length is reduced are analyzed.

Figures 14(*a*)–14(*d*) show CFD-predicted contours of midspan Mach number for Geometries 1–4, respectively, at a nominal pressure ratio $p_{exit}/p_{01} = 0.54$. The pressure ratio was defined as described in the earlier sections. The locations of planes w_{PS} and w_{SS} are marked.

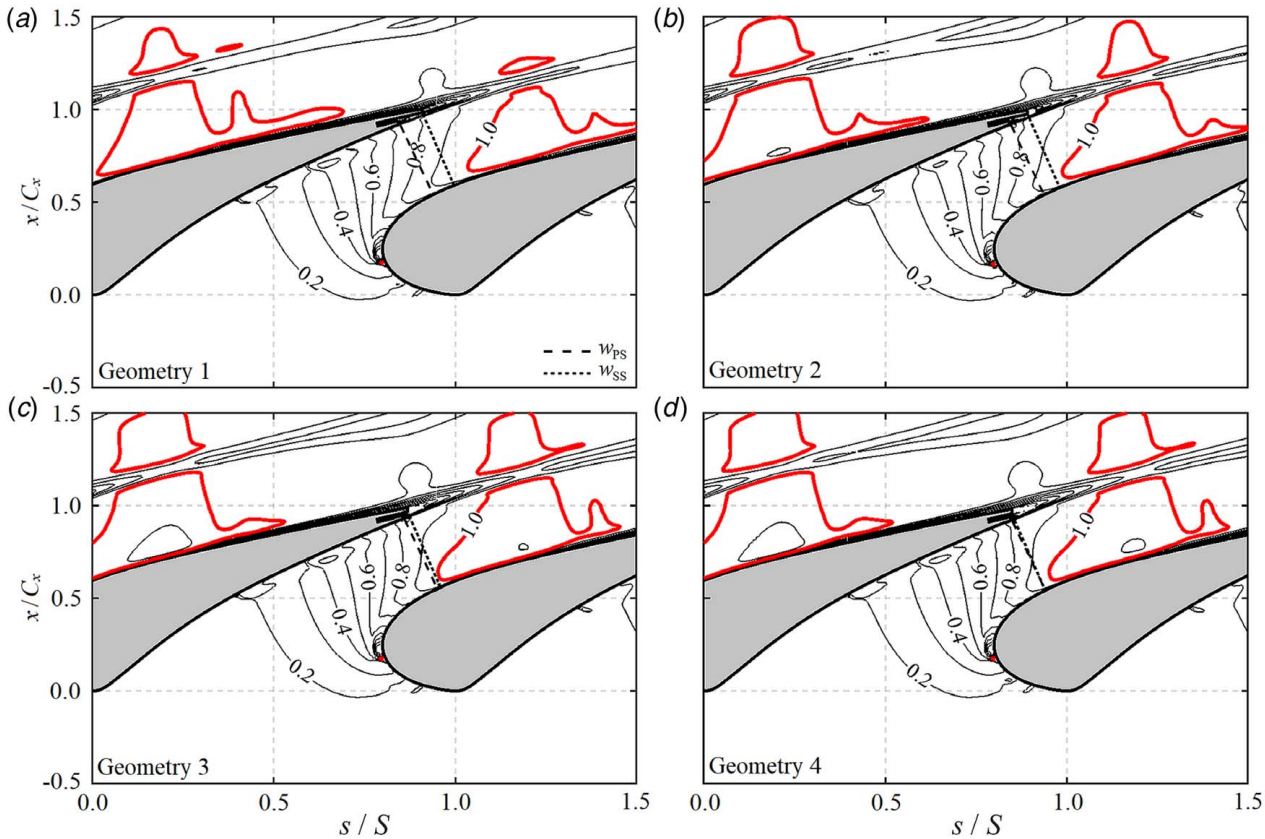


Fig. 14 Contours of Mach number in a section through the controlling region of the vane passage at the midspan radius for each TE geometry. $M = 1.0$ contour is marked in bold. The locations of the w_{PS} and w_{SS} areas are indicated by dashed lines.

Downloaded from http://asmedigitalcollection.asme.org/turbomachinery/article-pdf/143/5/051001/6672930/turbo_143_5_051001.pdf by guest on 05 July 2021

For all geometries, the contours of Mach number cross the midspan w_{PS} line at roughly 45 deg. This is due to the combined effect of streamwise acceleration and turning. The pressure field is strongly 2D, evidenced by the acute angle between Mach contours and the local flow direction, even for the moderately forward loaded vanes used in this study. For Geometry 1, the Mach number distribution along the line w_{PS} is from around 0.7 near the PS to 0.9 near the SS. The $M = 1.0$ contour (bold line in Fig. 14) lies wholly downstream of the plane w_{PS}.

As the TE overhang is reduced, moving from Geometries 1 to 3, three main effects occur: (i) the M contours gradually migrate upstream, leading to higher velocities at the plane w_{PS}; (ii) the mildly supersonic region on the late SS deepens, broadens, and penetrates through the wake region into the neighboring passage flow; and (iii) the wake region deepens and broadens, indicating increased total pressure loss. Between Geometries 3 and 4, changes in the flow field are almost negligible. These effects are in line with the observed changes in capacity with changing TE overhang length (Figs. 11 and 12) and—to the extent they are valid—with the models represented in Fig. 13.

The same trends can be observed by examining the isentropic Mach number distributions for each geometry, which are shown in Fig. 15. The abscissa for each curve is the axial distance normalized by the axial chord *for that specific geometry*. The location of the intersection on the vane SS of the plane w_{PS} is marked with a black circle for each geometry. This occurs at approximately 55% axial chord. Isentropic Mach number is normalized with respect to the mean exit Mach number for Geometry 1. The overall distributions are characteristic of a moderately forward loaded NGV. Apparent discontinuities in the profile are associated with local accelerations and diffusions around cooling holes. When presented in this way, the PS distributions for all geometries are extremely similar up to around 0.9 C_x. Acceleration continues up until the PS TE lip, which occurs at progressively later fractions of axial chord as the TE overhang is reduced (moving from Geometry 1 to Geometry 3). The peak Mach number at the TE lip increases incrementally between Geometries 1 and 3 as the M contours shift upstream (Fig. 14). Peak Mach numbers on the PS TE lip for Geometries 1–4 were 0.81, 0.92, 0.97, and 0.98, respectively.

Reducing TE overhang length leads to increased mid-to-late SS acceleration, with the most significant changes occurring around the *controlling region* of the passage, close to the intersection of w_{PS} with the vane SS. The peak Mach numbers achieved on the SS were 1.08, 1.10, 1.12, and 1.13 for Geometries 1 to 4, respectively, in agreement with the loading redistribution (Fig. 14).

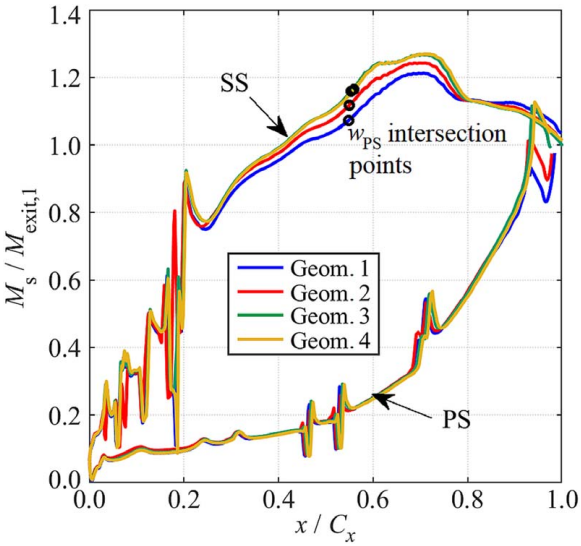


Fig. 15 Normalized vane surface isentropic Mach number distributions at midspan for each TE geometry

Mach number and total pressure distributions across the planes w_{PS} and w_{SS} are now examined. Figure 16 shows contours of Mach number on the planes w_{PS} and w_{SS} for each TE geometry. Axes correspond to normalized distance across the passage from PS to SS (x-axis) and normalized span (y-axis). Corresponding normalized total pressure distributions are presented in Fig. 17. Profiles along the midspan line (span fraction 0.5) are extracted and plotted in Fig. 18. Looking first at Mach number (Fig. 16), the following observations are made:

(i) The Mach distribution at plane w_{PS} is primarily 2D (streamwise and cross-passage) in nature, for all four geometries. This means that most of the behavior can be explained by examining 2D trends.
(ii) The distribution of M at plane w_{SS} is more 3D in nature (increased radial variation, especially between 0% and 25% span) than at w_{PS}. The radial variation is reduced for very short TE overhang length (Geometry 4).
(iii) The distribution of M at plane w_{SS} is less sensitive to TE overhang length than that at plane w_{PS}, particularly for Geometry changes 1–2 and 2–3. Recall from Fig. 14 that the M contours migrate gradually upstream, but note that plane w_{SS} also moves upstream somewhat in-step with the M contours, in contrast to plane w_{PS} which is fixed in place. The M distribution at plane w_{SS} is a greater function of the exit boundary condition and overall vane aerodynamics than that at plane w_{PS}, which additionally depends on the interaction between the mainstream and TE flows, and the two planes (see models of Fig. 13).
(iv) The low M region at the PS extremes of the w_{SS} planes, associated with the TE flow and the PS side of the wake region, deepens and broadens as TE overhang is reduced. This arises as the w_{SS} plane moves gradually closer to the PS TE and so less mixing has taken place between the mainstream and TE flows.

Notwithstanding the low M region associated with the TE flow and wake in the w_{SS} distributions, the M contours are very similar between w_{SS} and w_{PS} for Geometry 4, but quite different for Geometry 1. This is to be expected for two reasons: first, the two planes move gradually closer in space as we move incrementally from Geometry 1 to Geometry 4 (see Fig. 5); second, the interactive effect of the two controlling areas becomes less significant both as their values become closer in magnitude and also as the flow system transitions towards one in which two flows (mainstream and TE) pass through a common area (model (a) in Fig. 13) as opposed to two separate areas (model (b)).

Consider now the normalized total pressure distributions in Fig. 17. We observe the following:

(i) The distribution of normalized total pressure is essentially 2D in nature, for all geometries and in both planes. The behavior can be explained accurately by examining 2D trends.
(ii) Normalized total pressure is very uniform and approximately equal to unity over the central region of the passage (20–80% of passage width). Loss in this region is minimal, arising only from turbulent dissipation, so this result is expected.
(iii) There are reduced total pressure regions near to both the PS and SS surfaces, associated with film cooling flows. The total pressure deficit is greater on the SS (as expected for mixing at higher average freestream Mach number) and the mixing layer is thinner (as expected for the strongly accelerated, and therefore thinning, SS boundary layer).

The only significant difference between the total pressure profiles at w_{SS} and w_{PS} is due to the additional deficit associated with the wake from the PS TE and the relatively low-momentum TE slot flow. As in the M distributions, the low total pressure region changes in profile with TE overhang length. In Geometry 4, as w_{SS} and w_{PS} are very close, the region of pressure deficit is

Downloaded from http://asmedigitalcollection.asme.org/turbomachinery/article-pdf/143/5/051001/6672930/turbo_143_5_051001.pdf by guest on 05 July 2021

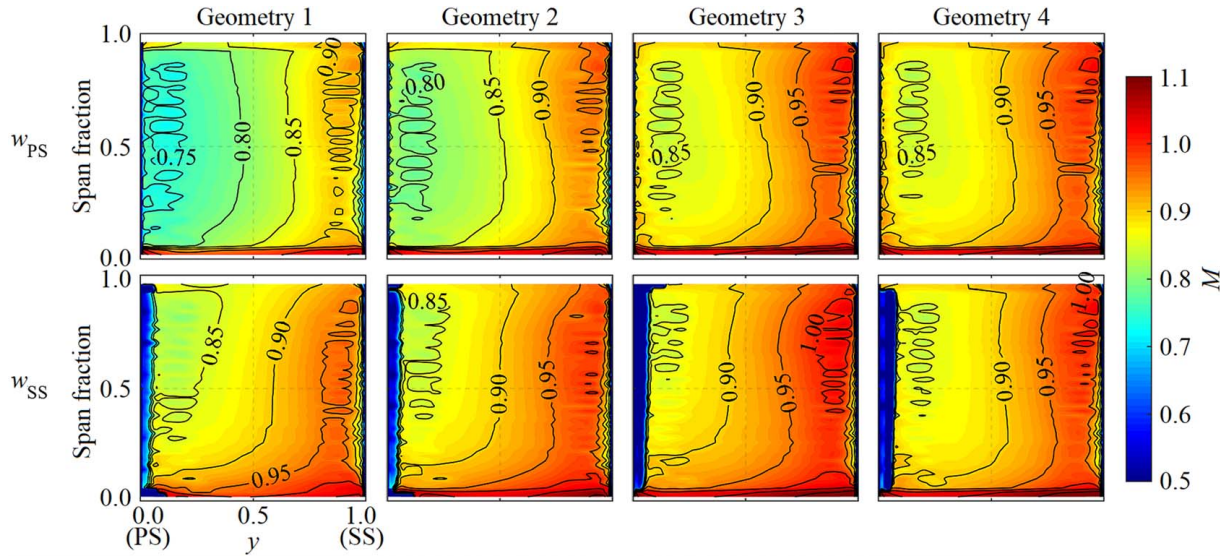


Fig. 16 Contours of Mach number in planes w_{PS} and w_{SS} for each TE geometry

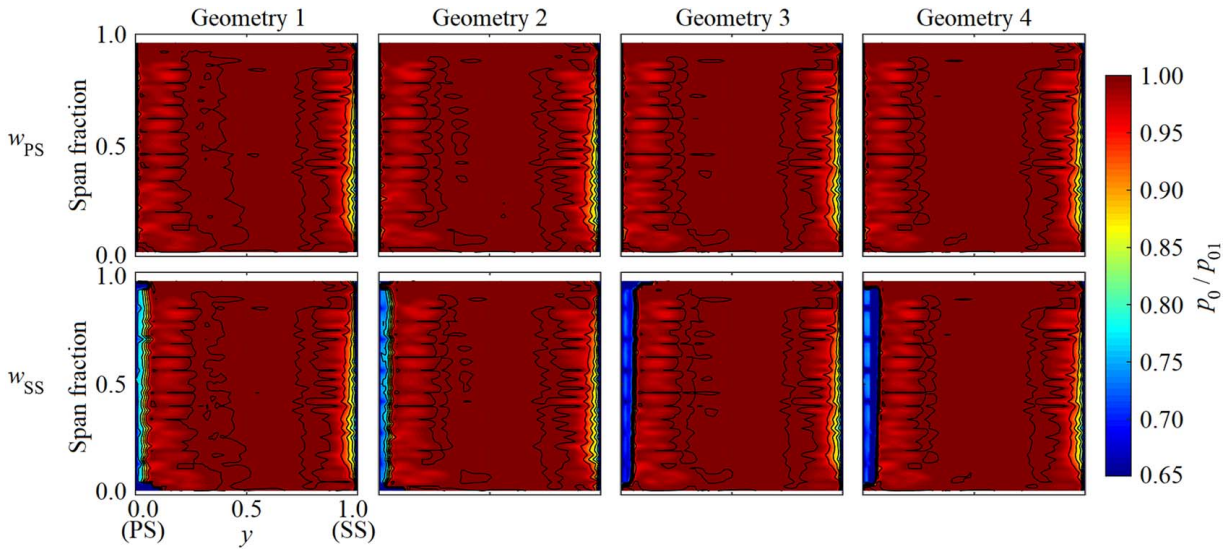


Fig. 17 Contours of normalized total pressure in planes w_{PS} and w_{SS} for each TE geometry

essentially unmixed and manifests as a thicker, more sharply defined layer than for Geometry 1, for which mixing has attenuated the depth of the low total pressure region.

Figure 18 presents midspan data (averaged over 45–55% of vane span) for all TE geometries at planes w_{PS} and w_{SS}. Subplots (a)–(f) show normalized total and static pressure, Mach number, whirl angle, deviation angle, and normalized mass flowrate, respectively. Schematic diagrams of the passage explaining the controlling area nomenclature, and angle definitions, are presented in (g) and (h), respectively. The plots of physical parameters are now analyzed in turn.

Figure 18(*a*) complements the normalized total pressure distributions in Fig. 17. For all geometries, total pressure is essentially equal to the inlet condition between 20% and 80% passage width at both w_{PS} and w_{SS}. As TE overhang is reduced (moving from Geometries 1 to 4), the high loss region on the extreme PS of the passage (0–8% passage width) deepens and the transition to the central region becomes much steeper as the plane w_{SS} approaches w_{PS}. There are very small changes in both the boundary layer and coolant mixing losses associated with aerodynamic changes for the vane.

Figure 18(*b*) shows static pressure profiles at midspan. All geometries and both planes exhibit a similar cross-passage pressure gradient, the result of the potential field effect due to upstream covered turning and downstream uncovered turning. At planes w_{SS}, the change in static pressure field between geometries is relatively small. We infer that for all geometries, the aerodynamic relationship (remaining turning, TE loss, mixing of adjacent streams, etc.) between the controlling area pressure distribution and the downstream pressure distribution (which was fixed in all cases) is similar.

In contrast, at plane w_{PS}, the static pressure is much higher than at plane w_{SS} for Geometry 1. This results from the competing controlling areas shown in model (a) in Fig. 13. As the TE overhang is reduced, the static pressure at plane w_{PS} continually decreases until, for Geometry 3, the difference from that at plane w_{SS} is very small. There is no further change in static pressure between Geometries 3 and 4. This is in accord with model (b) of Fig. 13. The average static pressure differences between planes w_{PS} and w_{SS} were 10.6%, 7.5%, 1.3%, and 1.2% of $p_{01} - p_{exit}$ for Geometries 1–4, respectively.

Figure 18(*c*) more clearly exemplifies the conclusions regarding the *M* distributions of Fig. 16. The *M* distributions (*c*) closely follow

Downloaded from http://asmedigitalcollection.asme.org/turbomachinery/article-pdf/143/5/051001/6672930/turbo_143_5_051001.pdf by guest on 05 July 2021

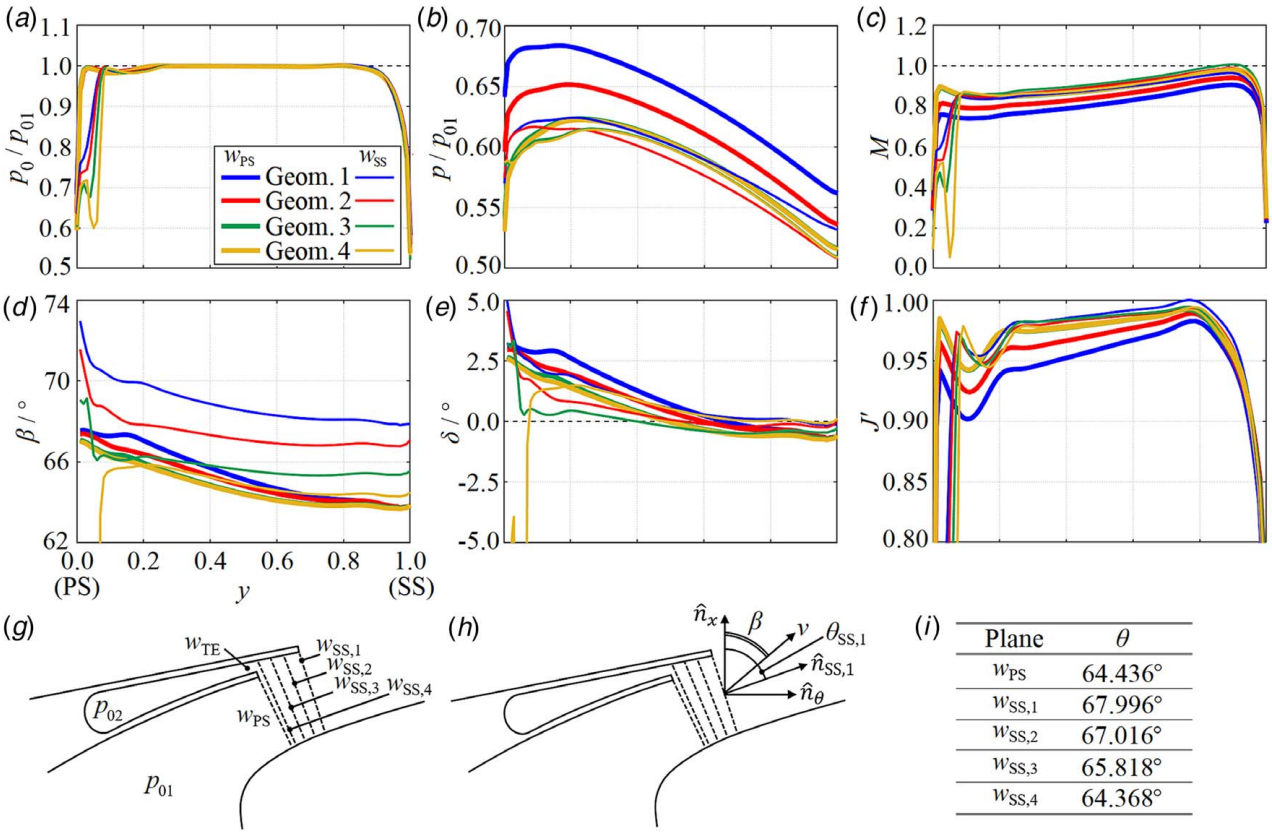
the static pressure distributions (*b*), due to the almost matched total pressures (*a*). In plane w_{SS}, the distribution changes little as TE overhang is reduced—the only significant change is in the separated region of the PS land wake and the low-momentum TE slot flow. The shift between Geometries 1 and 4 to a sharper drop in M occurs as plane w_{SS} moves closer to w_{PS}, leading to a less mixed out profile in the plane w_{SS}. In contrast, there is a significant change in M at plane w_{PS}. The trends at plane w_{PS} share a similar shape but are incrementally offset between the geometries, with peak values 0.91, 0.94, 0.98, and 0.98 for Geometries 1–4, respectively. The magnitudes of these increments are in line with the observed capacity trends (Figs. 11 and 12); the observed upstream shift in M contours with respect to the fixed w_{PS} plane between Geometries 1 and 3 but not 3 and 4 (Fig. 14) and also with the analysis presented in the context of Fig. 13. This indicates significant interaction between the areas w_{PS} and w_{SS} for Geometry changes 1–2 and 2–3 (model (a)) and low interaction for Geometry change 3–4 (model (b)). The magnitudes of the increments are also in line with the static pressure variation in Fig. 18(*b*), the total pressure profiles (Fig. 18(*a*)) being similar for all geometries.

Whirl angle, β, is plotted in Fig. 18(*d*). β is defined as the angle between the local velocity vector, v, and the axial direction, $\hat{n}_x$, as shown in Fig. 18(*h*). For controlling area $w_{SS,1}$, the associated unit normal vector, $\hat{n}_{SS,1}$, and the angle $\theta_{SS,1}$ between $\hat{n}_{SS,1}$ and $\hat{n}_x$ are also marked. θ angles for each plane are listed in Fig. 18(*i*). Similar definitions apply for other planes. In both the planes w_{PS} and w_{SS}, the whirl angle variation across the passage is relatively small, falling by approximately 2–3 deg between 20% and 80% of passage width moving from PS to SS.

Looking first at planes w_{SS}, whirl angle drops significantly as TE overhang length is reduced. The average changes between 20% and 80% passage width were −1.50 deg, −1.51 deg, and −0.69 deg for Geometry changes 1–2, 2–3, and 3–4, respectively. Unlike other variables, while the change between Geometries 3 and 4 is lower than those seen for the other changes, it is not negligible. This is expected both because the *covered turning length* is reduced and because the angle of the local surface tangent on the SS limit of the w_{SS} planes is also reduced with each incremental geometry change. Planes w_{PS} have much less sensitivity to the geometry changes. The average changes in whirl angle between 20% and 80% passage width were −0.33 deg, −0.37 deg, and −0.05 deg for Geometry changes 1–2, 2–3, and 3–4, respectively. The geometry upstream of w_{PS} is unchanged, but the flow still responds to static pressure changes (potential field effect) caused by the reduced covered turning downstream of the w_{PS} plane.

It is interesting to consider an effective *deviation angle*, $\delta = \beta - \theta$, with respect to the individual controlling planes. Deviation angle is plotted in Fig. 18(*e*). Positive deviation angles represent overturning with respect to a specific controlling area, and vice-versa. On the SS of the passage, deviation angles are close to zero. Here the flow follows the SS surface angle, and any deviation from zero (neglecting small boundary layer displacement effects, etc.) arises from the controlling area-normal direction ($\hat{n}_{SS,1}$, $\hat{n}_{SS,2}, \ldots, \hat{n}_{PS}$) not being precisely aligned with the local SS surface tangent. Towards the PS of the passage, deviation angles are positive. The gross trend results from the average metal angle at the PS limit of the planes w_{SS} and w_{PS} being greater than θ (the PS limit is at full-chord, while the SS limit is around half-chord, with remaining turning downstream).

An indication of the mass flow deficit that could be attributed to unaligned flow (angular difference between v and $\hat{n}$ at a particular plane) can be obtained by finding the average value of the cosine of δ over the 20–80% of passage width. For the planes w_{SS}, we get 0.0070%, 0.0004%, 0.0004%, and 0.0057% for Geometries



Plane	θ
w_{PS}	64.436°
$w_{SS,1}$	67.996°
$w_{SS,2}$	67.016°
$w_{SS,3}$	65.818°
$w_{SS,4}$	64.368°

Fig. 18 Midspan profiles in planes w_{PS} and w_{SS} of (*a*) normalized total pressure, (*b*) normalized static pressure, (*c*) Mach number, (*d*) whirl angle, (*e*) deviation angle, (*f*) normalized local capacity, and schematics of (*g*) controlling areas, (*h*) angle definitions, and (*i*) summary of area-normal angles, θ

Downloaded from http://asmedigitalcollection.asme.org/turbomachinery/article-pdf/143/5/051001/6672930/turbo_143_5_051001.pdf by guest on 05 July 2021

1–4, respectively. The corresponding values for planes w_{PS} are 0.0110%, 0.0042%, 0.0004%, and 0.0002%. These values are very small and show that while there are measurable changes in deviation between the geometries, this effect is not particularly significant in the context of the measured capacity changes.

Finally, we evaluate the local mass flowrates per unit area, normalized with respect to upstream total conditions (p_{01}, T_{01}) for each geometry. This can be considered a local capacity function. The maximum local mass flux occurs for Geometry 1 in plane $w_{SS,1}$. A *dimensionless local capacity* can therefore be defined as

$$J' = \frac{\left[(\delta\dot{m}/\delta A)\sqrt{T_{01}}/p_{01}\right]_{\text{local}}}{\left[(\delta\dot{m}/\delta A)\sqrt{T_{01}}/p_{01}\right]_{\text{SS,1,max}}} \tag{3}$$

where δA is a local area element, and $\delta\dot{m}$ is the associated element of mass flowrate. Profiles of J' for each geometry are plotted in Fig. 18(*f*). As expected, the profiles have significant local mass flow deficits near the PS ($y<0.2$) and SS ($y>0.8$) limits, caused by boundary layer loss and total pressure deficit due to coolant-mainstream mixing. In the near-PS flow, the coolant and boundary layer losses are distinct whereas in the near-SS flow, the two effects merge into a single deficit region. The general trend is towards lower J' on the lower Mach number PS of the passage (the flow being essentially subsonic).

We now consider changes in J' distribution across the passage as TE overhang length is reduced. *Changes in* J' with respect to Geometry 1 for each of Geometries 2–4 are shown in Fig. 19.

At the planes w_{SS}, the changes in J' between geometries are small and negative over most of the passage. In the relatively *clean* (i.e., unaffected by mixing interactions with boundary layers, cooling flows, or TE slot) flow region ($0.2<y<0.8$), the average changes in J' were −0.365%, −0.216%, and −0.594% for the Geometry changes 1–2, 1–3, and 1–4, respectively. The changes in w_{SS} between geometries, expressed as a percentage, and the changes in $\overline{\Delta J'}$ between geometries, expressed as a percentage, are listed in Table 4. An estimate of the capacity changes expected on the basis of area and aerodynamic changes in the clean flow region (due to the gross potential field) can be found by calculating the changes in the product of J' and w_{SS}. The changes in the product for each geometry change, expressed as a percentage, are listed in Table 4.

Comparing this with the CFD-predicted overall capacity changes (Table 3, reproduced in Table 4 for convenience), we see that this estimation is in good agreement for Geometry change 1–2, but overestimates the capacity changes for Geometry changes 1–3 and 1–4.

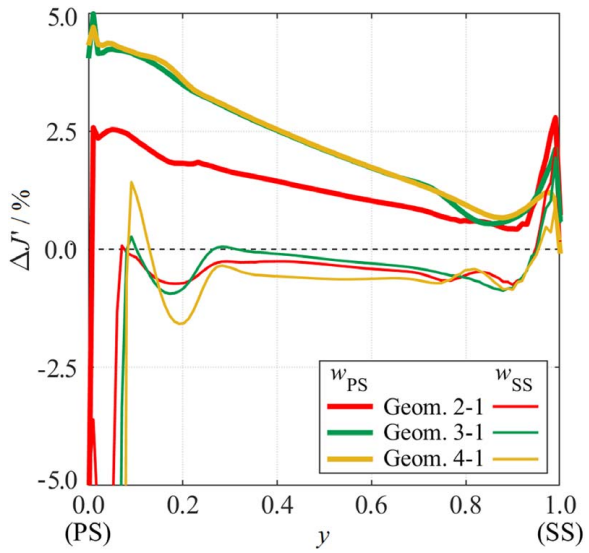


Fig. 19 Change in non-dimensional local capacity, J', as a function of cross-passage location for each geometry

Table 4 Summary of changes in passage width and average $\Delta J'$ between geometries for planes w_{SS} compared to CFD-predicted capacity changes

Geometry change	Δw_{SS} (%)	$\overline{\Delta J'}$ (%) ($0.2<y<0.8$)	$\Delta(w_{SS}\times\overline{J'})$ (%)	$\Delta\Gamma$ (%)
1–2	+1.534	−0.365	+1.116	+1.298
1–3	+3.522	−0.216	+3.241	+2.272
1–4	+5.290	−0.594	+4.587	+2.291

Table 5 Summary of changes in average $\Delta J'$ between geometries for planes w_{PS} compared to CFD-predicted capacity changes

Geometry change	$\overline{\Delta J'}$ ($0.2<y<0.8$) (%)	$\Delta\Gamma$ (%)
1–2	+1.204	+1.298
1–3	+2.078	+2.272
1–4	+2.087	+2.291

The deterioration in the accuracy of the estimation arises because there are changes in the mixing region between the TE flow and the mainstream (as the overhang length becomes short and the dynamics of the controlling region change as proposed in Fig. 13) which are not included in the assessment of the change in J'.

Performing the same analysis for planes w_{PS}, we see that changes in J' with geometry variation are significant, with large increments of change between Geometries 1–2 and 2–3, but almost no further change between Geometries 3–4. This trend is consistent with the observed overall capacity trend and the models (a) and (b) of Fig. 13. Changes in J' are greatest on the PS of the passage, where the flow is well below peak capacity (see Fig. 18(*c*)). Near the PS ($y\approx0.05$), the Mach numbers were 0.75, 0.81, 0.87, and 0.88 for Geometries 1 to 4, respectively. Near the SS ($y\approx0.90$), the higher Mach numbers (0.90, 0.94, 0.98, and 0.98) limit the potential field-induced changes in J' between geometries, due to the lower gradient of the capacity characteristic. The average changes in J' over $0.05\le y\le0.90$ (taken as the region unaffected by near-wall effects and hence $\Delta J'$ is due only to gross potential field effects) were 1.20%, 2.08%, and 2.09% for Geometry changes 1–2, 1–3, and 1–4, respectively. These values are listed in Table 5 and compared with the CFD-predicted capacity changes (from Table 3). The area w_{PS} is fixed between all geometries, the boundary layer effect has been established to be small, and the complex interactions associated with the mixing TE flow are far less significant than at plane w_{SS}. Good agreement is therefore expected between $\overline{\Delta J'}$ and $\Delta\Gamma$. From Table 5, we see that $\overline{\Delta J'}$ and $\Delta\Gamma$ agree to within 0.2% of absolute capacity, or, on average, to within 8.2% of the registered change.

We conclude by comparing the streamlines through a midspan section between Geometries 1 and 3. These are shown in Fig. 20. Streamlines originating from the TE coolant ejection slot are marked in bold.

Mainstream flow on the vane PS flows over the PS TE tip and turns into the PS base region (point 1 in Fig. 20(*a*)), where it meets coolant flow ejected from the TE slot. With a relatively long TE overhang (e.g., Geometry 1), the inner surface of the SS TE provides further turning—of the mixing TE coolant and PS mainstream flow—away from the axial direction. When the mixing PS mainstream and TE flows reach the SS TE tip, they then turn into the SS base region (point 2 in Fig. 20(*a*)). They meet with the SS mainstream flow at the so-called *point of confluence* (point 3 in Fig. 20(*a*)) and are turned to a common exit flow angle. This determines the location of the wake region with respect to the vane geometry.

As TE overhang length is reduced, the inside surface of the SS TE has less impact on the path of the mixing PS mainstream and TE flows. They therefore turn into the SS base region further

Downloaded from http://asmedigitalcollection.asme.org/turbomachinery/article-pdf/143/5/051001/6672930/turbo_143_5_051001.pdf by guest on 05 July 2021

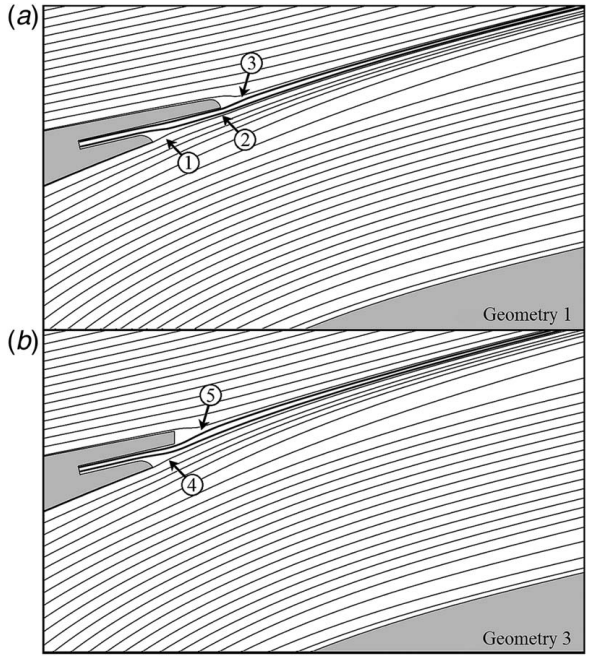


Fig. 20 Streamlines in a midspan section for (*a*) Geometry 1 and (*b*) Geometry 3

upstream (e.g., point 4 in Fig. 20(*b*)). The location of the point of confluence between mainstream flows from the PS and SS also moves circumferentially upstream (compare the location of point 5 in Fig. 20(*b*) relative to the PS TE tip with that of point 3 in Fig. 20(*a*)). The effect of this is to slightly shift the path of the wake with respect to the vanes.

When TE overhang becomes short (Fig. 20(*b*)), the PS and SS TE tips form a combined base region and the path of the mixing PS mainstream and coolant flows is not significantly affected by the short remaining SS overhang. Further reductions in overhang length (e.g., moving from Geometry 3 to 4) therefore have almost no impact on the streamlines, and the locations of the point of confluence and the wake region remain the same.

Summary and Conclusions

The impact of TE overhang length on capacity has been evaluated using both ultra-low uncertainty experimental methods and numerical methods. A parametric set of four different TE designs was investigated, providing an opportunity to understand the absolute and relative accuracies of the CFD method for this environment, the sensitivity to geometry changes of this type, and the fundamental mechanisms for capacity change. The conclusions in each of these areas were as follows:

Absolute and relative accuracies of CFD method: CFD capacity predictions agreed with experimental measurements to within −0.691%, −0.417%, −0.705%, and −0.812% for TE Geometries 1–4, respectively. The RMS error was 0.672%. The absolute accuracy of the CFD method was therefore extremely good. The *relative* accuracy of the CFD (in terms of the *changes* in capacity with changing TE overhang length) was good, matching observed experimental changes to within +0.330%, −0.033%, and −0.225% for respective changes of magnitude +1.298%, +2.272%, and +2.291%. The CFD method was therefore validated for aiding in the understanding of the underlying mechanisms responsible for the observed capacity changes.

Geometry sensitivity: A monotonic increase in vane capacity was observed as TE overhang length was reduced. The percentage capacity increases relative to Geometry 1 measured in experiments were +0.968%, +2.306%, and +2.516% for Geometries 2–4, respectively (nominally equal changes in overhang length). The gradient of the capacity trend reduced greatly when overhang length became small, partly explained by a change in the way the controlling areas interact.

Fundamental mechanisms for capacity change: Detailed analysis was conducted into the fundamental mechanisms responsible for the observed capacity shift between geometries and potential models through which the system behavior could be understood. This analysis was split into five areas, drawing the following conclusions:

(1) *Coolant stream capacity changes*: Neither changes in film cooling flows nor TE coolant flows between TE geometries were found to be significant in relation to the changes in vane capacity.
(2) *Changes in surface boundary layer profiles*: Analysis of the vane surface boundary layer displacement thicknesses and associated mass flow deficits showed that while there are small differences between the geometries, they are an order of magnitude smaller than the measured capacity changes. It was therefore concluded that this is not a significant mechanism responsible for the vane capacity shift.
(3) *Simplistic total pressure loss model*: A simple model of the vane was developed which included a total pressure loss model related to that of Fielding [2] and a *repeating area unit* to represent changes in area. A typical NGV is a fundamentally 2D system (sonic line far from aligned with the minimum area plane). The intrinsically 1D notion of a *throat* therefore provides a wholly inadequate description of the system. Even thinking of a *particular* controlling area is misleading and problematic, due to the necessary arbitrariness with which it must be ascribed in systems of this type. A more complete model of the vane should include *several* interacting controlling areas or a more general *controlling region*. This terminology is considered important as it sets the framework for thinking about the problem. Notwithstanding these deficiencies, the simple model performed moderately well for very small geometry changes (Geometries 1–2) when applied to both experimental and CFD data. For more significant geometric changes, the model significantly over-predicted the capacity change and could in no way predict the change in behavior once overhang length became small. We conclude that fundamentally 1D area-loss models cannot adequately represent the response of the physical system to even small aerodynamic changes and are therefore too simplistic to be useful.
(4) *Models of the controlling region*: Two more complex models of the vane were introduced, tailored to the two extremes of the TE geometry variation. The first model had a shared controlling area through which passed two interacting flows (and a wake). The second model had two non-interacting, independent controlling areas. While these models were incomplete, they represented an important aspect of the changing flow interactions between TE geometries that was necessary to progress more detailed analysis. The switch-over between the two models can be predicted by inspection of the controlling areas for each geometry.
(5) *Aerodynamic flow field changes*: The complex changes in the flow field between geometries have been understood by examining in detail the full-area and midspan 2D profiles of total and static pressure, Mach number, whirl angle, and local specific capacity, focusing on changes in the controlling region (considered in the framework of the two models proposed in this paper). The flow was primarily 2D in nature and well described by considering midspan trends (but with a radial pressure field superimposed). Total pressure profiles through the controlling region were similar between all geometries, as were static pressure distributions when examined at a downstream controlling area (w_{SS} planes), confirming a similar aerodynamic relationship between the pressure distributions at the controlling area and the far downstream system boundary.

Downloaded from http://asmedigitalcollection.asme.org/turbomachinery/article-pdf/143/5/051001/6672930/turbo_143_5_051001.pdf by guest on 05 July 2021

Static pressure distributions at an upstream controlling area (w_{PS} planes) were much more sensitive to TE geometry, due to a complex interaction in the controlling region, analyzed as an interaction between two controlling areas. These changes were the primary driver for significant changes in the Mach number and associated local specific capacity distributions at the w_{PS} planes. When analyzed at the w_{PS} planes, the combination of changes in area and local specific capacity closely reconcile the measured vane capacity changes for all TE geometries. This was not true for w_{SS} planes. This difference in behavior is attributed to the w_{SS} planes being affected by the separation downstream of the PS TE tip, something not included in the model.

In summary, we conclude that although the capacity changes between geometries *can* be explained using a model which includes the area and static pressure changes at a particular controlling area, the model is somewhat system-dependent, and a more complete description is provided by holistically analyzing the aerodynamic change in the entire controlling region. Low-order system representations of the type proposed in this paper are tempting because of the conceptual simplification they offer, but, we feel, are ultimately inadequate as descriptions of the system.

Acknowledgment

The support of Rolls-Royce plc is gratefully acknowledged, as is the contribution of Dominic Harris to the operation of the experimental facility.

Nomenclature

h = vane span, m
k = arbitrary constant
l = baseline PS TE overhang length, m
p = static pressure, Pa
s = circumferential distance, m
t = SS TE thickness, m
u = velocity, m s^{-1}
w = passage width associated with "repeating area unit" of vane passage, m
x = axial distance, m
y = wall-normal distance or normalized distance across passage, m
A = area, m^2
J = local capacity function, s K$^{1/2}$ m^{-1}
M = Mach number
S = vane pitch, m
U = velocity at edge of the boundary layer, m s^{-1}
Tu = turbulence intensity
$\dot{m}$ = mass flowrate, kg s^{-1}
$\dot{m}_{TOT}$ = total (mainstream + coolant) mass flowrate, kg s^{-1}
$\hat{n}$ = unit vector
J' = non-dimensional local capacity ratio
p_0 = stagnation pressure, Pa
p_{exit} = mean vane exit static pressure, Pa
w_{PS} = passage width in the plane of the PS TE tip, m
w_{SS} = passage width in the plane of the SS TE tip, m
w_{TE} = TE slot thickness, m
$y+$ = non-dimensional wall distance
C_x = axial chord length, m
M_{exit} = mean vane exit Mach number
M_s = isentropic Mach number
T_0 = stagnation temperature, K
Y_p = profile stagnation pressure loss coefficient

Greek Symbols

β = flow turning (or whirl) angle
Γ = capacity, m s K$^{1/2}$
Γ_i = isentropic capacity, m s K$^{1/2}$
Γ_{vane} = vane (or overall) capacity, m s K$^{1/2}$
δ = deviation angle
δ^* = boundary layer displacement thickness, m
θ = plane-normal angle
ρ = mass density, kg m^{-3}
φ = restriction factor (defined in Ref. [2])

Subscripts

0 = stagnation conditions
1 = mainstream vane inlet condition or TE Geometry 1
2 = film coolant inlet condition
3 = TE coolant inlet condition

Appendix A: Changes in Vane Capacity Due to Changes in Coolant Stream Capacities

Figures 21(*a*) and 21(*b*) show the mainstream and coolant capacity terms (deconstructed from the results presented in Fig. 10) for both experiment and CFD. At the design point, the total cooling flow (films and TE slot) makes up approximately 8% of the overall (mainstream and coolant) flow.

In Fig. 21(*b*), the overall cooling flow is further deconstructed into film cooling and TE slot flow characteristics. These two flows are not independently measured in the experiment, and the deconstruction is performed via a model. The model uses a series of CFD runs—performed at a range of off-design vane pressure ratios—to determine transfer functions between the vane pressure ratio and the individual film-row pressure ratios. The capacity characteristic for each row (including the TE slot) was assumed to have the isentropic form *when presented in terms of the local exit-static-to-inlet-total pressure ratio*. The ratio of magnitudes of the individual row characteristics came from the cooling design analysis for the engine part. The individual row characteristics were then expressed in terms of the vane pressure ratio using the transfer functions, and the total coolant capacity characteristic—as a function of p_{exit}/p_{01}—was determined by summing the individual row characteristics. The row characteristics were then scaled by a constant, $c = f(p_{exit}/p_{01})$, so that the model-predicted total coolant capacity characteristic matched the experimentally measured value for each vane pressure ratio. This method preserves the relative gradients of the individual coolant capacity characteristics and is believed to perform this deconstruction accurately.

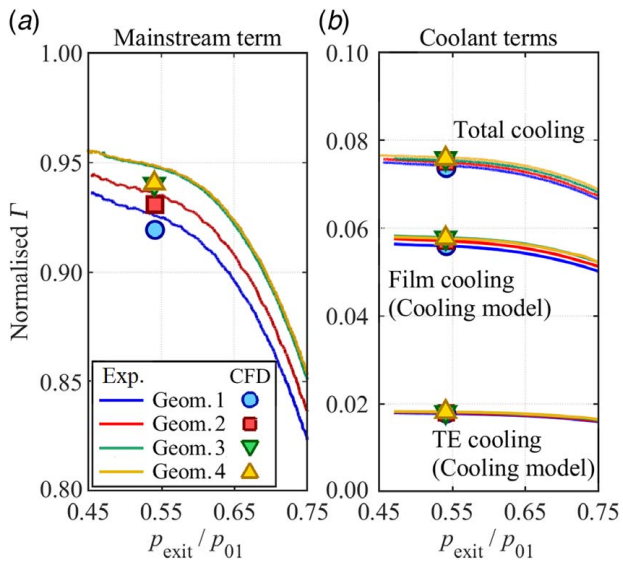


Fig. 21 Mainstream (*a*) and coolant (*b*) capacity terms for each TE geometry, normalized with respect to the experimental overall capacity for Geometry 1 at the design pressure ratio

Downloaded from http://asmedigitalcollection.asme.org/turbomachinery/article-pdf/143/5/051001/6672930/turbo_143_5_051001.pdf by guest on 05 July 2021

Consider first the *experimentally measured* total coolant capacity characteristics. From an absolute level of 7.4% of the total (mainstream plus cooling) capacity, the experimental changes between Geometries 1–2, 1–3, and 1–4 represented as *percentages of overall cooling flow* were +1.01%, +1.66%, and +2.42%, respectively. Expressed as *percentages of total capacity*, the corresponding numbers were approximately +0.08%, +0.12%, and +0.18%. These are very small changes, and not—in isolation—expected to significantly alter the state of the boundary layer flow passing through the controlling region. The film cooling model of Povey [6] estimated an exchange rate between film cooling mass flow (or capacity) and overall mass flow (or capacity) of −0.0269 at typical cold test rig conditions. Taking the largest change of +0.18% (between Geometries 1 and 4), this would lead to a predicted *decrease* in overall vane capacity of −0.0049%. The conclusion is that the effect of film cooling on boundary layer loss is entirely negligible in comparison to the observed change in overall capacity between Geometries 1 and 4 (+2.5%; see Table 3) and can be ignored.

We turn now to the TE coolant flow. Using the model-based deconstruction into film cooling and TE slot flows, it is predicted that approximately 85.8% of the mass flow increase (for all cases) is due to film cooling, with the remaining 14.2% due to the TE slot. Expressed as a percentage of total capacity, the predicted (model-based) changes in TE slot flow between Geometries 1−2, 1−3, and 1−4 are +0.014%, +0.031%, and +0.037%, respectively. These are very small changes in comparison to the observed change in overall capacity between Geometries 1 and 4 (+2.5%; see Table 3). It is worth noting that the TE slot flow is less sensitive both to local aerodynamic changes (the split we are currently discussing, at a fixed vane pressure ratio) and global aerodynamic changes (Fig. 21(*b*) shows lower gradient of capacity with p_{exit}/p_{01} for TE slot compared to film cooling rows) because it operated at a much higher overall pressure ratio than the (capacity) average overall pressure ratio of the film cooling rows.

Appendix B: Changes in Passage Mass Flow Deficit Due to Changes in Surface Boundary Layer Profiles

CFD-predicted boundary layer velocity profiles at the plane of minimum physical area (w_{PS}) at midspan are plotted in Fig. 22 for each of the four TE geometries. Both PS and SS profiles are plotted. Velocities are normalized with respect to the local free-stream velocity, U. In the case of the PS boundary layer, there is a fairly strong velocity gradient in the wall-normal direction, y, and therefore the value at a local peak (at a normalized passage width of approximately 0.018) is taken. The SS layer has a gradual velocity variation in the wall-normal direction, which makes the value of U rather arbitrary. For the purpose of plotting, U is defined as the velocity at a normalized wall-normal distance of $y/w_{PS} = 0.03$. Both surface profiles are characteristic of fully turbulent flow. This is expected at these locations (near PS TE and just over 50% of axial chord from the SS leading edge) for a fully cooled HP NGV.

Because of the difficulty in defining the outer edge of the boundary layer, the displacement thickness, δ^*, is computed for each of the eight boundary layer profiles for all integral heights between the wall ($y/w_{PS} = 0$) and $y/w_{PS} = 0.04$. The variation of normalized displacement thickness, δ^*/w_{PS}, with integration height is shown in Fig. 23. For a boundary layer with zero wall-normal velocity gradient, an asymptotic approach to a well-defined value of δ^* would be expected. In this case, because of the strong wall-normal velocity gradient over length scales comparable to the displacement thickness, the value of δ^* is poorly defined. The profiles of δ^*/w_{PS} as a function of integration height, y/w_{PS}, do plateau, however, allowing a displacement thickness to be estimated. Here we refer to the volume flow deficit caused both by shear with the wall and mixing in the film cooling layer. With reference to Fig. 23, the PS and SS integrals are seen to plateau for integration ranges of around $0 \le y/w_{PS} \le 0.015$ and $0 \le y/w_{PS} \le 0.030$, respectively. These limits are marked in the figure.

The values of δ^*/w_{PS} returned for these integration ranges are summarized in Table 6. Corresponding mass flowrate deficits are estimated as $\Delta\dot{m} = \rho U \delta^* h$, where h is the vane span. Here we make the approximation that δ^* is broadly uniform over the vane span. These deficits and the *changes* in mass flowrate deficit with respect to Geometry 1 are also tabulated in Table 6. In the final column, negative values indicate a *reduction* in mass flow *deficit* due to a thinner boundary layer region—i.e., a rise in overall passage mass flowrate. We see from Table 6 that, while there are small differences between the four geometry cases, these differences are an order of magnitude smaller than the observed capacity changes (see Table 3 and Fig. 12).

Appendix C: Application of the Simplistic Area-Total Pressure Loss Model

In an earlier section of this paper, the quasi-2D model of Fielding [2,13] was introduced. In this model, a *restriction factor* is defined as a way of describing the reduction in nozzle effective flow area

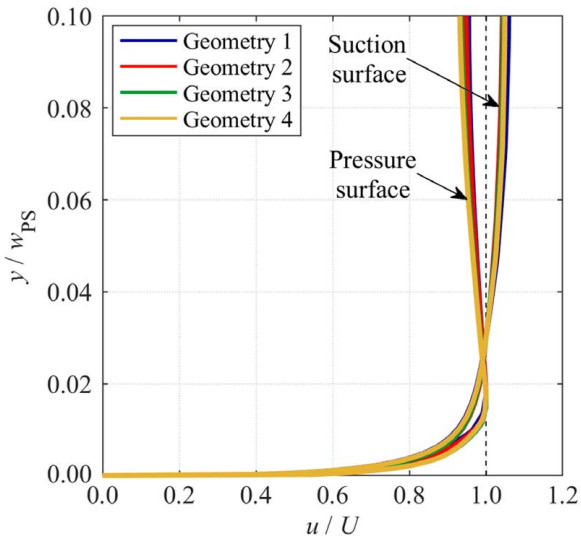


Fig. 22 Normalized PS and SS boundary layer velocity profiles in the w_{PS} plane at midspan for each TE geometry

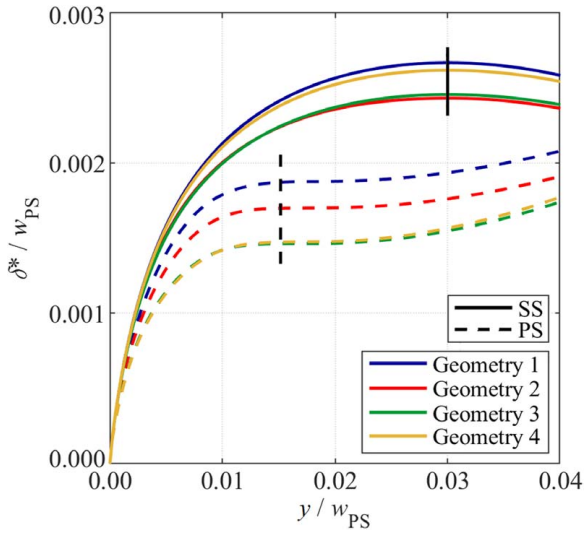


Fig. 23 SS and PS boundary layer displacement thicknesses as functions of wall-normal integration height, y, for each TE geometry

Downloaded from http://asmedigitalcollection.asme.org/turbomachinery/article-pdf/143/5/051001/6672930/turbo_143_5_051001.pdf by guest on 05 July 2021

Table 6 Estimated boundary layer displacement thickness, overall mass flowrate deficit, and change in mass flow deficit relative to Geometry 1

Geometry	PS $\delta^*/w_{PS} \times 10^{-3}$	SS $\delta^*/w_{PS} \times 10^{-3}$	SS + PS $\Delta\dot{m}/\dot{m}_{TOT}$(%)	SS + PS $\Delta\dot{m}/\dot{m}_{TOT}$ (related to Geometry 1)
1	1.88	2.67	0.403	–
2	1.70	2.43	0.372	−0.035%
3	1.47	2.46	0.358	−0.040%
4	1.48	2.62	0.374	−0.022%

due to frictional effects within the passage. The loss correlations of Ainley and Mathieson [14] and Dunham and Came [15] were used to estimate the boundary layer thickness integral parameters. For an exit Mach number $M_{exit} > 0.8$, the restriction factor φ resulting from the analysis was well approximated by the following simplified form:

$$\varphi = 1 - 0.56Y_p \tag{A1}$$

where the profile total pressure loss coefficient, Y_p, is defined as

$$Y_p = \frac{p_{01} - p_{02}}{p_{02} - p_{exit}} \tag{A2}$$

where p_{exit} is the area-mean static pressure in the traverse plane, p_{02} is the local total pressure in the traverse plane, and p_{01} is the vane inlet total pressure. This may be regarded as a quasi-2D approach, in that the vane model is that of a 1D system (single area, upstream total, and downstream static pressure) but with a loss correction model with a 2D component (distribution of loss across the passage). Loss confined to boundary layer regions has a lesser impact on capacity than uniformly distributed loss. This is represented in Eq. (A1) by the factor of 0.56 being less than unity. The restriction factor provides an estimate of the ratio of actual flow capacity to the 1D isentropic capacity, i.e., $\varphi = \Gamma/\Gamma_i$, where Γ_i is the isentropic capacity characteristic.

We now examine the extent to which this relatively simple quasi-2D analysis, combined with a measure of the change in passage area between different TE geometries, can reconcile the observed results. This requires that somewhat arbitrary choices be made about how the system is represented in terms of both total pressure and area. These choices are now considered in turn.

Because TE loss is an important aspect of the system, near-plane traverse data ($0.50C_x$ downstream of the TE) were chosen as a proxy for total and static pressure through *controlling regions* of the vane. In practice, this is the closest plane in which the entire vane loss, including TE loss, can be evaluated and gives the simplest representation of the back-pressure condition.

Turning to area, we choose a quasi-periodic *repeating area unit* (i.e., including all streamlines exactly once, when *repeated* through the system), related as closely as possible to a physical area in the guided part of the vane and aligned as normal as possible to the assumed flow direction. The purpose is to provide the most direct analogy possible to a 1D system. Noting the rather fundamental weakness in the 1D analogy, the repeating area units are taken as those lines represented by $w_1 = w_{SS,1} + t_1$, $w_2 = w_{SS,2} + t_2$, etc., with reference to Fig. 5. Figure 24 shows a schematic of the repeating area unit so formed. The repeating area unit is not strictly periodic due to the difference in SS boundary layer state between the two ends of the line w (between mid-chord and the TE). Table 7 summarizes the widths associated with each repeating area unit.

To calculate Y_p, experimental traverse measurements were conducted in an axial plane $0.50C_x$ downstream of the vane TE plane (five-hole pressure probe with tip diameter 2.80 mm), at a nominal pressure ratio $p_{exit}/p_{01} = 0.54$ or $M_{exit} = 0.975$. The downstream area was surveyed over 2.5 vane pitches. The loss characteristic was primarily 2D in nature and is well represented by the circumferential profiles of Y_p at midspan, shown in Fig. 25. The

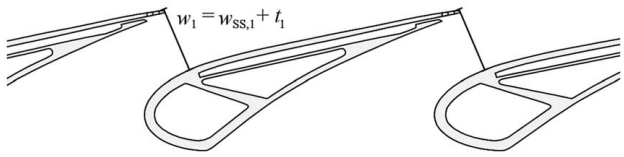


Fig. 24 Schematic diagram of the *repeating area unit*

Table 7 Summary of widths associated with repeating area units for each geometry

Geometry	1	2	3	4
w/w_1	1.000	1.018	1.042	1.064

characteristics have the classic quasi-normal distribution expected for a partially mixed out wake. Moving from Geometry 1 to 4 (reducing TE overhang length), the peak broadens and shifts to a lower value of s/S.

A comparison to CFD-evaluated midspan loss is also shown in Fig. 25. The prediction shows higher peak values of Y_p (wake center) when compared with experiments. This is in line with the well-known tendency of most CFD methods to under-predict the wake mixing rate. Moving from Geometry 1 to 4 (reducing TE overhang length), the change in the CFD-predicted trends agrees with experiment, with a broadening peak moving to lower values of s/S.

To evaluate an average total pressure loss coefficient, $\overline{Y_p}$, the circumferential profiles of local Y_p were mass flow-averaged over two vane pitches (centered on mid-passage to avoid sensitivities). Experimental and CFD averages are plotted in Fig. 26 as functions of TE overhang length, expressed as percentage changes with respect to the longest TE overhang (Geometry 1). The experimental

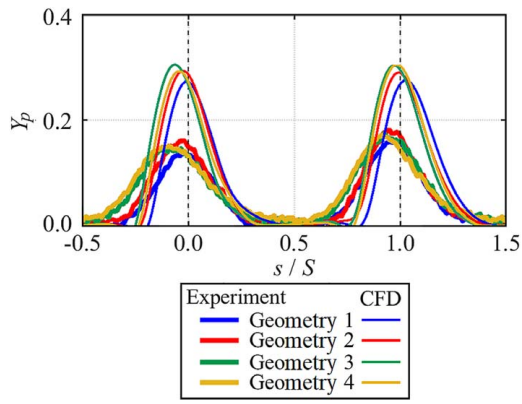


Fig. 25 Experimentally measured and CFD-predicted circumferential profiles of local total pressure loss coefficient, at midspan, $0.50C_x$ downstream of the TE

Downloaded from http://asmedigitalcollection.asme.org/turbomachinery/article-pdf/143/5/051001/6672930/turbo_143_5_051001.pdf by guest on 05 July 2021

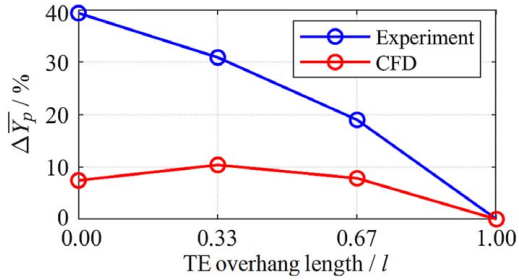


Fig. 26 Percentage change in circumferentially averaged Y_p with respect to Geometry 1 as a function of TE overhang length

Table 8 Summary of average total pressure loss coefficients

	$\Delta\overline{Y_p}$ from Geometry 1 (%)	
Geometry	Experiment	CFD
2	+18.99	+7.82
3	+30.91	+10.38
4	+39.39	+7.41

average value increases monotonically as TE overhang is reduced, up to a 39.4% increase between Geometries 1 and 4. This result is intuitively expected (complexities of interaction with the TE slot flow aside) as the TE becomes less aerodynamic with reducing overhang.

CFD over-predicts the average loss coefficient by an average of 31.9% (across all designs). Moving from Geometry 1 to 3, the predicted trend is similar to experiments, with increasing Y_p as TE overhang length is reduced. The predicted change between Geometries 3 and 4 differs from experiments, with CFD showing a small reduction in Y_p. Percentage changes in average Y_p relative to Geometry 1 are summarized in Table 8 for each of Geometries 2 to 4.

Following the Fielding [2, 13] analysis presented above, the simplest possible capacity model could be regarded as

$$\Gamma \propto w\frac{\Gamma}{\Gamma_{\mathrm{i}}} = w(1 - k\overline{Y_p}) \tag{A3}$$

where k is a constant and w is the width of the repeating area unit (see Fig. 24 and associated discussion). For typical loss distributions across the passage, Fielding [2] determined a value $k = 0.56$. The limiting value for uniformly distributed loss (yielding the smallest capacity change that could be predicted by this model for a given $\overline{Y_p}$) would be $k = 1.00$. We consider both of these values in our modeling to show the typical or extreme minimum capacity changes expected on the basis of this model.

Considering only the *changes* in capacity with TE overhang length (the absolute accuracy of the CFD has been discussed in the context of Figs. 10 and 11), from Eq. (A3), the expected capacity ratio between, e.g., Geometries 1 and 2 could be written as

$$\frac{\Gamma_2}{\Gamma_1} = \frac{w_2\,(1 - k\overline{Y_{p,2}})}{w_1\,(1 - k\overline{Y_{p,1}})} \tag{A4}$$

and similarly for ratios Γ_3/Γ_1 and Γ_4/Γ_1.

The model-predicted capacity changes with varying overhang length are now evaluated based on both CFD and experimental $\overline{Y_p}$ data. The predicted changes are compared with the corresponding experimentally measured and CFD-predicted changes. The data are tabulated in Table 9 and are plotted in Fig. 27, in terms of the percentage changes from Geometry 1, i.e., for example,

$$\Delta\Gamma_{1\text{–}2}\ (\%) = 100\left(\frac{\Gamma_2}{\Gamma_1} - 1\right) \tag{A5}$$

Data are presented for both $k = 0.56$ and $k = 1.00$. Looking first at the data for $k = 0.56$ (part (a) of Table 9), we see that the model performs reasonably well for small changes in overhang length (Geometry change 1–2), over-predicting the vane capacity change by only +0.323% and +0.197% for experiment and CFD, respectively. The agreement is worse for Geometry change 1–3 (over-predictions of +0.956% and +1.511% for experiment and CFD, respectively) and the performance becomes very poor for the largest change in overhang length (Geometry change 1–4), where the capacity changes are over-predicted by +2.714% and +3.790% for experiment and CFD, respectively.

The same data are plotted in Fig. 27, where capacity changes predicted by the quasi-2D model are plotted against those determined by CFD and experiment. Experimental and CFD points are represented by hollow circles and triangles, respectively. Points lying close to a line of unit gradient (dotted line) indicate accurate prediction. The model clearly shows increasing deviation from ideal prediction as the geometry change becomes more significant (1–3 and 1–4). The loss-based model is therefore a very poor predictor of capacity change.

We now consider data for $k = 1.00$ (part (b) of Table 9). This value maximizes the sensitivity of the capacity change to changes in measured total pressure loss. Due to the increasing total pressure loss with each successive geometry change (see Tables 8 and 9), increasing k has the effect of reducing the predicted increments of

Table 9 Summary of changes in vane capacity with respect to Geometry 1 predicted by the simple area-loss model applied to both experimental and CFD loss data for values (a) $k = 0.56$ and (b) $k = 1.00$

		Experiment				CFD			
Geometry change	$\frac{w}{w_1}$	$\frac{\overline{Y_p}}{\overline{Y_{p1}}}$	$\frac{(\Gamma/\Gamma_{\mathrm{i}})}{(\Gamma/\Gamma_{\mathrm{i}})_1}$	$\Delta\Gamma_{\mathrm{model}}$ (%)	$\Delta\Gamma_{\mathrm{meas.}}$ (%)	$\frac{\overline{Y_p}}{\overline{Y_{p1}}}$	$\frac{(\Gamma/\Gamma_{\mathrm{i}})}{(\Gamma/\Gamma_{\mathrm{i}})_1}$	$\Delta\Gamma_{\mathrm{model}}$ (%)	$\Delta\Gamma_{\mathrm{pred.}}$ (%)
(a) $k = 0.56$									
1–2	1.018	1.190	0.995	+1.291	+0.968	1.078	0.997	+1.495	+1.298
1–3	1.042	1.309	0.991	+3.262	+2.306	1.104	0.996	+3.783	+2.272
1–4	1.064	1.394	0.989	+5.230	+2.516	1.074	0.997	+6.081	+2.291
(b) $k = 1.00$									
1–2	1.018	1.190	0.990	+0.782	+0.968	1.078	0.994	+1.189	+1.298
1–3	1.042	1.309	0.984	+2.533	+2.306	1.104	0.992	+3.366	+2.272
1–4	1.064	1.394	0.979	+4.166	+2.516	1.074	0.994	+5.762	+2.291

Downloaded from http://asmedigitalcollection.asme.org/turbomachinery/article-pdf/143/5/051001/6672930/turbo_143_5_051001.pdf by guest on 05 July 2021

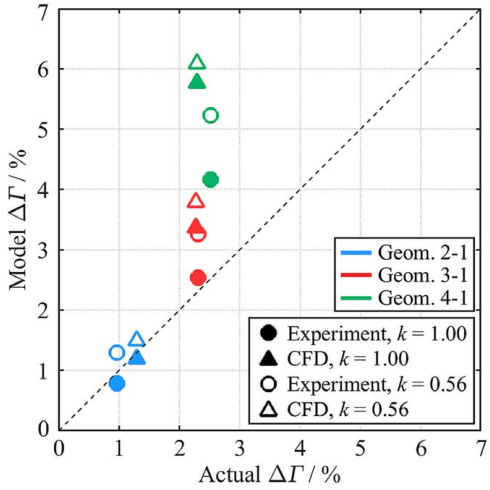


Fig. 27 Comparison of capacity changes predicted by the quasi-2D model and those determined by CFD and experiment

capacity change and hence improves the match with the measured vane capacity changes. The model performance is then very good for Geometry change 1–2 (under-predictions of −0.186% and −0.109% for experiment and CFD, respectively), reasonable for Geometry change 1–3 (over-predictions of +0.227% and +1.094% for experiment and CFD, respectively), and very poor for Geometry change 1–4 (over-predictions of +1.650% and +3.471% for experiment and CFD, respectively). These data are also plotted in Fig. 27, shown by solid circles and triangles.

Whether we take the empirically justified value of $k = 0.56$ from Fielding [2] or the limiting value of $k = 1.00$ for fully mixed loss, we see that the simple area-loss model cannot meaningfully reproduce the observed capacity changes for all geometries. The deteriorating performance of the model as the change in TE overhang length becomes greater is explained by increasing changes in aerodynamics not being included in the framework of the quasi-2D model. In general, the aerodynamic impact of a geometry change could be either positive or negative with respect to the model prediction (results of Fig. 27 and Table 9). This explains the relatively small sensitivity to the value of k and suggests that a model of this nature would be unlikely to give results applicable across a range of vane geometries.

References

[1] Afanasiev, I. V., Granovskiy, A. V., Karelin, A. M., and Kostege, M. K., 2004, "Effect of 3D Vane Shape on the Vane Capacity," Proceedings of ASME Turbo Expo 2004, Vienna, Jun. 14–17, Paper No. GT2004-53095.

[2] Fielding, L., 1981, "The Effect of Irreversibility on the Capacity of a Turbine Blade Row," Proc. Inst. Mech. Eng., **195**(1), pp. 127–137.

[3] Povey, T., Sharpe, M., and Rawlinson, A., 2011, "Experimental Measurements of Gas Turbine Flow Capacity Using a Novel Transient Technique," ASME J. Turbomach., **133**(1), p. 011005.

[4] Kirollos, B., Lubbock, R., Beard, P., Goenaga, F., Rawlinson, A., Janke, E., and Povey, T., 2017, "ECAT: An Engine Component Aerothermal Facility at the University of Oxford," Proceedings of ASME Turbo Expo 2017, Charlotte, NC, Jun. 26–30, Paper No. GT2017-64736.

[5] Burdett, D., Hambidge, C., and Povey, T., 2020, "Analysis of Ultra-Low Uncertainty Gas Turbine Flow Capacity Measurement Techniques," Proc. Inst. Mech. Eng. Part A: J. Power Energy., pp. 1–27.

[6] Kost, F., and Holmes, A., 1985, "Aerodynamic Effect of Coolant Ejection in the Rear Part of Transonic Rotor Blades," AGARD-CP-390, Heat Transfer and Cooling in Gas Turbine Blades, Paper 41.

[7] Uzol, O., and Camci, C., 2001, "Aerodynamic Loss Characteristics of a Turbine Blade With Trailing Edge Coolant Ejection: Part II—External Aerodynamics, Total Pressure Losses and Predictions," ASME J. Turbomach., **123**(2), pp. 249–257.

[8] Povey, T., 2010, "Effect of Film Cooling on Turbine Capacity," ASME J. Eng. Gas Turbines Power, **132**(1), p. 011901.

[9] Hambidge, C., and Povey, T., 2012, "Numerical and Analytical Study of the Effect of Film Cooling on HP NGV Capacity," Proceedings of ASME Turbo Expo 2012, Copenhagen, June 11–15, Paper No. GT2012-69066.

[10] Högner, L., Nasuf, A., Voigt, P., Voigt, M., Vogeler, K., Meyer, M., Berridge, C., and Goenaga, F., 2016, "Analysis of High Pressure Turbine Nozzle Guide Vanes Considering Geometric Variations," Proceedings of ASME Turbo Expo 2016, Seoul, June 13–17, Paper No. GT2016-57502.

[11] British Standards Institution, 2005, *BS EN ISO 9300:2005 Measurement of Gas Flow by Means of Critical Flow Venturi Nozzles*, British Standards Institution, London.

[12] Melzer, A. P., and Pullan, G., 2019, "The Role of Vortex Shedding in the Trailing Edge Loss of Transonic Turbine Blades," ASME J. Turbomach., **141**(4), p. 041001.

[13] Fielding, L., 2000, *Turbine Design: The Effect on Axial Flow Turbine Performance of Parameter Variation*, ASME Press, New York.

[14] Ainley, D. G., and Mathieson, G. C. R., 1951, *A Method of Performance Estimation for Axial Flow Turbines*, Aeronautical Research Council, London. No. ARC-R/M-2974.

[15] Dunham, J., and Came, P. M., 1970, "Improvements to the Ainley–Mathieson Method of Turbine Performance Prediction," ASME J. Eng. Power, **92**(3), pp. 252–256.

Downloaded from http://asmedigitalcollection.asme.org/turbomachinery/article-pdf/143/5/051001/6672930/turbo_143_5_051001.pdf by guest on 05 July 2021

ADDENDUM: SPECIFICATION OF MASS FLOW INLET BOUNDARY CONDITIONS FOR FILM AND TE SLOT COOLANT FLOWS

Mass flow inlet boundary conditions for the CFD film and TE slot coolant flows are determined from target coolant capacity terms based on total pressure and temperature conditions measured in the ECAT experiments in the coolant feed cavities in the coolant supply network inside the vanes. This location is not modelled in the present CFD study. Specifying inlet mass flow boundary conditions causes a potential issue because the total pressure conditions on the inlet boundaries are not directly specified and are effectively left as 'floating' (left for the solver to determine to meet the mass flow boundary condition). Because the internal cooling network of the vane is not simulated, there is a potential disconnect between the feed total pressure condition (which is used to define coolant capacity terms) and the total pressure at the ejection locations (which cannot be specified in this model and which is not known from the experiment, but which controls the mixing interactions between the coolant and mainstream flows). This is one important limitation of the simple source-terms model.

Specifying fixed inlet total pressure boundary conditions for each coolant flow in the CFD would likely be a more robust method, but it is very difficult to accurately match this to the experiment since there is no common location for measurement of coolant pressure conditions. Implementing such a method would require calibration of the capacity result against the experiment to determine the 'correct' total pressure boundary conditions, or a CFD method simulating more of the vane internal cooling network.

Another point worth mentioning is the suitability of specifying coolant inlet mass flow boundary conditions for unsteady CFD cases featuring TE vortex shedding. This is a particular concern regarding the TE slot inlet boundary, which ejects directly into the unsteady base region. The slot will effectively cycle up and down its capacity characteristic (based on local exit static-to-inlet total pressure ratio) during the periodic shedding cycle, and so its mass flow rate boundary condition ought to cycle accordingly. This will not be captured if the slot inlet boundary condition is specified as a fixed mass flow rate, allowing the total pressure on the inlet boundary to float. The specified mass flow rate should be relevant to the time-averaged situation, and the impact of this on the time-averaged unsteady CFD solution is expected to be minor.

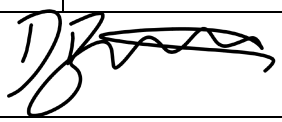
Statement of Authorship for joint/multi-authored papers for PGR thesis

To appear at the end of each thesis chapter submitted as an article/paper

The statement shall describe the candidate's and co-authors' independent research contributions in the thesis publications. For each publication there should exist a complete statement that is to be filled out and signed by the candidate and supervisor **(only required where there isn't already a statement of contribution within the paper itself).**

Title of Paper	Impact of trailing edge geometry on the flow capacity of transonic turbine nozzle guide vanes
Publication Status	Accepted for Publication
Publication Details	Burdett, D., Goenaga, F., Povey, T.; 2020; Impact of Trailing Edge Geometry on the Flow Capacity of Transonic Turbine Nozzle Guide Vanes; ASME J. Turbomach., Paper No. TURBO-20-1172 *(Accepted)*

Student Confirmation

Student Name:	D Burdett		
Contribution to the Paper	Performed experimental testing to collect data, ran numerical simulations, analysed and interpreted experimental and numerical data, developed intellectual arguments, and wrote manuscript.		
Signature		Date	13/02/2021

Supervisor Confirmation

By signing the Statement of Authorship, you are certifying that the candidate made a substantial contribution to the publication, and that the description described above is accurate.

Supervisor name and title: Professor Thomas Povey		
Supervisor comments: Dan conducted all of the research himself, and entirely wrote the paper himself, with technical contributions from his supervisor.		
Signature: Thomas Povey	Date	19/02/2021

This completed form should be included in the thesis, at the end of the relevant chapter.

ANALYSIS OF AVERAGING METHODS FOR NON-UNIFORM TOTAL PRESSURE FIELDS

Daniel Burdett, Thomas Povey*
Department of Engineering Science, University of Oxford, Oxford, OX2 0ES, United Kingdom
*Corresponding author—thomas.povey@eng.ox.ac.uk

ABSTRACT

A common objective in the analysis of turbomachinery components (nozzle guide vanes or rotor blades, for example) is to calculate performance parameters, such as total pressure or kinetic energy loss coefficients, from measurements in a non-uniform flow-field. These performance parameters can be represented in a range of ways. For example: line-averages used to compare performance between different radial sections of a 3D component; plane-averages used to assess flow (perhaps loss coefficient) development between different axial planes; and fully mixed-out values used to determine the total loss associated with a component.

In the literature, the weighting method used for line- and plane-averaging (e.g. area, volume flow, mass flow, or entropy flux) is sometimes regarded as an unimportant issue. Indeed, many authors neglect to even state which weighting method was used in their work. In certain low-speed test cases, or where measurements are made a long distance from the component, the non-uniformity in the flow will be relatively small and the practical difference between different weighting methods may be negligible. However, in high-speed applications or for measurements close to a component trailing edge, this becomes increasingly unlikely.

In this paper, we compare a range of methods for calculating aerodynamic performance parameters—for example, the kinetic energy loss coefficient—including plane-average methods with different weighting schemes and several mixed-out methods. We analyse the sensitivities of the different methods to the axial location of the measurement plane, the radial averaging range, and the exit Mach number. We use high-fidelity experimental data taken in several axial planes downstream of a cascade of engine parts: high pressure (HP) turbine nozzle guide vanes (NGVs) operating at transonic Mach number. The experimental data is complemented by CFD. We discuss the underlying physical mechanisms which give rise to the observed sensitivities. The objective is to provide guidance on the accuracy of each method in a relevant, practical application.

INTRODUCTION

The flow field downstream of a turbomachine blade row is—to first order—two-dimensional, but often with significant three-dimensional secondary features. For the purpose of basic performance assessment and comparison, simplified performance parameters are commonly used. Two of the most common performance parameters are the total pressure loss coefficient, Y, and the kinetic energy (KE) loss coefficient, ζ. The relative merits of these two metrics are considered later. Whichever performance parameter is preferred, however, there remain numerous questions about how to represent said parameter. In particular the following questions arise:

1) Do we wish to represent the performance parameter as a local value (at a point in a plane), a line-averaged value (to represent a circumferential or radial variation), a plane-averaged value (as a single numerical representation of the efficiency), or a *mixed-out* value at a hypothetical downstream plane?
2) In a line or plane *averaging process*, should the integral be weighted by area, volume-flux, mass-flux or entropy-flux?
3) In a *mixing process*, should the flow: be mixed to an entirely uniform static pressure defined at a single, swirl-averaged radius [6]; be mixed at every radius to a circumferentially-uniform static pressure, producing a radial profile [7] not necessarily satisfying a radial equilibrium condition; or be mixed to a pre-specified radial static pressure condition defined by a free or forced vortex (which does satisfy radial equilibrium)?

A tree of possible representations of a given performance metric is represented by Figure 1. For each performance parameter (e.g. Y or ζ) this leads to thirteen distinct methods of representing the variable. In this paper we compare and discuss these representations using both experimental and computational data, in particular considering the sensitivity to the weighting and averaging processes. These different representations of a loss parameter, are, of course, suited to different analysis objectives. For example:

- Local distributions allow identification of specific loss structures within a flow-field, and detailed local flow comparisons between different experiments or between experiment and CFD.
- Line-averages are useful for analysing wake characteristics (depth and thickness) and mixing rates.
- Plane-averages are useful for analysing overall mixing rates and as a simple method for analysing total loss.
- Mixed-out values are perhaps the most robust method for representing the total (plane-independent) loss associated with a component.

In many experiments in the open literature where averaged quantities are presented, a simple area-average is used, either because of the ease of calculation or because of difficulty in measuring the additional flow variables required for more sophisticated weighting methods. Whilst simplicity is clearly desirable, it is important to consider the sensitivity (to axial plane, Mach number, etc.) that the choice of weighting method

might imply. This is particularly important where comparing between different experiments, or between experiment and CFD.

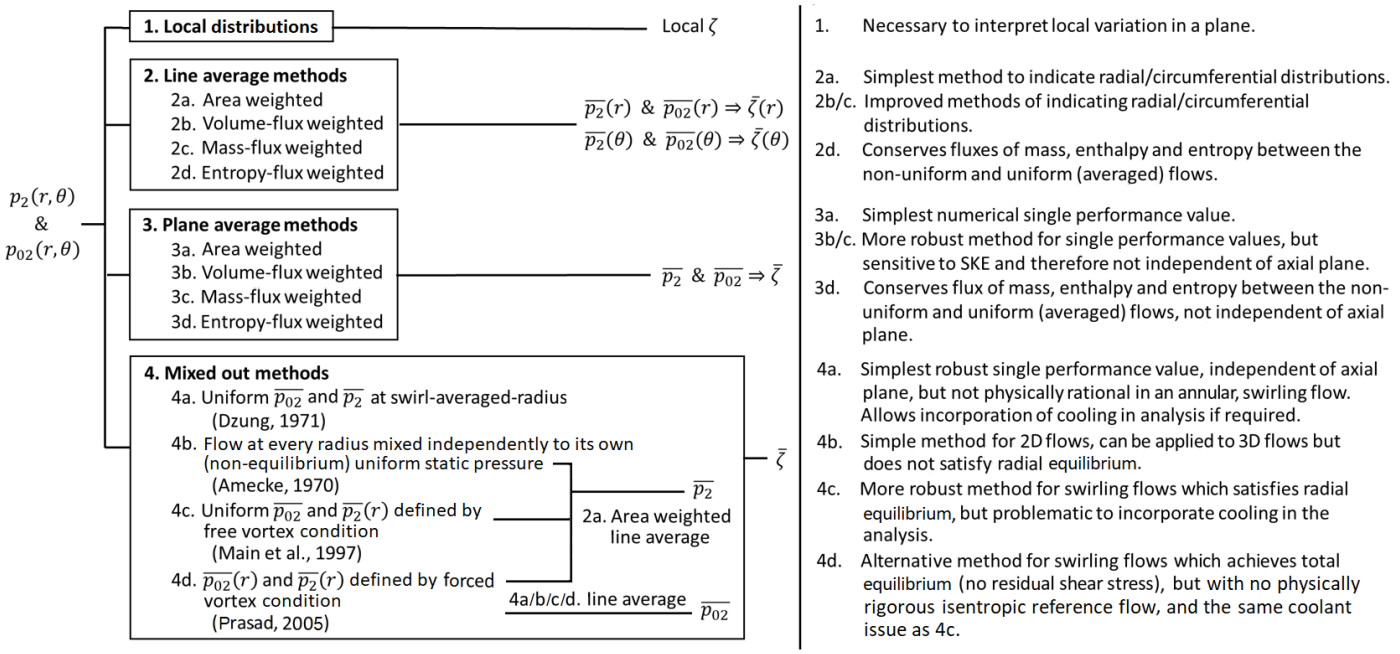


Figure 1: Tree of possible performance metric calculations.

In this paper, we examine the sensitivity of average loss representations to weighting method for the case of line-averaged and plane-averaged flows, and the sensitivity to mixing method for the case of mixed-out flows. We explain how differences between the methods arise (through examination of the non-uniform static pressure field), consider the sensitivity of the results to exit Mach number, and discuss the physical interpretation of the various representations of a performance parameter. We use experimental data from a transonic annular engine-parts facility, acquired at very high spatial resolution in several axial planes, alongside complimentary CFD data.

HISTORY OF TOTAL PRESSURE PERFORMANCE PARAMETERS, AVERAGING AND MIXING METHODS

It is generally accepted that averaging of total temperature should be done using a mass flux-weighted average. For a perfect gas (i.e. $h_0 = c_p T_0$), this conserves total enthalpy flux between the measured non-uniform and equivalent (hypothetical) uniform flows, and is required in order to satisfy the first law of thermodynamics ([1], [2], [3]).

In contrast, there is neither complete consensus regarding the most appropriate performance parameter to represent total pressure loss, nor the best way to calculate an average of that parameter. Some of this divergence may arise from misunderstanding about best practice, while in other cases it could be argued that it is the result of reasonable compromises having been made (prioritising practicality over rigour).

Review of performance parameters

Arguably the two most commonly used total pressure performance parameters (see, for example, Denton [4]) are the total pressure loss coefficient, Y, and the KE loss coefficient, ζ. We define Y for a turbine NGV or stage as

$$Y = \frac{p_{01} - p_{02}}{p_{01} - p_2} \tag{1}$$

where p_{01}, p_{02} and p_2 are the row inlet total pressure, row exit total pressure and row exit static pressure respectively. The denominator is therefore the ideal row exit dynamic pressure. A weakness of this variable is that in a compressible flow, the denominator is not directly proportional to the exit kinetic energy ($p_0 - p \neq 0.5\rho v^2$). If the primary purpose of the nozzle is taken to be the conversion of potential (pressure) energy to outgoing angular momentum flux, the non-linearity of definition (1) at compressible Mach numbers makes this variable problematic. The KE loss coefficient does not suffer from this problem because it can be related to the energy conversion efficiency, η, at all Mach numbers. We define η as

$$\eta = \frac{\text{Actual exit KE}}{\text{Ideal exit KE}} = \frac{{v_2}^2}{{v_{2s}}^2} = \frac{h_{02} - h_2}{h_{01} - h_{2s}} \tag{2}$$

where v_2 and v_{2s} are the actual (measured) and isentropic exit velocities, respectively. For an adiabatic nozzle, $h_{02} = h_{01} = h_0$. The simplified expansion process is shown in the h-s chart in Figure 2.

Defining the corresponding KE loss coefficient as $\zeta = 1 - \eta$, and using the isentropic relation $T_2 / T_1 = (p_2 / p_1)^{\chi}$ where $\chi = (\gamma - 1) / \gamma$, the loss coefficient becomes

$$\zeta = 1 - \frac{1 - \frac{h_2}{h_0}}{1 - \frac{h_{2s}}{h_0}} = 1 - \frac{1 - \left(\frac{p_2}{p_{02}}\right)^{\chi}}{1 - \left(\frac{p_2}{p_{01}}\right)^{\chi}} \tag{3}$$

In this paper we primarily use ζ as the measure of NGV loss, and reference Y only to compare the sensitivities of the two

parameters. For completeness, we note here that in the incompressible case, where $p_{02} - p_2 = 0.5\rho v_2^2$, ζ and Y converge to the same numerical value.

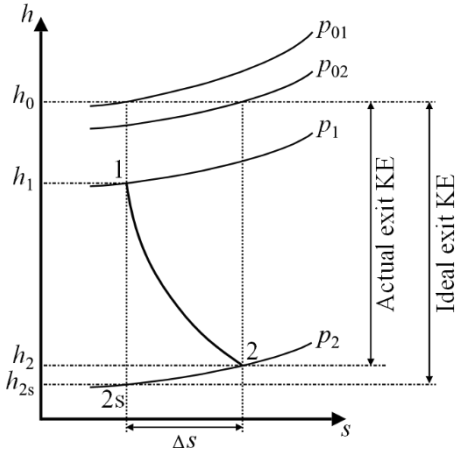


Figure 2: *h-s* chart showing the simplified turbine expansion process.

Review of averaging methods

Pianko and Wazelt [1] presented a comprehensive review of the methods in common use for averaging non-uniform internal flows in turbomachines. They concluded that it is not possible to replace a real, non-uniform flow with an equivalent uniform (i.e. averaged) flow matching all significant fluxes and parameters. The significant literature is in agreement on this point ([3], [5]).

Oates [2] discussed common methods for averaging non-uniform total pressure. For the simple case of two jets of different total pressure mixing adiabatically in a frictionless, constant-area duct, he showed that three different averaging methods produced average total pressure results with three different sensitivities to axial mixing distance: *mass-averaged* total pressure decreased with mixing distance (due to mixing out of secondary kinetic energy); *stream-thrust-averaged* total pressure (in which the flow is fully mixed to a uniform condition) was insensitive to mixing distance; and *continuity-averaged* total pressure (calculated from a measured duct area, mass flow rate, static pressure and total temperature by assuming the flow to be uniform over the whole area—sometimes employed in situations where the conditions of individual constituent flows are known, but direct traverse probe access to the mixed flow is not possible) increased with mixing distance.

Cumpsty and Horlock [3] propose that the "correct" method for averaging a non-uniform total pressure field is that which ensures that the properties of the averaged flow which are most relevant to a particular application are equal to their values in the actual, non-uniform flow at the same location (i.e. along the same line or in the same plane). In particular they discuss some common applications in turbomachinery flows: non-uniform flow entering a compressor or turbine (in which the work input or output is the important parameter); non-uniform flow entering a propelling nozzle (in which the gross thrust is the important parameter); and non-uniform flow entering a choked nozzle row (in which the flow capacity is the important parameter). They also note that, whilst there is no good physical basis for mass-averaging total pressure (flux-based averages such as the mass-flow-weighted average have no physical meaning when applied to intensive rather than extensive quantities), in many typical experimental situations the absolute variation in total pressure is sufficiently small that the difference between these methods is small.

Review of mixing methods

The most commonly used methods for calculating the fully mixed-out total pressure in a non-uniform field are: mixing to a uniform static pressure defined at a single swirl-averaged-radius (developed by Dzung [6]); uniform static pressure, proposed by Amecke [7]; and the free vortex method of Main et al. [8]. The history of these three methods is reviewed by Main et al. [8]. For the case of an annular NGV cascade, a maximum disagreement in the evaluated efficiency between the three methods of 0.12% was demonstrated, across a range of pressure ratio conditions and downstream traverse plane locations.

Prasad [9] conducts a similar analysis to Main et al. [8], but enforces a *forced vortex*—rather than *free vortex*—at the hypothetical mixed-out plane. The loss coefficient calculated in this manner is found to be insensitive to the location of the plane in which the non-uniform data are taken. There are advantages and drawbacks of both the mixed-out conditions (free or forced vortex). A forced vortex is the only possible swirling, annular flow that can be in complete kinematic (all elements of the strain rate tensor are zero) and thermal (flow supports no temperature gradients) equilibrium. However, the resulting mixed-out flow has a radial gradient of total pressure, $p_{02}(r)$, with higher total pressure at larger radii. This means it is not possible to define a reference isentropic forced-vortex condition (required to define a loss coefficient) when the inlet total pressure, p_{01}, is radially uniform. In contrast, a free vortex has a non-zero component of the strain rate tensor and hence is not entirely self-sustaining; but mixes the flow to a uniform total pressure, p_{02}. The free-vortex method therefore does not suffer from the issue of defining a reference isentropic condition.

DEFINITIONS FOR AVERAGING AND MIXING METHODS

In this section we define the calculation process for each of the possible performance metric representations in Figure 1. The KE loss coefficient is used in these examples.

Local loss parameters

The KE loss coefficient can be presented as a function of r and θ as follows

$$\zeta(r,\theta) = 1 - \frac{1 - \left(\frac{p_2(r,\theta)}{p_{02}(r,\theta)}\right)^{\chi}}{1 - \left(\frac{p_2(r,\theta)}{p_{01}}\right)^{\chi}} \qquad (4)$$

Where $p_2(r,\theta)$ and $p_{02}(r,\theta)$ are the static and total pressure distributions in the plane, and $\chi = (\gamma - 1) / \gamma$.

Line and plane-averaging methods

There are three principal steps in a line-averaging or plane-averaging process:

i) Calculation of area-average local static pressure. The average static pressure is defined from the net force acting on the reference area [3]

$$F = \int p\, dA = \overline{p}A \tag{5}$$

where $\overline{p}$ is the area-average static pressure. That area-averaging is the appropriate method for averaging static pressure is generally accepted, and is not debated in this paper. The plane-average of p_2, defined over a specific radial ($r_1 \le r \le r_2$) and circumferential ($\theta_1 \le \theta \le \theta_2$) range is

$$\overline{p_{2,\mathrm{A}}} = \frac{\int_{\theta_1}^{\theta_2}\int_{r_1}^{r_2} p_2(r,\theta) r \mathrm{d}r\mathrm{d}\theta}{\int_{\theta_1}^{\theta_2}\int_{r_1}^{r_2} r \mathrm{d}r\mathrm{d}\theta} \tag{6}$$

The corresponding line-averages (e.g. at constant r or θ) are calculated by integrating only in one dimension.

ii) Calculation of average local total pressure. Total pressure can be averaged using the chosen weighting method (methods 2a–d in Figure 1), by integrating the product of local total pressure and the local value of the weighting variable, and dividing by the integral of the weighting variable. For each of area-weighting, volume-flow-weighting, mass-flow-weighting, and entropy-flux-weighting, we get

$$\overline{p_{02,\mathrm{A}}} = \frac{\int_{\theta_1}^{\theta_2}\int_{r_1}^{r_2} p_{02}(r,\theta) r \mathrm{d}r\mathrm{d}\theta}{\int_{\theta_1}^{\theta_2}\int_{r_1}^{r_2} r \mathrm{d}r\mathrm{d}\theta} \tag{7}$$

$$\overline{p_{02,\mathrm{V}}} = \frac{\int_{\theta_1}^{\theta_2}\int_{r_1}^{r_2} p_{02}(r,\theta) v_x(r,\theta) r \mathrm{d}r\mathrm{d}\theta}{\int_{\theta_1}^{\theta_2}\int_{r_1}^{r_2} v_x(r,\theta) r \mathrm{d}r\mathrm{d}\theta} \tag{8}$$

where v_x is the magnitude of the velocity component normal to the integration plane

$$\overline{p_{02,\mathrm{M}}} = \frac{\int_{\theta_1}^{\theta_2}\int_{r_1}^{r_2} p_{02}(r,\theta) \rho(r,\theta) v_x(r,\theta) r \mathrm{d}r\mathrm{d}\theta}{\int_{\theta_1}^{\theta_2}\int_{r_1}^{r_2} \rho(r,\theta) v_x(r,\theta) r \mathrm{d}r\mathrm{d}\theta} \tag{9}$$

and

$$\frac{\overline{p_{02,\mathrm{S}}}}{p_{\mathrm{ref}}} = \exp\left\{\frac{\int_{\theta_1}^{\theta_2}\int_{r_1}^{r_2}\left[\ln\left(\frac{p_{02}(r,\theta)}{p_{\mathrm{ref}}}\right) - \frac{\gamma}{\gamma-1}\ln\left(\frac{T_{02}(r,\theta)}{\overline{T_{01}}}\right)\right]\mathrm{d}\dot{m}}{\int_{\theta_1}^{\theta_2}\int_{r_1}^{r_2}\mathrm{d}\dot{m}}\right\} \tag{10}$$

Where T_{01} and T_{02} are the mass-averaged inlet total temperature and the local distribution of total temperature in the measurement plane respectively, p_{ref} is an arbitrary non-zero reference pressure, and $\mathrm{d}\dot{m} = \rho(r,\theta)\, v_x(r,\theta)\, r\, \mathrm{d}r\, \mathrm{d}\theta$ represents a local element of mass flow rate (normal to the plane). The entropy-flux-weighted method is an alternative line-averaging or plane-averaging technique in which we choose to set the total entropy flux of the averaged flow to the same value as the measured (non-uniform) flow *at the same location* (e.g. in the same axial plane). The reason for this is because the change in entropy flux is the most direct measure of lost efficiency through the vane row. We note that this method is applicable only to local line or plane-averaging processes, and is not a mixed-out method (clearly entropy flux should not be conserved in a mixing process).

In the case of uniform total temperature ($T_{02} = T_{01} = T_0$), equation (10) simplifies to

$$\frac{\overline{p_{02,\mathrm{S}}}}{p_{\mathrm{ref}}} = \exp\left\{\frac{\int_{\theta_1}^{\theta_2}\int_{r_1}^{r_2}\ln\left(\frac{p_{02}(r,\theta)}{p_{\mathrm{ref}}}\right)\mathrm{d}\dot{m}}{\int_{\theta_1}^{\theta_2}\int_{r_1}^{r_2}\mathrm{d}\dot{m}}\right\} \tag{11}$$

That is, in the case of negligible total temperature variation, entropy-flux-weighted averaging is the same as mass-flow-averaging the natural logarithm of total pressure.

iii) Calculation of average value of the performance parameter based on area-averaged static pressure and weighted-average total pressure (whichever weighting method used). The average KE loss coefficient is expressed as

$$\overline{\zeta} = 1 - \frac{1 - \left(\dfrac{\overline{p_{2,\mathrm{A}}}}{\overline{p_{02}}}\right)^{\chi}}{1 - \left(\dfrac{\overline{p_{2,\mathrm{A}}}}{p_{01}}\right)^{\chi}} \tag{12}$$

Where $\overline{p_{02}}$ is the weighted average total pressure, calculated by any one of the four methods outlined above. A similar process is followed for the average total pressure loss coefficient $\overline{Y}$.

Mixed-out averaging methods

In mixed-out averaging methods, equations for conservation of mass, linear and angular momentum, and energy are solved between the non-uniform flow in the measurement plane, and a hypothetical fully mixed-out plane. To close the equations, it is necessary to specify the static pressure distribution in the mixed-out flow. The way this is specified is the primary difference between different methods. The mixed-out averaging processes can be thought of as effectively including the residual secondary kinetic energy (SKE) present in the measured non-uniform flow in the loss evaluation. The result is therefore less sensitive to the axial plane in which the data are measured. It could also be argued that the result is more relevant in situations where the SKE cannot be usefully recovered by the downstream machinery (as in most practical situations in compressors and turbines).

There are four mixed-out averaging methods in the literature:

1. Swirl-averaged mixing (method of Dzung, [6]; see also [10]). Average quantities of the mixed-out flow (including total and static pressures) are computed at a single, swirl-averaged radius (that is, a nominal radius at which swirl velocity has its average value). This method is recommended for linear cascade flows, but in annular swirling flows the implied mixed-out flow cannot satisfy radial equilibrium.
2. Two-dimensional mixing (method of Amecke [7]; see also [11]). The flow is conceptually split up into a series of thin, radial layers of 2D flow, which are individually mixed out without interaction with neighbouring layers. This gives a radial distribution of mixed-out flow parameters (including total and static pressures). The radial static pressure distribution would not necessarily satisfy a radial equilibrium condition due to the complete absence of radial

mixing. An overall loss coefficient is evaluated from single total and static pressures obtained by integrating the radial distributions (usually the area-integral of static pressure, and the mass-flow-integral of total pressure).

3. Free-vortex mixing (method of Main et al. [8]). The flow is mixed to a free-vortex condition; that is, the circumferential velocity component is constrained to be inversely proportional to radius. The mixed-out flow therefore has zero vorticity. The resultant mixed-out flow has uniform total pressure and a radial static pressure distribution which, unlike the other methods, does satisfy a radial equilibrium condition and is therefore closer to a physically realisable condition. This method has the drawback that in experiments it is problematic to include coolant flows in the definition of the ideal exit flow (for the purpose of defining a loss coefficient) unless the radial distribution of coolant input is known.
4. Forced-vortex mixing (method of Prasad [9]). The flow is mixed to a forced-vortex condition; that is, the circumferential velocity component is constrained to be linearly proportional to radius. The resultant mixed-out flow has non-zero vorticity and radial profiles of both static and total pressure (higher total pressure at higher radii). Unlike the free-vortex condition, this is a state of complete kinematic and thermal equilibrium (all shear stress components are zero). Like the free-vortex method, the inclusion of coolant flows in the loss coefficient definition is problematic.

Note on order of operations

In these calculations, it is the underlying physical variables (pressure, temperature, mass etc.) which are averaged. The performance parameter is then defined using those average quantities. The question could arise: should we instead calculate the local distribution of a performance parameter, e.g. $\zeta(r,\theta)$, then perform a weighted average of the parameter. Although in practice—despite non-linearity of the equations, e.g. (12)—the difference between the two process orders has minimal impact on the result, there is greater physical basis (control volume conservation arguments) for averaging the physical variables and this is therefore strongly preferred.

EXPERIMENTAL MEASUREMENT PROCESS

Experimental traverse measurements were performed in the Engine Component Aerothermal (ECAT) facility at the University of Oxford [12]. The ECAT facility is a high technology readiness level (TRL) short-duration (approximately 60 s run time), blowdown facility currently built as an annular cascade of NGVs. A simplified axisymmetric schematic diagram is shown in Figure 3. The NGVs are fully-cooled parts from a modern civil engine, operating at conditions (Mach number, Reynolds number, coolant-to-mainstream pressure ratio) non-dimensionally matched to the nominal engine operating point. The nominal operating conditions in ECAT tests are summarised in Table 1. The quoted Reynolds number is based on the vane tangential chord length and vane exit flow conditions. Inlet conditions of total pressure and temperature are measured at rakes located three axial chord lengths upstream of the cascade leading edge plane. A pressure regulator upstream of the working section maintains the inlet total pressure at steady-state for the duration of the test. Vane exit static pressure is measured at a large number (approximately 100) of surface tappings located on the vane exit platforms at hub and case. The ratio of vane exit-static to inlet-total pressures define the operating condition of the facility. Further details of these measurements and the associated uncertainties can be found in [13] and [14].

The vane cooling system includes approximately 10 rows of surface films and coolant ejection from a trailing edge slot. Coolant is fed from cavities at both hub and case (see Figure 3). The coolant feed mass flow rate is carefully controlled to achieve the target coolant-to-mainstream pressure ratio. The ECAT facility has previously been used to perform high-accuracy measurements of vane capacity ([13], [14], [15]), aerodynamic loss and metal effectiveness [12].

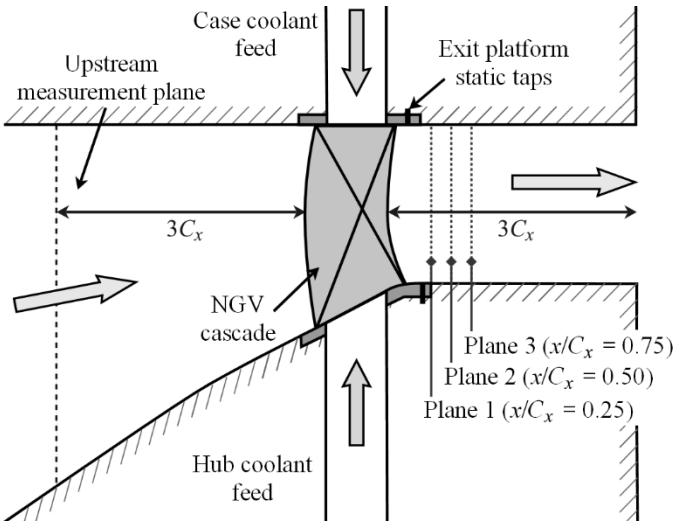


Figure 3: Simplified diagram of an axisymmetric cross-section through the ECAT facility working section.

Traverse measurements were made downstream of the NGV cascade using an automated radial-circumferential traverse mechanism. Measurements were performed in three axial planes located 0.25, 0.50 and 0.75 axial chord lengths downstream of the cascade trailing edge plane. These axial planes are indicated in Figure 4. Traverse measurements covered a circumferential range of 2.5 vane pitches. The traverse system was clocked in the circumferential direction between the axial planes so that wakes from the same vanes were measured at each axial position. A schematic is shown in Figure 4. The radial traverse range was approximately 95% of vane span. In this range approximately 60 discrete circumferential passes of the traverse probe were performed at fixed radius. The average radial step height was approximately 1.4 mm. A typical complete area-survey traverse path is shown in Figure 5. The complete path was made up of six separate experiments, represented by blocks in the figure. Adjacent blocks overlapped by at least one probe-pass to ensure consistency. Dashed black lines show the approximate locations of vane wakes.

The traverse probe used in this study was a five-hole pneumatic pressure probe with tip diameter 2.8 mm. The probe was calibrated over a range of flow Mach number $0.3 \leq M \leq 1.4$, and a range of incident flow angles (in two axes) of ±40°. The traverse speed was set based on the estimated dynamic response of the probe-transducer system, such that the effective

circumferential resolution was equivalent to half of the probe tip diameter (1.4 mm). This, in combination with the traverse pattern, given an effective resolution of approximately 1.4 mm in both the radial and circumferential directions.

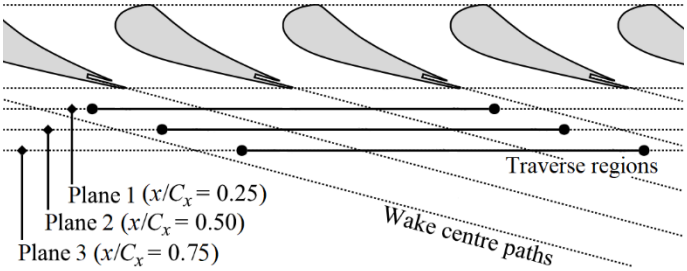


Figure 4: Locations of the three experimental axial traverse planes.

Table 1: Summary of nominal experimental test conditions.

Variable	Nominal value
Inlet total pressure, p_{01}	2.00 bar
Inlet total temperature, T_{01}	290 K
Exit static pressure, p_2	1.10 bar
Mass flow rate, $\dot{m}$	14.0 kg s^{-1}
Inlet turbulence intensity, Tu	~8%
Coolant-to-mainstream pressure ratio, p_{0c} / p_{01}	1.025
Vane pressure ratio, p_2 / p_{01}	0.550
Vane exit Mach number, M_2	0.965
Reynolds number, Re	1.3x10^6

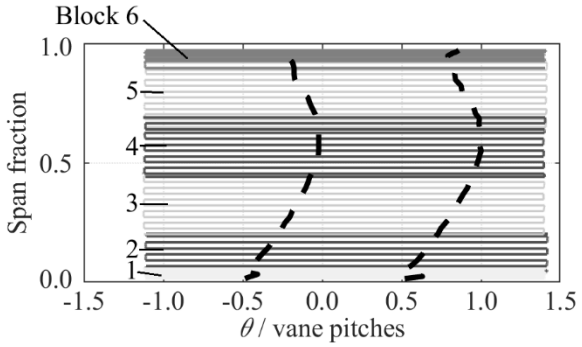


Figure 5: Example traverse blocking arrangement for a single area-survey. Six separate tests are represented by the six blocks. Dashed lines show the wake locations.

NUMERICAL METHOD

3D Reynolds-Averaged Navier-Stokes (RANS) CFD simulations were performed using the commercial solver ANSYS CFX. The SST k-ω model was employed for turbulence closure. The simulated geometry was an annular sector containing two vane pitches with rotational periodicity. The geometry is shown in Figure 6a. The vane geometries were taken from the design intent CAD drawing of the component tested in experiments, defeatured to remove film cooling holes from the vane surfaces. The domain was discretised with an Octree-based mesh using BoxerMesh. A cross-section through the mesh at midspan is shown in Figure 6b. The mesh was refined close to the vane surfaces, in the vicinity of the trailing edges, and in the paths of the wakes downstream of the cascade. The final mesh size was approximately 57 million cells.

Boundary conditions were set to match the operating conditions achieved in experiments (Table 1). Uniform total pressure and temperature were imposed at the inlet plane. An average static pressure was set at the exit boundary, with a radial equilibrium condition to be satisfied in determining the exit static pressure distribution. Static pressures were evaluated at the locations of the experimental pressure tappings on the hub and case vane exit platforms, and an iterative process (tuning the exit boundary average static pressure) was used to match the exit-static-to-inlet-total pressure ratio to the experimental value.

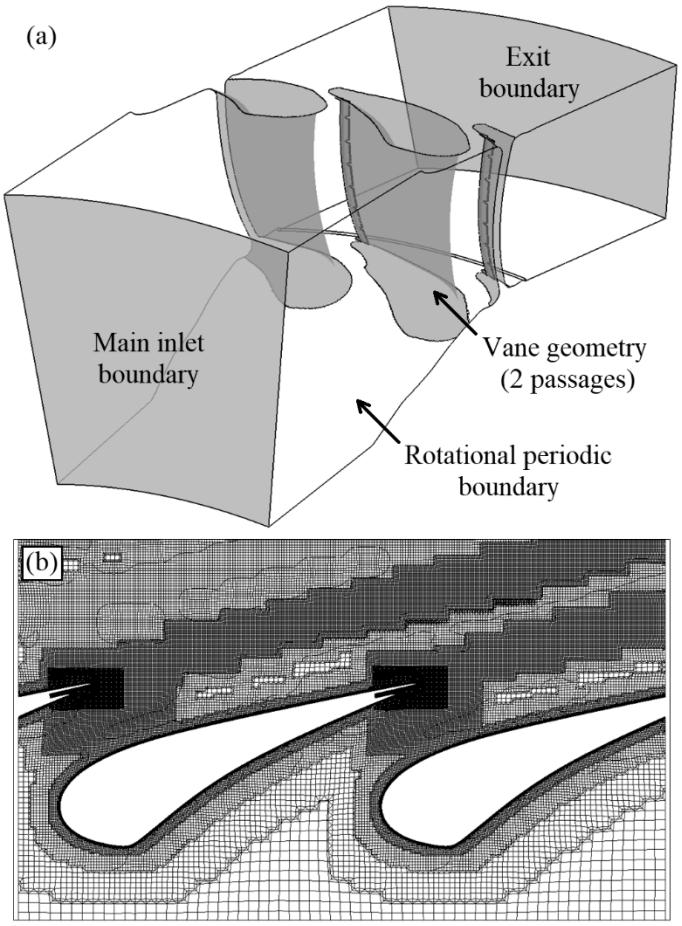


Figure 6: (a) CFD geometry; (b) Midspan mesh cross section.

Film cooling flows were modelled using the *source term* method. A coolant mass flow rate (specified as a fraction of the mainstream mass flow rate) was applied at each film exit location. Details of the model for calculating mass flow rates for individual films can be found in [15]. The trailing edge coolant flow was set at an inlet boundary some distance (approximately eight slot widths) inside the trailing edge slot (to ensure proper flow development before issuing into the mainstream). A mass flow boundary condition was used. Further details of the trailing edge slot modelling can be found in [15].

COMPARISON OF AVERAGING METHODS

In this section, we compare the results of the various averaging methods using both experimental and numerical data. We first introduce the non-uniform experimental and CFD flow fields. Figure 7 shows local distributions of KE loss coefficient, ζ,

(equation (4)) in three different axial planes, from experimental and numerical data respectively.

Most importantly for our purpose, we have high spatial resolution in the experimental measurements, and similar general trends between CFD and experiment with well resolved wakes and secondary flow features. The under-predicted mixing rates in CFD simulations are a well-known problem and this is reflected in higher values of ζ in the wakes with respect to experiment (at a particular axial plane), and narrower wake profiles. The absolute KE (or total pressure) deficit associated with film cooling is also over-estimated by the source terms model. Improved agreement with experiment would likely be achieved by fully resolving the geometry of all film cooling holes in the CFD model.

The radial pressure gradient, a characteristic feature of annular cascade flows, promotes migration of low momentum flow towards the hub and away from the case. This generates intense secondary loss cores in the wake near the hub—also exacerbated by higher Mach numbers in this region—and lower intensity of secondary flows near the case. The radial profile of total pressure loss in the wake centre over the vane span is also relatively well matched. The wake loss profile is broken up into a number of distinct sections separated by local minima in between. This effect is the result of internal cooling features within the trailing edge coolant slot. The wake regions decay in depth and broaden in width between the axial planes. The non-uniformity in the radial direction also gradually decays.

Although we describe the flow features for reference in later analysis, our primary purpose here is not good agreement between CFD and experiment, but rather a comprehensive data-set that shows typical differences between such results.

Plane-average weighting functions

We now compare area-weighted, volume-flow-weighted, and mass-flow-weighted methods for plane-averaging total pressure. The weighting functions are the multipliers for total pressure in the numerators of equations (7), (8), and (9). We do not treat the entropy-flux-average separately because in the isothermal simplification (equation (11)) the method reduces to weighting the natural logarithm of total pressure using the mass-flow-weighting function. The weighting functions for the axial plane 1 are shown in Figure 8, for both experimental data and CFD, normalised with respect to the maximum value in each case. Horizontal dashed lines indicate the radial limits used for the evaluation of the *profile* KE loss coefficient. We now consider the weighting functions in turn. To most clearly demonstrate the trends, the underlying (high-resolution) data are re-sampled onto a uniform grid in r and θ. The results presented are independent of this processing step, and raw data following the traverse pattern of Figure 5 could equally be used (with associated radial distortions in the weighting functions).

The area-weighting functions (frames (a) in Figure 8), have—trivially—a gradient in the radial direction on account of the uniform grid of data in r and θ.

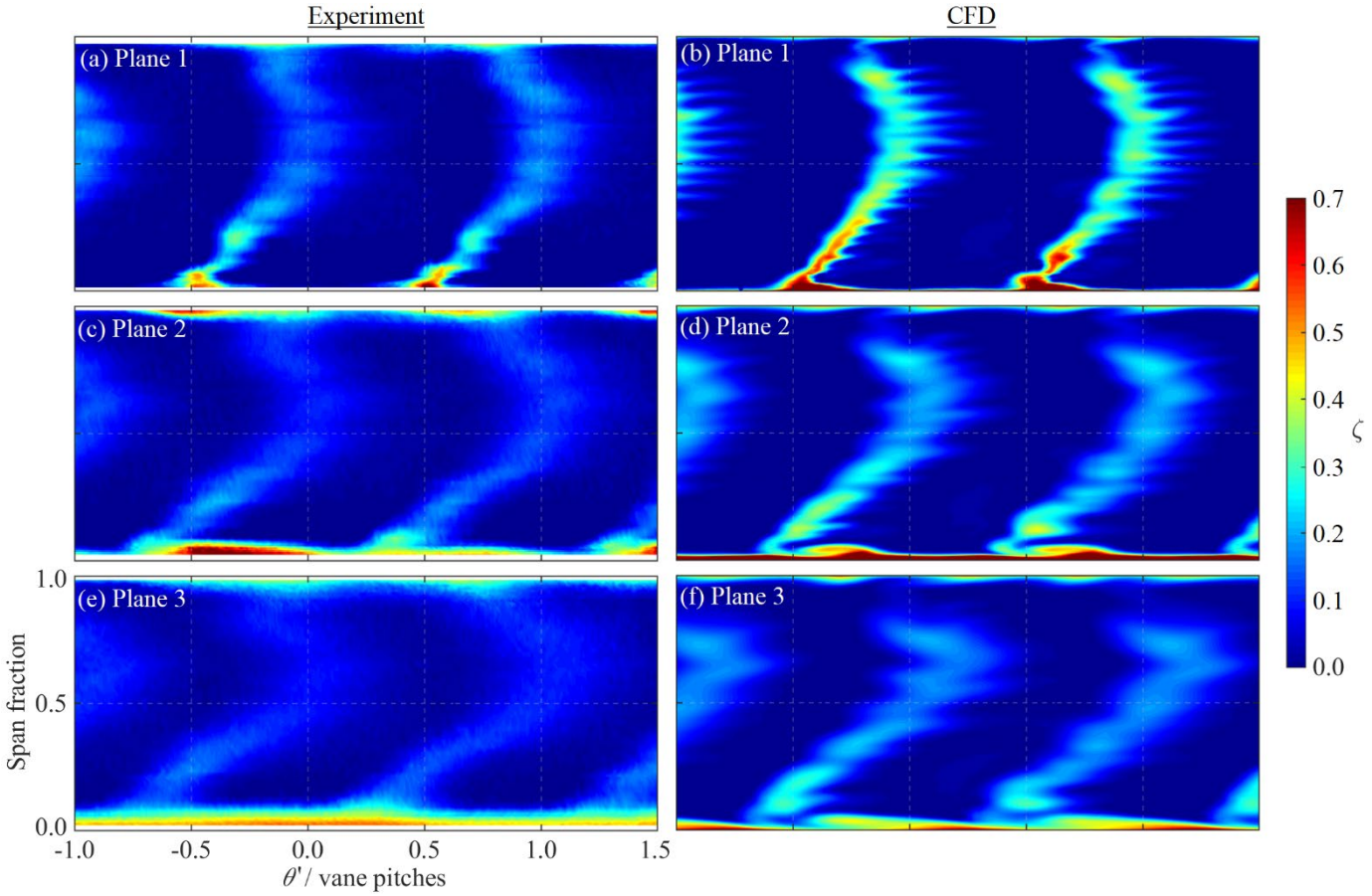


Figure 7: Experimentally-measured and CFD-predicted local distributions of kinetic energy loss coefficient, ζ, in the axial planes: (a) $x/C_x = 0.25$, (b) $x/C_x = 0.50$, (c) $x/C_x = 0.75$.

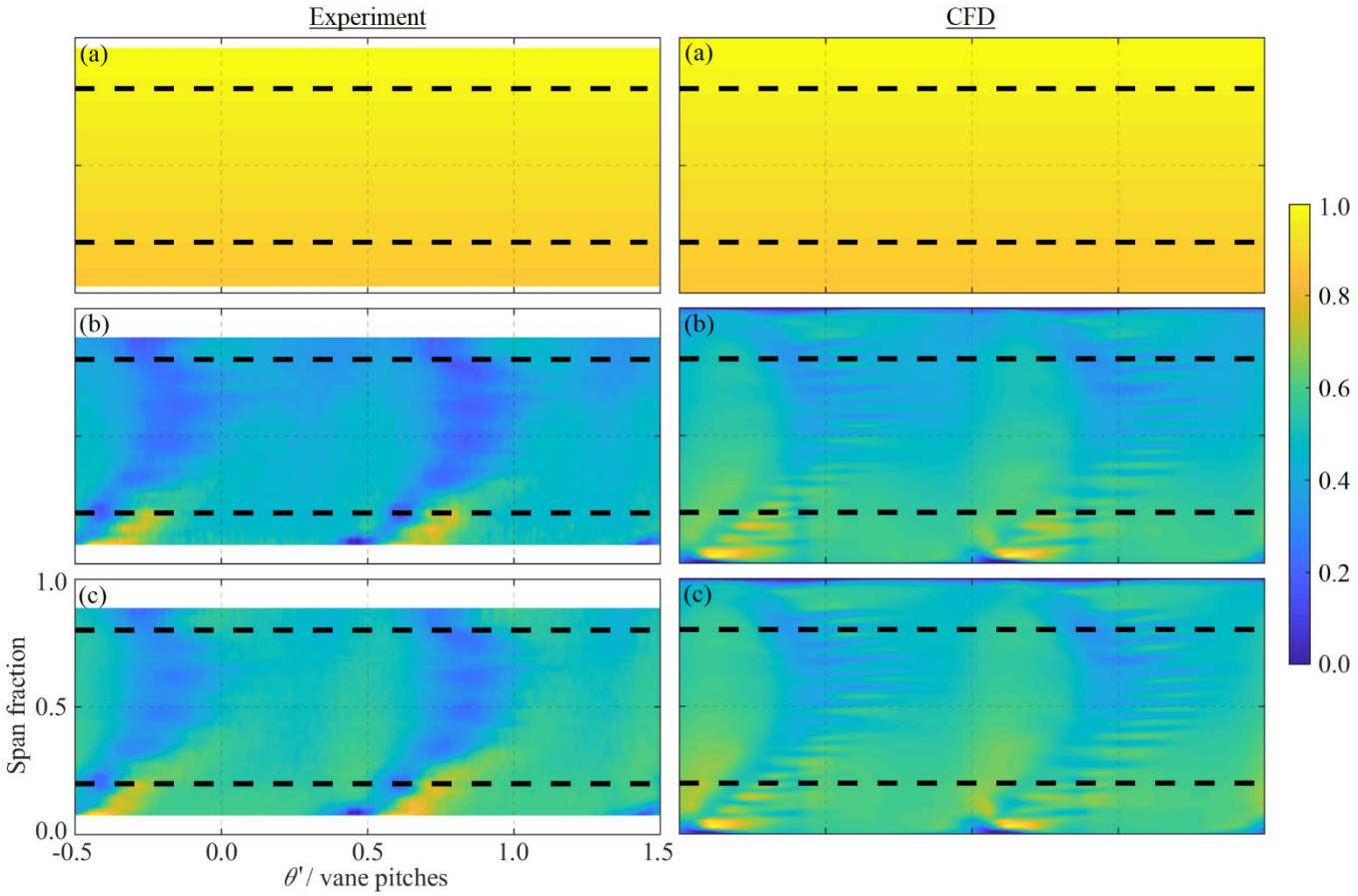


Figure 8: Experimental and CFD weighting functions in axial plane 1 for: (a) area-weighting, (b) volume-flow-weighting, (c) mass-flow-weighting

The volume-flow-weighting functions (frames (b) in Figure 8) have comparatively low weighting in the wake and film-mixing regions, associated with the low momentum in these areas. A strong radial pressure gradient from case to hub leads to slightly higher weighting at lower radii. The same effect can be seen with the cross-passage pressure gradient, with highest weighting near the vane SS, and lowest near the PS.

The mass-flow-weighting functions (frames (c) in Figure 8) are very similar to the volume-flow-weighting functions, but with small deviations associated with density variation.

To compare the weighting functions quantitatively, the values at midspan in planes 1, 2, and 3 are plotted as line-functions in Figure 9. The approximate locations of the wake centres are marked with dashed lines. Each trend is normalised with respect to its own maximum value. In all cases the area-weighting functions are constant at unity.

We now compare the volume flow and mass-flow-weighting functions. There is only a very slight difference moving between volume-flow-weighting and mass-flow-weighting, which results in biasing the average further in favour of the free stream regions (e.g. $0.4 \leq \theta \leq 0.6$) and against the wake regions (e.g. $-0.3 \leq \theta \leq 0.1$).

The general shape of the trends is very similar between CFD and experiment, but with significantly larger variation (from unity) for the experimental data compared to CFD. In the wake regions the experimental weighting functions have much deeper troughs than those for CFD (minimum values of normalised mass flow-weighting differ between experiment and CFD by 36.9%, 15.0% and 16.2% in planes 1, 2 and 3 respectively), and the troughs are shifted towards the SS. This is surprising: given the more mixed-out local loss distributions observed in the experimental data compared to CFD in the equivalent plane (Figure 7), we might have expected the opposite to be true. The differences can be explained by differences in exit whirl angle profiles, and total and static pressure fields between experiment and CFD. A comparison of whirl angle distributions at midspan between experiment and CFD is shown in Figure 10, whilst static and total pressure fields are presented in Figure 11.

Consider first the midspan whirl angle distributions in Figure 10, where whirl angle, β, is defined as the angle between the local velocity vector and the axial direction, in the axial-circumferential plane. The profiles differ significantly between the three planes, becoming generally more mixed out with successive movements downstream. At a particular plane, the variation in angle in the experimental data is greater than the CFD predictions. For example, in plane 1, β varies circumferentially by 8.8° in the experiment, and by only 2.9° in CFD. The under-prediction of whirl angle to the SS of the wake by CFD is thought to arise due to an exaggerated shock-boundary layer interaction, which causes the SS boundary layer to separate upstream of the trailing edge.

The larger whirl angle variation in the experimental data leads to greater circumferential variation in the axial velocity component, and therefore greater variation in the local volume flow rate and mass flow rate normal to the axial plane. This

explains the deeper troughs in the normalised experimental weighting functions—see Figure 9—which align with peaks (and associated lower local axial velocity) in the whirl angle distributions of Figure 10.

To understand the difference in whirl angle distribution between the three planes, we now consider the total and static pressure fields in the exit flow. CFD-predicted midspan profiles of total and static pressure are presented in Figures 11a and b respectively. Planes 1, 2 and 3 are marked in the figures by dashed black lines.

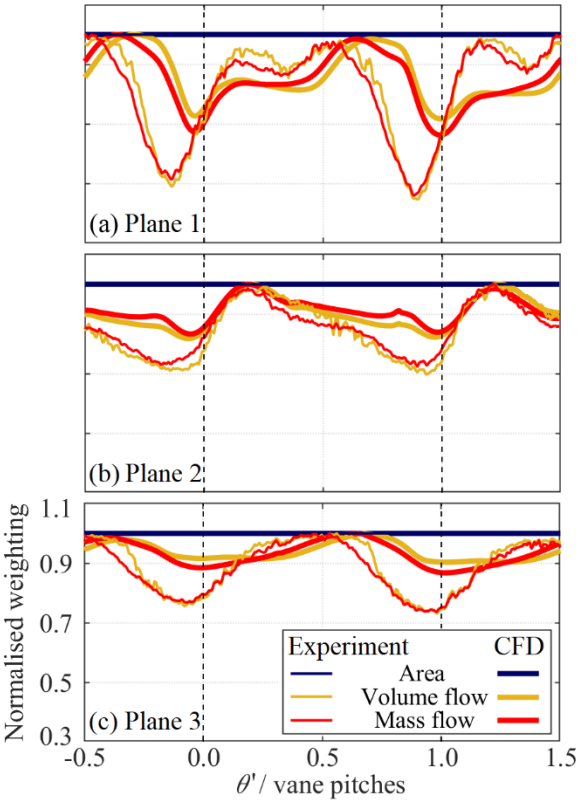


Figure 9: Normalised midspan weighting functions for each of the three in-plane averaging methods for experimental and CFD data at planes 1, 2 and 3. Dashed lines show approximate wake centre locations in each plane.

Looking first at the total pressure field (Figure 11a), there are characteristic wakes which broaden in width and reduce in depth with distance in the streamwise direction. Even at plane 3, the wakes remain well-defined.

The static pressure (Figure 11b) reduces through the covered part of the vane passage as the flow is accelerated. In the downstream flow between planes 1 and 3 (in the axial direction) the static pressure is relatively uniform over most of the domain, but with a significantly elevated region of pressure directly axially downstream of each trailing edge.

There are two interesting consequences of the interaction of the total and static pressure fields, which we now examine.

Firstly, we consider the development with axial distance of the whirl angle profiles shown in Figure 10. In Figure 12c we plot the normalised static pressure along the wake centreline (red line)—i.e. following one of the dashed white lines in Figure 11b—and in the centre of the free-stream region (blue line). The trends are periodic and approximately in anti-phase with each other. This effect arises because of the periodic intersection of the wake centrelines (and the free-stream centrelines) with the elevated static pressure regions extending axially downstream of each TE. Analysis of the entire flow-field is complicated by the fact that the flow is transonic, but in the region between planes 1–3, the flow is almost entirely high-subsonic (predominantly in the range $0.75 < M < 1.00$, but with a small region up to $M = 1.05$ at plane 1).

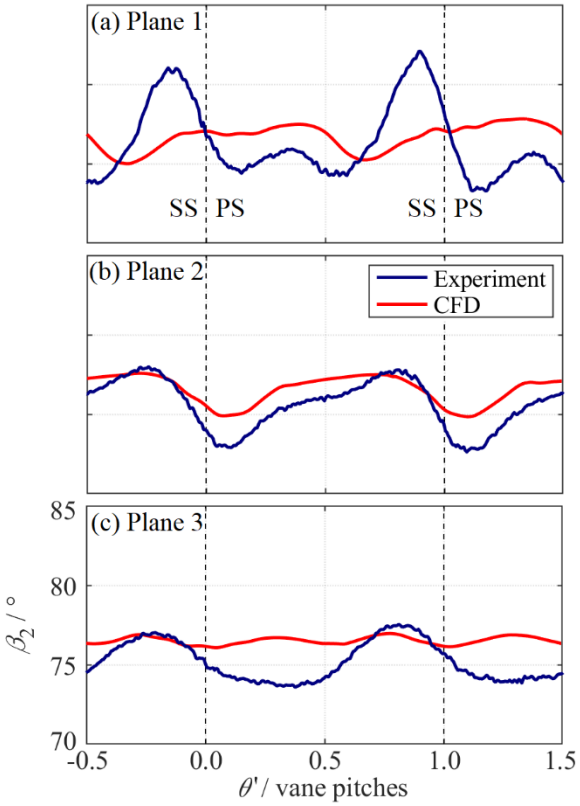


Figure 10: Circumferential distributions of whirl angle at midspan for experiment and CFD in planes 1,2 and 3. Dashed lines show approximate wake centre locations in each plane.

In subsonic flow, as streamlines enter the elevated pressure region (which extends in the downstream direction, almost perpendicular to the streamlines) they are diffused, and turned towards the axial. As streamlines leave the high-pressure region they are accelerated and turned away from the axial, towards higher whirl angle. The alignment between the wakes and the high pressure region differs between the three axial planes. In planes 1 and 3, streamlines approximately in the centre of the free-stream region pass through the high-pressure region and are thus turned towards the axial. In plane 2, streamlines approximately in the centre of the wake region pass through the high-pressure region. Therefore between planes 1 and 2, the effect is manifest as a relative *increase* in whirl angle in the free-stream regions, and a relative *decrease* in whirl angle in the wake regions (compare Figure 10a and b), and vice-versa between planes 2 and 3. This effect, in combination with the gradual mixing out of circumferential non-uniformity, accounts for the complex development with axial distance of the whirl angle distributions in Figure 10.

These distributions are important because they significantly impact the weighting functions for different

averaging methods. They also explain the apparently contradictory result that the experiment has greater variation in weighting functions across the plane than CFD (Figure 9). Whilst CFD is under-mixed with respect to the experiment, and therefore has narrower and deeper wakes, the more extreme variation in axial velocity in experiment—caused by greater whirl angle variation—is the dominant factor in determining the weighting function distributions.

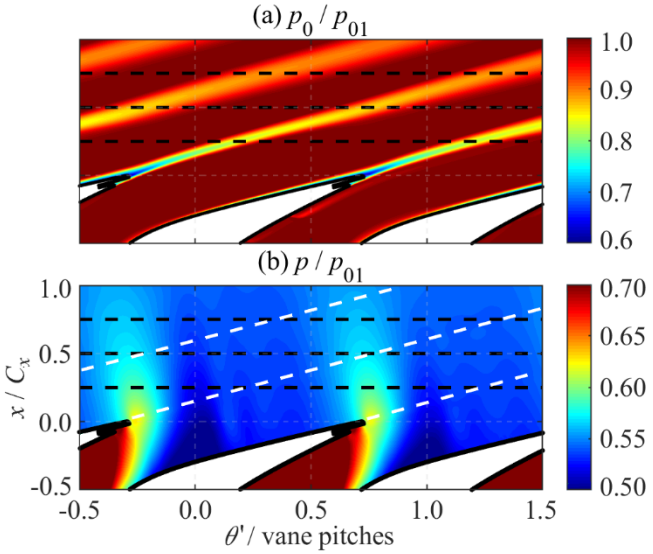


Figure 11: CFD-predicted midspan contours of: (a) normalised total pressure; and (b) normalised static pressure.

The second interesting effect is that the streamwise pressure gradient, which causes diffusion and acceleration of the wakes (red line in Figure 12c), significantly influences the decay process of the wake profiles. This in turn affects the sensitivities of different weighting methods to axial plane. We characterise the wakes in terms of the maximum value of ζ, which we refer to as $\hat{\zeta}$, and the width of the wake (over which ζ exceeds half of $\hat{\zeta}$), which we refer to as w. These two parameters are plotted in Figures 12a and b respectively, extracted from both experimental and CFD data at midspan.

Peak loss (Figure 12a) follows a quasi-exponential decay in both experiment and CFD. An offset between the two data arises from the familiar under-prediction of mixing by CFD, leading to higher peak loss along the wake centreline.

Axial trends in the wake width, w (Figure 12b), show a highly variable rate of increase. There is a reasonable correlation between regions of streamwise acceleration identified in Figure 12c ($0.00 < x/C_x < 0.15$, $0.45 < x/C_x < 0.60$, $0.95 < x/C_x < 1.00$) and regions of essentially constant w. That is, acceleration due to the local streamwise pressure gradient thins the wake (disproportional influence on low-momentum fluid) but the effect is in competition with mixing processes which always act to thicken the wake. The corollary is that diffusion acts to thicken the wake, and in regions where dp/dz is positive (where z is streamwise distance), there is significant growth in w. In these regions the effects of diffusion and mixing are additive. A sympathetic impact on the gradient of peak loss might be expected (increase in decay rate where the wake is accelerated, and vice-versa), but is hard to discern in the quasi-exponential decay. These results are in accord with [16], a study of wake flows exposed to different streamwise pressure gradients.

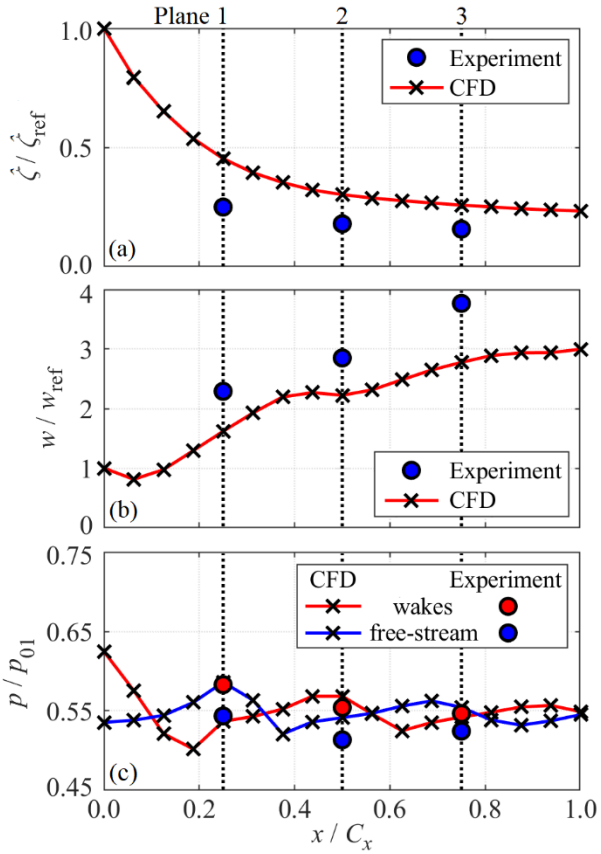


Figure 12: Axial trends at midspan of: (a) peak value of ζ in the wake centre; (b) wake width; and (c) static pressure along the wake centreline and in the free-stream.

Sensitivity to radial averaging range

To characterise the profile loss, it is necessary to understand the sensitivity to radial averaging range. Mass-flow-weighted ζ is plotted in Figure 13 as a function of the radial averaging range (expressed as a percentage of vane span, centred on midspan) for both experiment and CFD, and in three axial planes.

For radial averaging ranges between 2–10% of span, the returned value of $\overline{\zeta}$ is sensitive to localised spanwise non-uniformities caused by, for example, individual cooling flows or TE slot features. For radial averaging ranges between 10% and approximately 80% of span, the value of $\overline{\zeta}$ is insensitive to local variation, but slowly varying due to non-linear radial variation in loss coefficient. Near the upper end of this range—say, around 60% of span—may be taken as a sensible radial range for characterising profile loss. For radial averaging ranges between 80–100% of span, the endwall loss becomes more significant, resulting in significant increases in $\overline{\zeta}$. The depth and breadth of the endwall boundary layers increases with increasing x/C_x. In evaluating $\overline{\zeta}$ for the entire plane (both profile and endwall losses), it is possible to crudely infer the sensitivity to the closeness of approach to the wall (for experimental data) from the near-wall gradient of the trends in Figure 13.

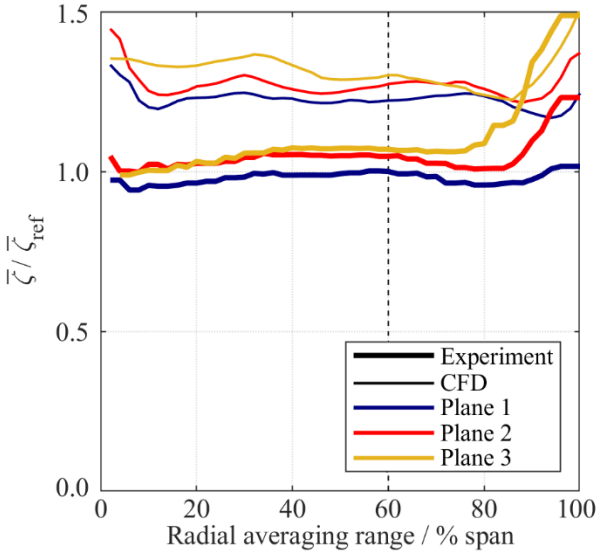


Figure 13: Mass-flow-weighted average ζ as a function of radial averaging range for experiment and CFD, in three axial planes.

Comparison of plane-average and mixed-out methods

Plane-average and mixed-out-average results for KE loss coefficient, ζ, are presented for each of the methods discussed, using data from a series of 2D axial planes. The relationships between the trends for total pressure loss coefficient, Y, are almost identical to those for ζ—though they differ in absolute level—and are not presented.

Average values of ζ are presented in Figure 14 as functions of axial location for CFD (16 evenly spaced planes in the range $0 \le x/C_x \le 1$) and experiment (traverse planes 1–3 at $x/C_x = 0.25$, 0.50 and 0.75, respectively). We first compare the trends between experiment and CFD, and conclude the following:

i) There is generally good agreement between the experimental and CFD data, both in terms of absolute level (average difference of +10.0% across all data) and in terms of trends, where the experimental data are in good accord with low-resolution sampling of the corresponding numerical trends. The relative ranking of the in-plane averaging methods (area-average, volume-flow-average, mass-flow-average and entropy-flux-average) between experiment and CFD in each of planes 1 to 3 is similar. In both the experimental and CFD data, the area-average is notably higher than the other three in-plane methods in plane 1, but in closer agreement in planes 2 and 3.

ii) The differences in absolute loss between experiment and CFD can generally be attributed to a combination of: the CFD being under-mixed; CFD over-predicting the loss associated with surface film cooling; CFD incorrectly predicting the complex TE shock structure and hence the losses associated with shock-boundary layer interaction on the vane suction surface; and inadequate turbulence modelling in the CFD. The differences in the deltas between different averaging methods between experiment and CFD can generally be attributed to the under-prediction of mixing by the CFD. For example, the differences between area-averaged and mass flow-averaged $\overline{\zeta}$ in plane 1 were 10.2% and 18.2% in experiment and CFD respectively, being smaller in the experimental case because the flow is more fully mixed out in the equivalent axial plane, with less remaining non-uniformity in the wake profile.

iii) The average discrepancy in the value of mixed-out KE loss coefficient, $\overline{\zeta}$, between CFD and experiment (4.3%) is significantly smaller than that in mass-flow-weighted plane-averaged $\overline{\zeta}$ (11.7%), when averaged across all data. On the basis that the CFD is under-mixed with respect to the experiment, this result is initially surprising: one would expect the SKE conversion to loss (difference between in-plane and mixed-out calculations) to be greater for the CFD than the experiment. A possible explanation is provided by Figure 10, in which we see that the whirl angle variation in the experimental data is great than the CFD data. This provides the experimental data with an additional mechanism for loss generation with axial distance, and may be part of the explanation for this apparently surprising result. Because the agreement is better for mixed-out coefficients, where absolute comparisons are to be made between experiment and CFD, and where inaccurate prediction of mixing rate is expected (most methods), mixed-out comparisons should be used.

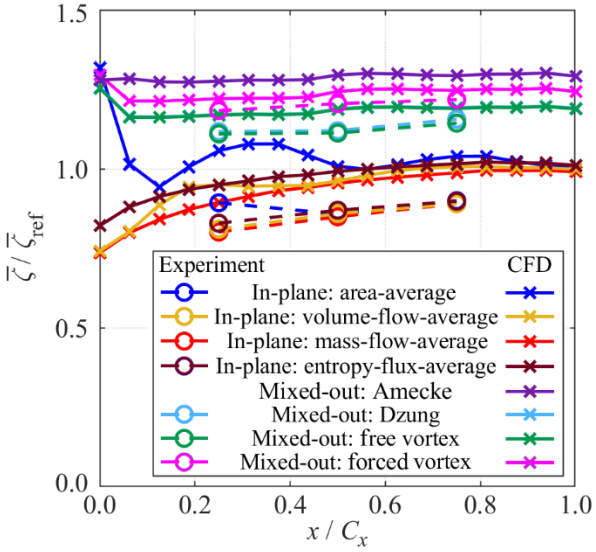


Figure 14: Axial trends in $\overline{\zeta}$ based on average total pressure according to a number of methods, for experimentally measured and CFD-predicted flows.

Comparing the different averaging methods, we draw the following key conclusions:

i) Trends of in-plane KE loss coefficient, $\overline{\zeta}$, based on volume-flow-averaged, mass-flow-averaged and entropy-flux-averaged total pressure are for the most part relatively similar to each other: well-behaved, and slowly and monotonically increasing with x/C_x due to the gradual conversion of SKE to total pressure loss. The average (across volume-flow-weighted, mass-flow-weighted and entropy-flux-weighted trends) change in $\overline{\zeta}$ between $x/C_x = 0.00$ and $x/C_x = 1.00$ was +23.4% of the latter value. This sensitivity should be considered when choosing an axial traverse plane for flow-averaging or comparing between systems. All of the in-plane methods (including area-weighted average) appear to reach a stable value by $x/C_x = 1.00$, and are in agreement in terms

of absolute value (to within 2.0%). The absolute convergence of $\overline{\zeta}$ based on the four in-plane total pressure weighting methods is expected, because the variations in the underlying flow-field which give rise to the differences between the weighting functions for the different methods decay rapidly with axial distance (see Figure 9 and associated analysis).

ii) The in-plane KE loss coefficient, $\overline{\zeta}$, based on area-averaged total pressure is *highly* sensitive to axial plane, departing from the other in-plane methods by up to +72.2% (at $x/C_x = 0.00$) and varying across the range $0.00 < x/C_x < 1.00$ by between −5.7% and +31.9% of the settled value (at $x/C_x = 1.00$). There are numerous problems with the accounting in this method. For example, the significant over-weighting of low-momentum wake regions with respect to other methods (which produces the large peak at $x/C_x = 0.00$ where the wake is deepest) and the strong sensitivity to local fluctuations in the wake characteristics (Figure 12). The simplicity of area-weighted averaging is attractive, but very high sensitivity to axial plane makes it an extremely poor choice for comparisons between CFD and experiment, or between different experiments. In the range $0.00 \le x/C_x \le 0.50$, the method should be regarded as unacceptably sensitive to axial location.

iii) Volume-flow-weighted averaging of total pressure is more sensitive to axial plane than the mass-flow-average and entropy-flux-average methods, but much less sensitive than the area-average method. The maximum deviation of the volume-flow-average $\overline{\zeta}$ from the mass-flow-average $\overline{\zeta}$ was +8.2%, at $x/C_x = 0.19$. Volume-flow-averaging total pressure therefore offers a compromise between achieving a relatively low sensitivity to axial location and practical measurement requirements (does not require measurement of local density variation which may be problematic in some experimental environments).

iv) The Dzung and free-vortex mixed-out methods give essentially indistinguishable results for both experimental and CFD data, in accord with the results of Main et al. [8]. The forced-vortex method gives a consistently higher loss with respect to all of the other methods, by an average of +5.8% across all of the data. This difference is attributed to the additional entropy generation associated with producing the required linear radial total pressure distribution. The Amecke method gives the highest loss coefficient of all of the mixed-out methods: and average of +8.8% greater than the Dzung method. The cause of this higher loss is not fully understood.

v) All of the mixed-out methods reference a numerically mixed-out flow so—as expected—there is relatively little sensitivity to axial plane. Between planes 1 and 3 ($0.25 \le x/C_x \le 0.75$) the average increases in mixed-out $\overline{\zeta}$ in CFD and experimental data were +1.8% and +3.1% respectively. Looking more closely at the CFD trend, we see that 85% of the rise in $\overline{\zeta}$ occurs within the range $0.44 < x/C_x < 0.56$, whilst all of the rise in experiment occurs downstream of plane 2. That is, the wakes passing through an adverse streamwise pressure gradient—i.e. positive dp/dz, where z is streamwise distance (see Figure 12c)—causes an increase even in the KE loss evaluated from the mixed-out methods. An adverse pressure gradient increases the velocity gradients in the free shear layers at the wake edges (see discussion related to Figure 12), and so increases the entropy generation associated with mixing out of the wake profile (rate of entropy generation is proportional to dv/dy, where y is streamwise-normal distance). Conversely, a favourable streamwise pressure gradient (negative dp/dz, where z is streamwise distance) causes a slight reduction in the mixed-out loss. These effects are very small at the operating conditions used in these tests.

Effect of Mach number

In this section we use CFD to consider the impact of vane exit Mach number, M_2, on the applicability of the general conclusions drawn above. We consider five distinct M_2 conditions in the range $0.63 \le M_2 \le 1.11$, including the target Mach number ($M_2 = 0.97$). Absolute values of plane-averaged and mixed-out $\overline{\zeta}$ computed from data at $x/C_x = 1.00$ are plotted as functions of M_2 in Figure 15. The data are normalised with respect to the mean of the four plane-average methods at $M_2 = 0.97$.

We established previously that at the nominal value $M_2 = 0.97$, the difference between the four plane-average methods was very small at $x/C_x = 1.00$. Figure 15 shows that this result is robust across a wide range of M_2. In terms of absolute level, all of the mixed-out methods give higher loss coefficient than the in-plane methods. This is due to the mixing out of SKE in the mixed-out methods. The Dzung and free-vortex methods agree almost exactly. The absolute levels of all trends of $\overline{\zeta}$ fall approximately linearly with M_2 in the range $0.63 \le M_2 \le 0.97$. We note that this trend is specific to average KE loss coefficient, $\overline{\zeta}$. The equivalent trends (with Mach number) for other performance parameters, e.g. average total pressure loss coefficient, will be different due to their different Mach number sensitivity.

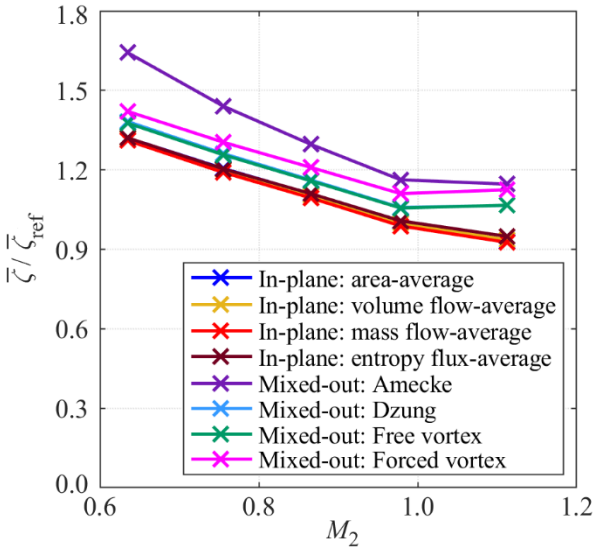


Figure 15: CFD-predicted plane-average and mixed-out KE loss coefficient, $\overline{\zeta}$, at $x/C_x = 1.00$, as functions of vane exit Mach number.

In the range $0.97 \le M_2 \le 1.11$, plane-average $\overline{\zeta}$ still falls with M_2, but at a slightly lower rate than at lower M_2. In contrast, mixed-

out $\overline{\zeta}$ *increases* slightly with increasing M_2. This suggests a rise in mixing loss at higher M_2. The additional loss is attributed to the presence of a SS trailing edge shock at $M_2 = 1.11$. There is a small amount of 'direct' loss across the shock (total pressure immediately downstream of the shock is slightly lower than that immediately upstream)—this is the cause of the very slight shallowing of the gradient of the in-plane trends in Figure 15. In poorly-resolved CFD there is smearing-out of the shock, producing an adverse static pressure gradient, which is capable of increasing mixing loss by increasing the rate of shear in regions of velocity gradient. This is a possible cause of the rise in mixed-out KE loss coefficient between $0.97 \leq M_2 \leq 1.11$ in Figure 15.

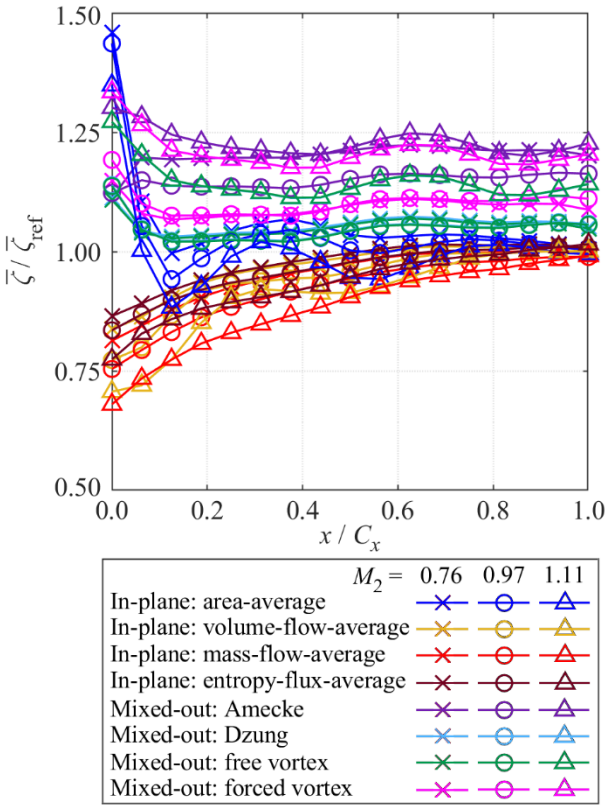


Figure 16: Variation of $\overline{\zeta}$ with axial distance for three exit Mach numbers: $M_2 = 0.76$, 0.97 and 1.11.

We now consider the impact of Mach number on the variation of $\overline{\zeta}$ with axial distance. To do this we normalise the trends (of the type presented in Figure 14) by the average value of the four in-plane methods at $x/C_x = 1.00$. The resulting trends with axial distance are shown in Figure 16, for the design Mach number ($M_2 = 0.97$; data of Figure 14) and also for $M_2 = 0.76$ and $M_2 = 1.11$. The primary conclusion is that, for a given averaging method, the variation of $\overline{\zeta}$ with axial distance is relatively independent of Mach number. This result is true for all averaging methods. That is, the conclusions drawn from the data of Figure 14 remain valid across the entire range of typical operating Mach numbers.

For completeness, we note an interesting second-order influence. The axial variation of both the area-weighted and volume-flow-weighted in-plane methods, and mixed-out methods, increases as Mach number is increased. This likely arises because of larger streamwise static pressure gradients (both adverse and favourable) in the flow-field, which amplify the changes in velocity gradient (and therefore changes in entropy generation rate) in the shear layers at the edges of the wakes. The magnitude of the effect discussed in the context of Figure 12 is therefore increased. Larger density gradients in the flow at higher Mach numbers also cause a slightly greater difference between the volume-flow-weighted and mass-flow-weighted methods.

SUMMARY AND CONCLUSIONS

In this paper, we have compared a range of methods for calculating aerodynamic performance parameters—e.g. KE loss coefficient—including plane-average methods with various weighting schemes (area, volume flow, mass flow, entropy flux) and mixed-out methods in which the flow is artificially mixed to a more uniform state. We do this for the case of a transonic HP NGV using high-fidelity experimental data from a transonic engine-parts facility, and using complementary CFD. We quantify the sensitivity of the various methods to: the axial location of the averaging plane; radial averaging range; and exit Mach number. The underlying physical mechanisms are discussed. The purpose is to provide guidance for a common practical situation on the accuracy of each method when used for comparisons between two or more experiments, or between experiment and CFD.

The key conclusions of this study are as follows:

1. The weighting functions for area, volume flow, and mass-flow-weighted plane-averaging methods are strongly influenced by static pressure gradients in the flow. Diffusion and acceleration of the flow cause development of the whirl angle distributions between axial planes and therefore cause changes in the volume flow and mass flow distributions at different planes.
2. The plane-averaged KE loss coefficient based on an area-averaged total pressure is highly sensitive to axial plane, showing variations over the range $0.0 \leq x/C_x \leq 1.0$ of up to −5.7% and +31.9% of the settled value (at $x/C_x = 1.0$). The axial sensitivity is considered to be unacceptable for measurements made within $0.5\,C_x$ of the trailing edge. Despite the simplicity of this method (which makes it a common choice in the literature), the results show that area-averaging is an extremely poor choice for comparing CFD and experiment or comparing different experiments.
3. The plane-average KE loss coefficients based on mass-flow-averaged and entropy-flux-averaged total pressure are very closely matched, and have the characteristic of slowly and monotonically increasing with axial distance due to the gradual conversion of SKE to total pressure loss. Plane-average KE loss coefficient based on volume-flow-averaged total pressure is closely matched to the mass-flow-averaged and entropy-flux-averaged methods in terms of both absolute values and axial sensitivity, but shows small differences close to the vane trailing edge due to local density variation. Volume-flow-averaging could be considered to offer a compromise between low axial sensitivity, and practical measurement requirements (does not require measurement of local density variation).

4. As expected, mixed-out KE loss coefficients calculated using four different methods are almost independent of axial plane. Small rises in mixed-out loss coefficient arise when the wakes pass through local streamwise pressure gradients, which increase the velocity gradients (and therefore the rate of entropy generation) in the shear layers at the wake edges. All four mixed-out methods provide closer comparisons between experiment and CFD than the plane-average methods. This highlights the importance of using mixed-out methods for comparing absolute KE loss coefficient between experiment and CFD, or in situations where inaccurate prediction of mixing rates is expected.
5. Mixed-out KE loss coefficients calculated using the Dzung and free-vortex methods were in excellent agreement. Absolute values of mixed-out loss coefficient calculated from the Amecke and forced-vortex methods were higher than the first two methods. If a single method is to be chosen, the Dzung method might be preferred due to its ease of implementation and unproblematic inclusion of coolant flows.
6. The axial sensitivity of KE loss coefficient is relatively independent of Mach number—a result that holds true for all plane-average and mixed-out methods. At higher Mach number, the associated larger density gradients in the flow slightly increase the axial variation in both plane-average and mixed-out loss coefficients.
7. For the NGV studied, radially averaging over the central 60% of vane span is robust for characterising profile loss. This range is sufficiently large to avoid sensitivities due to local radial non-uniformities (particular cooling features etc.) but not so large as to include sensitivity to endwall flows, which is often problematic where comparisons between situations (e.g. CFD and experiment) are required.

ACKNOWLEDGMENTS

The support of Rolls-Royce plc and Innovate UK is gratefully acknowledged.

NOMENCLATURE

Romans

A	Area, m^2
c_p	Specific heat at constant pressure, J kg^{-1} K^{-1}
C_x	Axial chord length, m
h	Static enthalpy, J kg^{-1}
h_0	Stagnation enthalpy, J kg^{-1}
M	Mach number, –
M_2	Vane exit Mach number, –
$\dot{m}$	Mass flow rate, kg s^{-1}
p	Static pressure, Pa
p_0	Stagnation pressure, Pa
$\overline{p_{02}}$	Mean total pressure in a downstream plane, Pa
$\overline{p_2}$	Mean static pressure in a downstream plane, Pa
p_{ref}	Arbitrary reference pressure, Pa
$\dot{q}$	Volume flow rate, m^3 s^{-1}
r	Radial position, m
r_1	Lower radial bound for integration, m
r_2	Upper radial bound for integration, m
Re	Reynolds number, –
s	Static entropy, J kg^{-1} K^{-1}
T_0	Stagnation temperature, K
Tu	Turbulence intensity, %
v	Velocity, m s^{-1}
v_x	Axial velocity component, m s^{-1}
w	Wake width, m
w_{ref}	Reference wake width at $x/C_x = 0.0$, m
x	Axial distance or direction, m
Y	Stagnation pressure loss coefficient, –
y	Streamwise-normal distance, m
z	Streamwise distance, m

Greeks

β	Flow turning (or whirl) angle, degrees
γ	Ratio of specific heats, –
ζ	Kinetic energy loss coefficient, –
$\hat{\zeta}$	Maximum kinetic energy loss coefficient, –
$\hat{\zeta}_{\mathrm{ref}}$	Reference maximum kinetic energy loss coefficient at $x/C_x = 0.0$, –
$\overline{\zeta}$	Average kinetic energy loss coefficient, –
$\overline{\zeta}_{\mathrm{ref}}$	Reference average kinetic energy loss coefficient (mean of plane-average methods at $x/C_x = 1.0$), –
η	Isentropic efficiency, –
θ	Circumferential position, degrees
θ'	Normalised circumferential position, vane pitches
θ_1	Lower circumferential bound for integration, degrees
θ_2	Upper circumferential bound for integration, degrees
ρ	Mass density, kg m^{-3}
χ	$(\gamma - 1) / \gamma$

Subscripts

0	Stagnation condition
1	Vane inlet station
2	Vane exit station
A	Area-weighted average value
M	Mass-flow-weighted average value
s	Isentropic condition
S	Entropy-flux-weighted average value
V	Volume-flow-weighted average value

Abbreviations

CFD	Computational fluid dynamics
HP	High pressure
KE	Kinetic energy
NGV	Nozzle guide vane
PS	Pressure side
SKE	Secondary kinetic energy
SS	Suction side

REFERENCES

[1] Pianko, M., Wazelt, F.; 1982; Propulsion and Energetics Panel Working Group 14 on Suitable Averaging Techniques in Non-Uniform Internal Flows; AGARD Advisory Report No. 182

[2] Oates, G.C.; 1997; Aerodynamics of Gas Turbine and Rocket Propulsion; AIAA Education Series, pp. 197–203, ISBN 978-1-56347-241-1

[3] Cumpsty, N.A., Horlock, J.H.; 2005; Averaging Non-Uniform Flow for a Porpoise; Proceedings of ASME Turbo Expo 2005, 6–9 June 2005, Reno-Tahoe, NV, USA, Paper No. GT2005-68081

[4] Denton, J.D.; 1993; Loss Mechanisms in Turbomachines; 1993 IGTI Scholar Lecture, ASME J. Turobmach., 115(4): 621–656; DOI: 10.1115/1.2929299
[5] Greitzer, E.M., Tan, C.S., Graf, M.B.; 2004; Internal Flow: Concepts and Applications; Cambridge University Press, ISBN 978-1-13945-111-6
[6] Dzung, L.S.; 1971; Konsistente Mittlewerte in der Theorie der Turbomaschinen für Kompressible Medien; BBC-Mitt., Vol. 58: 485–492
[7] Amecke, J.; 1970; Anwendung der Transsonischen Ähnlichkeitsregel auf die Strömung durch ebene Schaufelgitter; VDI Forschungsheft, Vol. 540, pp. 16–28
[8] Main, A.J., Oldfield, M.L.G., Lock, G.D., Jones, T.V.; 1997; Free Vortex Theory for Efficiency Calculations from Annular Cascade Data; ASME J. Turbomach., Vol. 119(2): 247–255, DOI: 10.1115/1.2841107
[9] Prasad, A.; 2005; Calculation of the Mixed-Out State in Turbomachine Flows; ASME J.Turbomach., Vol. 127(3): 564–572, DOI: 10.1115/1.1928289
[10] Pianko, M., Wazelt, F.; 1983; Suitable Averaging Techniques in Non-Uniform Internal Flows; NATO AGARD Advisory Report No. 182, Propulsion and Energetics Panel Working Group 14
[11] Dominy, R.G., Harding, S.C.; 1989; An Investigation of Secondary Flows in Nozzle Guide Vanes; AGARD-CP-469, Paper No. 7
[12] Kirollos, B., Lubbock, R., Beard, P., Goenaga, F., Rawlinson, A., Janke, E., Povey, T.; 2017; ECAT: An Engine Component Aerothermal Facility at the University of Oxford; Proceedings of ASME Turbo Expo 2017, Charlotte, NC, USA, 26–30 June 2017, Paper No. GT2017-64736, DOI: 10.1115/GT2017-64736
[13] Povey, T., Sharpe, M., Rawlinson, A.; 2011; Experimental Measurements of a Gas Turbine Flow Capacity Using a Novel Transient Technique; ASME J. Turbomach., Vol. 133:011005, DOI: 10.1115/1.4000481
[14] Burdett, D., Hambidge, C., Povey, T.; 2020; Analysis of Ultra-low Uncertainty Gas Turbine Flow Capacity Measurement Techniques; Proceedings of IMechE, Part A: J. Power and Energy; DOI: 10.1177/0957650920909718
[15] Burdett, D., Goenaga, F., Povey, T.; 2020; Understanding Capacity Sensitivity of Cooled Transonic Nozzle Guide Vanes; ASME J. Turbomach., Paper No. TURBO-20-1172 (*Accepted*)
[16] Thomas, F.O., Liu, X.; 2004; An Experimental Investigation of Symmetric and Asymmetric Turbulent Wake Development in Pressure Gradient; Physics of Fluids, Vol. 16(5): 1,725–1,745, DOI: 10.1063/1.1687410

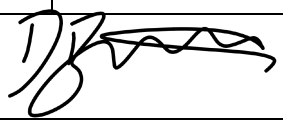
Statement of Authorship for joint/multi-authored papers for PGR thesis

To appear at the end of each thesis chapter submitted as an article/paper

The statement shall describe the candidate's and co-authors' independent research contributions in the thesis publications. For each publication there should exist a complete statement that is to be filled out and signed by the candidate and supervisor **(only required where there isn't already a statement of contribution within the paper itself).**

Title of Paper	Analysis of averaging methods for non-uniform total pressure fields
Publication Status	Submitted for Publication
Publication Details	Burdett, D., Povey, T.; 2021; Analysis of Averaging Methods for Non-Uniform Total Pressure Fields; ASME J. Turbomach. Paper No. TURBO-20-1403 *(Submitted)*

Student Confirmation

Student Name:	D Burdett		
Contribution to the Paper	Performed experimental testing to collect data, ran numerical simulations, analysed and interpreted experimental and numerical data, and wrote manuscript.		
Signature		Date	13/02/2021

Supervisor Confirmation

By signing the Statement of Authorship, you are certifying that the candidate made a substantial contribution to the publication, and that the description described above is accurate.

Supervisor name and title: Professor Thomas Povey		
Supervisor comments: Dan conducted all of the research himself, and entirely wrote the paper himself, with technical contributions from his supervisor.		
Signature: Thomas Povey	Date	19/02/2021

This completed form should be included in the thesis, at the end of the relevant chapter.

EXPERIMENTAL AND NUMERICAL ANALYSIS OF LOSS CHARACTERISTICS OF COOLED TRANSONIC NOZZLE GUIDE VANES

Daniel Burdett, Thomas Povey‡
Department of Engineering Science, University of Oxford, Oxford, OX2 0ES, United Kingdom
‡thomas.povey@eng.ox.ac.uk

ABSTRACT

This paper presents high-fidelity experimental traverse measurements downstream of an annular cascade of transonic nozzle guide vanes (NGVs) from a high-pressure (HP) turbine stage. The components are heavily-cooled real engine components from a modern civil gas turbine engine, operated at scaled engine conditions. Tests were conducted in the high technology readiness level (TRL) Engine Component Aerothermal (ECAT) facility at the University of Oxford.

High resolution full-area traverse measurements of local kinetic energy (KE) loss coefficient are presented in several axial planes. In particular, we present: circumferential loss coefficient profiles at several radial heights; full-area traverses at three axial planes; and fully mixed-out loss calculations. Analysis of these data gives insight into particular loss structures, overall aerodynamic performance, and wake mixing rates. The effect of exit Mach number on performance is also considered. The data address a gap in the literature for detailed analysis of traverse measurements downstream of HP NGV engine components.

Experimental data are compared with steady and unsteady RANS simulations, allowing benchmarking of typical CFD methods for absolute loss prediction of cooled components. There is relatively limited aerodynamic performance data in the literature for heavily cooled NGVs, and this study represents one of the most comprehensive of its type.

INTRODUCTION

The HP NGV plays a significant role in setting the overall engine performance. In particular, the designer must consider the simultaneous optimisation of NGV capacity, thermal/cooling performance, and aerodynamic performance. These three factors determine the stage and overall engine operating point. In this paper we consider the aerodynamic performance of heavily cooled parts, tested at non-dimensionally representative operating conditions. The importance of this topic is justified by the exchange rate between KE loss coefficient and HP turbine stage efficiency: at a typical turbine stage efficiency of 95%, a 1% change in NGV loss coefficient (as a % of loss coefficient) is equivalent to a 0.05% change in HP stage efficiency.

Early attempts to predict turbine stage performance parameters (stage efficiency and losses) primarily involved empirical correlations (e.g. Ainley and Mathieson [2]) or analytical models (e.g. Carter [1]) based on either simplistic linear (and often low speed) cascade tests or data from a bank of engine component tests (loss coefficient and flow angle measurements).These prediction methods were used in turbine design for many decades, despite their reliance on extrapolations from overly simplistic experimental correlations, and their increasingly common use in applications with complex geometric features not present in the original test cases. Denton [3] comprehensively reviews methods used to predict various aspects of loss generation in turbine stages. He warns strongly against relying on correlations obtained from simplified cascade tests in which real engine features were omitted, including: 3D vane geometry including lean, sweep, endwall fillets and endwall contouring; film cooling; realistic trailing edge geometries with (where relevant) coolant ejection; representative Mach and Reynolds number conditions; representative incident flow turbulence parameters; realistic surface roughness and surface defects. Instead he advocates for understanding of the fundamental mechanisms of loss generation.

Most of the experimental studies of NGV loss in the open literature have been conducted in simplified experiments designed to isolate the impact of particular design features, e.g. film cooling configurations ([4]–[7]); trailing edge (TE) coolant ejection ([8]–[11]); TE design ([12]–[14]); fillets at the vane surface-endwall junctions ([15]–[17]); 3D shaping ([18]–[22]); inlet flow conditions at the combustor-turbine interface ([23]–[25]). Such experiments are well-suited to understanding fundamental aspects of design, but poorly-suited to characterising engine parts in a realistic operating environment. This is important both for early-stage design and also for CFD calibration. Doing so requires the use of *actual* engine components operating at scaled engine conditions (Mach and Reynolds numbers, and coolant-to-mainstream pressure ratio), ideally (because of periodicity effects) in a fully-annular cascade.

A handful of studies in the open literature meet some of these requirements ([26]–[30]): these present aerodynamic traverse measurements from either annular sector or fully-annular cascades of vanes which are, to varying degrees, representative of typical engine geometries. Some of these cascades were uncooled and others were designed to study the effects of specific cooling features ([6], [8]). The studies cover a range of exit Mach number conditions from low speed to mildly supersonic. The primary focusses of these studies were: determining realistic secondary flow structures for modern vanes; studying the development of wake profiles and characterising mixing losses; and understanding the influence of the radial pressure gradient on the development of wakes and secondary flow structures in annular cascades.

Yasa et al. [31] tested an annular sector of cooled engine guide vanes at exit Mach numbers of 0.60 and 0.95. They compared wake characteristics (depth, breadth, and decay rates)

between the subsonic and transonic regimes, and studied the influence of endwall fillets on secondary flow development.

The importance of unsteady flow phenomena to the evaluation of NGV aerodynamic performance has been shown by the work of Sieverding et al. ([8], [32]) and Melzer et al. ([14], [33]), who demonstrated its central role in determining TE loss and downstream mixing losses, and its sensitivity to TE shape, thickness, coolant slot geometry, and blowing rate. So far as CFD is concerned, unsteady methods (i.e. URANS or LES) are therefore generally seen as a minimum requirement for assessing NGV performance.

Léonard et al. [34] compared RANS, URANS and LES methods applied to a typical turbine blade at high-subsonic Mach number. They illustrate the hierarchy of prediction accuracy between the three methods: RANS gives an estimate of the mean flow-field, but URANS or LES are required to properly resolve the TE flow dynamics. LES offers the most accurate prediction of the complex flow, capturing more of the unsteady interaction between the boundary layers and the TE vortex and shock structures.

In this paper, we present comprehensive experimental traverse data downstream of a full annulus of engine part NGVs from the high-TRL ECAT facility at the University of Oxford [35]. In particular, we present: detailed characterisation of the loss of a fully cooled NGV at engine representative conditions (represented as both local loss coefficient distributions and average loss coefficient values); axial development of the wake profile; and the effect of Mach number on loss. We also consider the limitations of CFD methods (steady and time-averaged unsteady RANS simulations) for accurate prediction of loss.

OVERVIEW OF EXPERIMENTAL FACILITY

Experiments were conducted in the Oxford ECAT facility [35]. This is a high-TRL blowdown facility with a full-annular cascade of engine parts (typically HP NGVs) operated at non-dimensionally engine-representative conditions of Mach number, Reynolds number and coolant-to-mainstream total pressure ratio. Kirollos et al. [35] provide further details of the facility operation, and demonstrate the capabilities of the facility for making capacity, aerodynamic loss, and metal effectiveness measurements. The tests presented here used HP NGVs from a large, modern civil turbofan engine. The operating conditions are summarised in Table 1.

Table 1: Typical ECAT facility operating conditions.

Parameter	Nominal Value
Vane inlet total pressure, p_{0m} (bar)	1.85–2.50
Vane pressure ratio, p_2/p_{0m} (–)	0.44–0.78
Vane exit Mach number, M_2 (–)	0.60–1.15
Vane exit Reynolds number, Re (–)	2×10^6–8×10^6
Coolant-to-mainstream pressure ratio, p_{0c}/p_{0m} (–)	1.025
TE slot-to-mainstream momentum flux ratio	0.48
Mainstream mass flow, $\dot{m}_m$ (kg s^{-1})	7.8–15.8
Inlet total temperature, T_{01} (K)	280–350
Inlet turbulence intensity, Tu. (%)	6–10%

A simplified axisymmetric cross-section through the ECAT facility working section is shown in Figure 1. The upstream measurement plane is located three axial chord lengths upstream of the leading edge plane. The inlet duct converges and slopes radially outwards on approach to the cascade leading edge. The inlet flow is radially and circumferentially uniform in total pressure and temperature. The vane exit flow passes into a constant-area duct extending three axial chord lengths downstream of the TE plane, before exhausting into the downstream plenum. Traverse measurements were made in three different axial planes located ¼, ½ and ¾ of an axial chord length downstream of the TE. These planes are referred to as planes 1, 2 and 3 respectively, as marked in Figure 1.

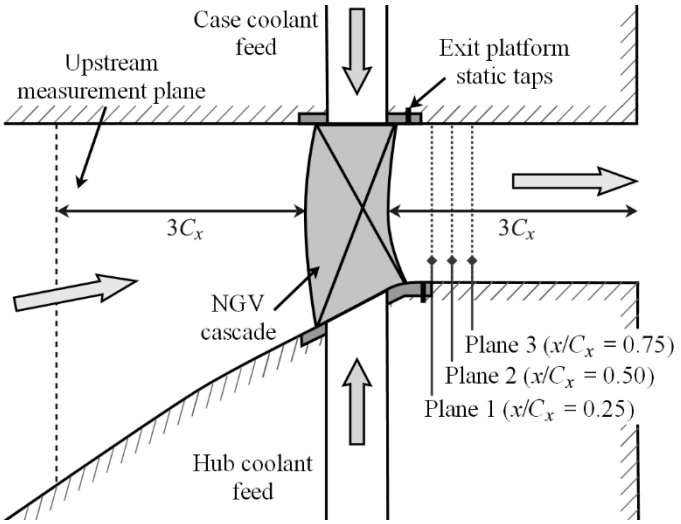


Figure 1: Axisymmetric cross-section schematic of the ECAT facility working section.

The ECAT facility can be operated in two different modes: *blowdown* mode and *regulated* mode ([35], [36]). These modes achieve varying and steady-state vane exit Mach number conditions during a run, respectively. The area-survey data for this study was collected in regulated mode operation—i.e. at a single, steady operating condition. This can be maintained, with almost no deviation from the target vane pressure ratio ($p_2 / p_{0m} = 0.55$), for a typical duration of 35 seconds. Vane exit hub and case static-pressure-to-upstream-total pressure ratios are shown for a typical regulated run in Figure 2a. The normalised mean pressure ratio is also plotted. During the period 30–65 s, the RMS fluctuation about the target value was 0.17%, showing very well controlled test conditions. A small number of blowdown mode tests were also performed, to examine the sensitivity of loss coefficient to exit Mach number. The traverse process in each type of test is outlined in the following section.

The vanes are supplied with coolant from the hub and case (see Figure 1), feeding film cooling holes distributed over the vane suction and pressure surfaces (six SS rows and five PS rows), and a TE slot with a suction side overhang of length 13.4% of axial chord. The hub and case coolant flows are independently metered to high accuracy, giving precise control

over the mass flows during a run. Typical coolant-to-mainstream pressure ratio characteristics are plotted in Figure 2b, showing good control within a tight band (approximately ±0.02% of the target value). It has been established that the coolant capacity characteristic is relatively insensitive to p_{0c} / p_{0m} [36]. The overall mass flow rate variation expected due to this variation is ±0.005% of the target value.

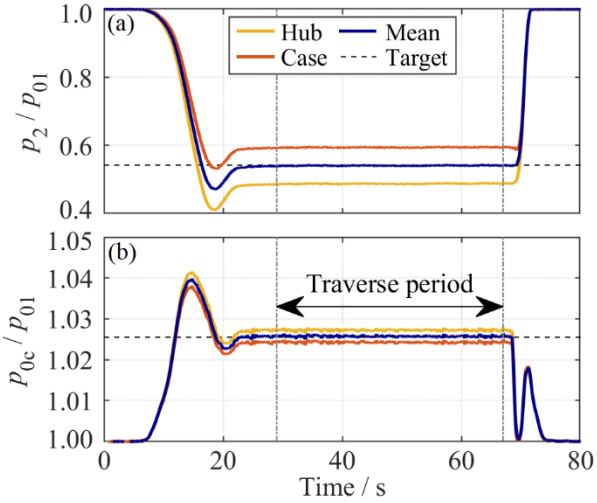


Figure 2: (a) Vane exit-static-to-inlet-total pressure ratios and (b) vane coolant-to-mainstream pressure ratios during a typical regulated (steady-state) run.

INSTRUMENTATION AND MEASUREMENT PROCESS

Vane upstream total pressure, p_{0m}, was measured using four fixed Pitot rakes, each with eight measurement points distributed across the vane span (i.e. 32 total pressure measurements). Vane exit static pressure was measured on six vanes (from a total of 40), at tappings located on the hub and case platform overhangs approximately 5 mm downstream of the cascade TE plane. These locations are shown in Figure 1. Each of the six vanes was instrumented with six tappings at the hub and eight at the case (i.e. 84 tappings in total). The estimated bias and precision errors in the measurement of operating pressure ratio were ±0.365% and ±0.007%, to 95% confidence. A detailed uncertainty analysis is given in [36].

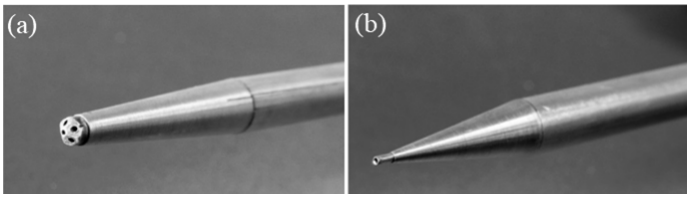


Figure 3: Photographs of the traverse probe tips: (a) five-hole probe; (b) Pitot probe.

Traverse measurements were conducted using a two-axis (radial-circumferential) hub-mounted traverse gear, capable of traversing the entire annulus in a series of 40° sectors. The traverse equipment is described in [35]. Measurements were conducted using a five-hole pneumatic pressure probe (tip diameter 2.8 mm) calibrated over the range of Mach numbers $0.3 \le M \le 1.4$. This allowed determination of total and static pressures, Mach number, and pitch and yaw angles. A single-hole Pitot probe was used very close to the hub and case endwalls. Photographs of the probe tips are shown in Figure 3.

Area surveys were conducted in *regulated mode*, at a nominal exit Mach number $M_2 = 0.97$, with typical variation of ±0.14% of the target value. These were performed over a circumferential range of 2.5 vane pitches (covering two complete vane wakes) and a radial range as close to the complete span as was practicably possible (around 3–97% of span). The circumferential limits in each of the three traverse planes were carefully set to measure wakes from the same two vanes in each case. This is demonstrated schematically in Figure 4. A full area survey required six runs of the facility and a total of 50–60 circumferential passes of the traverse probe in alternating circumferential directions at different radii. The radial step size was approximately 1.4 mm. The resulting traverse pattern is illustrated in Figure 5. Alternating line weights indicate the six individual runs. The two sections immediately adjacent to the hub and case boundaries were surveyed with the Pitot probe.

Midspan circumferential traverses were conducted in blowdown mode, the probe being continuously traversed back and forth at midspan, whilst the exit Mach number falls slowly through the range $1.15 > M_2 > 0.60$. The traverse pattern (composite of two runs: see overlapping lines) is illustrated in both (θ, r)-space and $(\theta\text{-}M_2)$-space in Figure 6. Midspan circumferential traverses were conducted in the same three axial planes as the area surveys, and over the same circumferential ranges (see Figure 4).

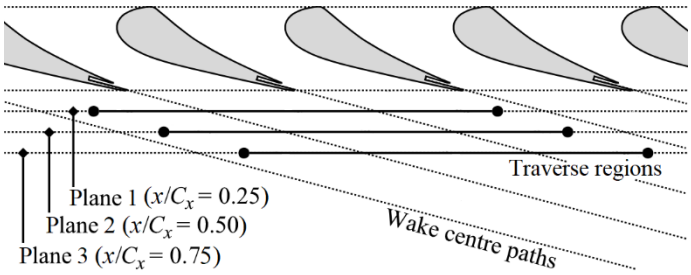


Figure 4: Schematic of experimental traverse planes and circumferential limits.

The probe-transducer measurement system was experimentally [37] and theoretically [38] determined to have a frequency response of 120 Hz. At a traverse speed of 9.0 deg s^{-1} (approximately 58.3 mm s^{-1} at midspan), this is equivalent to an effective spatial resolution of 0.49 mm. The impulse response deconvolution technique presented by Burdett et al. [37]) was employed to improve the system frequency response—with almost no loss of fidelity of underlying signal—to approximately 720 Hz, or a spatial resolution of 0.08 mm (at midspan). In the impulse response technique, the inverse impulse response function (that is, the transfer function which takes as its input the

measured signal (filtered by the probe-transducer system) and outputs the underlying 'true' signal) for the probe-transducer system is approximated, and applied as a digital filter to the measured pressure signal. This technique will be familiar to the heat transfer community where it is commonly used to extract transient heat flux signals from a measured temperature history. For area surveys with a traverse pattern made up of alternating sweep directions (Figure 5)—almost universal—it is necessary to have adequate frequency response to avoid apparent spatial discontinuities at sharp gradients in the underlying flow. That is, inadequate system frequency response causes apparent circumferential offsets in alternating sweeps of the traverse (space-time transformation effect).

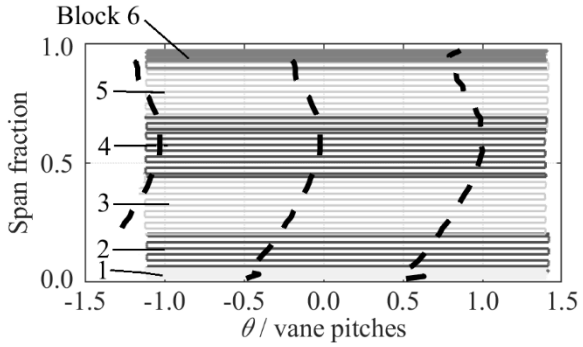


Figure 5: Typical traverse pattern for a steady-state area survey, showing six individual traverse sections. NGV wake locations are marked by bold dashed lines.

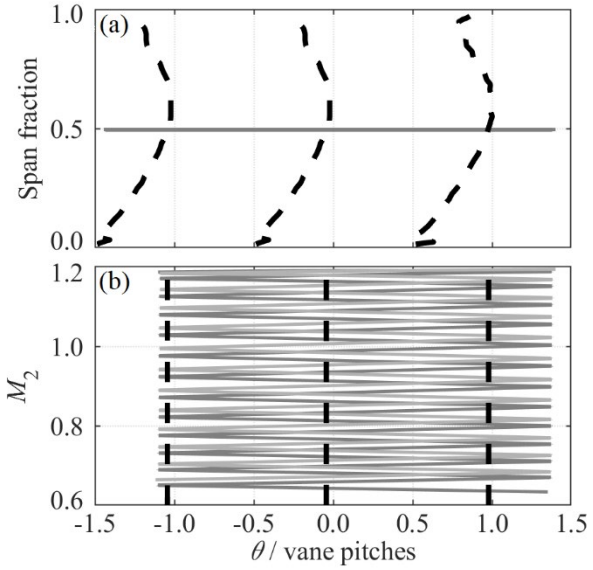


Figure 6: Typical traverse patterns for a blowdown midspan circumferential traverse: (a) in (θ, r)-space; (b) in (θ, M_2)-space, showing two runs. Wake locations are marked by dashed lines.

NUMERICAL METHODS

Steady and unsteady 3D RANS simulations were performed using ANSYS CFX. The 3D domain is shown in Figure 7. Two vane passages were meshed, with rotational periodicity. The solid boundaries were set as adiabatic walls. The NGV geometry was engine representative, but with different treatment of the film cooling holes in different simulations—as will be described. The mesh was octree-based, generated using BOXERmesh. A midspan cross-section through the mesh is shown in Figure 8. Fine mesh refinement was concentrated close to the vane TE, with moderate mesh refinement following the expected path of the vane wakes. A grid sensitivity study was conducted to ensure the results were grid-independent, using three grids with cell counts of approximately 18 M, 33 M, and 57 M cells. Grid independence was assessed using a range of metrics including vane capacity, and radial and circumferential distributions of velocity, static and total pressure. The finest of the three meshes (57 million cells) was taken forwards for the main study.

Uniform conditions of total pressure and temperature were specified at the inlet boundary, matched to nominal experimental conditions (Table 1). Flow angles (whirl and pitch angles) on the main inlet boundary were unconstrained. The annulus lines of the inlet duct between the inlet boundary and the NGV leading edge were matched to the ECAT facility, so that the spanwise profile of the flow radial angle approaching the cascade was closely matched to the experiment. At the exit boundary, an area-average static pressure was set to match the design vane exit Mach number. The radial and circumferential exit static pressure distributions were unconstrained, but with the condition that radial equilibrium was satisfied. To ensure precise comparisons of exit Mach number between experiments and CFD, the static pressure field in the CFD solutions was interrogated at the locations of the *experimental* tappings on the hub and case vane exit platforms. The specified average static pressure at the CFD exit boundary was adjusted by trial-and-error until the mean static pressure across the tapping locations (14 locations for one vane pair) was matched to the value measured in the experiment.

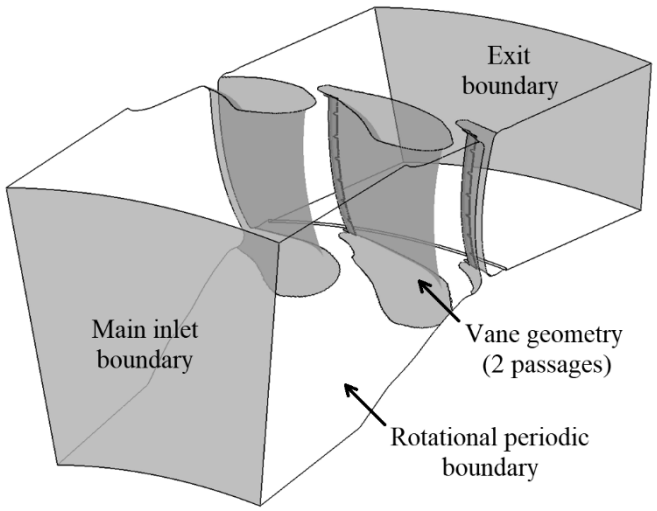


Figure 7: Geometry for CFD simulations.

The modelling of the TE slot is illustrated in Figure 9. The coolant flow inlet boundary was located eight slot thicknesses upstream of the slot exit plane. The slot was segmented into

seven distinct sections in the spanwise direction by six internal ribs. The rib geometry was modelled on the engine component, with fully-resolved elliptical TEs. This allowed realistic development of the coolant flow prior to exiting into the mainstream flow, and therefore aims to achieve realistic prediction of non-uniform coolant flow distribution at the slot exit. A mass flow boundary condition was set over the inlet boundary as a whole, with the solver free to determine the distribution over the individual boundary faces.

The solver settings were second-order discretised, and density-based. The *k-ω* SST model was used for turbulence closure (hybrid model, with *k-ε* formulation in the free stream, and *k-ω* model in inner boundary layer regions), a popular choice for simulations of complex 3D vane geometries. Further details of the numerical setup are provided in.

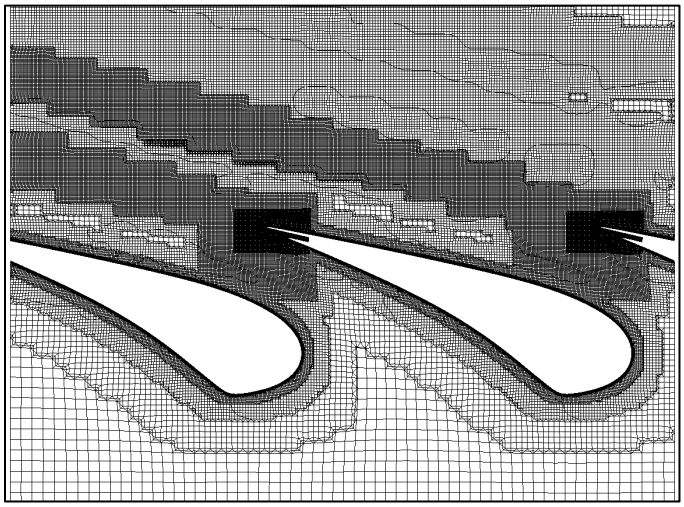


Figure 8: Section through the mesh at midspan.

To understand the requirements of CFD for accurately predicting loss, three different types of numerical simulations were run, with increasing sophistication. These are now described.

Simulation 1: Steady RANS simulations without film cooling but with TE slot flow. These were intended to help separate the effects of film cooling by first studying the underlying flow, and also to aid in understanding the impacts of smaller features which can be obscured by the film flows.

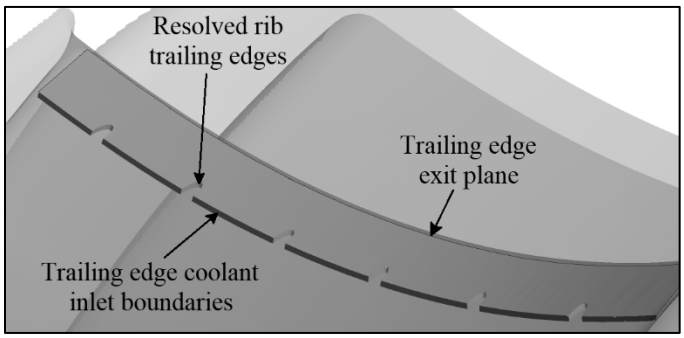


Figure 9: Detail of TE slot internal cooling geometry.

Simulation 2: Steady RANS simulations with film cooling flows modelled using a point-source model. In these simulations, additional mass flows (specified as fractions of the mainstream mass flow) and associated direction vectors were added to the continuity equation at the vane surface locations corresponding to every film cooling hole exit on the physical part. Individual row mass flow rates were determined from the coolant system design data for the component, and scaled to match the total coolant capacity measured in the experimental facility. The mass flow split between individual holes in a particular row was estimated using a simple model based on local exit static pressures (evaluated using a pressure field from uncooled simulations) and feed total pressure.

Simulation 3: Unsteady RANS simulations with point-source film cooling. These simulations were initiated from the converged steady RANS results. The time step was set to one tenth of the estimated TE vortex shedding period. Simulations progressed until the equation residuals were converged to within 10^{-6}, and the values at strategically placed monitor points in the wake region had converged to essentially periodic fluctuations. Time-averaged solutions were then evaluated over 20 shedding periods. The Strouhal number associated with unsteady fluctuations, based on the TE diameter and the free-stream exit velocity, was 0.27, equivalent to a shedding frequency of 43.6 kHz. It was evaluated at three points along the vane span and found to be radially invariant to within 8%.

DEFINITIONS OF LOSS COEFFICIENT

We denote loss using a KE loss coefficient, ζ, expressed in terms of total and static pressure:

$$\zeta = 1 - \frac{1 - \left(\frac{p_2}{p_{02}}\right)^{\chi}}{1 - \left(\frac{p_2}{p_{01}}\right)^{\chi}} \qquad (1)$$

where $\chi = (\gamma - 1) / \gamma$. Detailed discussion of the suitability of this definition is provided in Appendix A. The analysis presented in this paper considers a series of different representations of losses: local distributions in a particular axial plane; radial distributions of circumferentially-averaged loss coefficient; average values in a particular axial plane; and fully mixed-out loss coefficient values. In each of these cases we settle on a slightly different practical definition of loss coefficient. The rationale through which each of these was reached is covered in Appendix A, but the final definitions are repeated here for clarity.

A *local* kinetic energy loss coefficient is defined at every point in the flow by

$$\zeta'(r,\theta) = 1 - \frac{1 - \left(\frac{p_2(r,\theta)}{p_{02}(r,\theta)}\right)^{\chi}}{1 - \left(\frac{p_2(r,\theta)}{p_{01}}\right)^{\chi}} \qquad (2)$$

where p_2 (r,θ) and p_2 (r,θ) are measured in the plane of interest, and p_{01}, T_{01} are assumed uniform. The circumferential-average loss coefficient at a particular radial height is defined by

$$\zeta'''(r) = 1 - \frac{1 - \left(\frac{\overline{p_2}(r)}{\overline{p_{02}}(r)}\right)^{\chi}}{1 - \left(\frac{\overline{p_2}(r)}{p_{01}}\right)^{\chi}} \tag{3}$$

where $\overline{p_2}(r)$ is the circumferentially-area-averaged static pressure, and $\overline{p_{02}}(r)$ is the circumferentially-mass-flux-averaged total pressure. The average loss coefficient for an entire 2D plane is defined by

$$\zeta'''' = 1 - \frac{(\dot{m}_\mathrm{m} + \dot{m}_\mathrm{c})\left[1 - \left(\frac{\overline{p_2}}{\overline{p_{02}}}\right)^{\chi}\right]}{\dot{m}_\mathrm{m}\left[1 - \left(\frac{\overline{p_2}}{p_{01}}\right)^{\chi}\right] + \dot{m}_\mathrm{c}\left[1 - \left(\frac{\overline{p_2}}{p_{0c}}\right)^{\chi}\right]} \tag{4}$$

where $\overline{p_2}$ and $\overline{p_{02}}$ are the plane-area-averaged static pressure and plane-mass-flux-averaged total pressure, respectively, and $\dot{m}_\mathrm{m}$ and $\dot{m}_\mathrm{c}$ are the mainstream and coolant mass flow rates. Finally, the mixed-out KE loss coefficient is defined by

$$\zeta''''' = 1 - \frac{(\dot{m}_\mathrm{m} + \dot{m}_\mathrm{c})\left[1 - \left(\frac{\overline{p_2}'}{\overline{p_{02}}'}\right)^{\chi}\right]}{\dot{m}_\mathrm{m}\left[1 - \left(\frac{\overline{p_2}'}{p_{01}}\right)^{\chi}\right] + \dot{m}_\mathrm{c}\left[1 - \left(\frac{\overline{p_2}'}{p_{0c}}\right)^{\chi}\right]} \tag{5}$$

where $\overline{p_2}'$ and $\overline{p_{02}}'$ are the mixed-out values of static and total pressure, respectively, evaluated using the method of Dzung [39].

EXPERIMENTAL AND COMPUTATIONAL RESULTS

The experimental and computational results are now considered. We begin by analysing local distributions of KE loss coefficient in three axial planes.

Local kinetic energy loss coefficient distributions

Full-area experimental surveys of local KE loss coefficient, ζ' (equation (10)) in planes 1, 2 and 3 are shown in Figure 10a–c, for a vane exit Mach number $M_2 = 0.97$. Corresponding time-averaged URANS-predicted ζ' distributions (i.e. simulation 3) in the same three axial planes (planes 1–3) are shown in Figure 10d–f. The time-average was computed over 20 vortex shedding periods, equivalent to an averaging period of 4.6×10^{-4} s. The data are viewed from downstream to upstream (PS to the left of the wake and SS to the right, as indicated in Figure 10a and b).

First consider the experimental data, starting with plane 1 (Figure 10a). The wake signature is curved, in line with the *compound lean* in the aft chord region of the vane (see Figure 7). The peak value of ζ' in the wake centre is higher close to the hub, corresponding with a higher average local surface Mach number. There are also a series of distinct peaks along the line of the wake, separated by loss coefficient minima. This pattern corresponds with the non-uniform coolant ejection from the TE slot (see Figure 9).

Secondary flow loss cores can be seen at the junctions between the wakes and the hub endwall, but no clear secondary loss cores are visible at the case. This difference is attributed to the influence of the radial pressure gradient, which stimulates radial migration of low momentum flow towards the hub (causing accumulation and keeping secondary cores close to the wall) and away from the case (causing rapid dispersal of secondary cores). We examine this effect in more detail below.

Moving downstream to planes 2 (Figure 10b) and 3 (Figure 10c), the peak values of ζ' successively drop in magnitude, and the wakes broaden in width, as the flow gradually mixes out. This axial development is examined in more detail in the later section. The flow field becomes increasingly uniform, both radially and circumferentially. The distortion of the characteristic bowed shape of the wake becomes increasingly exaggerated due to the action of secondary flows induced by the momentum disparity between the high-loss wake and low-loss passage flow. The overall detail of the data is fairly exceptional for experimental measurements of engine hardware.

Consider now the difference between the experimental and numerical data in equivalent planes. URANS performs well in reproducing the general wake shapes, as well as the difference in endwall boundary layer thickness and secondary flow intensity between hub and case. The peak values of ζ' in the wake centre are greater in CFD than in experiment, and the wakes are narrower. This stems from the well-known weakness of many CFD methods in predicting the rate of mixing, due to inadequate turbulence modelling.

A particular manifestation of this effect can be seen in the horizontal striations to the PS (right-hand side) of the wakes in Figure 10d. There are 17 regions of locally high loss coefficient across the span. These features can be traced back in the CFD result to the 17 individual film flows on the rear-most PS row (74% tangential chord). There are similar features originating from the earlier films, but they are far more mixed out. It should be noted that this is a different effect than the radial loss coefficient variation seen in the experimental data, which originates from the TE slot traverse. The persistence of these discrete film cooling features so far downstream is unrealistic, and is thought to be caused by inadequacy of the source-terms method for modelling the mixing behaviour between the mainstream and film flows, and the general under-prediction of mixing rate by the CFD method. The excessive protrusion of these features into the free-stream on the PS of the wakes is additionally exaggerated because the flow-field is visualised in axial planes (to match the experimental traverse measurements). Axial planes cut across the wakes at an oblique angle (approximately 75°), and therefore stretch the local loss coefficient distribution circumferentially across the passage.

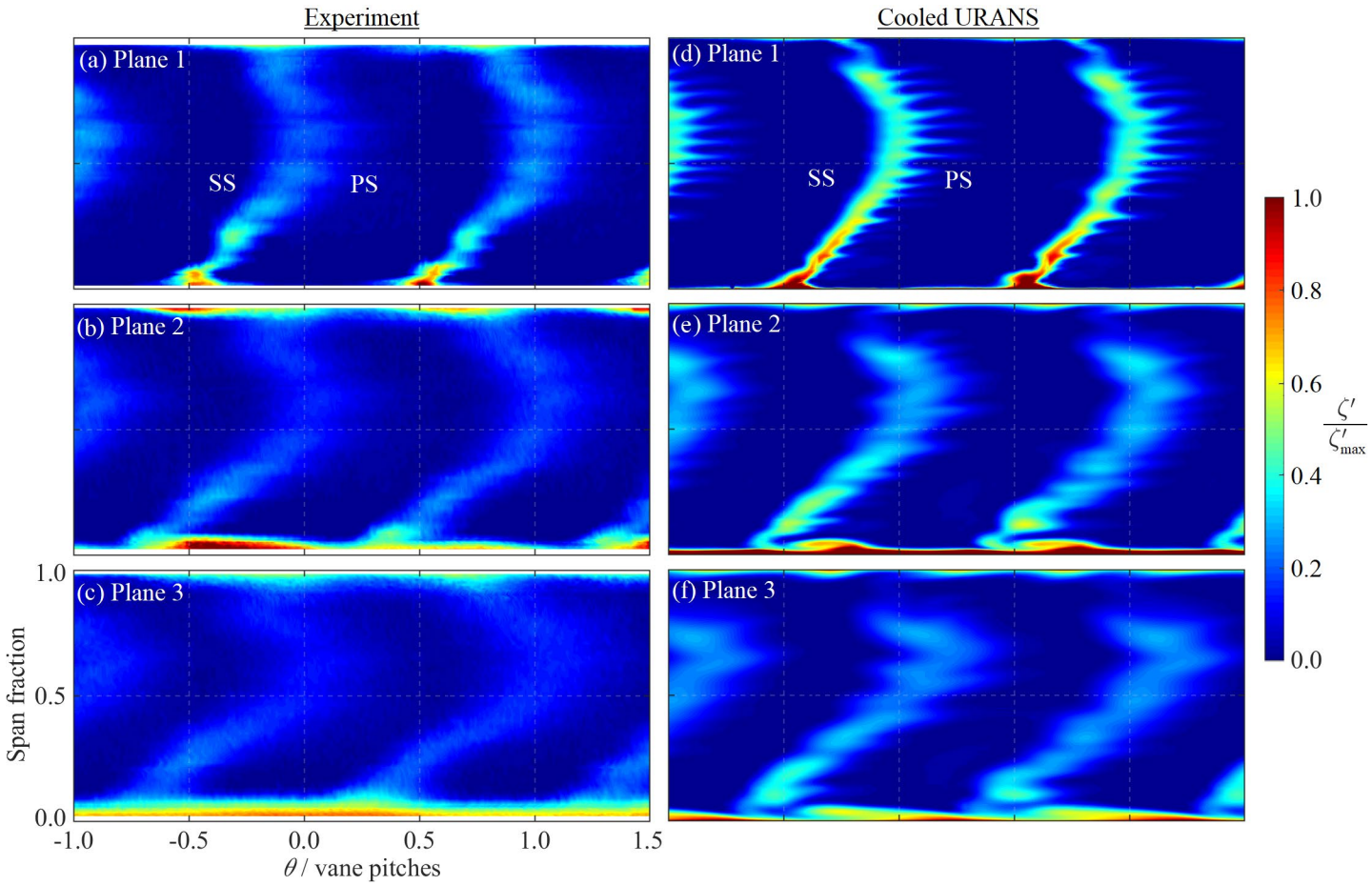


Figure 10: Local distributions of KE loss coefficient, ζ', from experiment and cooled URANS in planes 1, 2 and 3.

The general development of the CFD-predicted flow-field between the three planes is very similar to the experimental data, but always under-mixed in comparison.

We now examine the secondary flow regions in detail. Close-up views of these regions in plane 1 at both hub and case are shown in Figure 11 for experiment, cooled RANS and time-averaged cooled URANS. Consider first the case regions (Figure 11a–c). The case secondary flows are significantly less intense than at the hub. This is due to a combination of lower Mach numbers, and spreading of the loss caused by downwash due to the radial pressure gradient.

The CFD cases differ from the experiment in that the near-wall loss core (marked A in frames a, b and c) and the wake loss region (marked B in frames a, b and c) are separated by a region of low loss coefficient, as opposed to being joined. This is likely the result of over-prediction of the downwash effect within the low-momentum boundary layer region as a secondary consequence of under-mixing of the near-wall flow with the main flow. This effect is even greater in cooled URANS, with the wake loss region beginning at around 90% span as opposed to 93% in cooled RANS.

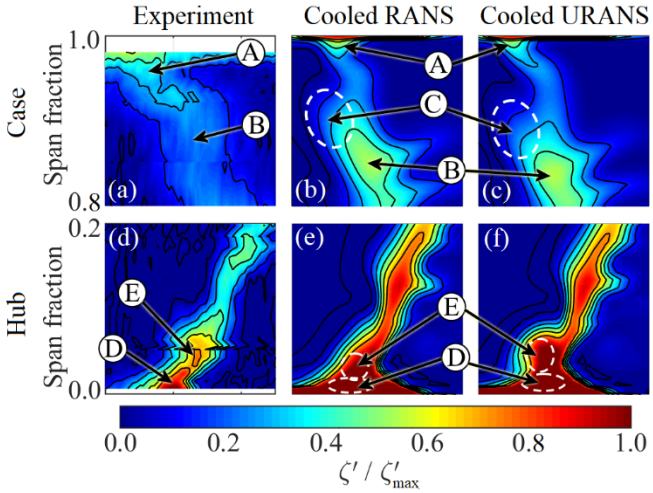


Figure 11: Comparison of case, (a)–(c), and hub, (d)–(f), secondary loss cores between experiment, cooled RANS and cooled URANS.

In CFD, specific secondary loss cores are identified by inspection of 3D flow structures with significant streamwise vorticity. The vortex identification parameters proposed in [40] were used for this purpose. In both CFD cases, the case passage

vortex loss core (the PS leg of the leading edge horseshoe vortex) is located on the SS of the wake at the outer edge of the wake loss region (marked C in frames b and c, with the rough core boundary indicated by a dashed white line). This core is identified by having negative vorticity (clockwise rotation when viewed from downstream). No passage vortex core can be distinguished in the experimental data, being largely mixed out even at plane 1. Under-prediction of mixing is the likely cause of stronger secondary flows in CFD compared to the experimental data, whilst over-prediction of inlet boundary layer thickness is a possible additional contributing factor.

We now turn to the hub regions (Figure 11d–f). Two distinct secondary loss cores can be seen in the experimental data (frame d): a larger, high intensity core at approximately 2% span, (marked D in frame d), and a smaller, lower intensity core at approximately 7% span, (marked E in frame d). These two cores likely correspond with the PS (passage vortex) and SS legs of the leading edge horseshoe vortex, respectively.

In the two CFD cases (frames e and f), the same loss cores D and E can be seen within a larger hub secondary loss core. We can identify them as likely originating from the PS and SS legs of the leading edge horseshoe vortex, by confirming that they have positive and negative vorticities respectively. The PS leg (core D) lies flat on the hub endwall, with the SS leg (core E) just above it at around 5–7% span. The rough locations of the two individual cores are indicated by dashed white lines. The shape of core E differs between cooled RANS and URANS, having greater protrusion to the SS of the wake in frame f.

Spanwise variation in circumferential profiles of local kinetic energy loss coefficient

In Figure 12 we plot circumferential profiles of ζ' at 75%, 50% and 25% span, in each of planes 1–3. Each profile is radially averaged over ±5% span at each location, to reduce sensitivity to individual coolant films etc. As expected, at all three spanwise locations, we see the wake profiles mix out in the downstream direction (moving between planes 1 to 3) with an incremental reduction in peak loss coefficient in the wake centre, and an increase in wake width. We consider the decay rate of peak loss coefficient and the growth of the wake width in a later section.

The wake profiles are quasi-normal in distribution, with a slight asymmetry: the gradient of ζ' is steeper moving away from the SS of the trailing edge than from the PS. This is despite the SS boundary layer at the trailing edge being approximately five times thicker than the PS boundary layer based on CFD-predicted displacement thicknesses (gradual diffusion on the late SS with some shock-boundary layer interaction, compared to rapid acceleration on the late PS). The wake region is—of course—more complex than simply the confluence of the two surface boundary layers, featuring two distinct trailing edge *base regions* with different associated base pressures. Coolant flow ejects from the trailing edge slot into the cutback region upstream of the SS TE, reducing the gradient on the PS of the wake.

We now compare the measured circumferential profiles of local KE loss coefficient *between* spanwise locations. The results at 75% and 50% span are very similar. In plane 1, the peak heights differ by just 6.7% and the wake widths (defined as the range over which ζ' exceeds 50% of the peak value) by 6.5%. At 25% span, however, the peak losses are notably higher. Comparing to 50% span data, the peak loss coefficient values at 25% span are higher by +36.3%, +35.4% and +30.9% in planes 1, 2 and 3 respectively. The difference is primarily due to spanwise variation of the axial location of the vane TE with respect to the traverse plane: the test vane has moderate positive compound lean and sweep such that the hub and case sections are further axially downstream (hub more so than case) than the midspan section. Thus, the near-hub wake is under-mixed with respect to other vane sections at a particular traverse plane, an effect that is more pronounced at plane 1 than further downstream.

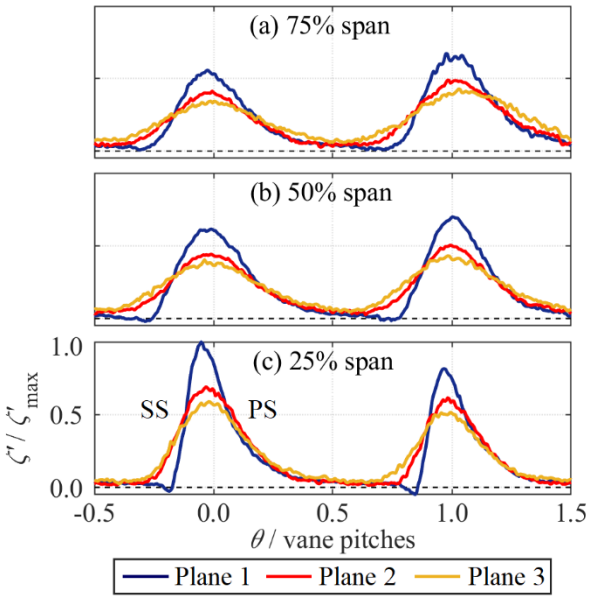


Figure 12: Circumferential profiles of ζ' extracted from experimental traverse measurements at planes 1–3 at: (a) 75% span; (b) 50% span; and (c) 25% span.

Axial variation in circumferential profiles of local kinetic energy loss coefficient

In Figure 13 we compare the axial development of midspan circumferential profiles of ζ' from experiment and from the three different CFD cases (steady cooled; steady uncooled and unsteady cooled).

The most striking feature of the comparison is the significant over-prediction of loss, and under-prediction of mixing, in all of the CFD simulations. This is true in all three axial planes. Broadly speaking, the predicted *peak* loss (due both to over-prediction of overall loss, and under-mixing of the wake) is approximately double that measured experimentally. This is a fairly significant result for multi-row analysis: in our particular example a rotor leading edge would typically sit in the range $0.30 < x/C_x < 0.60$, and all three CFD methods would grossly over-predict the arising unsteadiness and forcing function.

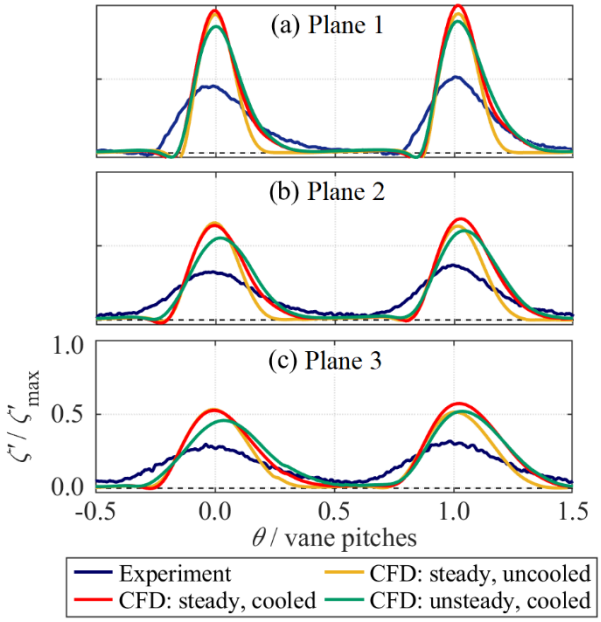


Figure 13: Comparison of midspan circumferential profiles of ζ' between experiment and three CFD methods at: (a) plane 1; (b) plane (2); and (c) plane 3.

We now compare the three CFD methods. Adding film cooling to the steady simulation has two effects. Firstly, a small (around 3–5%) increase in peak loss (expected due to the thicker boundary layers), and secondly a broadening of the PS edge of the wake profile (by around 14%), where the presence of late-PS film cooling rows widens the wake by increasing the accumulation of low-momentum flow, and enhancing the mixing loss. This increases the asymmetry in the profile shape, more closely matching the experiment.

The effect of moving between steady and time-averaged unsteady predictions (both with film cooling) is a small drop in peak loss (approximately 11.5%), and a rise in wake width (by 14.0% at the half-height points). The effect on overall loss coefficient is relatively small, so these are the concomitant effects of enhanced mixing, particularly due to TE vortex shedding. The result is a marginally improved match with experiment.

Radial profiles of local kinetic energy loss coefficient: comparison of experimental data at different axial planes

We now consider radial profiles of circumferentially-mass-flux-averaged KE loss coefficient, ζ''' (equation (12)). Experimentally measured radial profiles of ζ''' at planes 1, 2 and 3 are compared in Figure 14. Note that radial profiles we present have no radial averaging or smoothing: each data point represents an individual sweep of the traverse probe.

In the region between 20–80% span, the average loss coefficient is fairly constant and relatively similar between the three planes. This region is dominated by 2D *profile* loss, so this result is expected. Examining this region in more detail, we see small radial fluctuations, particularly noticeable at plane 1. Local minima can be seen at approximately 14%, 28%, 40%, 54%, 70% and 86% span. The same minima are present in downstream planes, but are more mixed out. These radial locations match the position of the minima in the wake signatures observed in Figure 10a. Recall that we noted these features in the local loss coefficient distributions (Figure 10) align with the internal cooling *lands* (solid ribs) within the TE slot (see Figure 9). Loss coefficient minima—indicated by a narrower and shallower wake in the local distribution, and a local minimum of ζ''' in the radial profile—occur directly downstream of solid ribs within the TE slot. At these locations a local deficit of coolant flow is expected, with higher losses between ribs where coolant is injected.

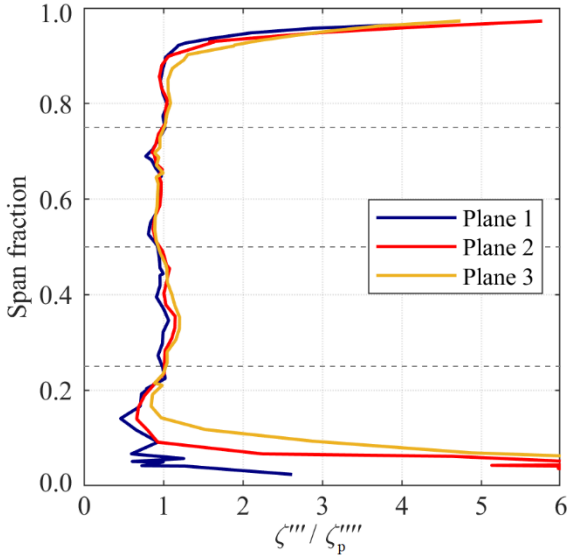


Figure 14: Experimentally-measured radial profiles of circumferentially-mass-flux-averaged KE loss coefficient, ζ''', in three axial planes.

The regions 0–20% span and 80–100% span have contributions from both profile loss and endwall loss. Moving from plane 1 to 3, the loss coefficient in this region increases and the region of deficit expands. At the hub, the mean loss (between 0–20% spam) rises by +301.6% between planes 1 and 2, and by +34.7% between planes 2 and 3. The corresponding rises at the case (80–100% span) were +30.3% and +2.4%. These increases can be attributed to both mixing out of SKE and endwall boundary layer growth. The particularly strong rise between planes 1 and 2 at the hub is likely dominated by the mixing out of strong secondary flows (e.g. the distinct secondary loss core just outside of the hub boundary layer at ~10% span, corresponding with the hub passage vortex core).

Radial profiles of local kinetic energy loss coefficient: comparison of CFD and experimental data

We now compare radial profiles of circumferentially-mass-flux-averaged KE loss coefficient, ζ''', between experiment and CFD. Figure 15 compares experimental and CFD data (three methods) at plane 2. In the range 80-95% span, there is a significant minimum in loss coefficient in all three CFD simulations, not

seen in the experimental data (see also Figure 11b and c). This is associated with radially-inward migration of low momentum secondary flow and wake region flow, an effect which is significantly more pronounced in CFD than in experiment.

All three CFD methods over-predict the average loss coefficient over the 20-80% span profile region. The over-predictions with respect to the experimental mean in this region were +2.3%, +22.4% and +24.9% for the uncooled RANS, cooled RANS, and cooled URANS methods, respectively. That is, ζ''' is slightly over-predicted by uncooled RANS, and greatly over-predicted by both the cooled RANS and URANS methods. We infer that approximately 90% of the over-prediction in the two cooled CFD methods might be attributed to over-prediction of the total pressure loss associated with film cooling. A significant improvement could likely be achieved by replacing the source-terms film cooling model with fully-resolved cooling hole geometries (at the cost of computation time). The remaining small differences between experimental data and uncooled RANS are likely caused by a combination of inaccurate predictions of base pressures and boundary layer thicknesses, and over-prediction of radial migration (downwash) resulting in the region of very low loss coefficient between 80–95% span (profile loss region confined to a smaller radial range, giving a slightly higher average ζ''').

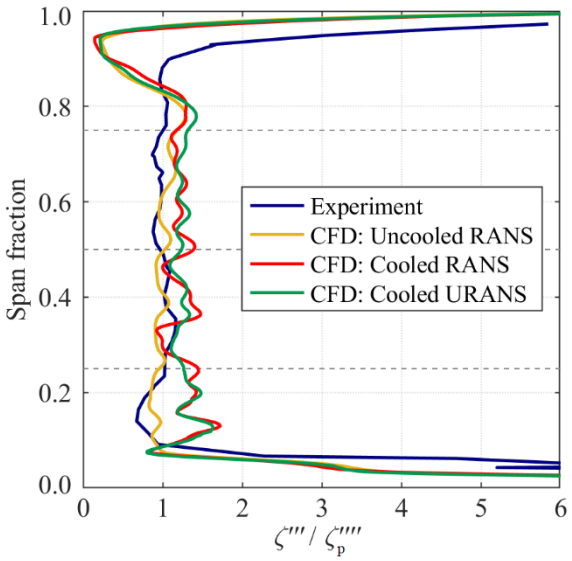


Figure 15: Radial profiles of circumferentially-mass-flux-averaged ζ''' for experiment and three CFD methods at plane 2.

We now examine more closely the secondary radial variation in ζ''' within the profile region (20-80% span). Recall that our local definition of ζ'''—equation (10)—does not include the KE of coolant flow in the denominator (a necessity because local coolant mass-fraction is unknown). The consensus in the literature is that, for a KE loss coefficient not accounting for changes in coolant mass flow rate in the denominator, loss coefficient first rises with the introduction of moderate TE coolant flow, before reaching a maximum and then falling as the flow rate becomes large ([9],[10],[41]). The trend in the experimental data (see Figure 14 and analysis) is for ζ''' minima directly downstream of the solid ribs (lower coolant flow rate), and ζ''' maxima downstream of the open TE (higher coolant flow rate). This suggests that in the experiment, the local coolant mass flow rates are distributed on the rising part of the curve—before the point of maximum loss (for the given geometry).

Looking now at the uncooled RANS profile, we see an opposing trend, with ζ''' *maxima* directly downstream of the solid ribs at 14%, 27%, 39%, 52%, 66% and 79% span (lower coolant flow rate), and ζ''' *minima* downstream of the open TE (higher coolant flow rate). This suggests that the CFD-predicted *local* coolant mass flow rate downstream of the open TE is located on the falling part of the curve, beyond the maximum point (similar overall mass flow rate, but locally higher due to under-mixing as it emerges from the slot). The results for the cooled RANS and cooled URANS methods have a more ambiguous trend. The TE slot radial signature is conflated with distinct ζ''' maxima associated with individual film rows (these being significantly under-mixed with respect to the experiment). URANS slightly damps out the radial variation due to the enhanced mixing induced by vortex shedding close to the TE.

Circumferential distributions of whirl angle

In Figure 16 we compare circumferential profiles whirl angle, β, at midspan in planes 1, 2 and 3 between experiment and all three CFD methods. Here β is defined as the angle between the local velocity vector and the axial direction, in the axial-circumferential plane. Vertical dashed lines indicate approximate wake centre locations.

The profile shapes vary significantly between the three axial planes and between experiment and CFD, but the variation between the CFD methods is small. That is, the result is relatively independent of the fidelity of the method, and of film coolant introduction, other than a small ($< 0.7°$) local β-reduction to the PS of the wakes, where film concentration is high.

The most striking difference between experiment and CFD is that, in all three planes, the variation in β over the profile is greater in the experiment (range of 8.8°, 5.5°, and 4.1° in planes 1, 2 and 3 respectively) than CFD (range of 2.7°, 2.7°, and 0.9° in planes 1, 2 and 3 respectively). This difference in trend (as opposed to absolute magnitude) appears to be dominated by the failure of CFD to adequately predict the peak in β to the SS of the TEs ($\theta \approx -0.2$ and 0.8). This is thought to be due to over-prediction of shock-boundary layer interaction causing the SS boundary layer to separate upstream of the TE, leading to local under-turning on the SS.

We now consider the different circumferential β distributions between the three planes. The profile in plane 2 has the expected shape: a steep whirl angle gradient from a maximum on the SS to a minimum on the PS (corresponding to the difference in TE metal angles) and a shallow β-gradient across the passage.

The circumferential profile in plane 1 has an additional secondary minimum near the passage centre ($\theta = 0.55$) instead of a continuous, shallow gradient. This is caused by a local static pressure maximum, which diffuses the flow, and turns it towards

the axial (mildly subsonic flow turning into greater area)—i.e. towards lower β. This effect is analysed in detail in [42]. The same excursion in the static pressure field intersects plane 2 near the wake centre, and is responsible (in combination with mixing) for the reduction in whirl angle at the SS peak (by −2.8°) and at the PS minimum (by −1.5°) between planes 1 and 2.

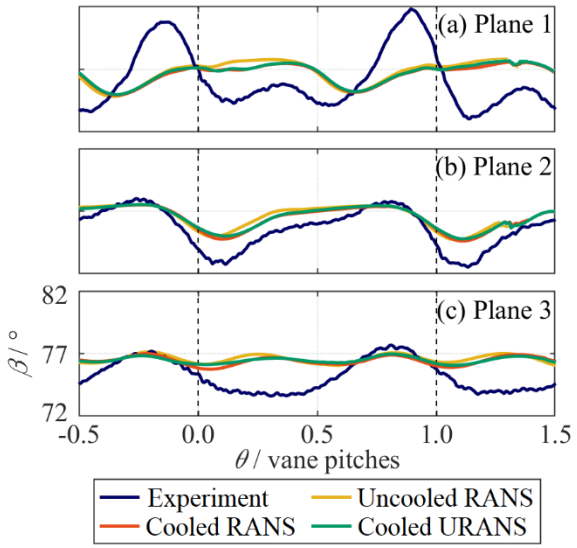


Figure 16: Circumferential profiles of whirl angle at midspan for experiment and three CFD methods, in three axial planes.

Radial distributions of whirl angle

Figure 17a and b show radial profiles of circumferentially-mass-flux-averaged β, in the axial planes 1 to 3, for experiment and cooled URANS respectively. The general shape of the radial profile was closely matched between experiment and CFD, showing a gradual rise in mean turning angle moving radially outwards between 17–66% span, and an approximately constant value between 66–93% span. Below 10% span, all profiles have the expected characteristic over-turning of the endwall boundary layer and under-turning of the secondary flow just outside the boundary layer. In experiment, the under-turned secondary flow was only visible in plane 1, before being overwhelmed by the over-turned boundary layer in planes 2 and 3. CFD shows some under-turning at the location of the secondary flow in all three planes, due to the lower rate of boundary layer growth.

The experimental data show a small reduction in mean turning angle from plane 1 to 3 over most of span. The average changes in $\overline{\beta}$ over the range 20–80% span were −0.45° between planes 1–2, and −0.15° between planes 2–3. In contrast, cooled URANS show almost no change in whirl angle between the three axial planes (< 0.10°).

The absolute values of circumferential-mean whirl angle are slightly over-predicted in CFD. The average offsets between experiment and each of the three CFD methods, evaluated over 20–80% span, were +0.74°, +0.66° and +0.70°, for uncooled RANS, cooled RANS and cooled URANS respectively. These absolute offsets are considered to be remarkably small: well within the combined bias error of the probe due to absolute rotational positional accuracy, which is estimated as ±1.72°. For completeness, we note that the change in average whirl angle between the three CFD methods (not shown) was extremely small (within 0.09° over most of the span).

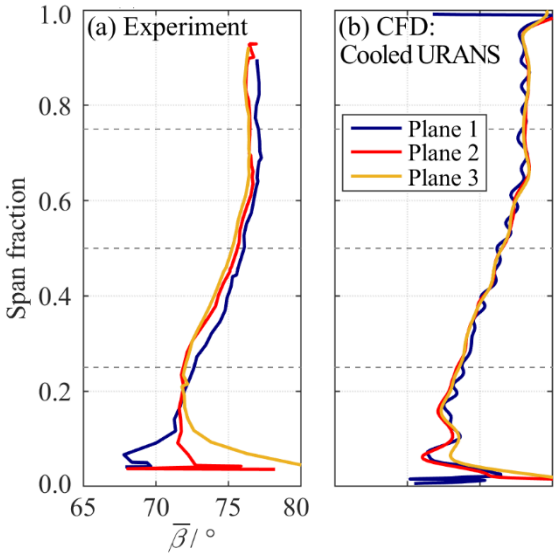


Figure 17: Radial profiles of circumferentially-mass-flux-averaged flow turning angle, β, for: (a) experiment; and (b) cooled URANS, in three axial planes.

Method for characterising wakes

The tendency of CFD methods to significantly over-predict peak loss coefficient and under-predict wake width gives poorly defined inlet conditions to the following rotor row. The implications of this for design are significant, both in terms of the performance penalty due to unsteady inlet flow (off-design incidence angles) and the optimisation of the rotor cooling system. By understanding and quantifying this, we aim to provide better guidelines for CFD characterisation and turbine design.

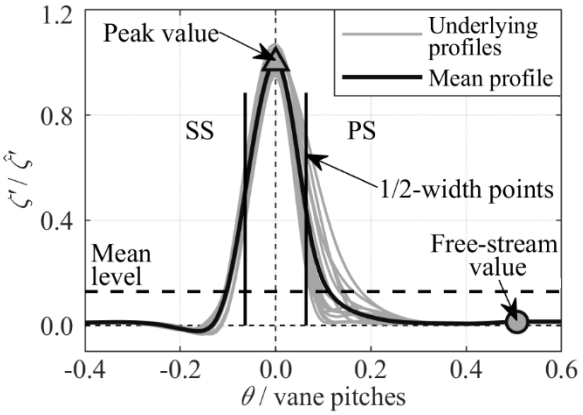


Figure 18: Circumferential variation of local KE loss coefficient in a 10% span range around midspan.

In order to do this, we now characterise a *mean profile* obtained by averaging a series of underlying profiles over a 10% span range. In experiments, the underlying profiles are individual passes of the traverse probe (see Figure 5) within the averaging range, and in CFD they are rows of a uniformly-spaced grid within the averaging range. The underlying and mean profiles are shown in Figure 18, taking an example from cooled URANS CFD. We see that the main difference between underlying profiles is in the width of the distribution on the PS of the peak, caused by radial variations in local film coolant concentration. We characterise the wake by peak height, peak width (circumferential range over which ζ' exceeds 50% of the peak height, indicated by solid black lines), and circumferential average value (dashed black line). The axial variation of each of these parameters is now examined in turn.

Variation in wake peak height with axial distance

Figure 19 shows axial trends in the peak value of ζ' at 25% (downward-pointing triangles), 50% (circles) and 75% span (upward-pointing triangles), for experiment, uncooled RANS and cooled URANS. As expected, all of the data follow a quasi-exponential decay. As observed previously, the CFD methods predict higher peak loss coefficient than in experiment due to both the under-prediction of mixing and the over-prediction of overall loss. Peak ζ' is higher close to the hub (see also Figure 12 and analysis), with the trends at 50% and 75% span being similar. The greater peak loss coefficient at 25% span is primarily driven by vane sweep and turning profile differences with radius, which lead to different streamline path lengths between the TE and the measurement planes at the three span locations.

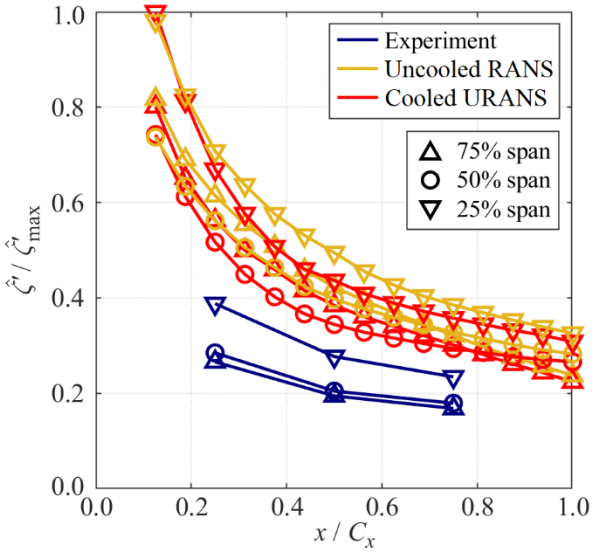


Figure 19: Axial trends in peak KE loss coefficient, ζ', at three spanwise locations, for experiment and two CFD methods.

Considering both the *spanwise-local* axial distance between the TE and each measurement plane, x', and the mean turning angle at each span location, $\overline{\beta}$, we calculate the actual streamwise path length, d, between the local TE and the measurement plane, for each of 25%, 50% and 75% span, as $d = x' \cos\overline{\beta}$. The results for each of planes 1, 2 and 3 are shown in Figure 20. We see that the streamwise path length is greatest at 60% span and reduces moving away in either direction, becoming particularly small near to the hub.

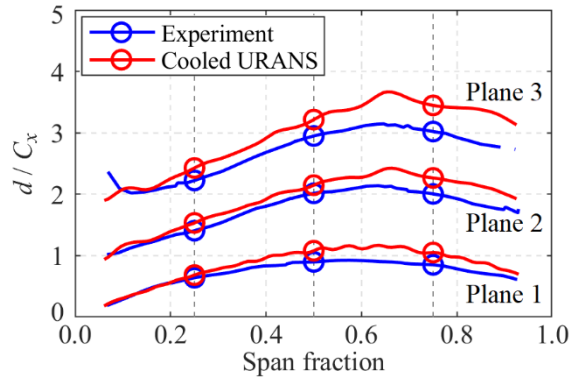


Figure 20: Spanwise profiles of streamwise path length, d, between the local TE and each of planes 1, 2 and 3.

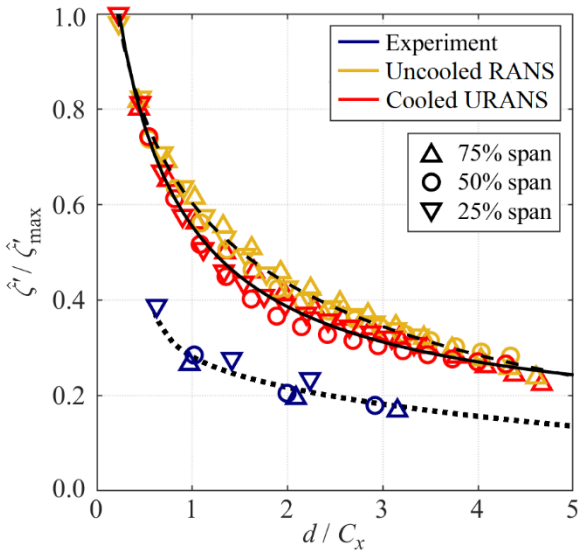


Figure 21: Trends in peak KE loss coefficient, ζ', at three spanwise locations, with local streamwise path length.

In Figure 21, we then replot the data in Figure 19 as a function of d/C_x (in place of x/C_x). The collapse of the data at the three spanwise locations on to a single trend for each of experiment, uncooled RANS and cooled URANS is quite compelling. Best-fit curves (least-squares method) give $d^{-0.45}$ for uncooled RANS, and order $d^{-0.90}$ for cooled URANS (steeper initial decay due to the enhanced mixing close to the TE associated with TE vortex shedding). These are close to the $d^{-0.50}$ characteristic observed by previous studies (e.g. [43], [44]). Experimental data are well-fitted with a $d^{-0.50}$ characteristic (R-squared equal to 0.94) but the data are too sparse to estimate a meaningful best-fit decay rate.

The good collapse of this data suggests that, even for vanes of moderate sweep, care should be taken when interpreting data at a single axial plane. The collapse also provides a basis for a

model of peak loss coefficient decay based on local streamwise path length.

Streamwise development of wake width

Figure 22 shows axial trends of wake width, w, at 25%, 50% and 75% span for experiment, uncooled RANS and cooled URANS as a function of local streamwise path length, d/C_x. In both experimental and CFD trends, wake width increases monotonically with streamwise distance as the wakes mix out. With respect to experiment, the CFD simulations are under-mixed, and the absolute wake width at an equivalent streamwise path length is lower. For all of the data, mixing rate is highest at the case and lowest at the hub.

There is a modulation in the gradient of wake width with streamwise distance, with regions of reduced gradient at $d/C_x \approx 2.0$ and $d/C_x \approx 4.0$. This is clearly seen in both CFD methods, and supported by the experimental data (despite its low streamwise resolution. The modulation is caused by periodic streamwise pressure gradients which the flow passes through as it develops downstream of the cascade. A narrow region of high pressure extends almost axially downstream of each TE, resulting in periodic diffusion (enhanced rate of wake spreading) and acceleration (reduced rate of wake spreading) of the flow, in phase with the vane pitch spacing (approximately every $d/C_x \approx 2.0$ in the streamwise direction). The same effect is responsible for influencing the whirl angle profiles in different axial planes (Figure 16 and associated discussion). This effect is discussed in detail in [42], and is in accord with the results of Thomas and Liu [44] who studied the response of turbulent wakes to different streamwise pressure gradients.

For completeness, we note that trends in wake width as a function of axial distance from the midspan TE (x/C_x, not presented) are similar, but with greater variation between the different spanwise locations.

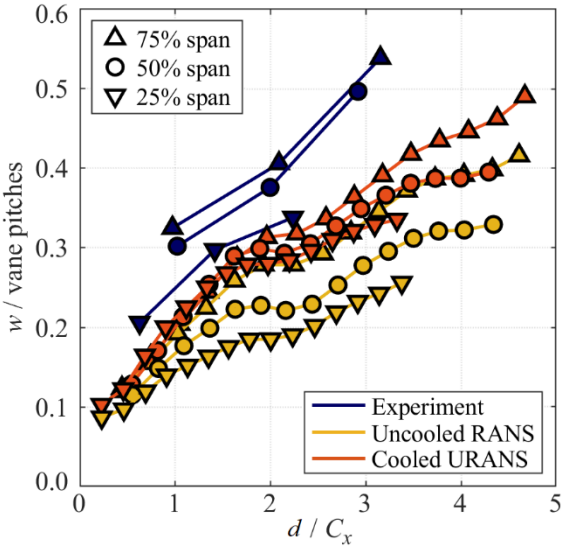


Figure 22: Trends in wake width, w, at three spanwise locations, as a function of local streamwise path length.

Streamwise development of circumferential mean KE loss coefficient

Figure 23 plots circumferentially-mass-flux-averaged KE loss coefficient at 25%, 50% and 75% of span as a function of streamwise distance, d/C_x. The data are averaged over a 10% span region centred on the relevant spanwise location. Presented in this way, both the experimental and cooled URANS data have reasonably good agreement between spanwise locations in their respective trends. In contrast, uncooled RANS simulations show significantly higher mean loss coefficient at 75% span than other span locations. For $0 < d/C_x < 3$, all of the characteristics have very similar trends with a gradual rise in ζ''' with streamwise distance. This is expected on the basis of gradual mixing out of SKE. The cooled URANS simulations over-predict the average loss coefficient by approximately +27.0% with respect to the experimental data.

Explaining secondary variations in the trends is more complex, and influenced by the modulation of wake mixing rate under the influence of the periodic streamwise pressure gradient (see discussion around Figure 22). We can see, for example, that both the uncooled RANS and cooled URANS trends at 50% span reach a plateau at around $d/C_x = 2$, before rising again further downstream. A second effect is radially-inward migration of lower momentum secondary and coolant flows, which changes the composition of the flow being averaged with increasing streamwise distance. As an example of this, looking at 75% span data, we see that both CFD simulations show a sharp reduction in KE loss coefficient for $d/C_x > 3$. This is attributed to the region of very low loss coefficient predicted by CFD near the case (see Figures 10 and 15) starting to encroach on the 75% span averaging region.

The average KE loss coefficient evaluated at a specific spanwise location is clearly sensitive to a number of factors and requires careful interpretation.

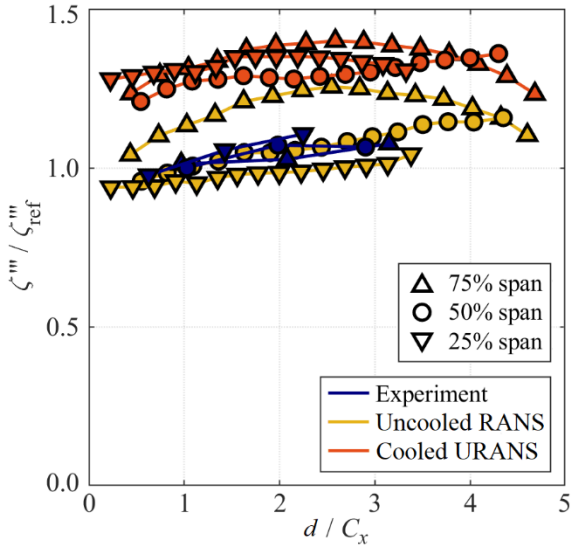


Figure 23: Trends in mass-flux-averaged KE loss coefficient, ζ''', at three spanwise locations as a function of local streamwise path length.

Axial development of plane-average and mixed-out KE loss coefficients

We now consider the axial development of plane-average loss coefficient, ζ'''' (equation (13)), and mixed-out loss coefficient, ζ''''' (equation (14)), for experimental data and cooled URANS. These data are presented in Figure 24, normalised with respect to the experimental mixed-out loss coefficient in plane 3. Plane-average loss coefficient is further separated into *profile* and *endwall* components (common practice, following e.g. [1]) using integration regions that distinguish the two: a detailed explanation of the method is given in Appendix B. In line with arguments presented earlier in this paper, we refer to the difference between mixed-out loss coefficient and plane-average loss coefficient as *residual SKE*. This is also shown in the figure. Finally, for cooled URANS simulations, the KE loss due to viscous dissipation in the vane surface boundary layers is also plotted. This is estimated from velocity profiles extracted at midspan, assuming uniform thickness across the span, using the method of [43]. The remaining difference between profile plane-average loss coefficient and boundary layer loss can be attributed to TE and mixing losses upstream of the traverse plane. Table 2 summarises the magnitudes of each loss component in each of planes 1 to 3, expressed as percentages of the total mixed-out loss coefficient in that plane.

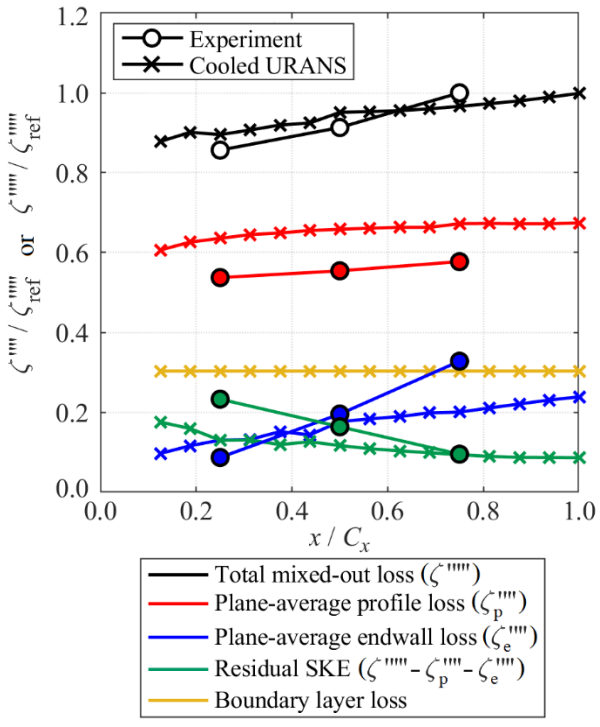


Figure 24: Axial trends of plane-average KE loss coefficient, ζ'''', and mixed-out KE loss coefficient, ζ''''', for experiment and cooled URANS.

The following observations are drawn:

1. Axial gradients of loss coefficient are broadly as expected. Plane-average profile loss coefficient increases slowly in the downstream direction, as SKE is gradually converted to total pressure loss. Plane-average endwall loss coefficient rises more rapidly with axial distance due to both boundary layer growth, and concentration of SKE in the endwall flow. Residual SKE falls in the downstream direction as it mixes out. There is a positive axial gradient of total mixed-out loss coefficient, explained by endwall boundary layer growth.

2. Cooled URANS over-predicts the absolute plane-average profile loss coefficient with respect to experiment by an average (between planes 1, 2 and 3) of 17.9%. The difference in the absolute value of profile loss coefficient is primarily attributed to over-prediction of the total pressure loss associated with film cooling. The difference between the uncooled and cooled CFD results indicates that this accounts for approximately 90% of the over-prediction of absolute loss coefficient. Inaccurate prediction of base pressures and boundary layer thicknesses, and over-prediction of the radial downwash effect of lower momentum flow (including coolant flow) are likely smaller contributing effects.

3. There is good agreement between experiment and cooled URANS for the total mixed-out loss coefficient. The average (across data in planes 1, 2 and 3) discrepancy between experimental and numerical data is 4.0%. This result is somewhat contrary to expectation, as the under-prediction of mixing rates by CFD would lead us to expect greater residual SKE in CFD than in experiment. Close to the TE (for example in plane 1), both plane-average profile and endwall loss coefficients are over-predicted by URANS. The good agreement in total mixed-out loss coefficient arises from a higher residual SKE in experiment compared to CFD. This could potentially be explained by the greater whirl angle variation observed in the experimental data compared to CFD (see Figure 16). This may provide the experimental data with an additional mixing loss mechanism. Further downstream (for example in plane 3), URANS over-predicts plane-average profile loss coefficient but significantly under-predicts plane-average endwall loss coefficient (due to under-predicting the boundary layer growth rate on the exit duct endwalls), whilst the residual SKE is identical. The result is a closely matched total mixed-out loss coefficient. When comparing results between experiment and CFD, the use of mixed-out loss coefficients is therefore strongly recommended.

4. The axial gradients of plane-average profile loss coefficient and total mixed-out loss coefficient were reasonably matched between experiment and CFD over most of the range. Plane-average profile loss coefficient increased between planes 1 and 3 by +7.4% in experiment and by +5.8% in cooled URANS. Total mixed-out loss coefficient increased between planes 1 and 2 by +6.6% in experiment and by +6.2% in cooled URANS. Between planes 2 and 3, however, the rise measured in the experiment (+9.5%) was greater than that

predicted by CFD (+1.6%) because of significant under-prediction of endwall boundary layer growth.

5. The gradient of plane-average endwall loss coefficient was significantly under-predicted by CFD (under-prediction of the rate of endwall boundary layer growth). Plane-average endwall loss coefficient rose between planes 1 and 3 by a factor of 3.78 in experiment, compared to 1.54 in cooled URANS.
6. Boundary layer loss (vane surface boundary layers in the profile loss region) is estimated to account for 45.1% of the CFD-predicted plane-average profile loss coefficient in plane 3, and 31.4% of the mixed-out loss coefficient.

Table 2: Summary of percentage contributions to mixed-out KE loss coefficient for experiment and cooled URANS in planes 1–3.

Loss component	$\frac{\zeta''''}{\zeta'''''}$ (%) at plane 1 ($x/C_x = 0.25$)		$\frac{\zeta''''}{\zeta'''''}$ (%) at plane 2 ($x/C_x = 0.50$)		$\frac{\zeta''''}{\zeta'''''}$ (%) at plane 3 ($x/C_x = 0.75$)	
	Experiment	Cooled URANS	Experiment	Cooled URANS	Experiment	Cooled URANS
Plane-average profile loss	62.7%	71.0%	60.7%	69.2%	57.7%	69.6%
Boundary layer loss	–	33.9%	–	31.9%	–	31.4%
Plane-average endwall loss	10.1%	14.5%	21.4%	18.5%	32.8%	20.7%
Residual SKE	27.2%	14.5%	17.9%	12.2%	9.5%	9.7%

SENSITIVITY OF LOSS COEFFICIENT TO EXIT MACH NUMBER

All of the data presented so far has been at a common, fixed vane exit Mach number condition $M_2 = 0.97$. We now consider the effect of varying the M_2 condition. Experimental tests were conducted in the ECAT facility operating in blowdown mode (as described in the earlier section). Corresponding numerical simulations were performed at five distinct exit Mach numbers (in the range $0.63 \leq M_2 \leq 1.11$) by varying the downstream static pressure boundary condition. Only cooled RANS simulations were performed at the off-design Mach number conditions, to reduce computational time.

Circumferential profiles of ζ' in plane 1 at midspan are plotted in Figure 25a and b for experiment and cooled RANS respectively, at the five distinct M_2 conditions. All of the data are normalised with respect to the maximum value of ζ' at $M_2 = 0.97$. We can see that increasing M_2 has two primary effects. Firstly, the peak loss coefficient in the wake centre gradually reduces, and secondly the wake width gradually reduces, mainly due to a significant decrease in loss coefficient to the PS of the peak.

Figure 26 plots peak loss coefficient and wake width at midspan as functions of M_2. All of the data are normalised with respect to the values at $M_2 = 0.97$. In both experiment and CFD, peak loss coefficient falls with increasing M_2. CFD under-predicts the gradient by approximately 54%. The wake width follows almost the same trend in experiment and CFD for $M_2 < 1.0$—dropping by 21.4% between $0.63 \leq M_2 \leq 0.97$. However, whilst in experiments there is an abrupt increase in width of +10.9% for $0.97 \leq M_2 \leq 1.11$, CFD predicts a reduction in width. The change in behaviour at the supersonic M_2 condition is caused by the presence of a shockwave just upstream of the SS TE. This accounts for the widening of the wake profiles in Figure 25 to the SS of the peaks (sudden late SS diffusion causing rapid boundary layer growth). We further interrogate the difference between the experimental and CFD cases by comparing average loss coefficient values.

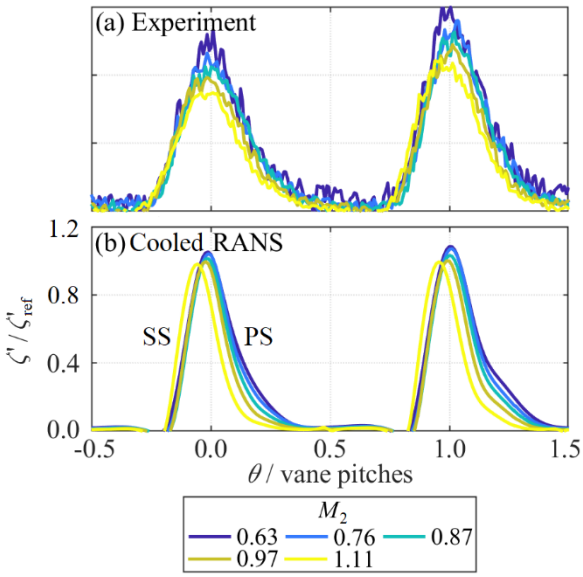


Figure 25: Circumferential profiles of ζ' at midspan in plane 1, at five different vane exit Mach number conditions.

Figure 27 compares trends in circumferentially-mass-flow-averaged KE loss coefficient, ζ''' (equation (12)) with M_2 between experiment and cooled RANS, at midspan in plane 3. The experimental data represent an average over two vane pitches and over a thin radial strip around midspan (single pass of the traverse probe, see Figure 6). Each numerical data point represents an average over two vane pitches and ±5% span around midspan. All of the data in Figure 27 are normalised with respect to the experimental-measured loss coefficient at $M_2 = 0.97$.

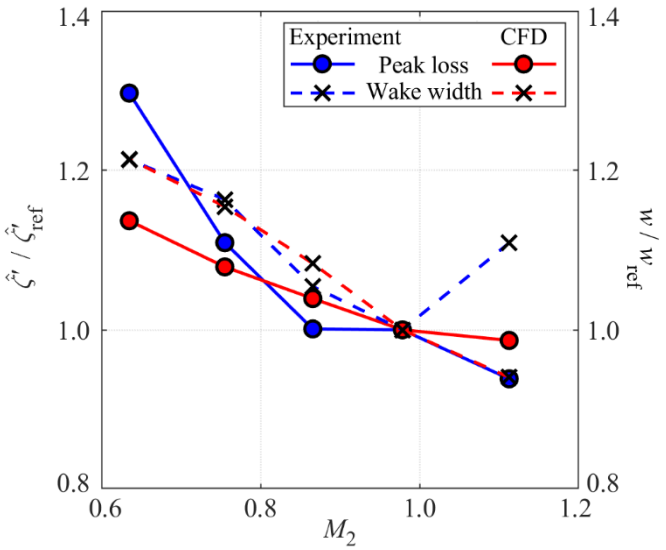


Figure 26: Midspan trends in peak loss coefficient and wake width, with exit Mach number.

For $M_2 < 1.0$, both experiment and CFD show an almost linear fall in ζ''' with rising M_2. Between $0.63 < M_2 < 0.97$, ζ''' fell by −23.8% in experiment, compared to −27.0% in CFD. For $M_2 > 1.0$, whilst the numerical trend deviates only marginally from the linear relationship (slightly shallower gradient), the experimental trend increased by +6.2% between $0.97 \leq M_2 \leq 1.11$. The difference in ζ''' between the experiment and cooled RANS at $M_2 = 1.11$ was only 15.5% compared to an average of 40.5% across the four subsonic conditions.

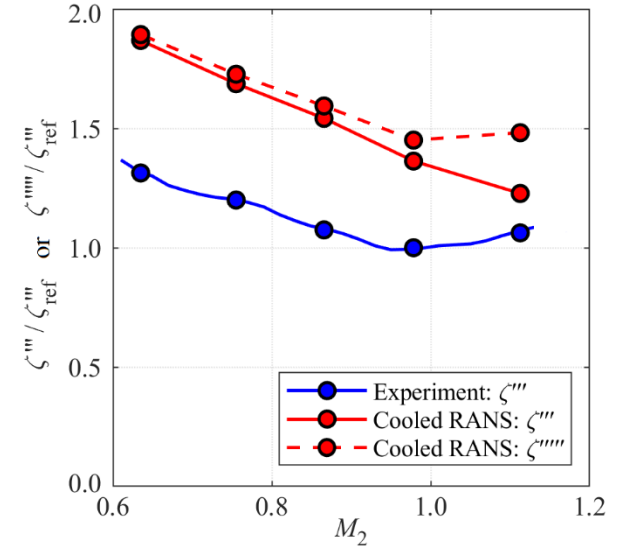


Figure 27: Circumferentially-mass-averaged KE loss coefficient, ζ'', at midspan in plane 3, as a function of M_2.

The CFD-predicted trend in *mixed-out* loss coefficient does show an increase between $0.97 < M_2 < 1.11$, but by only +2.2%. That is, the increased loss coefficient observed in the experimental data at $M_2 = 1.11$ was also present in CFD but to a lesser degree and only when the flow was fully mixed-out. Based on this evidence, the difference between experimental and cooled RANS data is thought to be caused by two effects. Firstly, the shockwave at the SS TE was somewhat poorly resolved in the CFD result, and was therefore 'smeared out' to give an adverse pressure gradient rather than a sharp discontinuity. This explains why most of the additional loss coefficient associated with the shock is only seen in the CFD data when the flow is fully mixed out (adverse pressure gradient increases the rate of shear in regions of velocity gradient at the edge of the wake). Secondly, the shockwave in the experimental case may be moving unsteadily. Such an unsteady effect would increase the mixing of the wake profile close to the TE for approximately the same level of overall (mixed-out) loss coefficient. Unsteady movement of the shock would not be expected to be predicted by steady RANS, but may contribute to the smearing out of the shock.

SUMMARY AND CONCLUSIONS

In this paper, we have presented high-fidelity experimental traverse data downstream of an annular cascade of engine component HP turbine NGVs, in three axial planes. The data address a gap in the literature for detailed aerodynamic traverse measurements downstream of actual engine parts complete with film and TE cooling flows. They also provide an important benchmark for high-TRL numerical predictions of HP NGV aerodynamic performance. The data have been compared with CFD models at a range of fidelity levels.

All of the CFD models (steady and unsteady, excluding and including surface film cooling) under-predict the rate of mixing out of the non-uniform exit flow-field, and significantly over-predict the profile loss coefficient (by an average of 17.9%) determined in a given axial plane. The over-prediction of profile loss coefficient is primarily attributed to over-prediction of the total pressure loss associated with the mixing of surface film cooling. Fully-resolving the film cooling holes, in place of a source-terms model, would likely improve the quality of prediction. Inaccurate prediction of base pressures and boundary layer thicknesses, and over-prediction of the radial migration effect of lower momentum flow (including coolant flow) are smaller contributing effects.

The agreement between experiment and CFD for mixed-out loss coefficient was significantly better than for plane-average loss coefficient (average difference of 4.0%, compared with 17.9%). The improved comparison arises because the combined discrepancy in the plane-average endwall loss coefficient (under-predicted due to under-prediction of the endwall boundary layer growth rate) and the mixing loss coefficient (associated with the mixing out of residual SKE in the flow) is approximately equal in size but opposite in sign to the discrepancy (over-prediction) in plane-average profile loss coefficient. When comparing results between experiment and CFD, the use of mixed-out loss coefficients is therefore strongly recommended.

The local distributions of loss coefficient downstream of the NGV cascade measured in experiments and predicted by

CFD were also examined in detail, and from this the key conclusions were:

1. The experimental wake profile had a distinctive radial non-uniformity in local loss coefficient caused by the presence of internal rib cooling features within the TE slot. This was a significant effect, and the sort that would be difficult to detect without testing engine components. CFD methods failed to reproduce the deviations in the radial loss coefficient trend. We propose a mechanism that could explain the discrepancy, but feel this warrants further investigation.
2. Significant differences in circumferential local loss coefficient distributions were observed between different radial sections in the same axial plane. These differences arise because of radial variations in lean, sweep and turning angle, which cause the streamwise path length between the TE and a specific axial plane to vary with radial height. A corollary of this radial variation was that axial trends in both peak local loss coefficient and wake width measured at different radial heights did not collapse to a common trend when presented in terms of axial distance. However, when presented as functions of streamwise path length the collapse to a common characteristic was compelling. This illustrates that significant care must be taken when interpreting data measured downstream of real vane geometries. The data also provide a basis for a model of wake profile decay based on local streamwise path length. This is an extremely important outcome for predicting thermal and aerodynamic rotor forcing effects.
3. The sensitivity of midspan loss coefficient to exit Mach number was examined. In the subsonic regime, increasing exit Mach number reduced both the peak local loss coefficient, and the wake width, producing a drop in average loss coefficient. A rise in loss coefficient was observed when Mach number exceeded unity, associated with the presence of a shockwave at the SS TE.

NOMENCLATURE

Romans

c_p Specific heat at constant pressure, J kg^{-1} K^{-1}
C_x Axial chord length, m
d Path length in streamwise direction, m
h Static enthalpy, J kg^{-1}
h_0 Stagnation enthalpy, J kg^{-1}
M Mach number, –
M_2 Mean vane exit Mach number, –
$\dot{m}$ Mass flow rate, kg s^{-1}
p Static pressure, Pa
p_0 Stagnation pressure, Pa
$\overline{p_{02}}$ Plane-average downstream stagnation pressure, Pa
$\overline{p_{02}}'$ Mixed-out average downstream stagnation pressure, Pa
p_2 Mean vane exit static pressure, Pa
$\overline{p_2}$ Plane-average downstream static pressure, Pa
$\overline{p_2}'$ Mixed-out average downstream static pressure, Pa
r Radial position, m
Re Reynolds number, –
s Static entropy, J kg^{-1} K^{-1}
T Static temperature, K
T_0 Stagnation temperature, K
v Velocity, m s^{-1}
w Wake width, m
x Axial distance, m
x' Local axial distance between TE and axial plane, m
Y Stagnation pressure loss coefficient, –

Greeks

α Flow pitch angle, degrees
β Flow turning (or whirl) angle, degrees
$\overline{\beta}$ Circumferential-average whirl angle, degrees
γ Ratio of specific heats, –
ζ Kinetic energy loss coefficient, –
ζ' Local kinetic energy loss coefficient, –
$\hat{\zeta}'$ Peak local kinetic energy loss coefficient, –
ζ'' Kinetic energy loss coefficient accounting for energy input of coolant flow, –
ζ''' Circumferential-average kinetic energy loss coefficient at a particular radius, –
ζ'''' Plane-average kinetic energy loss coefficient, –
ζ''''' Mixed-out kinetic energy loss coefficient, –
η Row efficiency, –
ρ Mass density, kg m^{-3}
θ Normalised circumferential distance, vane pitches
χ $(\gamma - 1) / \gamma$

Subscripts

0 Stagnation conditions
1 Vane inlet condition
2 Vane exit conditions
c Coolant stream
e Endwall
m Mainstream
max Maximum value
p Profile
ref Reference condition for normalisation
s Isentropic condition

Acronyms

CFD Computational fluid dynamics
HP High pressure
KE Kinetic energy
NGV Nozzle guide vane
PS Pressure side
RANS Reynolds-averaged Navier-Stokes
SKE Secondary kinetic energy
SS Suction side
TE Trailing edge
TRL Technology readiness level
URANS Unsteady Reynolds-averaged Navier-Stokes

ACKNOWLEDGMENTS

The support of Rolls-Royce plc is gratefully acknowledged.

REFERENCES

[1] Carter, A.D.S.; 1948; Three-Dimensional-Flow Theories for Axial Compressors and Turbines; Proc. Inst. Mech. Eng., Vol. 159(1): 255–268, DOI: 10.1243/PIME_PROC_1948_159_023_02

[2] Ainley, D.G., Mathieson, G.C.; 1951; A Method of Performance Estimation for Axial-Flow Turbines; Aeronautical Research Council London (UK), No. ARC-R/M-2974

[3] Denton, J.D.; 1993; Loss Mechanisms in Turbomachines; Proceedings of ASME 1993 International Gas Turbine and Aeroengine Congress and Exposition; Cincinnati, OH, USA, 24–27 May 1993, Paper No. 93-GT-435, V002T14A001, DOI: 10.1115/93-GT-435

[4] Osnaghi, C., Perdichizzi, A., Savini, M., Harasgama, P., Lutum, E.; 1997; The Influence of Film-Cooling on the Aerodynamic Behaviour of a Turbine Nozzle Guide Vane; Proceedings of ASME International Gas Turbine and Aeroengine Congress and Exhibition 1997, Orlando, FL, USA, 2–5 June 1997, Paper No. 97-GT-522, V001T03A105, DOI: 10.1115/97-GT-522

[5] Ardey, S., Fottner, L.; 1998; A Systematic Experimental Study on the Aerodynamics of Leading Edge Film Cooling on a Large Scale High Pressure Turbine Cascade; Proceedings of ASME International Gas Turbine and Aeroengine Congress and Exhibition 1998, Stockholm, Sweden, 2–5 June 1998, Paper No. 98-GT-434, V004T09A074, DOI: 10.1115/98-GT-434

[6] Day, C.R.B., Oldfield, M.L.G., Lock, G.D.; 1999; The Influence of Film Cooling on the Efficiency of an Annular Nozzle Guide Vane Cascade; ASME J. Turbomach., Vol. 121(1): 145–151, DOI: 10.1115/1.2841223

[7] Chappell, J., Ligrani, P., Sreekanth, S., Lucas, T., Vlasic, E.; 2010; Aerodynamic Performance of Suction-Side Gill Region Film Cooling, ASME J. Turbomach., Vol. 132(3): 031020, DOI: 10.1115/1.3151603

[8] Sieverding, C.H., Arts, T., Dénos, R., Martelli, F.; 1996; Investigation of the Flow Field Downstream of a Turbine Trailing Edge Cooled Nozzle Guide Vane; ASME J. Turbomach., Vol. 118(2): 291–300, DOI: 10.1115/1.2836639

[9] Pappu, K.R., Schobeiri, M.T.; 1999; Optimization of Trailing Edge Ejection Mixing Losses: A Theoretical and Experimental Study; ASME J. Fluids Eng., 121(1): 118–125, DOI: 10.1115/1.2821991

[10] Uzol, O., Camcı, C.; 2001; Aerodynamic Loss Characteristics of a Turbine Blade with Trailing Edge Coolant Ejection: Part II—External Aerodynamics, Total Pressure Losses and Predictions; ASME J. Turbomach., Vol. 123(2): 249–257, DOI: 10.1115/1.1351817

[11] Johnson, J.D., Fiala, N.J., Ames, F.E.; 2009; Gill Slot Trailing Edge Aerodynamics: Effects of Blowing Rate, Reynolds Number, and External Turbulence on Aerodynamic Losses and Pressure Distribution; ASME J. Turbomach., Vol. 131(1): 011016, DOI: 10.1115/1.2813002

[12] Kapteijn, C., Amecke, J., Michelassi, V.; 1994; Aerodynamic Performance of a Transonic Turbine Guide Vane with Trailing Edge Coolant Ejection: Part I—Experimental Approach; Proceedings of ASME 1994 International Gas Turbine and Aeroengine Congress and Exposition, Den Haag, Netherlands, 13–16 June 1994, Paper No. 94-GT-288, V001T01A099, DOI: 10.1115/94-GT-288

[13] Fiala, N.J., Johnson, J.D., Ames, F.E.; 2010; Aerodynamics of a Letterbox Trailing Edge: Effects of Blowing Rate, Reynolds Number, and External Turbulence on Aerodynamic Losses and Pressure Distribution; ASME J. Turbomach., Vol. 132(4): 041011, DOI: 10.1115/1.3195035

[14] Melzer, A.; 2018; Aerodynamics of Transonic Turbine Trailing Edges; PhD thesis, University of Cambridge

[15] Sauer, H., Müller, R., Vogeler, K.; 2000; Reduction of Secondary Flow Losses in Turbine Cascades by Leading Edge Modifications at the Endwall; ASME J. Turbomach., Vol. 123(2): 207–213, DOI: 10.1115/1.1354142

[16] Becz, S., Majewski, M.S., Langston, L.S.; 2004; An Experimental Investigation of Contoured Leading Edges for Secondary Flow Loss Reduction; Proceedings of ASME Turbo Expo 2004, Vienna, Austria, 14–17 June 2004, Paper No. GT2004-53964, DOI: 10.1115/GT2004-53964

[17] Turgut, Ö.H., Camcı, C.; 2013; Influence of Leading Edge Fillet and Nonaxisymmetric Contoured Endwall on Turbine NGV Exit Flow Structure and Interactions with the Rim Seal Flow; Proceedings of ASME Turbo Expo 2013, San Antonio, TX, USA, 3–7 June 2013, Paper No. GT2013-95843, DOI: 10.1115/GT2013-95843

[18] Braünling, W., Lehthaus, F.; 1986; Investigations of the Effect of Annulus Taper on Transonic Turbine Cascade Flow; ASME J. Eng. Gas Turbines Power, Vol. 108(2): 285–292, DOI: 10.1115/1.3239901

[19] Pullan, G., Harvey, N.W.; 2006; Influence of Sweep on Axial Flow Turbine Aerodynamics at Midspan; ASME J. Turbomach., Vol. 129(3): 591–598, DOI: 10.1115/1.2472397

[20] Harrison, S.; 1992; The Influence of Blade Lean on Turbine Losses; ASME J. Turbomach., Vol. 114(1): 184–190, DOI: 10.1115/1.2927982

[21] Bagshaw, D.A., Ingram, G.L., Gregory-Smith, D.G., Stokes, M.R.; 2005; An Experimental Study of Reverse Compound Lean in a Linear Turbine Cascade; Proc. Inst. Mech. Eng., Part A, Vol. 219(6): 443–449, DOI: 10.1243/095765005X31199

[22] Rosic, B., Xu, L.; 2012; Blade Lean and Shroud Leakage Flows in Low Aspect Ratio Turbines; ASME J. Turbomach., Vol. 134(3): 031003, DOI: 10.1115/1.3106002

[23] Ames, F.E., Plesniak, M.W.; 1997; The Influence of Large-Scale, High-Intensity Turbulence on Vane Aerodynamic

Losses, Wake Growth, and the Exit Turbulence Parameters, ASME J. Turbomach., Vol. 119(2): 182–192, DOI: 10.1115/1.2841100

[24] Barringer, M.D., Thole, K.A., Polanka, M.D.; 2009; Effects of Combustor Exit Profiles on Vane Aerodynamic Loading and Heat Transfer in a High Pressure Turbine; ASME J. Turbomach., Vol. 131(2): 021008, DOI: 10.1115/1.2950051

[25] Beard, P.F., Smith, A.D., Povey, T.; 2014; Effect of Combustor Swirl on Transonic High Pressure Turbine Efficiency; ASME J. Turbomach., Vol. 136(1): 011002, DOI: 10.1115/1.4024841

[26] Binder, A., Romey, R.; 1983; Secondary Flow Effects and Mixing of the Wake Behind a Turbine Stator; ASME J. Eng. Power, Vol. 105(1): 40–46, DOI: 10.1115/1.3227396

[27] Sieverding, C.H., Van Hove, W., Boletis, E.; 1984; Experimental Study of the Three-Dimensional Flow Field in an Annular Turbine Nozzle Guide Vane; ASME J. Gas Turbines Power, Vol. 106(2): 437–444

[28] Yamamoto, A., Yanagi, R.; 1985; Production and Development of Secondary Flows and Losses Within a Three Dimensional Turbine Stator Cascade; Proceedings of ASME 1985 International Gas Turbine Conference and Exhibit, Houston, TX, USA, 18–21 March 1985, Paper No. 85-GT-217, DOI: 10.1115/85-GT-217

[29] Williamson, R.G., Moustapha, S.H.; 1986; Annular Cascade Testing of Turbine Nozzles at High Exit Mach Numbers; ASME J. Fluids Eng., Vol. 108(3): 313–320, DOI: 10.1115/1.3242579

[30] Treiber, M., Abhari, R.S., Sell, M.; 2002; Flow Physics and Vortex Evolution in Annular Turbine Cascades; Proceedings of ASME Turbo Expo 2002, Amsterdam, Netherlands, 3–6 June 2002, Paper No. GT2002-30540, DOI: 10.1115/GT2002-30540

[31] Yasa, T., Paniagua, G., Fridh, J., Vogt, D.; 2010; Performance of a Nozzle Guide Vane in Subsonic and Transonic Regimes Tested in an Annular Sector; Proceedings of ASME Turbo Expo 2010, Glasgow, UK, 14–18 June 2010, Paper No. GT2010-22901, DOI: 10.1115/GT2010-22901

[32] Sieverding, C.H.; 1982; The Influence of Trailing Edge Ejection on the Base Pressure in Transonic Turbine Cascades; Proceedings of ASME 1982 International Gas Turbine Conference and Exhibit; London, UK, 18–22 April 1982, 82-GT-50, DOI: 10.1115/82-GT-50

[33] Melzer, A.P, Pullan, G.; 2019; The Role of Vortex Shedding in the Trailing Edge Loss of Transonic Turbine Blades; ASME J. Turbomach., Vol. 141:041001

[34] Léonard, T., Gicquel, L.Y.M., Gourdain, N., Duchaine, F.; 2015; Steady/Unsteady Reynolds-Averaged Navier-Stokes and Large Eddy Simulations of a Turbine Blade at High Subsonic Outlet Mach Number; ASME J. Turbomach., Vol. 137(4): 041001, DOI: 10.1115/1.4028493

[35] Kirollos, B., Lubbock, R., Beard, P., Goenaga, F., Rawlinson, A., Janke, E., Povey, T.; 2017; ECAT: An Engine Component Aerothermal Facility at the University of Oxford; Proceedings of ASME Turbo Expo 2017, Charlotte, NC, USA, 26–30 June 2017, Paper No. GT2017-64736, DOI: 10.1115/GT2017-64736

[36] Burdett, D., Hambidge, C., Povey, T.; 2020; Analysis of Ultra-Low Uncertainty Gas Turbine Flow Capacity Measurement Techniques, Proc. Inst. Mech. Eng., Part A: J. Power and Energy, DOI: 10.1177/0957650920909718

[37] Burdett, D., Lubbock, R., Povey, T.; 2018; An Impulse Response Technique to Improve the Effective Frequency Response of Pressure Probes; XXIV Biennial Symposium on Measuring Techniques in Turbomachinery; Prague, Czech Republic, 29–31 August 2018; Paper No. MTT2418B23

[38] Hall, B.F., Povey, T.; 2018; A Practical Model for Pressure Probe System Response Estimation (with Review of Existing Models); Meas. Sci. Technol., 29(4), DOI: 10.1088/1361-6501/aaa58f

[39] Dzung, L.S.; 1971; Konsistente Mittlewerte in der Theorie der Turbomaschinen für Kompressible Medien; BBC-Mitt., Vol. 58, pp. 485–492

[40] Straccia, M., Hofmann, R., Gümmer, V.; 2019; New Methods for Secondary Flow Phenomena Visualization and Analysis; Proceedings of ASME Turbo Expo 2019, Phoenix, AZ, USA, 17–21 June 2019, Paper No. GT2019-91378, DOI: 10.1115/GT2019-91378

[41] Montis, M., Niehuis, R., Guidi, M., Salvadori, S., Martelli, F., Stephan, B.; 2009; Experimental and Numerical Investigation on the Influence of Trailing Edge Bleeding on the Aerodynamics of a NGV Cascade; Proceedings of ASME Turbo Expo 2009, Orlando, FL, USA, 8–12 June 2009, Paper No. GT2009-59910, DOI: 10.1115/GT2009-59910

[42] Burdett, D., Povey, T.; 2020; Analysis of Averaging Methods for Non-Uniform Total Pressure Fields; ASME J. Turbomach., Paper No. TURBO-20-1403 (*in review*)

[43] Mee, D.J., Baines, N.C., Oldfield, M.L.G., Dickens, T.E.; 1990; An Examination of the Contributions to Loss on a Transonic Turbine Blade in Cascade; ASME J. Turbomach., Vol. 114(1): 155–162, DOI: 10.1115/1.2927979

[44] Thomas, F.O., Liu, X.; 2004; An Experimental Investigation of Symmetric and Asymmetric Turbulent Wake Development in Pressure Gradient; Physics of Fluids, Vol. 16(5): 1,725–1,745, DOI: 10.1063/1.1687410

[45] Day, C.R.B, 1997; Aerodynamics of an Annular Film-Cooled Turbine Cascade; D.Phil thesis, University of Oxford

[46] Day, C.R.B., Oldfield, M.L.G., Lock, G.D.; 2000; Aerodynamic performance of an annular cascade of film cooled nozzle guide vanes under engine representative conditions; Experiments in Fluids, Vol. 29, pp.117–129

[47] Kost, F.; 2009; The Behaviour of Probes in Transonic Flow Fields of Turbomachinery; 8th European Conference on Turbomachinery, 23–27 March 2009, Graz, Austria

[48] Amecke, J., 1970; Anwendung der Transsonischen Ahnlichkeitsregel auf die Stromung Durch Ebene Schaufelgitter; VDI Forschungsheft 540: 16–28
[49] Nicholson, J.H.; 1981; Experimental and Theoretical Studies of the Aerodynamic and Thermal Performance of Modern Gas Turbine Blades; D.Phil thesis, University of Oxford
[50] Main, A.J., Oldfield, M.L.G., Lock, G.D., Jones, T.V.; 1997; Free Vortex Theory for Efficiency Calculations from Annular Cascade Data; ASME J. Turbomach., Vol. 119(2): 247–255, DOI: 10.1115/1.2841107
[51] Main, A.J.; 1994; Annular Cascade Aerodynamics; D.Phil thesis, University of Oxford
[52] Pianko, M., Wazelt, F. (eds); 1983; Suitable Averaging Techniques in Non-Uniform Internal Flows, AGARD Advisory Report AR-182

APPENDIX A: DEFINITIONS OF LOSS COEFFICIENT AND EFFICIENCY

The literature is divided on the best way to quantify loss (either local or global) and efficiency. We find the clearest summary of the key issues to be given by Day [45], and Day et al. [46]. The key points are revised here.

Basic loss coefficient definitions

The purpose of an NGV is to supply angular momentum flux to the downstream rotor. The local momentum flux is proportional to the local kinetic energy (KE) per unit volume. This leads to the following practical definition of vane efficiency

$$\eta = \frac{\text{Actual exit KE}}{\text{Ideal exit KE}} \tag{6}$$

The actual KE can be measured, but—even for a completely uniform flow—the ideal KE must be defined. One rational choice is the kinetic energy obtained in an isentropic expansion from the inlet total pressure to the exit static pressure. That is

$$\eta = \frac{{v_2}^2}{v_{2s}^2} = \frac{h_0 - h_2}{h_0 - h_{2s}} \tag{7}$$

where v_2 is the measured flow velocity at vane exit, v_{2s} is the *isentropic velocity* at vane exit, and, for an adiabatic nozzle, $h_{01} = h_{02} = h_0$. This is represented on the *h-s* chart in Figure 28a, for a process between inlet conditions p_{01}, p_1, and exit conditions p_{02}, p_2. Expressing the efficiency, η, as a kinetic energy loss coefficient, $\zeta = 1 - \eta$, we get

$$\zeta = 1 - \frac{\left(1 - \frac{h_2}{h_0}\right)}{\left(1 - \frac{h_{2s}}{h_0}\right)} \tag{8}$$

For constant c_p, and recalling the isentropic relation $T_2 / T_1 = (p_2 / p_1)^{\chi}$, where $\chi = (\gamma - 1) / \gamma$, this can be cast as

$$\zeta = 1 - \frac{1 - \left(\frac{p_2}{p_{02}}\right)^{\chi}}{1 - \left(\frac{p_2}{p_{01}}\right)^{\chi}} \tag{9}$$

Here, for completeness, we note that in the incompressible limit equation (9) is identical to the total pressure loss coefficient, $Y = (p_{01} - p_{02}) / (p_{01} - p_2)$. This is a poor measure of loss in transonic flows as strictly speaking $p_{01} - p_2$ is not proportional to the local KE, because, in general, $p_0 - p \neq 0.5\rho v^2$.

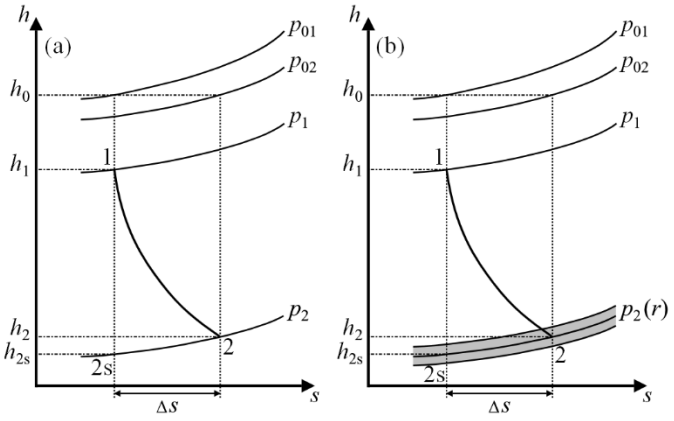


Figure 28: *h-s* charts showing the expansion process for: (a) uniform exit static pressure; (b) radial profile of exit static pressure.

Definitions of loss coefficient with non-uniform exit flow

In most practical cases, even for the case of uniform inlet flow (constant p_{01} and T_{01}), the cascade exit pressures will be non-uniform. The total pressure, p_{02}, will vary on account of non-uniformly distributed loss. The static pressure, p_2, will vary due to cross-passage pressure gradients, and—in the case of annular cascades—the radial pressure gradient required to maintain radial equilibrium. The situation is shown in Figure 28b, where the shaded region shows the range of exit static pressures.

In a non-uniform static pressure field (such as downstream of an NGV) there are a number of common loss metrics and representations of those metrics (averaging methods etc.) for loss. Some of these metrics and representations are discussed in [42], ranging from local distributions, to 1D circumferential-averages and 2D plane-averages at particular locations (primarily used to examine spatial loss variations in the radial, circumferential or axial directions), to fully mixed-out loss coefficient values. Although mixed-out loss is the most conventional way of presenting overall component performance, and whilst it can be argued that in most turbomachinery situations any residual secondary kinetic energy (SKE) will eventually manifest as loss (i.e. cannot usefully be used by the following row), it is also true that the flow entering the downstream row is generally only partially mixed (rows relatively close together). Thus, whilst the mixed-out loss is arguably the most relevant value, it is not necessarily the value manifest at the inlet to the next row.

If the aim is to examine the distribution of kinetic energy loss coefficient at a downstream plane, a *local* kinetic energy loss coefficient can be defined at every point in the flow by

$$\zeta'(r,\theta) = 1 - \frac{1 - \left(\frac{p_2(r,\theta)}{p_{02}(r,\theta)}\right)^{\chi}}{1 - \left(\frac{p_2(r,\theta)}{p_{01}}\right)^{\chi}} \qquad (10)$$

where p_2 (r,θ) and p_2 (r,θ) are measured in the plane of interest, and p_{01}, T_{01} are assumed uniform. We use this definition to compare *distributions* of kinetic energy loss.

It is worth making two comments about ζ'. Firstly, now we have a local loss coefficient, it is tempting to define an *overall* loss coefficient—for the vane row—based on an average value of ζ'. Notwithstanding the intricacies of the averaging process (choice of weighting method, whether we average the underlying physical input variables or average ζ' directly, etc.), this is probably a valid approach but is restricted to uniform inlet flows. The complications of non-uniform inlet flows are dealt with in the next section. Secondly, there is the question of the sensitivity of ζ' to errors in p_2. This is worth considering, because in transonic multi-hole probe measurements the static pressure is usually subject to the largest error (Mach number calibration coefficient often has low sensitivity to Mach number in the transonic range, leading to high uncertainty in Mach number and therefore static pressure [47]), and in alternative definitions of loss the exit static pressure could be determined from hub and case platform measurements rather than probe tip measurements. Figure 29 shows the sensitivity of ζ to both p_{02} and p_2, and indicates that the sensitivity to p_2 is relatively low. A systematic error in p_2 of ±1.0% would result (at a typical ratio $p_{02} / p_{01} = 0.95$) in an error in ζ of ±1.81%.

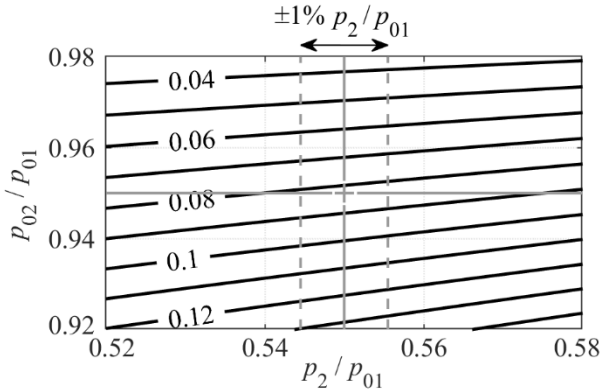


Figure 29: Sensitivity of ζ to both p_2 / p_{01} and p_2 / p_{01} in typical ranges.

Definitions of loss coefficient and efficiency with coolant injection

The simplest possible expression of a cooled vane system is that with uniform p_{01} and T_{01}, and a second inlet stream with coolant plenum total temperature $T_{0c} = T_{01}$, total pressure $p_{0c} > p_{01}$, and of the same specific heat as the mainstream. This represents our system. Even in this case, it is necessary to account for the energy of the coolant flow, which enters the system (defined here as the plenum inlet) at a modestly higher total pressure than the mainstream flow. Naïvely, we could extend the arguments leading to definition (9) to include both streams. The result would be a new local KE loss coefficient in which the ideal exit KE is the sum of two ideal expansions

$$\zeta'' = 1 - \frac{(\dot{m}_{\mathrm{m}} + \dot{m}_{\mathrm{c}})\left[1 - \left(\frac{p_2}{p_{02}}\right)^{\chi}\right]}{\dot{m}_{\mathrm{m}}\left[1 - \left(\frac{p_2}{p_{01}}\right)^{\chi}\right] + \dot{m}_{\mathrm{c}}\left[1 - \left(\frac{p_2}{p_{0c}}\right)^{\chi}\right]} \qquad (11)$$

Where $\dot{m}_{\mathrm{m}}$ and $\dot{m}_{\mathrm{c}}$ are the mainstream and coolant mass flow rates, respectively. All the information required to calculate this local parameter is known, and for a uniform—i.e. fully mixed—exit flow, it is well-defined. In the case of non-uniform exit flow, however, the problem arises that we additionally require the *local mass flux ratio* (local value of $\dot{m}_{\mathrm{c}}/\dot{m}_{\mathrm{m}}$) to compute the denominator. In most experiments, not only is this information unavailable, but significant gradients of $\dot{m}_{\mathrm{c}}/\dot{m}_{\mathrm{m}}$would be expected downstream of the vane (coolant confined primarily to wake regions). The conclusion is that the ideal kinetic energy is not sufficiently defined for the local kinetic energy loss coefficient ζ''—as defined—to have clear meaning. Noting the compromises inherent in the definition, the local KE loss coefficient of equation (10) provides an adequate alternative.

Practical way forward for radial loss coefficient distributions

To establish the radial distribution of loss in a situation with cooling—i.e. a series of circumferential line-averages—the problem arises that the local coolant-to-mainstream mass flux ratio at each radius is generally unknown (unless, in an experiment, by separate temperature measurement, or, in CFD, by—for example—implementation of a scalar tracking method), having both significant concentration in the wakes, but also radial variation. It is therefore hard to use a formulation based on equation (11). A practical way forward is to extend equation (10) to a circumferential average definition by replacing the local value of p_2 with a circumferentially-area-averaged static pressure, $\overline{p_2}(r)$, and replacing the local value p_{02} with a circumferentially-mass-flux-averaged total pressure, $\overline{p_{02}}(r)$. Detailed consideration of the sensitivity to the choice of weighting method for total pressure averaging can be found in [42]. The circumferential-average loss coefficient at a particular radial height then becomes

$$\zeta'''(r) = 1 - \frac{1 - \left(\frac{\overline{p_2}(r)}{\overline{p_{02}}(r)}\right)^{\chi}}{1 - \left(\frac{\overline{p_2}(r)}{p_{01}}\right)^{\chi}} \qquad (12)$$

Practical way forward for calculation of plane-average loss coefficient

In the case of a plane-average, the coolant-to-mainstream mass flux ratio *for the entire plane* is generally known. We can

therefore define an average loss coefficient, in which the ideal exit KE is the sum of two terms as in equation (11), by replacing p_2 in equation (6) with a plane-area-averaged static pressure, $\overline{p_2}$, and replacing p_{02} with a plane-mass-flux-averaged total pressure, $\overline{p_{02}}$. The average loss coefficient for a 2D plane becomes

$$\zeta'''' = 1 - \frac{(\dot{m}_\mathrm{m} + \dot{m}_\mathrm{c})\left[1 - \left(\frac{\overline{p_2}}{\overline{p_{02}}}\right)^{\chi}\right]}{\dot{m}_\mathrm{m}\left[1 - \left(\frac{\overline{p_2}}{p_{01}}\right)^{\chi}\right] + \dot{m}_\mathrm{c}\left[1 - \left(\frac{\overline{p_2}}{p_{0c}}\right)^{\chi}\right]} \qquad (13)$$

The flow at the row exit may be considered to have loss *already manifest* as a total pressure deficit, and loss *inevitable* as a result of the mixing out of non-uniformity (secondary kinetic energy). We can consider equation (13) to *count* only the loss already manifest. It is generally accepted, however, that when comparing the *total* row loss between vanes it is the sum of the two loss terms that should be compared. We refer to this as the *mixed-out loss*, which we now consider.

Practical way forward for calculation of mixed-out loss coefficient

The process of *mixing-out* requires conservation of mass, momentum, and enthalpy fluxes, in a process of mixing to a well-defined reference flow. The three most commonly used mixing methods are those of Amecke ([47],[48]), Dzung [39], and Main et al. ([49],[50]). Discussion of the relative merits of these three methods can be found in [42] and [49]. The method of Main et al. ([49],[50]), in which the flow is mixed to a radial distribution defined by a free-vortex condition producing a uniform total pressure and a radial profile of static pressure satisfying radial equilibrium, is considered to be the most physically representative of annular cascade flows. However, the problem arises that the local distribution of coolant mass fraction may be unknown, in which case it must be prescribed to perform the mixing. The alternative method of Dzung [39], in which the flow is mixed to a uniform static pressure at a single swirl-averaged radius (nominal radius at which swirl velocity has its average value), avoids this problem and can be considered as a practical compromise. The method of Dzung is favoured by several authors (e.g. [45],[46],[51]), and has been shown to produce very similar results to the free-vortex method ([42],[49]).

The outputs of the mixing process are either uniform (i.e. single) values or radial distributions of $\overline{p_2}'$ and $\overline{p_{02}}'$ (and, for completeness, although they are not used in our process, mixed-out values $\overline{\alpha}'$, $\overline{\beta}'$, $\overline{\rho}'$ and $\overline{T_0}'$). Here we use a prime to distinguish average variables resulting from a mixing process from those according to some in-plane weighting (area, mass-flow, volume-flow etc.) scheme.

Not only does the Dzung method provide a more rational way of making total loss comparisons between planes, but—happily— the process of swirl-averaged mixing (normally at a midspan radius) to a single static pressure, provides a well-defined ideal exit KE (or ideal expansion) in which the problem of mass-flux-attribution is resolved. We modify equation (11) by replacing p_2 with $\overline{p_2}'$, and p_{02} with $\overline{p_{02}}'$, to give the mixed-out KE loss coefficient

$$\zeta''''' = 1 - \frac{(\dot{m}_\mathrm{m} + \dot{m}_\mathrm{c})\left[1 - \left(\frac{\overline{p_2}'}{\overline{p_{02}}'}\right)^{\chi}\right]}{\dot{m}_\mathrm{m}\left[1 - \left(\frac{\overline{p_2}'}{p_{01}}\right)^{\chi}\right] + \dot{m}_\mathrm{c}\left[1 - \left(\frac{\overline{p_2}'}{p_{0c}}\right)^{\chi}\right]} \qquad (14)$$

It is worth noting that in all our experiments and simulations, the coolant-to-mainstream mass flow ratio is fixed, and therefore the problem of implementing equation (14) reduces to finding the mixed-out values $\overline{p_2}'$ and $\overline{p_{02}}'$.

APPENDIX B: METHODS FOR DISTINGUISHING PROFILE AND ENDWALL LOSS COEFFICIENTS

Figure 30 illustrates three possible integral areas for profile loss (red) and endwall loss (blue) in an example traverse plane (uncooled RANS at plane 1). The local loss coefficient distribution is shown by black contours. The three methods are referred to as methods (a), (b) and (c) respectively.

In method (a), profile and endwall regions are defined by tight boundaries enclosing the identifiable loss regions associated with the wakes, and the hub and case endwall boundary layer flow regions. Free-stream regions are assumed to carry no loss.

In method (b), the integral area *for the profile loss region* is extended (from method (a)) to include all areas not yet included in an integral. If the loss coefficient in the free stream were exactly zero, the total (profile + endwall) loss coefficient evaluated by methods (a) and (b) would be identical. In practice the loss coefficient in free-stream regions is small but non-zero, leading to a small discrepancy between methods (a) and (b).

In method (c), the irregular profile and endwall region integral regions are simplified by using fixed hub and case radial limits. The radial locations of these limits require judgement, but should be set so that most of the endwall loss is included in the endwall integration region. Method (c) is the easiest to implement in practice for obvious reasons.

Loss coefficients determined using each of the three methods (a)–(c) are plotted in Figure 31 as functions of axial distance for experiment (blue lines) and cooled URANS (red lines). Consider first the profile loss coefficients. A small and consistent offset can be seen between the loss coefficients evaluated from methods (a) and (b). This reflects the loss contribution of the free-stream region (excluded in method (a)). The average difference (over all axial planes) was 5.5% in experiment and 3.5% in CFD. The profile loss coefficients evaluated from methods (b) and (c) are nearly identical over most of the axial range, differing by an average of 0.6% in experiment and 1.0% in CFD. Turning to the endwall loss coefficients, we see that the data agree very closely between all three methods for both experimental and CFD data.

The conclusion is that simple radial bounds (method (c)) achieve the same result as the more sophisticated method (b), and that both are advantageous over method (a). In this paper we

have used method (c) for distinguishing profile and endwall components of loss coefficient, and recommend this as good practice (balance of simplicity and robustness) in most situations.

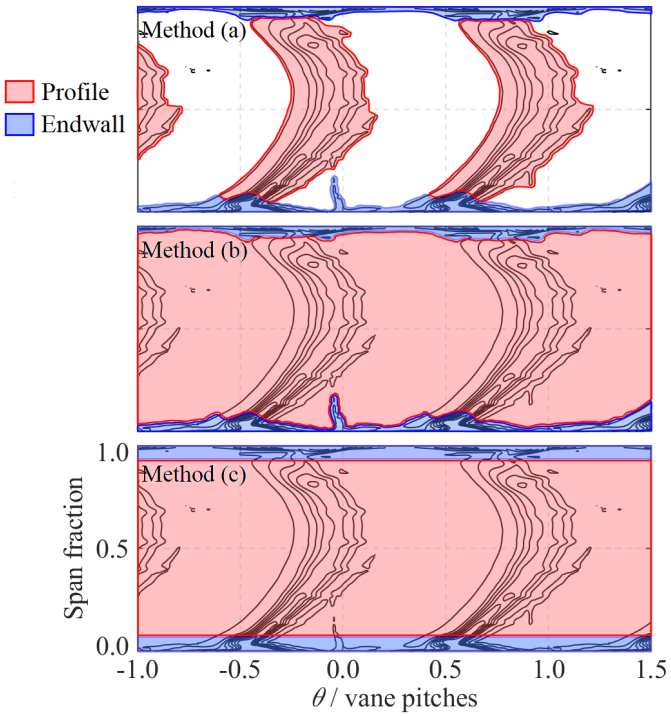


Figure 30: Illustrations of methods for defining profile and endwall integration regions: (a) Tight boundaries around specific features; (b) remaining plane area included in the profile-loss integral region; (c) simple radial limits.

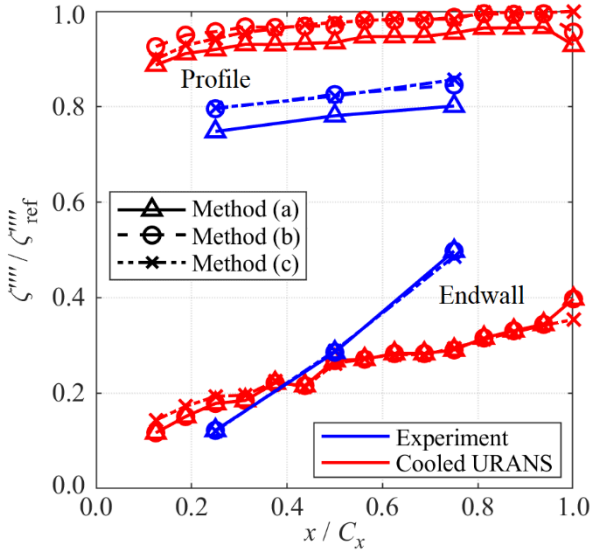


Figure 31: Axial trends of profile and endwall components of KE loss coefficient, evaluated using each of methods (a)–(c).

Statement of Authorship for joint/multi-authored papers for PGR thesis

To appear at the end of each thesis chapter submitted as an article/paper

The statement shall describe the candidate's and co-authors' independent research contributions in the thesis publications. For each publication there should exist a complete statement that is to be filled out and signed by the candidate and supervisor **(only required where there isn't already a statement of contribution within the paper itself).**

Title of Paper	Experimental and numerical analysis of loss characteristics of cooled transonic nozzle guide vanes
Publication Status	Submitted for Publication
Publication Details	Burdett, D., Povey, T.; 2021; Experimental and Numerical Analysis of Loss Characteristics of Cooled Transonic Nozzle Guide Vanes; ASME J. Turbomach., Paper No. TURBO-21-1040 (*Submitted*)

Student Confirmation

Student Name:	D Burdett		
Contribution to the Paper	Performed experimental testing to collect data, ran numerical simulations, analysed and interpreted experimental and numerical data, and wrote manuscript.		
Signature		Date	13/02/2021

Supervisor Confirmation

By signing the Statement of Authorship, you are certifying that the candidate made a substantial contribution to the publication, and that the description described above is accurate.

Supervisor name and title: Professor Thomas Povey		
Supervisor comments: Dan conducted all of the research himself, and entirely wrote the paper himself, with technical contributions from his supervisor.		
Signature: Thomas Povey	Date	19/02/2021

This completed form should be included in the thesis, at the end of the relevant chapter.

IMPACT OF TRAILING EDGE OVERHANG LENGTH ON THE LOSS CHARACTERISTICS OF FULLY COOLED TRANSONIC NOZZLE GUIDE VANES

Daniel Burdett, Thomas Povey‡
Department of Engineering Science, University of Oxford, Oxford, OX2 0ES, United Kingdom
‡thomas.povey@eng.ox.ac.uk

ABSTRACT

The trailing edge (TE) design of a cooled high-pressure (HP) nozzle guide vane (NGV) requires consideration of both cooling and aerodynamic performance. Two designs are in common use: the centred-ejection design, in which coolant is ejected through a slot in the TE with roughly symmetrical suction-side (SS) and pressure side (PS) TE tips; and the SS-overhang design, in which the SS and PS TE tips are staggered. This second design has been favoured in recent years because it has been presumed to be aerodynamically advantageous. In this paper we re-examine this assumption by studying a parametric design set between these two design extremes. We do this using extensive high-fidelity experimental measurements performed at engine-scaled conditions (matched Mach number, Reynolds number, and coolant-to-mainstream pressure ratio) on real engine parts. To provide insight into the mechanisms affecting loss, we use complimentary unsteady CFD simulations. We analyse the changes in flow structure, local loss coefficient distribution, wake mixing rate, average profile loss coefficient and base pressures.

INTRODUCTION AND LITERATURE REVIEW

High turbine inlet temperatures necessitate cooling of the HP NGV. Most HP NGVs use both internal (impingement, pedestal/fin banks, etc.) and film cooling. The cooling comes with an aerodynamic and thermodynamic penalty to the cycle. The TE overhang is exposed and cannot be internally cooled, and is therefore particularly reliant on good film coverage. This is normally achieved through ejecting coolant from the trailing part of the vane through a TE slot. The region immediately downstream of the TE is one of relatively low static pressure (on account of flow acceleration) and total pressure (separated flow), which is favourable in terms of the pressure drop offered across the internal system. There are two common design variants for the cooled TE: *centred-ejection*, and *SS-overhang* (also commonly called *PS-cutback*). The centred-ejection design has an approximately symmetric centred slot, in which both the PS and SS TE tips have the advantage of being both internally and film cooled. However, this comes with the aerodynamic penalty of a thicker TE. In the *SS-overhang* design, the SS TE tip extends further in the chordwise direction than the PS TE tip (it overhangs). This offers the advantage of a thinner (ultimate) TE, but at the cost of increased cooling requirement for the overhanging length.

At transonic conditions, there is a complex interaction between the TE slot coolant flow, the TE shock structure, the separated base region, and the development of the downstream free shear layers. The loss generated in this region typically accounts for about a third of total profile loss of the NGV [1]. Aerothermal optimisation of this region is therefore important.

Most early cooled TE designs had a centred-ejection design. More recent engine designs have favoured SS-overhang geometries, because of the supposed aerodynamic advantages of the thinner (ultimate) separated TE region (often called *base region*). However, the literature is not in consensus on this point, as we demonstrate in the following review. To confuse matters further, there is more recent evidence that suggests that shorter overhangs may offer both aerodynamic and thermal advantages at low-transonic Mach numbers. This has become more relevant as designers consider the possibility of twin-HP turbines, with HP NGV exit Mach numbers in the range 0.8–0.9 (compared to the typical value of 0.95).

The lack of consensus in the existing literature is our primary motivation for more carefully re-examining the impact of TE design. We take advantage of high-TRL experimental data using fully-cooled engine parts operated at non-dimensionally engine-representative conditions. A secondary motivation is to clarify the penalty (or otherwise) associated with deliberate removal of TE material as part of the repair process of damaged in-service components.

Early studies of TE loss focussed on the sensitivity to TE thickness in uncooled vanes (e.g. [2], [3]). The first studies of cooled TE geometries were those of Whitney et al. [4] and Prust et al. ([5], [6]), who tested centred-ejection designs with different TE and slot thicknesses at a range of coolant-to-mainstream mass flow ratios. These early results presented row efficiency as a function of coolant-to-mainstream mass flow ratio and found that, in most cases, efficiency rose significantly with mass flow ratio. The exception was for very narrow slots with mass flow ratios below 1.0%, where a minimum efficiency condition was seen. The change in efficiency arose due to a combination of the KE of the coolant jet in relation to that of the mainstream, and also the impact of coolant flow on TE loss (affecting the base pressure distribution and the effective TE blockage). At mass flow ratios below approximately 2.0%, the kinetic energy (KE) of the coolant jet was low and the latter effect was relatively strong, producing higher efficiency from wider slot designs, whereas for mass flow ratios above 2.0% the former effect was dominant and narrower slots performed better. The positive impact of high coolant KE on efficiency was conflated by the fact that the efficiency definition took no account of the coolant flow in setting the ideal reference flow. This problem was addressed in more recent studies by including the coolant energy input in the definitions of efficiency and loss coefficient.

Sieverding [9] studied the impact of TE coolant ejection from a central slot on base pressure in the transonic regime. The coolant jet split the base region into two sections of significantly different base pressure (by typically 3% of the mean base pressure). The base pressure asymmetry was attributed to a small misalignment between the slot exit angle and the direction of the

wake path (classical deviation effect). As the coolant-inlet-pressure-to-base-pressure-ratio increased from 1.00 to 1.48, average base pressure rose to a maximum value 11.9% above the uncooled base pressure, before gradually falling as the injection pressure ratio was increased further. To the extent that we can take base pressure as a proxy for TE loss (it is a good measure of the pressure drag, but does not account for mixing losses between the mainstream and TE coolant flows or the KE introduced by the coolant, so the analogy is only partial), the maximum base pressure condition is expected to be associated with (though not exactly coincident with) a minimum loss coefficient.

There are many studies in the literature (e.g. [10]–[15]) of the impact of varying TE coolant flow rate (expressed as either a coolant-to-mainstream mass flux ratio, velocity ratio, or blowing ratio) on aerodynamic loss for both centred-ejection and SS-overhang type TE designs. Defining a KE loss coefficient so as to account for the energy input of coolant flow, all of these studies show that loss coefficient first decreases (with respect to the uncooled condition) with the introduction of TE coolant flow, with a minimum value of loss coefficient at moderate mass-flux, velocity or blowing ratio, then increases again for higher ratios. Acknowledging the caveats noted above for the analogy between TE loss and base pressure, this result is in line with that of Sieverding [9], who showed a maximum base pressure at moderate coolant flow rate.

Raffel and Kost [11] used schlieren imaging and PIV to visualise and understand the influence of TE coolant ejection on the TE shock structure. To do this they used a simplified flat plate working section designed to replicate the flow structures in the vicinity of the TE of an NGV cascade. They operated at a Mach number of 1.27. The introduction of a moderate TE coolant flow ($\dot{m}_c/\dot{m}_m$ = 0.5–1.0%) resulted in each of the oblique shockwaves on either side of the TE each being replaced by a pair of weaker oblique shocks. The change in TE shock structure reversed at higher coolant mass flow rates ($\dot{m}_c/\dot{m}_m$ = 1.5–2.5%).

Several authors have directly compared the loss produced by different cooled TE geometries, and these are now briefly reviewed. In 1985, Kost and Holmes [10] experimentally compared TE geometries with a central slot, and with film rows close to the TE, at a Mach number of 1.15. The latter design provides a thinner ultimate TE (akin to a modern SS-overhang design) and surface film coverage near the TE. The centred-ejection design had 76.2% higher loss coefficient (expressed as a percentage of the film-cooled TE loss coefficient) at zero coolant flow, due to having its ultimate TE thickness being approximately 2.7 times greater to accommodate the internal slot. However, as the coolant-to-mainstream mass flow ratio rose from zero to 3.5%, the percentage difference in loss coefficient between the two designs fell to 11.2%. That is, the reduction in loss coefficient with TE ejection was significantly greater for the centred ejection design.

In 1994, Kapteijn et al. [17] compared centred-ejection and SS-overhang TE geometries in the Mach number range 0.7–1.2. At zero coolant flow rate and Mach number 1.1, schlieren images showed a distinct shockwave originating at the PS TE lip, in addition to the normal shock-pair at the TE which was observed for both TE designs. The PS-lip shock was suppressed by moderate TE coolant flow (coolant flow reduces the effective step height at the PS-lip). At subsonic conditions, the loss coefficient of the SS-overhang design was approximately 24% higher than the centred-ejection design. Direct comparison is difficult, however, because neither the overall thickness of the ultimate TE (42% higher for centred-ejection design) nor the minimum metal thickness (25% higher for SS-overhang design) were matched between the designs. As Mach number passed unity, both designs showed a rapid rise in loss coefficient and the difference between them grew to approximately 36%. This increase was attributed to shock-boundary layer interaction caused by the PS-lip shock.

In 2001, Uzol and Camcı [18] experimentally compared centred-ejection and SS-overhang TE designs (with equal minimum metal thicknesses) at four different coolant-to-mainstream mass flow ratios at subsonic conditions. PIV measurements showed that the SS-overhang design gave both a shallower and more asymmetrical wake (more gradual velocity profile decay on the PS), and a 16% lower total pressure loss coefficient than the centred ejection design. The variation in total pressure loss coefficient with mass flow ratio was in accord with [10]–[15] for both TE designs, although the magnitude of the sensitivity was considerably higher for the SS-overhang design than the centred-ejection. This was attributed to the effect of changing mass flow ratio on the effective height of the surface discontinuity at the PS lip and consequently on deviation of the PS mainstream flow.

In 2012, Rehder [14] experimentally compared centred-ejection and SS-overhang TE designs in a linear cascade, using coolant-to-mainstream mass flow ratios in the range 0–2% and Mach numbers 0.9 and 1.2. In this comparison, the ultimate TE thickness of the SS-overhang design had the same thickness as that of the *entire* centred-ejection design, giving more than double the minimum metal thickness for the SS-overhang design. Although this led to one sort of like-for-like comparison, it is unrepresentative of engine design constraints. At a Mach number of 0.9, the SS-overhang design produced approximately 50% higher loss coefficient than the centred-ejection at a mass flow ratio of 0.5%, and up to 200% higher at 2.0% mass flow ratio. The authors consider the interaction between mainstream and coolant flows in the separated region downstream of the PS lip as a possible explanation for the performance difference, but the larger overall thickness of the SS-overhang design (including the PS lip) may also have been responsible for some of the difference.

In 2016, Wang et al. [15] presented perhaps the most comprehensive computational study of cooled TE designs in the literature to date. They used 2D RANS to study a typical HP rotor geometry with a SS-overhang TE design, at a Mach number of 1.2. They compared five different SS-overhang lengths (between 6–14% of tangential chord) at coolant-to-mainstream mass flow ratios between 0–6%. The ranking of different overhang lengths in terms of loss coefficient depended on mass flow ratio. At mass

flow ratios below 2%, overhang lengths of 10–12% tangential chord provided the lowest loss coefficient, whilst for higher mass flow ratios (above approximately 3%) the optimum overhang length fell to 6–8% of tangential chord. The overhang length affected the entire cascade aerodynamics, primarily through influencing the TE shock structure.

In 2018, Melzer [7] experimentally studied the impact of TE vortex shedding in the transonic regime, noting periodic shock generation in phase with the shedding of vortices from the TE. Both centred-ejection and SS-overhang designs were studied, with equal minimum metal thicknesses in all cases, over a Mach number range 0.4–1.0. In the transonic range, the unsteady flow behaviour varied significantly with TE blowing ratio. At blowing ratios up to around 0.3, vortices were shed from the entire width of the separated *base region*. A long overhang length (approximately 6.0% of tangential chord) was able to suppress the vortex shedding even in the absence of cooling, producing a reduction in loss coefficient of up to 43% relative to TE designs which did not suppress vortex shedding. Moderate blowing ratios (in the range 0.3–0.7) suppressed vortex shedding in all TE designs, with loss coefficients within ±22% of each other. At blowing rates above approximately 0.7, there was a transition in the structure of vortex shedding to vortices being shed from the individual SS and PS TE tips, in most cases. An exception to this was seen for a short overhang length (approximately 1.5% of tangential chord), for which the vortices shed from the two TE tips coalesced into a single vortex street. This effect was associated with a rise in loss coefficient of up to 43% relative to shedding from the two separate tips. Differences in vortex shedding in the transonic regime (as described above) were the only significant source of differences in the sensitivity of loss coefficient to Mach number between TE geometries. These results demonstrate the high sensitivity of TE loss in the transonic range to TE vortex shedding behaviour, and illustrate the importance of employing an unsteady numerical method to predict TE loss.

In a closely associated study, Melzer and Pullan ([7], [8]) investigated a number of different uncooled TE shapes (round, square, elliptical) and demonstrated the role that vortex shedding in the transonic regime plays in determining TE loss. They showed that square TE designs limited the extent of vortex shedding (when compared to round TEs) at Mach numbers above around 0.8. This led to the square TE having approximately 8% lower loss coefficient than the round TE, opposite to their loss ranking at low-subsonic conditions.

Taking the literature as a whole, we see a number of comparisons of particular SS-overhang and centred-ejection designs, and some parametric studies of different overhang lengths. In many cases, however, the designs were not equivalent in terms of TE thickness, TE slot width, etc. and very little attempt has been made in previous studies to correct for such dissimilarities. In part, this problem is inherent, in that direct equivalents (between SS-overhang and centred-ejection) might not be easy to clearly define. Broadly, the data suggest that, when designs are normalised by minimum metal thickness (such that similar thermal and mechanical duty might be expected), an SS-overhang design might be favoured over centred-ejection. Comparisons of different overhang lengths show that the optimum overhang length from an aerodynamic perspective is dependent on the entire cascade aerodynamic field, which is—in turn—partly dependent on the unsteady behaviour of the wake. The unsteady behaviour is difficult to accurately predict, further justifying the necessity of detailed experimental aerodynamic measurements in a high-TRL environment.

The purpose of this study is to fill a gap in the literature, by performing a very detailed analysis of loss characteristics for a series of well-defined cooled TE designs of varying SS-overhang length, constrained by achievable manufacturing limits. The four TE designs we study form a parametric set between a pure centred-ejection design and SS-overhang design (up to 6.3% of tangential chord). Fully-cooled engine parts were used for the study, which was conducted at engine-representative conditions of Mach number, M_2, Reynolds number, Re, and coolant-to-mainstream pressure ratio, p_{0c} / p_{0m}. The study was performed in the high-TRL Engine Component AeroThermal (ECAT) facility [22] at the University of Oxford. Experimental results are compared to URANS predictions. The performance of the four TE designs is assessed in terms of average profile loss coefficient values, local loss coefficient distributions, and wake mixing rates. Fundamental mechanisms responsible for the observed effects are discussed.

OVERVIEW OF EXPERIMENTAL FACILITY

Experiments were performed in the ECAT facility [22], a high-TRL blowdown annular cascade. For the experiments performed for the current study, the facility was built with HP NGVs from a modern civil turbofan engine. The same set of vanes was used for the entire test campaign, with geometry variation achieved by sequential machining of the TE. Tests were conducted at engine-representative conditions of M_2, Re and p_{0c} / p_{0m}. Test conditions are summarised in Table 1.The mass flow ratio between TE coolant and mainstream flows was approximately 0.02 in all tests. The TE-to-mainstream blowing ratio (product of the mass flow ratio and the nominal passage-to-TE slot area ratio) was approximately 0.53.

An overview of the facility operation and its general capabilities is provided in [22]. A description of the working section instrumentation and associated uncertainty analysis is provided in [23], and the traverse measurement process, and analysis of aerodynamic loss measurement capabilities, is provided in [21]. These details are not repeated in this paper. Figure 1 shows a cross-section schematic of the NGV ring and measurement planes.

Independently (of the mainstream) metered coolant air is fed from both the hub and case (see Figure 1), allowing coolant-to-mainstream pressure ratio to be maintained to within approximately ±0.02%. The vane has both film cooling and TE slot cooling. Tests were performed at an exit Mach number of $M_2 = 0.97$ (typical variation of ±0.14% of the target value).

Table 1: Test operating conditions in the ECAT facility.

Parameter	Nominal Value
Vane inlet total pressure, p_{0m} (bar)	2.00 bar
Vane inlet total temperature, T_{0m} (K)	290 K
Vane inlet turbulence intensity, Tu. (%)	6–10%
Vane pressure ratio, p_2 / p_{0m} (–)	0.54
Vane exit Mach number, M_2 (–)	0.97
Vane exit Reynolds number, Re (–)	1.6×10^6
Coolant-to-mainstream pressure ratio, p_{0c} / p_{0m} (–)	1.025
Trailing edge-to-mainstream mass flow ratio, $\dot{m}_{TE} / \dot{m}_m$ (–)	0.02
Trailing edge-to-mainstream blowing ratio, $\rho_{TE} v_{TE} / \rho_m v_m$ (–)	0.53

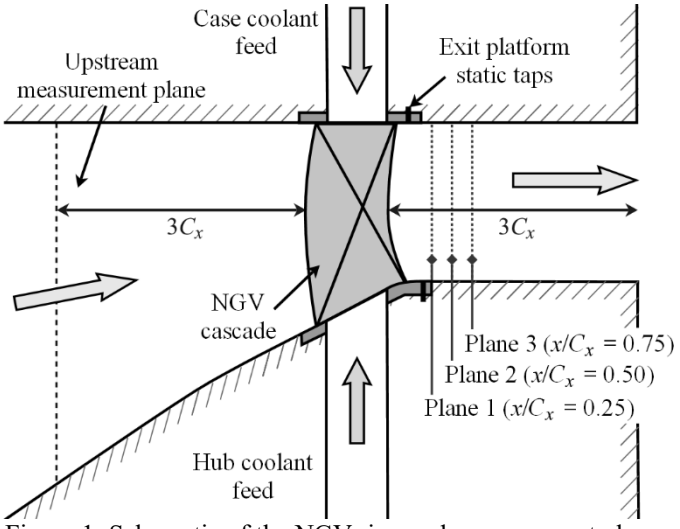


Figure 1: Schematic of the NGV ring and measurement planes.

INSTRUMENTATION AND MEASUREMENT PROCESS

Vane inlet total pressure, p_{0m}, and total temperature, T_{0m}, were measured at an upstream measurement plane three axial chord lengths upstream of the cascade leading edge, using four fixed pitot rakes and four fixed thermocouple rakes, each with eight measurement points distributed over the vane span (32 measurements each of p_{0m} and T_{0m}). Vane exit static pressure was measured on the hub and case vane exit platform extent (see Figure 1), at 0.17 C_x downstream of the TE. Six vanes (from the total of 40) were instrumented with platform tappings (total of 84 tappings across the six vanes). The cascade operating pressure ratio was taken as the ratio of mean-exit-static to mean-inlet-total pressure. The bias and precision uncertainties in vane pressure ratio were estimated as ±0.365% and ±0.007% to 95% confidence, respectively. A detailed uncertainty analysis is provided in [23].

Traverse measurements were conducted in three axial planes using a two-axis (radial-circumferential) hub-mounted traverse gear. Details of the traverse equipment are given in [22]. The three traverse planes (planes 1, 2 and 3, marked in Figure 1) were located ¼, ½, and ¾ of axial chord downstream of the TE plane. Measurements were made using a five-hole pneumatic pressure probe, with tip diameter 2.8 mm, and a single-hole pitot probe (for near-wall measurements) of diameter 0.8 mm. Further details of the probes are given in [21]. The five-hole probe was calibrated over a Mach number range $0.3 \le M \le 1.4$, to allow evaluation of total and static pressures, Mach number, yaw and pitch angles.

Full-area surveys in each of the three traverse planes were conducted over a circumferential range of 2.5 vane pitches (including two complete wakes) and a radial range of approximately 3–97% of span. Wakes from the same two vanes were tracked between the three axial planes by changing the circumferential traverse limits. The probes were traversed slowly in a pattern of circumferential sweeps in alternating directions, with radial spacing of 1.4 mm. The frequency response of the probe-transducer system was estimated as 120 Hz. An impulse response deconvolution technique [24] was used to improve the frequency response to approximately 720 Hz, without compromising the fidelity of the underlying signal. The resulting spatial resolution of traverse data in the circumferential direction (at midspan) was 0.08 mm.

LOSS COEFFICIENT DEFINITIONS

We quantify aerodynamic loss using a kinetic energy (KE) loss coefficient, ζ, defined by

$$\zeta = 1 - \eta = 1 - \frac{v_2^2}{v_{2s}^2} = 1 - \frac{1 - \left(\frac{p_2}{p_{02}}\right)^{\chi}}{1 - \left(\frac{p_2}{p_{01}}\right)^{\chi}} \qquad (1)$$

where the vane efficiency, η, is defined as the ratio of actual exit KE to ideal exit KE, v_2 is the measured exit flow velocity, v_{2s} is the isentropic exit velocity, and $\chi = (\gamma-1) / \gamma$.

In this paper we use four representations of loss coefficient: a *local KE loss coefficient* to present full area-survey data at particular axial planes; a *circumferentially-averaged KE loss coefficient* to present radial distributions of loss; a *plane-averaged KE loss coefficient* value as a summary of *already-manifest loss*; and a *fully mixed-out KE loss coefficient* as a summary of *unavoidable loss.* These definitions are discussed in detail in [21]. We now briefly re-iterate the definitions. From equation (1), we define the *local KE loss coefficient* as

$$\zeta'(r,\theta) = 1 - \frac{1 - \left(\frac{p_2(r,\theta)}{p_{02}(r,\theta)}\right)^{\chi}}{1 - \left(\frac{p_2(r,\theta)}{p_{01}}\right)^{\chi}} \qquad (2)$$

where r and θ denote radial and circumferential position, respectively. From equation (2), we define the circumferential-average KE loss coefficient (at a specific radius) by replacing the local variables $p_2(r, \theta)$ and $p_{02}(r, \theta)$ with a circumferentially-area-averaged static pressure, $\overline{p_2}(r)$, and a circumferentially-mass-flux-averaged total pressure, $\overline{p_{02}}(r)$, respectively (choice of weighting method for circumferential and plane-average total pressures is examined in detail in [25]) giving

$$\zeta''(r) = 1 - \frac{1 - \left(\frac{\overline{p_2}(r)}{\overline{p_{02}}(r)}\right)^{\chi}}{1 - \left(\frac{\overline{p_2}(r)}{p_{01}}\right)^{\chi}} \quad (3)$$

We define the plane-averaged KE loss coefficient as

$$\zeta''' = 1 - \frac{(\dot{m}_\mathrm{m} + \dot{m}_\mathrm{c})\left[1 - \left(\frac{\overline{p_2}}{\overline{p_{02}}}\right)^{\chi}\right]}{\dot{m}_\mathrm{m}\left[1 - \left(\frac{\overline{p_2}}{p_{01}}\right)^{\chi}\right] + \dot{m}_\mathrm{c}\left[1 - \left(\frac{\overline{p_2}}{p_{0c}}\right)^{\chi}\right]} \quad (4)$$

where $\overline{p_2}$ is the area-weighted-average static pressure, $\overline{p_{02}}$ is the mass-flux-weighted-average total pressure, and $\dot{m}_\mathrm{m}$ and $\dot{m}_\mathrm{c}$ are the mainstream and coolant mass flow rates respectively.

Finally, we define the mixed-out average KE loss coefficient as

$$\zeta'''' = 1 - \frac{(\dot{m}_\mathrm{m} + \dot{m}_\mathrm{c})\left[1 - \left(\frac{\overline{p_2}'}{\overline{p_{02}}'}\right)^{\chi}\right]}{\dot{m}_\mathrm{m}\left[1 - \left(\frac{\overline{p_2}'}{p_{01}}\right)^{\chi}\right] + \dot{m}_\mathrm{c}\left[1 - \left(\frac{\overline{p_2}'}{p_{0c}}\right)^{\chi}\right]} \quad (5)$$

where $\overline{p_2}'$ and $\overline{p_{02}}'$ are the *mixed-out* average static and total pressures (method of Dzung, [26]).

TRAILING EDGE GEOMETRIES

Figure 2 shows a diagram of the four TE geometries that were tested. We refer to these as Geometry 1 to Geometry 4. The designs form a systematic parametric set with SS-overhang lengths: 6.3%, 4.2%, 2.1%, and 0.0% of tangential chord. The geometries were formed on the same set of parts by sequential machining back of the SS TE. The unique construction of the ECAT facility allows this operation to be performed without any movement of the NGV ring (see [27]).

The machined SS TE tip of Geometries 2, 3 and 4 had a square-edge, unlike the rounded tip of Geometry 1 which had a hand-dressed rounded edge. The impact of TE shape on TE loss was examined by Melzer and Pullan [8], the key effect being a change in the location of the shear layer separation point. Whilst rounded TEs generally offer lower loss coefficient at low-subsonic conditions (Mach numbers below around 0.8), some square TEs were shown to have a preferential vortex shedding structure in the transonic regime, with lower overall loss coefficient.

The SS TE thickness, t_{SS}, changed as overhang length was reduced, due to the taper in the engine part. Table 2 summarises the SS TE thicknesses for each geometry. t_{SS} rose by +28.8% between Geometries 1 and 4. This is a necessary artefact of the way the test was set up (to preserve exact similarity between the geometries in all other respects) and is accounted for in the analysis that follows.

Table 2: Summary of SS TE tip thicknesses for each geometry.

Geometry	1	2	3	4
t_{SS} / mm	0.559	0.603	0.667	0.720
t_{SS} / $t_{SS,1}$	1.000	1.078	1.193	1.288

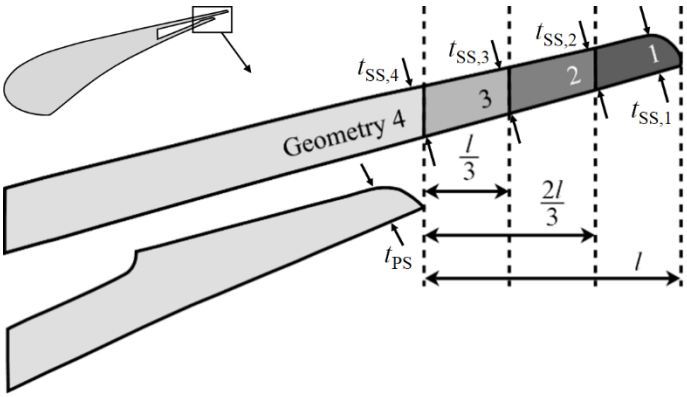


Figure 2: Diagram showing the vane (top left), and a magnified view of the four TE geometries. The SS overhang length for Geometry 1 is marked *l*.

NUMERICAL METHOD

URANS simulations of all TE geometries were performed using ANSYS CFX. The domain was a rotationally periodic annular sector of two vane passages. This is shown in Figure 3a. An octree-based mesh was generated using BOXERmesh. A midspan cross section (Geometry 1) is shown in Figure 3b. The mesh was moderately refined in the paths of the wake centres, and strongly refined very close to the TE. Figure 3c shows close-up views of the near-TE mesh for each of the four TE geometries. Care was taken to ensure that changes in the mesh between geometries were limited to the immediate vicinity of the SS TE tip. A grid sensitivity study was conducted to ensure the results were independent of grid density. The final mesh contained approximately 57 million cells. The solver was second order discretised, and density-based. The *k-ω* SST model was used for turbulence closure.

At the main inlet boundary, uniform conditions of total pressure, total temperature and turbulence intensity were specified, matched to the experimental conditions (Table 1). The annulus lines of the inlet duct between the inlet boundary and the NGV leading edge were matched to the ECAT facility, so that the spanwise profile of the flow radial angle approaching the cascade was closely matched to the experiment. At the exit boundary, an area-average static pressure was specified, with the requirement to satisfy radial equilibrium. The exit pressure was set in the following iterative manner: the CFD-predicted static pressure field at nominal pressure ratio was interrogated at the locations of the hub and case platform static tappings (see Figure 1) and a mean vane pressure ratio was evaluated; this was compared to the nominal experimental value; the exit static pressure was then adjusted to achieve a better match and the CFD re-run. This process was repeated until a high level of convergence was reached, ensuring precise matching of the vane pressure ratio between CFD and experiment.

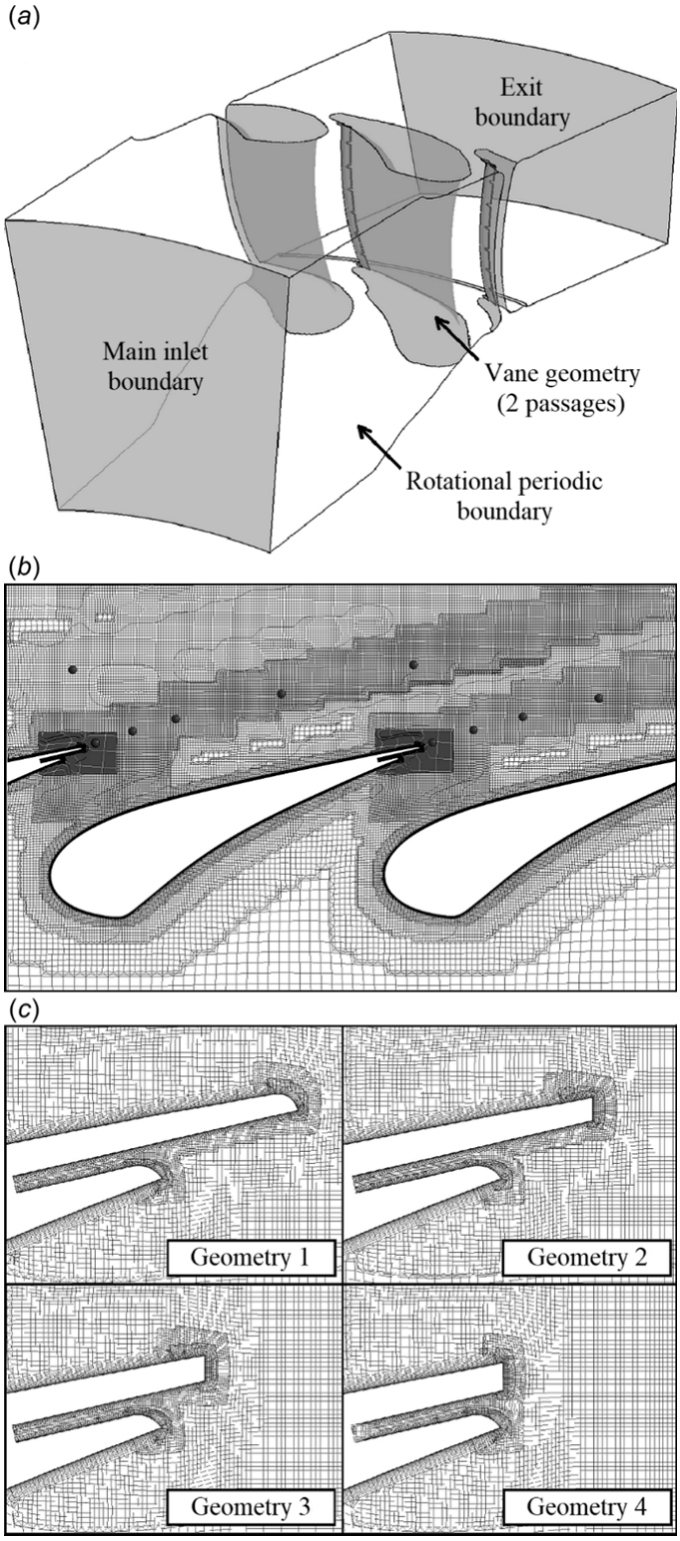


Figure 3: (a) CFD geometry; (b) Midspan mesh cross section for Geometry 1; (c) Near-TE mesh detail for all geometries.

Film cooling (210 holes per vane in 11 rows) was simulated using source-terms with a specified mass flow rate and direction vector. Mass flow rates for each *row* were established from the cooling system design for the component, which is a sophisticated network-analysis-with-potential-field model. A single scale factor (close to unity) was then applied to all *row* mass flows to match the total coolant capacity to that measured in the experiment. The individual *hole* mass flow rates were estimated using the CFD-predicted local surface static pressure distribution (evaluated from preliminary uncooled CFD results) and area-scaled nominal capacity characteristics for each hole, constrained so the particular row mass flow rate was satisfied. Individual hole mass flow rates were used as the boundary conditions in the CFD.

The TE slot was fully resolved, with a mass flow inlet boundary eight slot widths upstream of the slot outlet (see Figure 3). The mass flow rate was established by the same process as the film row mass flows, described above. The slot was split into seven separate sections along the vane span, with walls between. This was designed to simulate the presence of ribs within the slot. Further details of the geometry can be found in [21].

For each TE geometry, simulations were first converged as steady solutions. These results were then used to initialise the unsteady calculations. A time step of one tenth of the estimated TE vortex shedding period was used, with solutions run until the equation residuals were converged to within 10^{-6}. We also required that solution values at strategically located monitor points in the wake region were converged to approximately periodic fluctuations. Solutions were then time-averaged over the last 20 shedding periods (an averaging period of 4.6×10^{-4} s).

UNSTEADY BEHAVIOUR OF NUMERICAL RESULTS

The unsteady behaviour predicted by URANS for each TE geometry was analysed by inspecting the temporal variation of the pressure field at a number of monitor points in the wake (marked in Figure 3b). The non-dimensional magnitude (defined as the RMS value of the periodic signal, expressed as a percentage of the local time-mean isentropic dynamic head) and non-dimensional frequency (expressed as a Strouhal number, St, based on the mean exit flow velocity and the TE thickness) of periodic static pressure fluctuations in the wake flow for each TE geometry at three spanwise locations are plotted in Figure 4. The midspan data are also summarised in Table 3.

Table 3: Midspan wake pressure fluctuations for each of the four geometries, characterised by normalised RMS magnitude and Strouhal number.

Geometry	Overhang length / l	$\Delta p_{\mathrm{RMS}}/(p_{01}-\overline{p})$	St
1	1.00	0.13%	0.27
2	0.67	0.06%	0.30
3	0.33	0.11%	0.28
4	0.00	0.80%	0.20

For each geometry, the Strouhal numbers were in reasonably good agreement at the three spanwise locations, with St varying by no more than 0.02 across the span. The St values range from 0.20 to 0.32 between geometries. This is in reasonable agreement with a cylinder in crossflow which, for the same Reynolds

number, has a characteristic Strouhal number of approximately 0.23 [28]. For Geometries 1, 2 and 3 the magnitude of normalised pressure fluctuations was very low, in the range 0.06–0.13% of local isentropic dynamic head ($p_{01} - \overline{p}$, where $\overline{p}$ is the temporal mean of the unsteady pressure signal). In contrast, the normalised pressure fluctuation for Geometry 4 was approximately 0.80%, or 8.0 times larger than the average for Geometries 1 to 3. The magnitude of fluctuations at 75% span for Geometry 4 is approximately half that at 25% and 50% span. This is thought to be due to a Mach number dependence of the shedding for Geometry 4 (reduced Mach number towards the case).

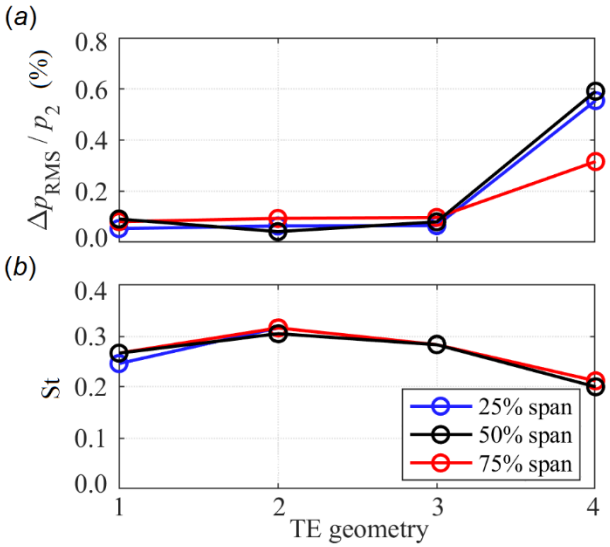


Figure 4: Wake pressure fluctuations for each of the four geometries at three span locations characterised by: (a) normalised RMS magnitude; and (b) Strouhal number.

The increase in the magnitude of pressure fluctuations for Geometry 4 is thought to be caused by a change in the shedding mode as the overhang length becomes short. Figure 5 shows URANS-predicted instantaneous snapshots of the unsteady flow-field at midspan for Geometries 1 and 4, focussing on the wake region immediately downstream of the TE. Figures 5a–b show the normalised local KE loss coefficient. The wake region for Geometry 4 is significantly wider than for Geometry 1, and has greater unsteady fluctuation from the average position. Figures 5c–d show corresponding plots of the λ_2-criterion, to provide an indication of the vortex street arrangement in the wake region. Figures 5e–f are schematic representations of the vortex street structures for Geometries 1 and 4.

We see three key differences moving between Geometries 1 and 4: firstly, that the vortices become more intense (higher λ_2); secondly, the vortex street becomes wider; and thirdly, the vortices have wider spacing in the streamwise direction, indicating a lower shedding frequency. These observations, which are in line with the pressure fluctuation magnitude and shedding frequency data in Figure 4 and Table 3, are caused by a change from vortices being shed from the narrow overhanging SS TE land in Geometry 1, to vortices being shed from the entire (SS + PS) base region in Geometry 4 (wider than the SS TE land in Geometry 1 by a factor of 3.2). We refer to these vortex street arrangements as *Mode 1 shedding* and *Mode 2 shedding*, respectively. Shedding from a much wider base region results in the formation of larger eddies at a lower shedding frequency. We return to the idea of Mode 1 and Mode 2 shedding in later sections to explain and understand changes in both the local distribution and average value of loss coefficient between TE geometries.

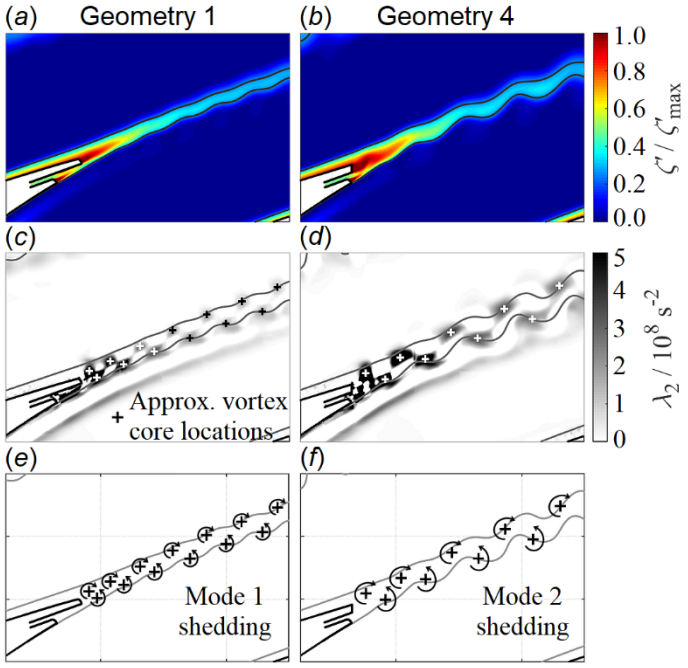


Figure 5: Midspan URANS CFD snapshots for Geometries 1 and 4 showing: (a–b) contours of local KE loss coefficient, ζ', in the wake region; (c–d) contours of λ_2-criterion in the wake region; (e–f) schematic diagrams of vortex street layouts.

LOCAL LOSS COEFFICIENT DISTRIBUTIONS

Full area surveys of local KE loss coefficient, ζ' (equation (2)), measured in experiments in plane 1 are presented in Figure 6 for all four TE geometries. The data are viewed from downstream to upstream (SS to the left of the wake and PS to the right). URANS CFD data in the same axial plane are presented in Figure 7.

The wakes have a characteristic bowed shape, reflecting the compound lean of the vanes (see [21]). The depth of the wake is significantly over-predicted by URANS, and the wake width under-predicted. The agreement between the experiment and URANS CFD in terms of absolute loss coefficient is examined in detail in [21], where it is concluded that approximately 90% of the over-prediction of average loss coefficient in the CFD result is caused by over-prediction of the total pressure loss associated with film cooling. When comparing local loss coefficient data in an axial plane, the well-known problem in many CFD methods of under-predicting mixing rates also contributes significantly to the disagreement.

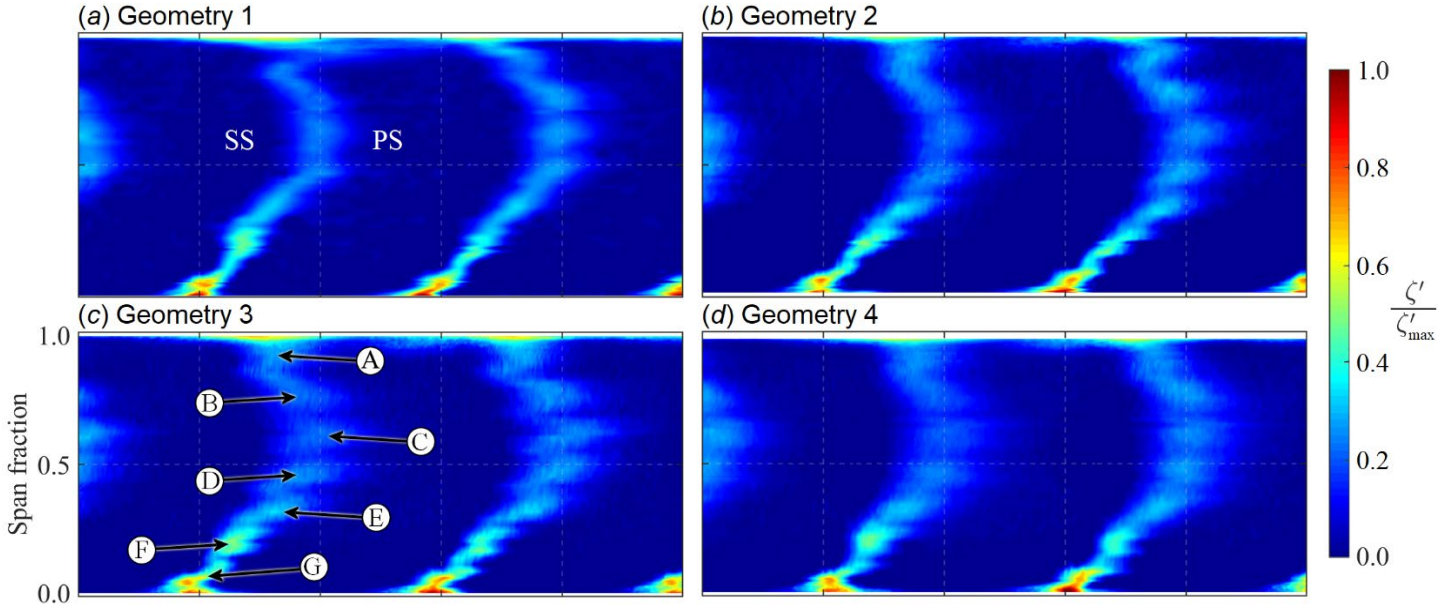


Figure 6: Experimental distributions of local KE loss coefficient, ζ', in plane 1 ($x/C_x = 0.25$) for each TE geometry.

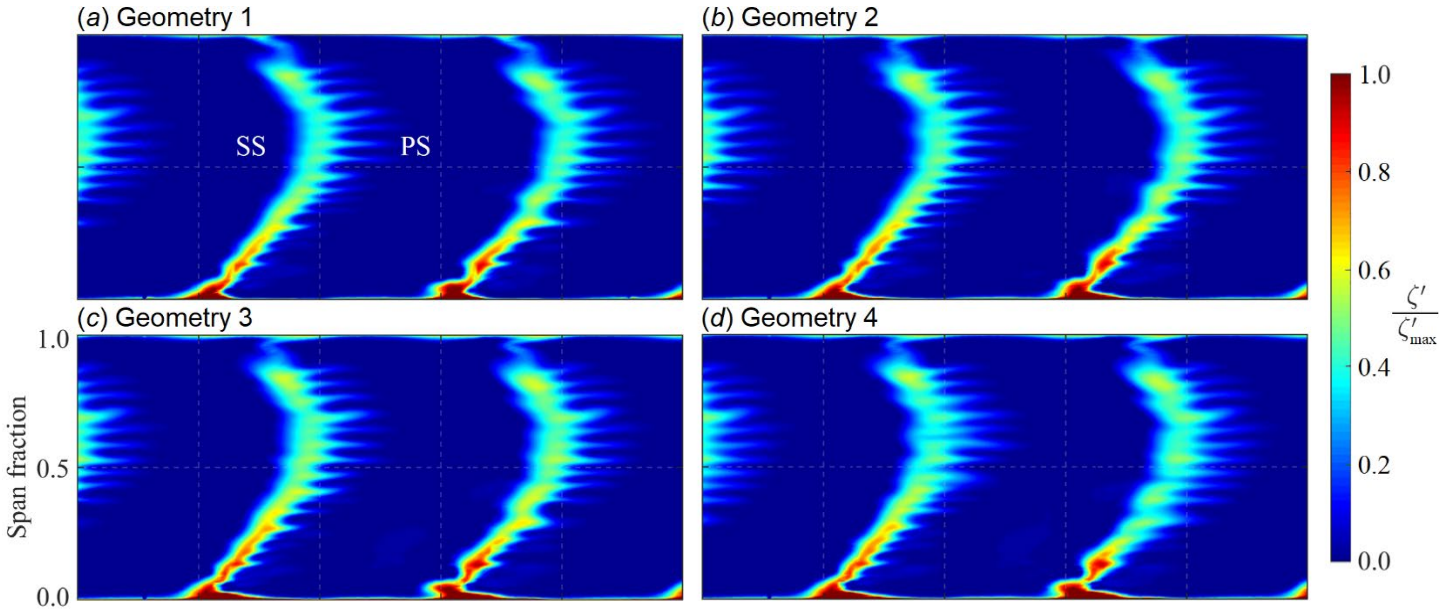


Figure 7: CFD distributions of local KE loss coefficient, ζ', in plane 1 ($x/C_x = 0.25$) for each TE geometry.

In both experiment and CFD, the wake profile has significant radial variation, being deeper and narrower close to the hub. This is caused in part by the lean, sweep and turning profiles of the vane which cause the path length between the local TE and the traverse plane to be lower near the hub (0.64 C_x at 25% span in plane 1) than near the case (0.85 C_x at 75% span in plane 1) (see also [21]). In the experiment in particular, we also see that the wake is marked by seven discrete peaks in loss coefficient (marked A to G in Figure 6), separated by local loss coefficient minima. These minima align with the ribs in the internal cooling system. This effect is considered in detail in [21]. The peaks and minima are much less prominent in the CFD solutions, as they are conflated with horizontal striations to the PS of the wakes. These significantly shorter-scale features can be traced directly to the 17 films on the aft PS row (74% tangential chord). Their high prominence in the downstream flow-field is thought to be caused by inadequate modelling of the mixing interaction between the films and the mainstream flow by the source-terms model, and significant under-prediction of mixing rates. The high protrusion of these features to the PS of the wakes is

exaggerated due to the flow being viewed in axial planes, which cut the wakes at an oblique angle (approximately 75°). Notwithstanding these differences in mixing behaviour between the CFD and experiment, we note that otherwise the experiment and CFD are in reasonable agreement.

We now compare the local distributions between the four TE geometries. We make the following observations:

1. The change in the general shape of the wake signature between geometries is very small. The differences are slightly greater in the experimental data than in CFD.
2. Wake breadth increases slightly with decreasing overhang length—an effect that we examine quantitatively in a later section.
3. In the experiment, the radial non-uniformity of the wakes varies significantly between geometries. The spanwise peaks are more pronounced for Geometries 2 and 3 than for Geometries 1 and 4. This might be explained by the following competing effects: in the covered region upstream of the SS TE the TE coolant can radially mix, but this effect becomes weaker as overhang length is reduced (shorter covered region) leading to greater radial non-uniformity of the coolant flow as the SS-overhang is progressively shortened; between Geometries 3 and 4 there is a sudden increase in mixing which outweighs the effect of the reduction in covered radial mixing. The latter effect is thought (based on analysis of local loss coefficient data presented in the later sections) to be caused by the structural shift in the vortex shedding mode (analysis of Figure 4), although no unsteady experimental measurements were made to confirm this.
4. In CFD, the radial non-uniformity changes very little between Geometries 1, 2 and 3, with only small changes in individual film cooling striations. The Geometry 4 striations are slightly more mixed-out, an effect that is attributed to enhanced mixing due to TE vortex shedding.
5. The secondary loss cores at hub and case have some sensitivity to TE geometry. We analyse these immediately.

Sensitivity of secondary flow cores to TE geometry

Figure 8 shows close-up views of the wake-endwall junction regions at hub and case for each geometry. The difference in intensity of secondary losses between hub and case is attributed primarily to the downwash effect generated by the radial pressure gradient, which causes low momentum secondary flow to migrate away from the case (case secondary loss cores rapidly disperse) and towards the hub (secondary flow accumulates at the hub and forms intense loss cores).Consider first the case regions shown in Figure 8a–d and i–l. In CFD, the near-wall loss core (marked A) is clearly separated from the wake loss region (marked B) by a region of low loss coefficient (90–97% span). In contrast, in the experimental data the near-wall loss core and wake loss region are connected. This difference is attributed to an over-prediction of the downwash effect of the radial pressure gradient.

The relative circumferential positions of cores A and B move significantly between geometries. In Geometry 1, core A is slightly to the SS (left) of core B. As overhang length reduces, core A gradually extends out to the PS. This change, also seen in CFD, arises because the TE machining operations left a small amount of uncut material at the TE-endwall junction (approximately 2 mm). Therefore, as the SS-overhang was progressively shortened, the endwall section and its associated loss core extended further downstream of the SS TE and appear stretched to the right. The extended endwall section is thought to suppress vortex formation from this corner, acting like a splitter plate to disrupt vortex roll-up.

In CFD, the two legs of the hub horseshoe vortex are contained within a single loss region. Dashed circles indicate the locations of the distinct vortices. The PS leg (passage vortex), marked D in frames m–p, is flattened against the hub endwall. The SS leg, marked E in frames m–p, sits just above it (around 4% span) and protrudes to the SS of the wake. These two vortices form a contra-rotating pair with opposing vorticity. The size and shape of cores D and E varies slightly between geometries, but is not significant to the change in aerodynamic performance.

An additional loss core is located against the hub endwall to the PS of the wake centreline (marked F in frames m–p). Core F corresponds with the blockage of the TE-endwall junction, and a vortex shed from the corner of the TE slot (equivalent to core A at the case). Core F grows as overhang length is reduced, extending further out to the PS of the wake. Again, this change results from vestigial overhang material at the TE-endwall corner (same cause as the shift in core A).

Radial profiles of KE loss coefficient and whirl angle

In Figure 9 we present radial profiles of circumferentially-mass-flux-averaged KE loss coefficient, $\zeta''(r)$ (equation (3)), for each TE geometry in plane 2. This data is analysed further downstream of the TE than that in Figures 6 and 7 (0.50 C_x as opposed to 0.25 C_x), to reduce the degree to which radial non-uniformity obscures other changes between geometries. Comparisons between planes are omitted for brevity.

We first observe that there is a large region of relatively constant loss coefficient which extends between 20–85% span in experiment, and between 10–80% span in CFD. We refer to this as the *profile loss region* because in this region the flow is relatively 2D and unaffected by secondary flow. Outside the profile loss region, the loss coefficient grows rapidly due to a combination of secondary flow and accumulation of endwall boundary layer fluid. In the CFD solutions there is a very pronounced loss coefficient minimum just outside the case boundary layer. This arises because of an over-prediction of the downwash effect, resulting from under-mixing of the low momentum case boundary layer fluid.

In the experimental data we measure a clear rise in average loss coefficient as we move progressively from Geometry 1 to 4. We see the same rise in the CFD data, but the magnitudes of the changes are smaller, and the effect is less visually obvious due to greater radial variation in the loss coefficient profile. Considering the profile loss region, between Geometries 1 and 4 ζ'' rose by an average of +27.3% in experiment, and by +11.8%

in CFD. The percentage increases for each geometry change are summarised in Table 4.

The experimental data show a moderate rise in ζ'' between Geometries 1 and 2, a large rise between Geometries 2 and 3, and a relatively small rise between Geometries 3 and 4. In CFD, there were roughly equal, moderate increases for the Geometry changes 1–2 and 2–3, and only a very small increase for the Geometry change 3–4. The mechanisms explaining these trends are explored later in this paper.

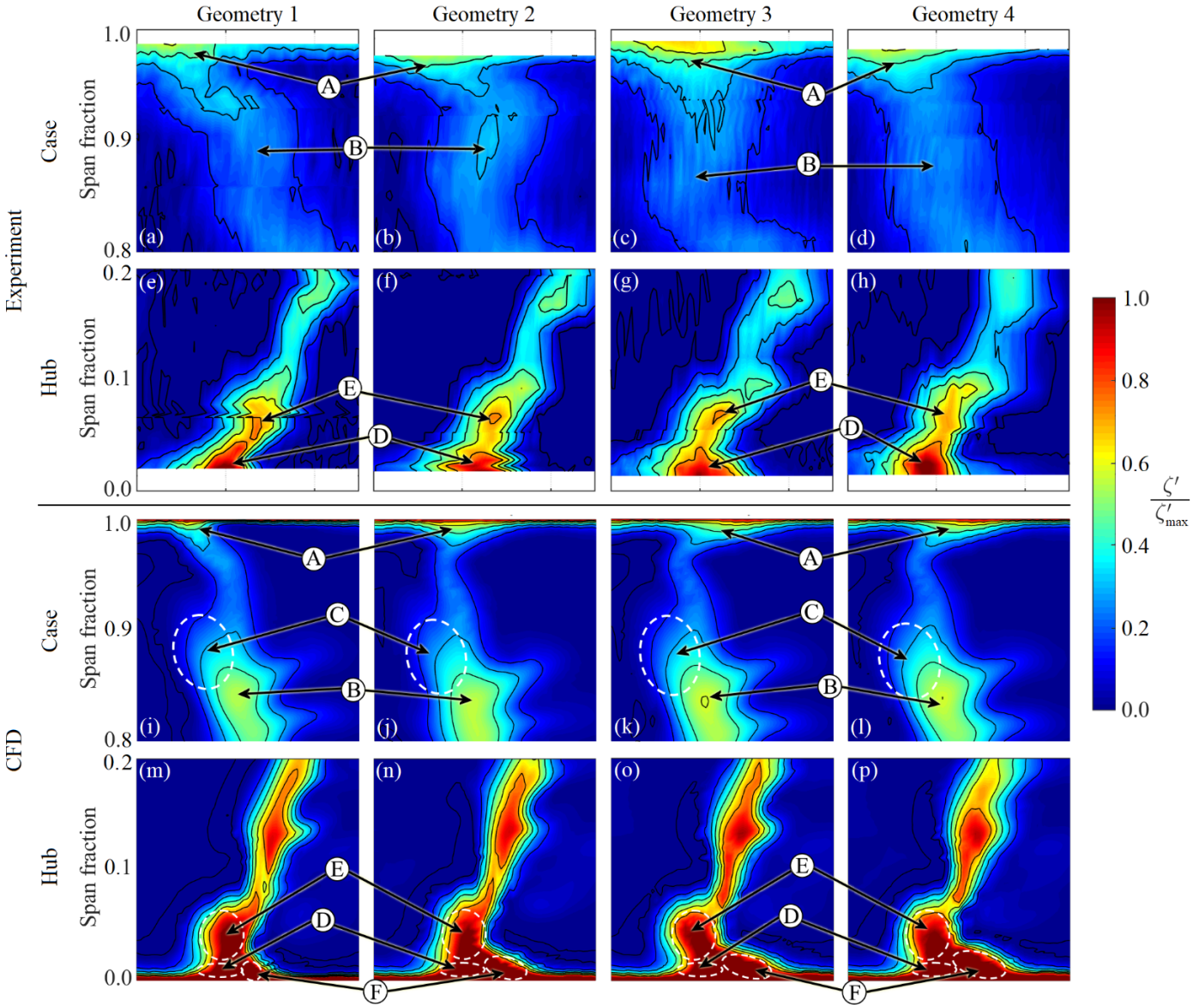


Figure 8: The wake-endwall junction regions at hub and case for all four TE geometries in experiment (a to h) and CFD (i to p).

Table 4: Percentage changes in average loss coefficient (ζ'') in the profile loss region for plane 2.

Geometry change	% change in average ζ'' with respect to geom. 1	
	Experiment	CFD
1–2	+8.59%	+5.79%
1–3	+24.49%	+10.39%
1–4	+27.27%	+11.75%

We now quantify the radial non-uniformity in the profiles by comparing the RMS amplitude of fluctuations over the profile loss region. These are tabulated in Table 5, expressed as a percentage of ζ'. In all cases the magnitude of fluctuations is greater in CFD than in experiment (average of 11.68% across all geometries, compared to 8.21% for experiment), due to the under-mixed individual films (striations in Figure 7). In CFD, the amplitude of radial fluctuations first rises between Geometries 1 and 3, but then falls between Geometries 3 and 4. This fall in magnitude reflects the enhanced mixing rate close to the TE,

caused by the increased magnitude of TE vortex shedding and the structural change from Mode 1 to Mode 2 shedding. In the experimental data we see the same effect, but the amplitude starts to fall between Geometries 2 and 3. This result suggests that the structural change in TE vortex shedding occurs at longer SS-overhang length in the experiment than in the CFD (noting that unsteady experimental evidence was not available). We return to this idea in later sections.

The corresponding radial profiles of circumferentially-mass-flux-averaged turning (or whirl) angle, β, in plane 2 are plotted in Figure 10. β is defined as the angle between the local flow direction and the axial direction in an axial-circumferential plane. Higher values of β therefore indicate flow further from axial (higher turning). The experimental profiles extend close to the hub and case endwalls, but the small regions of missing data result from the finite size of the five-hole probe.

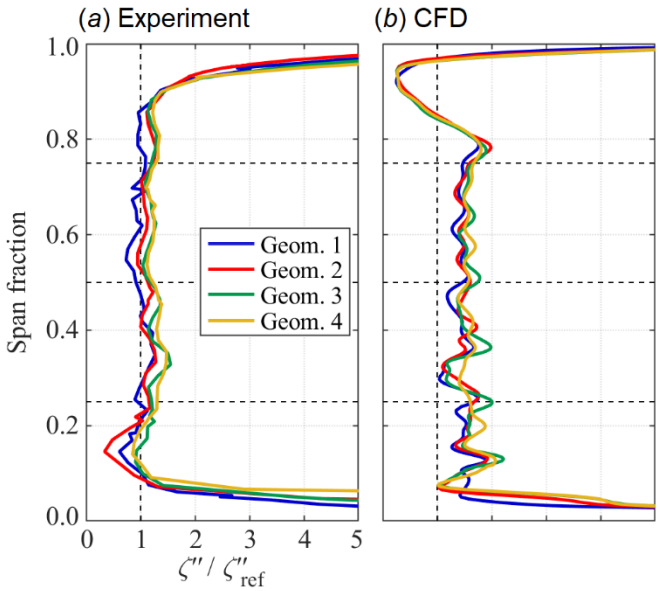


Figure 9: Radial profiles of circumferentially-mass-flux-averaged KE loss coefficient, $\zeta''(r)$, in plane 2.

Table 5: RMS amplitudes of radial fluctuations in ζ'', in plane 2.

Geometry	$\Delta\zeta''_{RMS} / \zeta''_{mean}$ (%)	
	Experiment	CFD
1	8.30%	11.21%
2	9.71%	11.67%
3	8.75%	14.06%
4	6.09%	9.78%

The radial profile shape was very well-matched between experiment and CFD. Mean whirl angle steadily increases from 17 to 66% span, and is approximately constant from 66 to 93% span. The difference in mean whirl angle between experiment and CFD, averaged over the profile loss region (same radial ranges as in Figure 9) and across all four TE geometries, was 0.84°. This is a small absolute offset, showing good capability in this prediction, and is of the same order of magnitude as the estimated overall bias error of the probe (combined uncertainties associated with ECAT measurements and in the probe calibration process).

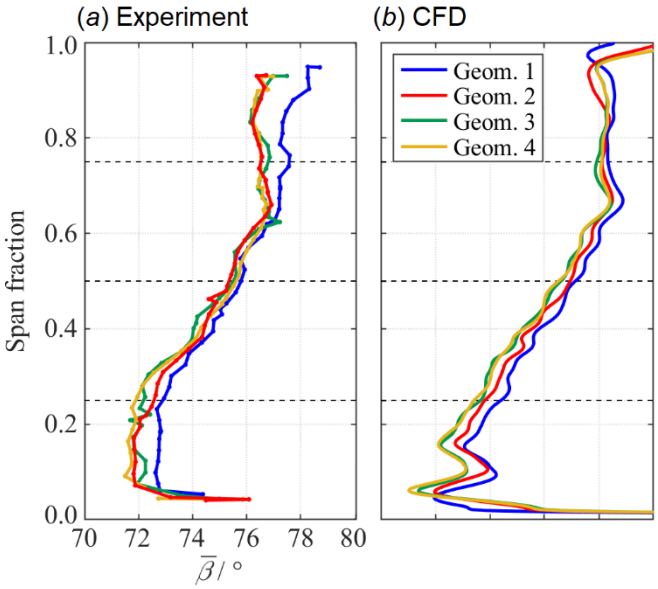


Figure 10: Radial profiles of circumferentially-mass-flux-averaged whirl angle, β, in plane 2.

The radial profile of whirl angle is largely unchanged with TE geometry. There is a small reduction in mean whirl angle in the profile loss region as overhang length reduces. The offsets in $\overline{\beta}$ (averaged over the profile loss region) for each of Geometries 2 to 4 with respect to Geometry 1 are tabulated in Table 6.

In the experiment, the reduction in mean whirl angle with respect to Geometry 1 is almost the same for Geometries 2 to 4. That is, the changes between Geometries 2, 3 and 4 are insignificant. CFD and experiment are in reasonable agreement, but there is a further significant reduction in mean whirl angle between Geometry 2 and 3 in the CFD predictions, which was not recorded in the experiment. The small reduction in whirl angle is attributed to a reduction in the guided length offered by the TE overhang as overhang length is reduced. Once the overhang is sufficiently short (at Geometry 2 in the experiment and Geometry 3 in the CFD), further reduction appears to cause negligible change in the mean whirl angle: this would be expected in a largely separated base region. The difference between CFD and experiment are most likely caused by differences in the unsteady interaction, mixing and shedding of the mainstream and TE flows around the TE slot exit.

Outside of the profile loss region the CFD profiles show regions of over-turned secondary flows just outside of the hub boundary layer. In the experimental data these over-turned regions are more fully mixed-out. The experimental data also show a notably higher mean whirl angle for Geometry 1 outside of the profile loss region (below 20% span and above 70% span) than the other geometries. This is likely caused by deviations of the hand-dressed SS-overhang from the nominal CAD geometry. The effect is not present for Geometries 2 to 4, which have a

sharp-edged termination of the TE. The differences in whirl angle between the TE geometries were approximately the same outside the profile loss region as within it.

Table 6: Changes in circumferentially-averaged whirl angle in plane 2 averaged over the (radial extent of) profile loss region

Geometry change	Change in $\overline{\beta}$ with respect to geom. 1	
	Experiment	CFD
1–2	−0.45°	−0.32°
1–3	−0.48°	−0.65°
1–4	−0.47°	−0.64°

ANALYSIS OF WAKE CIRCUMFERENTIAL PROFILES

In this section, we consider the impact of TE geometry on circumferential profiles of local loss coefficient and whirl angle at a number of radial heights. Figure 11 presents circumferential profiles of local KE loss coefficient, ζ' (equation (2)), over a single wake period at three spanwise locations in plane 1. Each profile is radially averaged over ±5% of span to reduce sensitivity to small radial non-uniformities.

All of the profiles (Figure 11a to f) have a quasi-normal distribution with slight asymmetry, such that the decay in loss coefficient from the peak is steeper on the SS than on the PS. This is not a simple function of accumulated deficit: the SS boundary layer momentum thickness just upstream of the TE separation point is approximately 20 times larger than that on the PS (based on boundary layer profiles at the TE predicted by fully-cooled URANS simulations; note that the extremely large ratio is at the extreme SS TE downstream of a shock-impingement region). This analysis is described in more detail in [27]. Indeed, the overall deficit in the wake is dominated by the separation loss (or *pressure drag*), with the integrated boundary layer loss accounting for only approximately 30% of the overall loss in the profile region. Thus, such a result should not necessarily be surprising. A further contributing effect worth noting is that the streamwise path length between the PS TE lip a given traverse plane (e.g. plane 1) is greater than the equivalent dimension for the SS TE lip—by as much as 0.14 C_x for Geometry 1, dropping to 0.02 C_x for Geometry 4. The effect arises because (as is convention) we traverse in an axial plane, as opposed to a streamwise-normal plane. We see later in the context of analysing the wake width as a function of axial distance (Figure 14) that this could account for approximately 45% of the observed asymmetry in the wake profile (when the SS-overhang is relatively long, and the traverse plane is relatively close to the TE, e.g. plane 1).

Continuing this theme, the differences in peak height and width between the three spanwise locations are driven largely by radial variations in vane lean, sweep, and whirl angle, which cause differences in the streamwise path length between the TE and the traverse plane. This is an interesting effect that has been analysed in detail in [21] and the analysis will not be repeated here. It was shown that if the data is presented (unconventionally) in terms of *streamwise path length from the TE*, a good collapse of the wake width trends at different radial heights can be achieved.

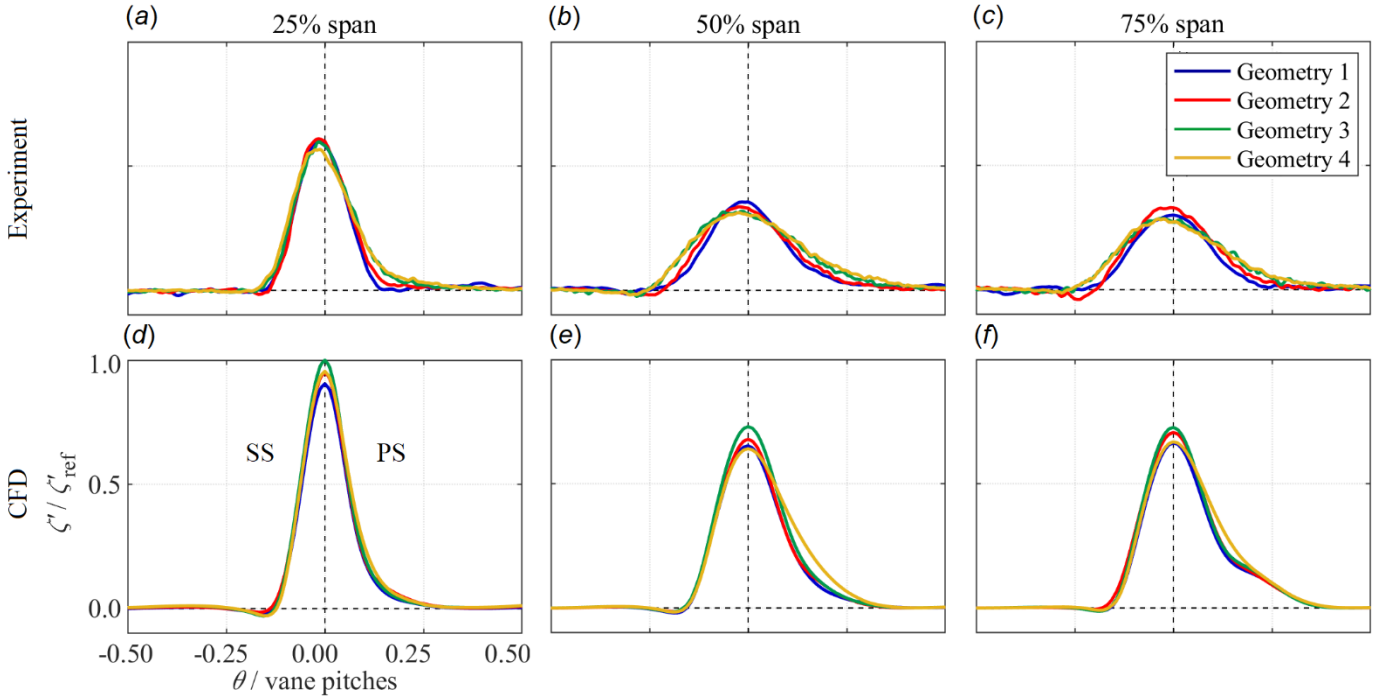


Figure 11: Circumferential profiles of local loss coefficient, ζ', compared between the four TE geometries at 25%, 50% and 75% span in plane 1: (a–c) experiment; (d–f) URANS CFD.

An interesting secondary feature in the CFD data of Figure 11f is the weak secondary peak between $0.15 < \theta < 0.25$, caused by partially mixed late-PS films. This was discussed in the context of Figure 7.

Consider now the differences in wake profile shape between the four TE geometries. The CFD profiles in Figure 11d–f show almost identical profile shapes between Geometries 1 to 3 at all three spanwise locations, differing only in the peak height. Peak height rises on average (of three spanwise locations) by +5.16% between Geometries 1 and 2, and by +5.19% between Geometries 2 and 3. Geometry 4 differs from the general trend in two ways: firstly, the peak height falls relative to Geometry 3; and secondly, the PS of the wake profile broadens at 50% and 75% span. These effects are attributed to enhanced mixing close to the TE, due to stronger vortex shedding (Mode 2 shedding) in Geometry 4 (Figure 4). At 25% span the effect is much weaker because the streamwise path distance between the TE and plane 1 is significantly shorter, and thus the additional mixing has less path length in which to cause an effect.

Looking at the experimental profiles in Figure 11a–c, we see two distinct pairs: Geometries 3 and 4 have a lower peak height (by an average of −8.1%), and a greater width, than Geometries 1 and 2, for all three spanwise locations. Again, the difference is smaller at 25% span. The suggestion is that the apparent additional mixing seen in Geometry 4 in URANS CFD (evidence of reduced radial non-uniformity in Table 5 and lower and broader peak in Figure 11) is present for *both* Geometries 3 and 4 in the experimental data. That is, as mentioned previously, the structural change from Mode 1 to Mode 2 shedding occurs at longer SS-overhang length in the experiment than in the CFD.

Midspan circumferential profiles of whirl angle in plane 1 are plotted in Figure 12. The difference in profile shapes between experiment and URANS CFD is immediately noticeable. Experimental profiles show the expected transition across the wake centre from a maximum on the SS to a minimum on the PS, corresponding with the difference in exit metal angle. In contrast, the URANS simulations predict very little circumferential variation in whirl angle across the wake. This is attributed to an over-prediction of shock-boundary layer interaction on the late-SS, causing early separation. The effect is discussed in more detail in [21].

Comparing the midspan whirl angle distributions between TE geometries, we see two main differences. Firstly, there are small offsets in local whirl angle in the free-stream away from the wake ($\theta < -0.25$ and $\theta > 0.40$), in agreement with the offsets in average whirl angle in the profile loss region (Figure 10 and associated analysis). This effect is caused by the changes in covered turning of the vane as the SS-overhang is progressively shortened.

Secondly, in the experimental data there is a notable rise in the minimum whirl angle just to the PS of the wake ($0.0 < \theta < 0.2$) between Geometries 2 and 3. The difference between the SS peak and PS trough drops from an average of 8.1° for Geometries 1 and 2 to an average of 6.7° for Geometries 3 and 4. This is thought to be due to a change to more aggressive and larger length scale (Mode 2) mixing, which enhances the low near-PS whirl angles by averaging over larger length scales in the TE region.

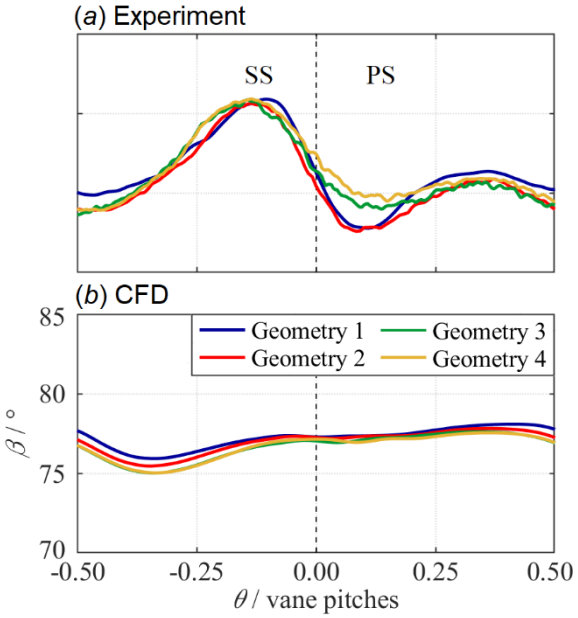


Figure 12: Circumferential profiles of whirl angle at midspan in plane 1 from: (a) experiment; (b) URANS CFD.

ANALYSIS OF WAKE MIXING RATE

In this section, we examine the change in wake mixing rate with TE overhang length. We characterise the circumferential profiles of local loss coefficient (Figure 11) using a peak local loss coefficient, $\hat{\zeta}'$, and a wake width, w. Here the width is defined as the fraction of vane pitch over which local loss coefficient exceeds 50% of the peak value. These two parameters are plotted in Figures 13 and 14 respectively as functions of *true axial distance* from the TE normalised by axial chord length, x'/C_x, using data from the midspan section. The true axial distance is the distance measured from the midspan TE extent *for each geometry*. This distinction corrects for the small changes in axial location of the SS TE tip between geometries as the SS-overhang is progressively shortened. Notwithstanding small differences in the whirl angle at midspan (see Figure 10), x' can be taken as a proxy for the true streamwise distance between the TE and the measurement plane. The purpose of this clarification is to distinguish the differences in wake shape *due to changes in TE geometry*, from differences that arise due to changes in distance between the TE and the traverse plane. It has been demonstrated in previous work [21] that apparently dissimilar wake profiles can be collapsed to a large extent when moving from an absolute axial co-ordinate system to a local streamwise co-ordinate system. In the current case we demonstrate that this is not a significant factor, because the predominant effects arise due to TE design changes.

Consider first the peak loss coefficient data of Figure 13. The peak loss coefficient values for both experimental and CFD data follow a quasi-exponential decay with x'/C_x. Absolute values of peak loss coefficient in a particular axial plane follow

the trends observed in Figure 11: in CFD $\widehat{\zeta}'$ rises between Geometries 1, 2 and 3 and falls for Geometry 4; in experiment $\widehat{\zeta}'$ is higher for Geometries 1 and 2 than Geometries 3 and 4, but the differences between geometries are much smaller than in the CFD predictions. The experimental values of peak loss coefficient are approximately half those for CFD, due to under-mixing in the CFD solution. For the CFD data, the shape of the trends are almost identical for Geometries 1 to 3, but Geometry 4 has a steeper rate of decay close to the TE, and a shallower gradient further downstream. This is caused by stronger vortex shedding close to the TE. The same pattern is true in the experimental data, but with steeper initial decay for both Geometries 3 and 4. This supports the hypothesis of a shift to Mode 2 vortex shedding for both Geometries 3 and 4 in the experiment, promoting mixing close to the TE. For completeness we note (by inspection of the trends) that the impact on the differences between trends of moving from absolute to *true* axial distance is small in comparison to the differences due to TE design.

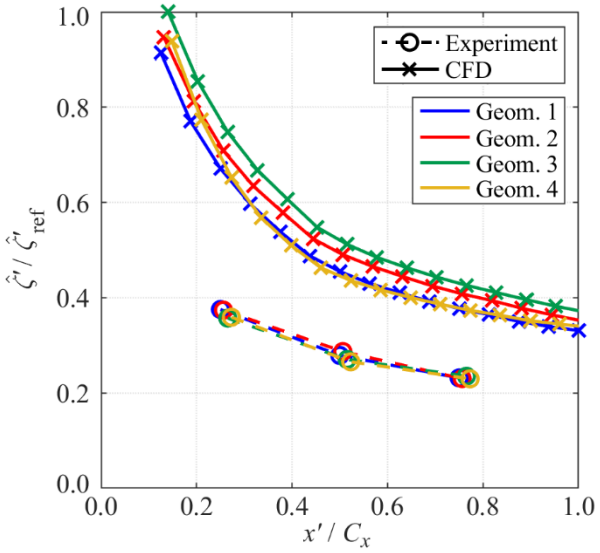


Figure 13: Peak KE loss coefficient, $\widehat{\zeta}'$, at midspan as a function of true axial distance.

We now consider the trend of wake width with x'/C_x in Figure 14. Looking first at the experimental data, we see an approximately linear increase in wake width with axial distance (as the wakes mix out) and an increase in width as the overhang length is reduced. The differences in wake width between geometries are significantly larger in the experiment than in the CFD data, in line with the observations of Figure 11. There is a distinct separation between the trends for Geometries 1 and 2 and those for Geometries 3 and 4, supporting the structural change in the vortex shedding.

The CFD data, analysed at finer axial resolution, show a more complex trend with local plateaus at $x'/C_x = 0.50$ and 0.90. These modulations in the gradient of the wake width arise as the wakes pass through periodic streamwise pressure gradients—this is analysed in more detail in [21]. We note that whilst the experimental data are relatively sparse, the data are consistent with a similar plateau at approximately $x'/C_x = 0.50$. There is a significant difference between Geometry 4 and all other geometries, both in terms of the initial rate of increase of wake thickness (in the range $0.00 < x'/C_x < 0.40$) and the absolute thickness at every axial station. This supports the argument for a shift from Mode 1 to Mode 2 shedding between Geometries 3 and 4 in the CFD.

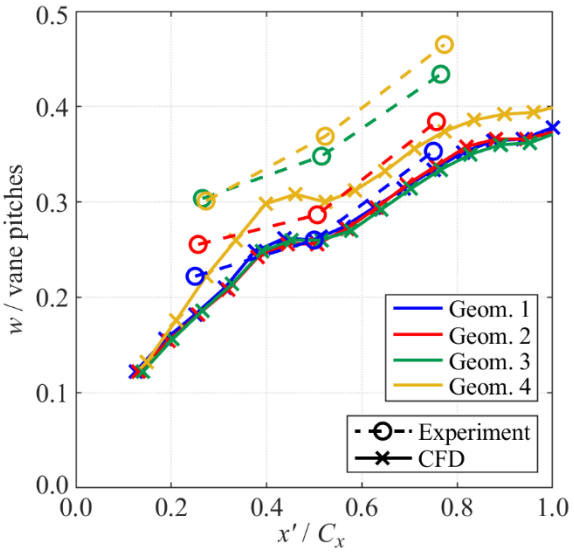


Figure 14: Wake width, w, at midspan as a function of true axial distance.

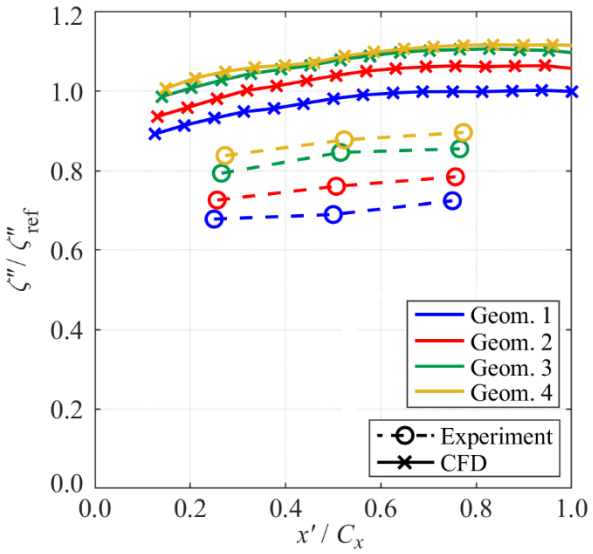


Figure 15: Circumferentially-mass-flow-averaged KE loss coefficient, ζ'', at midspan as a function of true axial distance.

In Figure 15 we present midspan trends with true axial distance of circumferentially-mass-flow-averaged KE loss coefficient, ζ'' (equation (3)). Both experiment and CFD show an increase in average loss coefficient moving axially downstream as remaining secondary kinetic energy (SKE) is mixed out and

becomes manifest as loss. The URANS simulations over-predict average loss coefficient by an average of 32.1% (across all geometries and axial stations). The axial gradient of average loss coefficient is very similar between the four TE geometries, and between CFD and experiment. As overhang length is progressively reduced, the average loss coefficient in a given axial plane increases. We analyse this effect in more detail in the following section.

The primary conclusion is that TE overhang length has only a very small impact on the wake mixing rate. In cases where Mode 2 shedding occurs, mixing is biased towards the TE leading to higher rates of peak local loss coefficient decay, and of wake thickening, near the TE. Shorter TE overhangs have a higher average loss coefficient but the effect must be separated from changes in the SS TE thickness.

ANALYSIS OF OVERALL AERODYNAMIC PERFORMANCE

We now assess the overall change in aerodynamic performance between the four TE geometries, by comparing plane-averaged and mixed-out average KE loss coefficients for the profile loss region. We consider only this region, so as to isolate the effect of the change in TE design, having already shown (Figure 8 and associated analysis) secondary losses do not change significantly with overhang length, being primarily a function of the detailed TE-endwall junction geometry.

Plane-average KE loss coefficients, ζ''' (equation (4)), and mixed-out average KE loss coefficients, ζ'''' (equation (5)), are presented in Figure 16. Data are taken from plane 3, to reduce the sensitivity to local gradients (flow more mixed out) and to reduce the sensitivity to inaccurate estimation of the SKE (lower absolute value due to partial mixing out by this plane). The profile loss region, over which the average was taken, was between 20% and 80% span. The experimental and CFD data are each normalised with respect to their *respective mixed-out* average loss coefficient for Geometry 1, ζ_1''''. The mixed-out average loss coefficient was calculated using the method of Dzung [26], which is discussed in detail in the context of the current experiment in [21] and [25].

It is worth briefly expanding on the two choices implied by the chosen normalisation method. The reason the *respective* condition was chosen is to highlight the changes in aerodynamics with TE design, as opposed to focussing on the absolute accuracy of the CFD method: it has been shown above, and by more comprehensive analysis in [21], that the URANS simulations over-predict absolute mixed-out average KE loss coefficient by approximately 4.0%. The *mixed-out* condition was chosen (for a detailed discussion of the choice of methods see [25]) because it gives the best representation of overall loss generation by the vane (i.e. both loss already manifest, and inevitable additional loss due to mixing out of SKE), and removes the sensitivity in the comparison to SKE at a particular plane. This is particularly important because of the well-known tendency of URANS to under-predict the mixing rate.

First, we consider the plane-averaged and mixed-out average values of loss coefficient (solid red and blue lines in Figure 16 respectively). The difference between these is the *residual SKE* (yellow line). This is an estimate of the unavoidable additional mixing loss downstream of plane 3. The residual SKE in the experiments is approximately double that predicted by URANS. This is attributed to the greater circumferential variation in whirl angle in the experiment (Figure 12), which provides an additional mechanism for generating mixing loss [25].

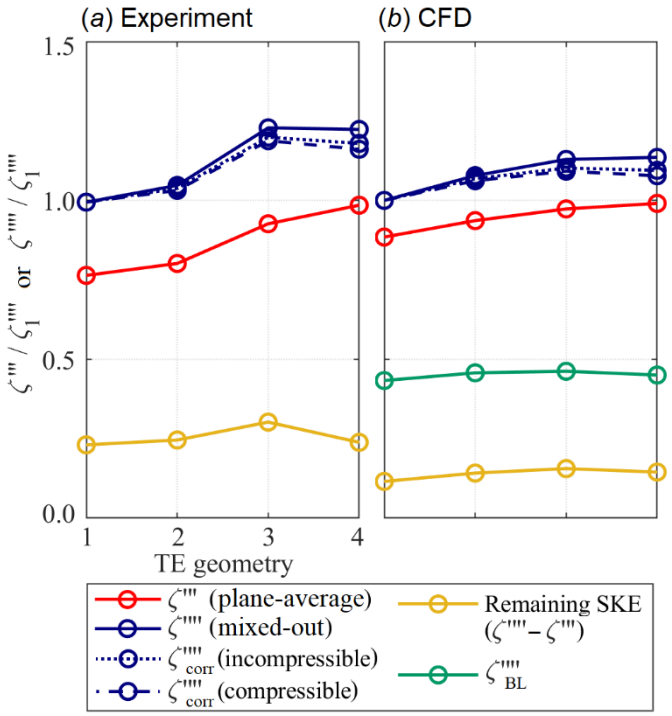


Figure 16: Plane-average and mixed-out average KE loss coefficients in the profile loss region, normalised with respect to ζ_1'''' (data from plane 3).

The trends in both experiment and CFD are for increasing mixed-out average KE loss coefficient as the SS-overhang is progressively shortened. We now attempt to separate the effect due to aerodynamics from that due to TE overhang thickness (t_{SS}, see Figure 2). We do this by scaling the mixed-out average KE loss coefficients for each geometry in knowledge of the SS TE thickness. The scale factors were calculated using an adaptation of the control-volume-based method first described by Stewart [29] and developed by Deckers and Denton [30]. The adapted model is described in Appendix A, and the resultant scale factors for each of Geometries 2 to 4 are summarised in Table 7. Scale factors for both compressible and incompressible conditions are presented for completeness, but we focus on the compressible condition.

The compressible scale factors imply reductions in the mixed-out KE loss coefficient to account for variation in the SS TE thickness of 1.5%, 3.3% and 5.1% for Geometry changes 1–2, 1–3 and 1–4, respectively. These can be compared with the thickness changes in Table 2, but it is worth nothing that the SS TE land is only one of several low base pressure regions in the

control volume method. Applying the compressible correction factors to the data of Figure 16 results in the *corrected* mixed-out average profile loss coefficient ($\zeta''''_{\mathrm{corr}}$) and modifies the trend of mixed-out average loss coefficient to the dotted (incompressible) and dashed (compressible) lines. This is the best estimate of the mixed-out loss coefficient scaled to a common SS TE thickness ($t_{\mathrm{SS},1}$). This correction changes the trend from a monotonic increase to a slight drop in mixed-out average loss coefficient between Geometries 3 and 4.

Table 7: Scale factors for each of Geometries 2 to 4.

Geometry	2	3	4
ζ'''' scale factor (incompressible)	0.991	0.976	0.964
ζ'''' scale factor (compressible)	0.985	0.967	0.949

For completeness, percentage changes in both plane-average and *corrected* mixed-out average profile loss coefficient for each geometry change are tabulated in Table 8. The experimental and CFD percentage changes are referenced to their *respective mixed-out* average loss coefficient for Geometry 1, ζ_1''''.The remainder of the analysis focusses on corrected mixed-out average profile KE loss coefficients.

The experimental data show a small rise in corrected mixed-out average KE loss coefficient between Geometries 1 and 2 (+3.8%), a large rise between Geometries 2 and 3 (+15.6%), and a small *decrease* between Geometries 3 and 4 (−2.7%). The gross trend in the CFD was similar to the experiment, but with corresponding changes +6.2%, +3.0% and −1.5%. That is, changes of approximately half the magnitude, and with a much smaller change in corrected mixed-out average loss coefficient between Geometries 2 and 3 than in the experiment. In the next section we try to understand these changes.

Table 8: Changes in plane-average, corrected mixed-out average, and boundary layer KE loss coefficients for the profile loss region with respect to Geometry 1 (data from plane 3).

Geometry change	Experiment		CFD		
	ζ'''	$\zeta''''_{\mathrm{corr}}$	ζ'''	$\zeta''''_{\mathrm{corr}}$	ζ''''_{BL}
1–2	+3.8%	+3.8%	+5.2%	+6.2%	+0.0%
1–3	+16.3%	+19.4%	+8.9%	+9.2%	+1.3%
1–4	+22.1%	+16.7%	+10.6%	+7.7%	−0.4%

BOUNDARY LAYER LOSS, BASE PRESSURE, AND VORTEX SHEDDING MECHANISMS

In this section we consider the contributions of boundary layer loss, base pressure loss and vortex shedding mechanisms to the overall corrected mixed-out average KE loss coefficient, in an attempt to reconcile the observed changes between geometries (Table 8). We first consider the boundary layer loss.

Boundary layer loss

The green line in Figure 16b shows the estimated KE loss coefficient associated only with the surface boundary layers for each TE geometry in the CFD. We refer to this as ζ''''_{BL}. These data were calculated from the SS and PS boundary layer velocity profiles at the TE at midspan (we assume that the boundary layer profiles are sufficiently radially uniform over the profile loss region for our present purpose), using the method described in [31]. Boundary layer profiles for the same data set are presented in [27]. The changes in KE loss coefficient associated with boundary layers were +0.0%, +1.3%, and −0.4% of ζ_1'''' for the Geometry changes 1–2, 1–3, and 1–4 respectively. These contributions are summarised in the last column of Table 8. These very small changes in loss coefficient (with respect to Geometry 1) are primarily caused by small differences in the SS boundary layer thickness, driven by changes in shock-boundary layer interaction on the mid-to-late SS.

Comparing the changes in KE loss coefficient associated with boundary layers with the overall URANS-predicted changes in *corrected* mixed-out average KE loss coefficient (Table 8), we see that on average (across the three geometry changes), ζ''''_{BL} accounts for only 3.5% of the change in $\zeta''''_{\mathrm{corr}}$.

We conclude that whilst the changes in SS shock-boundary layer interaction do contribute to the change in $\zeta''''_{\mathrm{corr}}$, they are almost insignificant in the overall result. In the next sub-sections, we consider changes in base pressure loss and in vortex shedding behaviour.

Base pressure drag

We now consider the contribution of base pressure loss to overall corrected mixed-out average profile KE loss coefficient. Note that the analysis in this section is based on base pressure data from the CFD study only—no experimental base pressure measurements were made.

Figure 17 compares normalised pressure distributions over the SS and PS TE bases at midspan for each TE geometry, from the URANS CFD simulations. The abscissa represents distance normal to the TE slot exit direction, with the origin at the slot centreline. The left and right-hand sides of the figure show the pressure distributions around the SS and PS bases, respectively. Base pressure distributions were compared between different radial locations (not shown), and whilst the absolute pressures varied in line with the radial pressure gradient (higher pressures close to the case), the shape of the distributions and the changes with TE geometry varied little with span. We therefore consider the change with span unimportant, and analyse midspan data only.

On the PS, mainstream flow expands around the PS TE corner, then separates from the TE. The expansion results in the sharp dip at $y/t_{\mathrm{s}} \approx 1.5$. The pressure then settles to an approximately constant value over the PS *base region* (marked by vertical dashed lines). Another expansion can be seen at the inner corner of the PS base region, where TE coolant flow expands slightly around the inside TE corner. In the approach to the SS TE corner, the mainstream flow is diffused slightly (approaching the mean TE pressure, and consistent with a small

deviation angle *towards* axial) before settling to an approximately constant value in the SS base region. There is a sharp diffusion at the SS inner corner where flow expands around the TE inner corner.

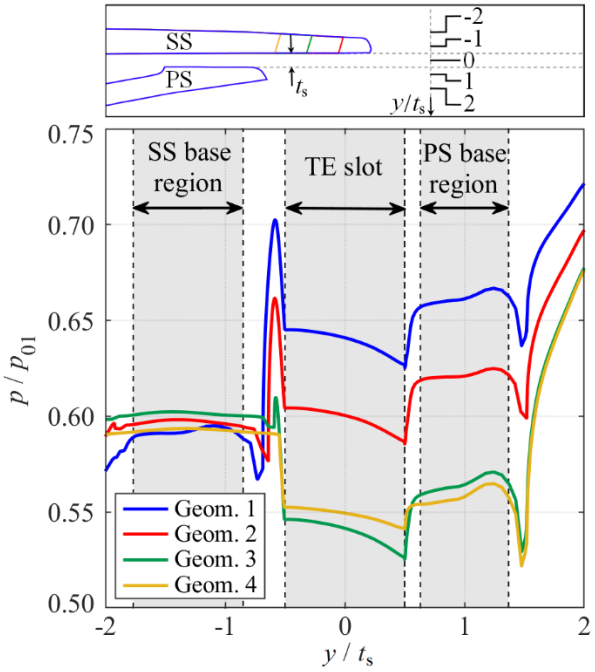


Figure 17: Midspan base pressure distributions.

We now compare PS and SS base region pressure distributions for each of the four geometries. The SS base region pressure distributions are almost flat, and change relatively little between geometries (very slight rise in pressure between Geometries 1 and 3, then a small drop in pressure to Geometry 4). The PS base region pressure distributions are also relatively flat, but, in contrast to the SS base region distribution, have large falls in pressure between Geometries 1, 2 and 3, but little further drop between Geometries 3 and 4. All four geometries have significant differences in pressure between the SS and PS base regions.

Average SS and PS base region pressures ($\overline{p_b}$) for each geometry were calculated by taking the mean over the regions of approximately constant pressure indicated by the shaded regions in Figure 17. The average values are plotted in Figure 18, as both fractions of inlet total pressure, $\overline{p_b} / p_{01}$ (Figure 18a), and as base pressure coefficients, C_{pb} (Figure 18b), defined by

$$C_{pb} = \frac{\overline{p_b} - \overline{p_2}}{p_{01} - \overline{p_2}} \qquad (6)$$

where $\overline{p_2}$ is the circumferentially-averaged static pressure at the cascade exit plane. Although this is a conventional definition of base pressure coefficient, we note that the choice of reference pressure (i.e. $\overline{p_2}$) is arbitrary because of the separation between the TE location and the nominal cascade exit plane, and also the significant static pressure variation across the passage (see analysis in [23]). Notwithstanding this point, the base pressure coefficient is taken to provide a more useful expression of base pressure drag than $\overline{p_b} / p_{01}$, because it is normalised with respect to the dynamic head of the free-stream flow.

The trends of $\overline{p_b} / p_{01}$ (Figure 18a) are in accord with the observations of Figure 17: the SS base pressures are relatively insensitive to overhang length (maximum difference between any two geometries of 0.9% of p_{01}); but the PS base pressures fall sharply between Geometries 1 and 3 as overhang length is progressively reduced. An explanation for the change in base pressure trends is given in [27]. The relevant points are now briefly summarised.

As overhang length is reduced between Geometry 1 and 3, the downstream region of low static pressure (associated with the uncovered turning of the vane) extends further upstream, into the vane passage. This is the result of a change in overall vane aerodynamics around the *controlling region* of the vane passage. Here by controlling region, we mean the region around unit Mach number, to which we traditionally ascribe the term *throat* in a 1D framework. This is discussed in detail in [27].

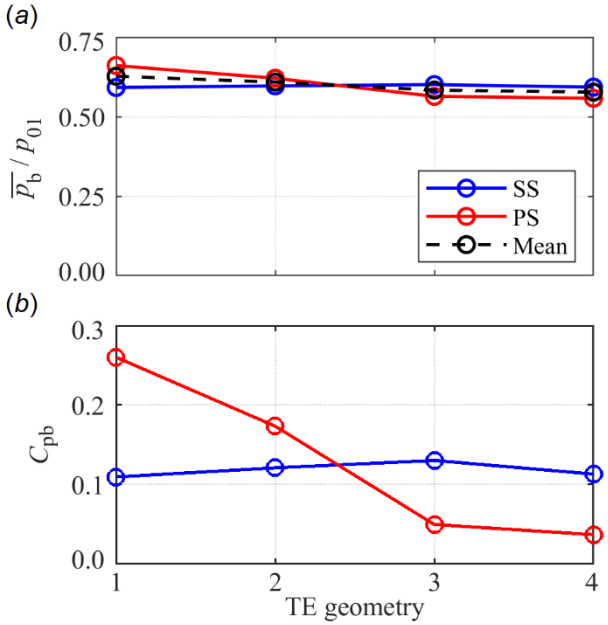


Figure 18: (a) Normalised average base region pressures; (b) base pressure coefficients.

As the low static pressure region migrates upstream, it affects the base region pressure. As the SS-overhang is progressively shortened, the location of the SS TE moves upstream (see Figure 2). For the particular geometry studied, this displacement is similar in magnitude to the displacement of the static pressure contours, and therefore SS TE base region pressure has low sensitivity to overhang length. In contrast, the location of the PS TE remains fixed as the SS-overhang is shortened (see Figure 2), so the PS TE base region pressure has higher sensitivity to upstream migration of the low static pressure region.

We now briefly consider base pressure coefficient trends in Figure 18b. The C_{pb} trends are (of course) broadly similar to

those for $\overline{p_b} / p_{01}$. We note that the coefficient values are everywhere positive. This is due to uncovered turning which occurs between the SS and PS base regions and the cascade exit plane which is located a short distance downstream of the TE.

We conclude by noting that, in the literature, a close association between base region pressure and overall (mixed-out average) loss has been drawn. This is natural because low base region pressure should intuitively be associated with higher *pressure drag* on a component. However, in an attempt to correlate the two we have noted that, for our geometries, the change in base region pressure is associated with a change in overall vane aerodynamics at the same nominal operating point (based on pressure ratio). This latter effect is significant, and means that the base region pressure change cannot be analysed in isolation. That is, correlations between loss coefficient and base region pressure may have little meaning without a more holistic analysis of the vane pressure field. We feel this is a topic that merits more detailed analysis.

Vortex shedding mode and transonic vortex shedding

In this section we briefly review an apparent discrepancy between the CFD and experimental results in terms of corrected mixed-out average loss coefficient, which we believe may arise because of the inability of the URANS CFD method to accurately predict a transonic vortex shedding effect.

Accepting corrected mixed-out average KE loss coefficient as the best measure of overall loss, we recall that the rise in corrected mixed-out average loss coefficient between Geometry 2 and 3 was much larger in the experiment than in CFD. This was discussed in the context of Figure 16 and Table 8.

The wake width data (Figure 14) provide clear evidence of an enhancement of near-TE mixing between Geometry 2 and 3 in the experiment, and between Geometry 3 and 4 in the CFD. We suggest that this effect is associated with a structural change between Mode 1 and Mode 2 vortex shedding. Direct analysis of vortex sheet patterns (Figure 5) and indirect evidence from the Strouhal number changes (Table 3) confirm that that such a mode change occurs between Geometry 3 and 4 in the CFD. It is tempting to assume that the change in shedding mode should be related to a significant rise in loss coefficient. Such an assumption would be compatible with the experimental data of this study (provided we believe that a change in shedding mode may occur between Geometry 2 and 3, without direct experimental evidence), but would not be in agreement with the CFD data.

In the *transonic vortex shedding* phenomenon described by Melzer and Pullan [8] (see also [7])—a study conducted in parallel with the current work, and for the same purpose—the authors demonstrate (by means of unsteady schlieren imaging) periodic shedding of pressure waves from the TE vortex structures. These pressure waves propagate away from the TE, and, in the case of the PS wave, impinge on the SS of the adjacent vane, stimulating rapid thickening of the boundary layer and additional total pressure loss. The primary component of the additional loss is not the direct result of the interaction of the strengthened vortex with the base region, but rather a secondary result of the pressure wave caused by the vortex impinging on the adjacent vane.

Considering this quantitatively, the corrected mixed-out average loss coefficient increase measured in experiment between Geometries 2 and 3 was +15.6% (Table 8) of ζ_1'''' (or, equivalently $\zeta_{1,\mathrm{corr}}''''$). This is 12.6% (of ζ_1'''') greater than the corresponding rise predicted by URANS. We believe this difference may be substantially due to the inability of the URANS CFD method to accurately predict the effects arising from shed pressure waves associated with vortex shedding in the transonic range. This is broadly in accord with Melzer [7], who measured increases in mixed-out average KE loss coefficient of between 10–20% at transonic Mach numbers between cooled TE geometries which exhibited shed pressure waves associated with vortex shedding, and those which did not. We reinforce again that no direct evidence of a change in shedding mode was available in the experimental data of this study, but we propose that it is likely based on very similar trends analysed in the experimental and time-averaged URANS data (analysis of Figures 9, 11, and 13).

Noting that whilst the URANS method may be adequate for predicting the shedding mode shift (albeit at a slightly different SS-overhang length), it appears to be poor at accurately predicting shed pressure waves (see e.g. [32], [33]) and therefore the boundary layer interaction on the adjacent vane SS. This, in combination with the Melzer and Pullan [8] mechanism, seems a likely explanation for the differences in corrected mixed-out loss coefficient trend between experiment and CFD. A more sophisticated unsteady numerical method (i.e. LES) would give greater insight into this theory, and we believe would likely close the gap.

CONCLUSIONS

In this paper, we have studied the impact of TE overhang length on the aerodynamic performance of fully-cooled transonic HP NGVs. High-fidelity experimental traverse measurements and unsteady numerical simulations were used for the study. Four different overhang lengths were tested. To account for differences in TE thickness between designs (an issue that has not been addressed in previous studies), a corrected mixed-out average KE loss coefficient was used as the representation of overall loss, where a correction for TE thickness was performed using a control volume method.

The key conclusions of the study are as follows:

1. There was a large rise in the magnitude of unsteady pressure fluctuations in the base region when SS-overhang length became short, and a fall in shedding frequency. This was attributed to a change in vortex shedding mode, from one in which small vortices are shed at relatively high frequency from the extended SS TE tip, to one in which larger eddies are shed (at lower frequency) from the entire base region. There was conclusive evidence for this effect in the URANS simulations. Unsteady measurements were not available from the experiment, however very similar changes (smaller spanwise fluctuations in radial profiles of local KE loss

coefficient, and lower and broader peaks in circumferential profiles of local KE loss coefficient—characteristic of enhanced mixing close to the TE) were observed in the experimental data and time-averaged URANS data when overhang length became small. This led to the suggestion that this effect was likely also present in the experiment. The mode shift appears to have occurred at slightly longer overhang length in the experimental data than the CFD data.

2. For both experiment and CFD, the longest overhang length tested (6.3% of tangential chord) gave the lowest corrected mixed-out average loss coefficient. The corrected mixed-out average loss coefficient for the centred-ejection type design was 22.1% greater than for the longest overhang in experiment, and 7.7% greater in CFD. We therefore conclude that, for a typical engine component NGV operating at high-subsonic Mach number, SS-overhang designs do provide an aerodynamic advantage over the centred-ejection design.

3. URANS CFD predicted a gradual increase in corrected mixed-out average profile loss coefficient as overhang length was reduced, before plateauing at very short overhang length. The experimental data were largely in agreement with URANS in terms of the trend in mixed-out average profile loss coefficient between TE geometries, but showed an additional +12.6% increase in corrected mixed-out average loss coefficient at intermediate overhang lengths, which was not captured by the CFD. The discrepancy is thought to be caused by shed pressure waves associated with vortex shedding in the transonic range in the experimental data, which are not captured in the CFD simulations (a known limitation of the URANS method). The additional loss arises due to significant thickening of the SS boundary layer.

4. Notwithstanding the boundary layer thickening effect associated with shed pressure waves in the experiment, we observe only small changes in boundary layer loss coefficient in the CFD data. Likewise, the impact of overhang length on secondary and endwall flows was shown to be small, and affected by changes in the precise geometry of the TE-endwall junction. The overall KE loss coefficient characteristic was therefore assumed to be dominated by changes in base pressure drag and aerodynamic changes in the vane passage.

5. Analysis of the base region pressure distributions predicted by URANS shows a substantial fall in PS base region pressure with decreasing overhang length but very little sensitivity of the SS base region pressure. The different behaviours of the PS and SS base regions are explained by changes in the entire vane aerodynamics, associated with upstream migration of a low-pressure region. Interestingly, and contrary to some previous studies, there does *not* seem to be a simple relationship between changes in base region pressure and loss coefficient, suggesting that the overall loss cannot be understood without considering the aerodynamic change within the entire passage. This is an interesting area for future analysis.

6. The mean exit whirl angle fell slightly as SS-overhang length was reduced (differences of up to 0.65°), due to a gradual reduction in the guided turning length provided by the SS-overhang.

NOMENCLATURE

Romans

C_{pb}	Base pressure coefficient, –
c_p	Specific heat at constant pressure, J kg^{-1} K^{-1}
C_x	Axial chord length, m
F	Isentropic capacity function
k	Total trailing edge blockage (defined in Appendix A), m
l	Baseline suction side trailing edge overhang length, m
M	Mach number, –
M_2	Mean vane exit Mach number, –
$\dot{m}$	Mass flow rate, kg s^{-1}
p	Static pressure, Pa
$\overline{p}$	Time-mean value of unsteady pressure signal, Pa
p_0	Stagnation pressure, Pa
$\overline{p_{02}}$	Plane-average downstream stagnation pressure, Pa
$\overline{p_{02}}'$	Mixed-out average downstream stagnation pressure, Pa
p_{0c}/p_{0m}	Coolant-to-mainstream stagnation pressure ratio, –
$\overline{p_2}$	Plane-average downstream static pressure, Pa
$\overline{p_2}'$	Mixed-out average downstream static pressure, Pa
$\overline{p_b}$	Average base region pressure, Pa
r	Radius, m
Re	Reynolds number, –
s	Vane pitch, m
St	Strouhal number, –
T_0	Stagnation temperature, K
t	Trailing edge thickness, m
t_s	Trailing edge slot width, m
Tu	Turbulence intensity, %
v	Velocity, m s^{-1}
w	Passage width, m
x	Axial distance, m
x'	True axial distance, m
y	Distance in slot-normal direction, m

Greeks

α	Cascade stagger angle, degrees
β	Flow turning (or whirl) angle, degrees
$\overline{\beta}$	Circumferential-average whirl angle, degrees
γ	Ratio of specific heats, –
δ	Deviation angle, degrees
δ^*	Boundary layer displacement thickness, m
ζ	Kinetic energy loss coefficient, –
ζ'	Local kinetic energy loss coefficient, –
$\hat{\zeta}'$	Peak local kinetic energy loss coefficient, –
ζ''	Circumferential-average kinetic energy loss coefficient at a particular radius, –
ζ'''	Plane-average kinetic energy loss coefficient, –
ζ''''	Mixed-out average kinetic energy loss coefficient, –
ζ_1''''	Mixed-out average kinetic energy loss coefficient for Geometry 1, –

ζ''''_{BL} Kinetic energy loss coefficient associated with boundary layer flows, –
ζ''''_{corr} Corrected mixed-out average kinetic energy loss coefficient, –
ζ^* Kinetic energy loss coefficient resulting from the model in Appendix A, –
η Row efficiency, –
θ Normalised circumferential distance, vane pitches
θ* Boundary layer momentum thickness, m
λ_2 Lambda-2 criterion, –
ρ Mass density, kg m^{-3}
χ $(\gamma - 1) / \gamma$

Subscripts

0 Stagnation conditions
1 Vane inlet condition / TE Geometry 1
2 Vane exit condition / TE Geometry 2
3 TE Geometry 3
4 TE Geometry 4
c Coolant stream
m Mainstream
ref Reference condition for normalisation
RMS Root-mean-square value
PS Pressure side
s Isentropic condition
SS Suction side
TE Trailing edge coolant stream

Abbreviations

CFD Computational fluid dynamics
ECAT Engine Component AeroThermal facility
HP High pressure
KE Kinetic energy
LES Large Eddy Simulation
NGV Nozzle guide vane
PS Pressure side
RANS Reynolds-averaged Navier-Stokes
RMS Root mean square
SKE Secondary kinetic energy
SS Suction side
TE Trailing edge
TRL Technology readiness level
URANS Unsteady Reynolds-averaged Navier-Stokes

ACKNOWLEDGMENTS

The support of Rolls-Royce plc is gratefully acknowledged.

REFERENCES

[1] Denton, J.D., Xu, L.; 1990; The Trailing Edge Loss of Transonic Turbine Blades; ASME J. Turbomach., Vol. 112(2): 277–285, DOI: 10.1115/1.2927648
[2] Reeman, J., Simonis, E.A.; 1943; The Effect of Trailing Edge Thickness on Blade Loss; RAE Technical Note Eng. 116
[3] Johnston, I.H., Dransfield, D.C., Fullbrook, D.J.; 1967; Experiments Concerning the Effect of Trailing Edge Thickness on Blade Loss and Turbine Stage Efficiency; Ministry of Aviation Aeronautical Research Council Reports and Memoranda No. 3459
[4] Whitney, W.J., Szanca, E.M., Behning, F.P.; 1969; Cold-Air Investigation of a Turbine with Stator-Blade Trailing-Edge Coolant Ejection: Part I–Overall Stator Performance; NASA Technical Memorandum X-1901
[5] Prust, H.W., Bartlett, W.M.; 1974; Cold-Air Study of the Effect on Turbine Stator Blade Aerodynamic Performance of Coolant Ejection from Various Trailing-Edge Slot Geometries: Part I–Experimental Results; NASA Technical Memorandum X-3000
[6] Prust, H.W.; 1975; Cold-Air Study of the Effect on Turbine Stator Blade Aerodynamic Performance of Coolant Ejection from Various Trailing-Edge Slot Geometries: Part II–Comparison of Experimental and Analytical Results; NASA Technical Memorandum X-3190
[7] Melzer, A.; 2018; Aerodynamics of Transonic Turbine Trailing Edges; PhD thesis, University of Cambridge
[8] Melzer, A.P, Pullan, G.; 2019; The Role of Vortex Shedding in the Trailing Edge Loss of Transonic Turbine Blades; ASME J. Turbomach., Vol. 141(4): 041001, DOI: 10.1115/1.4041307
[9] Sieverding, C.H.; 1982; The Influence of Trailing Edge Ejection on the Base Pressure in Transonic Turbine Cascades; Proceedings of ASME 1982 International Gas Turbine Conference and Exhibit; London, UK, 18–22 April 1982, 82-GT-50, DOI: 10.1115/82-GT-50
[10] Kost, F.; Holmes, A.; 1985; Aerodynamic Effect of Coolant Ejection in the Rear Part of Transonic Rotor Blades; AGARD-CP-390, Heat Transfer and Cooling in Gas Turbine Blades, Paper 41
[11] Raffel, M., Kost, F.; 1998; Investigation of Aerodynamic Effects of Coolant Ejection at the Trailing Edge of a Turbine Blade Model by PIV and Pressure Measurements; Experiments in Fluids, 24(5–6), 447–461
[12] Pappu, K.R., Schobeiri, M.T.; 1999; Optimization of Trailing Edge Ejection Mixing Losses: A Theoretical and Experimental Study; ASME J. Fluids Eng., 121(1): 118–125, DOI: 10.1115/1.2821991
[13] Montis, M., Niehuis, R., Guidi, M., Salvadori, S., Martelli, F., Stephan, B.; 2009; Experimental and Numerical Investigation on the Influence of Trailing Edge Bleeding on the Aerodynamics of a NGV Cascade; Proceedings of ASME Turbo Expo 2009, Orlando, FL, USA, 8–12 June 2009, Paper No. GT2009-59910, DOI: 10.1115/GT2009-59910
[14] Rehder, H.J.; 2012; Investigation of Trailing Edge Cooling Concepts in a High Pressure Turbine Cascade: Aerodynamic Experiments and Loss Analysis; ASME J. Turbomach., Vol. 134(5): 051029, DOI: 10.1115/1.4004748
[15] Wang, Y., Zhou, X., Liu, X., Wang, S.; 2016; Influence of Trailing Edge Coolant Ejection Rate and Cut-back Length on Energy Loss and Shockwave Intensity of a Transonic Turbine Blade; Proceedings of ASME Turbo Expo 2016,

Seoul, Korea, 13–17 June 2016, Paper No, GT2016-56859, DOI: 10.1115/GT2016-56859
[16] Saha, R., Fridh, J., Fransson, T.H., Mamaev, B.I., Annerfeldt, M., Utrainen, E.; 2014; Shower Head and Trailing Edge Cooling Influence on Transonic Vane Aero Performance; ASME J. Turbomach. 136(11): 111001, DOI: 10.1115/1.4028024
[17] Kapteijn, C., Amecke, J., Michelassi, V.; 1994; Aerodynamic Performance of a Transonic Turbine Guide Vane with Trailing Edge Coolant Ejection: Part I—Experimental Approach; Proceedings of ASME 1994 International Gas Turbine and Aeroengine Congress and Exposition, Den Haag, Netherlands, 13–16 June 1994, Paper No. 94-GT-288, V001T01A099, DOI: 10.1115/94-GT-288
[18] Uzol, O., Camcı, C.; 2001; Aerodynamic Loss Characteristics of a Turbine Blade with Trailing Edge Coolant Ejection: Part II—External Aerodynamics, Total Pressure Losses and Predictions; ASME J. Turbomach., Vol. 123(2): 249–257, DOI: 10.1115/1.1351817
[19] Johnson, J.D., Fiala, N.J., Ames, F.E.; 2009; Gill Slot Trailing Edge Aerodynamics: Effects of Blowing Rate, Reynolds Number, and External Turbulence on Aerodynamic Losses and Pressure Distribution; ASME J. Turbomach., Vol. 131(1): 011016, DOI: 10.1115/1.2813002
[20] Fiala, N.J., Johnson, J.D., Ames, F.E.; 2010; Aerodynamics of a Letterbox Trailing Edge: Effects of Blowing Rate, Reynolds Number, and External Turbulence on Aerodynamic Losses and Pressure Distribution; ASME J. Turbomach., Vol. 132(4): 041011, DOI: 10.1115/1.3195035
[21] Burdett, D., Povey, T.; 2021; Experimental and Numerical Analysis of Loss Characteristics of Cooled Transonic Nozzle Guide Vanes; ASME J. Turbomach., Paper No. TURBO-21-1040 (*Submitted*)
[22] Kirollos, B., Lubbock, R., Beard, P., Goenaga, F., Rawlinson, A., Janke, E., Povey, T.; 2017; ECAT: An Engine Component Aerothermal Facility at the University of Oxford; Proceedings of ASME Turbo Expo 2017, Charlotte, NC, USA, 26–30 June 2017, Paper No. GT2017-64736, DOI: 10.1115/GT2017-64736
[23] Burdett, D., Hambidge, C., Povey, T.; 2020; Analysis of Ultra-low Uncertainty Gas Turbine Flow Capacity Measurement Techniques; Proc. Inst. Mech. Eng., Part A: J. Power and Energy, DOI: 10.1177/0957650920909718
[24] Burdett, D., Lubbock, R., Povey, T.; 2018; An Impulse Response Technique to Improve the Effective Frequency Response of Pressure Probes; XXIV Biennial Symposium on Measuring Techniques in Turbomachinery; Prague, Czech Republic, 29–31 August 2018; Paper No. MTT2418B23
[25] Burdett, D., Povey, T.; 2021; Analysis of Averaging Methods for Non-Uniform Total Pressure Fields; ASME J. Turbomach. Paper No. TURBO-20-1403 *(Submitted)*
[26] Dzung, L.S.; 1971; Konsistente Mittlewerte in der Theorie der Turbomaschinen für Kompressible Medien; BBC-Mitt., Vol. 58, pp. 485–492
[27] Burdett, D., Goenaga, F., Povey, T.; 2020; Impact of Trailing Edge Geometry on the Flow Capacity of Transonic Turbine Nozzle Guide Vanes; ASME J. Turbomach., Paper No. TURBO-20-1172 *(Accepted)*
[28] Blevins, R.D.; 1990; Flow-Induced Vibration (2nd Edition); Van Nostrand Reinhold Co. Inc., New York, ISBN 978-1-57524-183-8
[29] Stewart, W.L.; 1955; Analysis of Two-Dimensional Compressible-Flow Loss Characteristics Downstream of Turbomachine Blade Rows in Terms of Basic Boundary Layer Characteristics; NACA Technical Note 3515.1955
[30] Deckers, M., Denton, J.D.; 1997; The Aerodynamics of Trailing-Edge-Cooled Transonic Turbine Blades: Part 2—Theoretical and Computational Approach; Proceedings of ASME International Gas Turbine and Aeroengine Congress and Exhibition 1997, Orlando, FL, USA, 2–5 June 1997, Paper No. 97-GT-519, DOI: 10.1115/97-GT-519
[31] Mee, D.J., Baines, N.C., Oldfield, M.L.G., Dickens, T.E.; 1990; An Examination of the Contributions to Loss on a Transonic Turbine Blade in Cascade; ASME J.Turbomach., 114(1): 155–162, DOI: 10.1115/1.2927979
[32] Léonard, T., Gicquel, L.Y.M., Gourdain, N., Duchaine, F.; 2015; Steady/Unsteady Reynolds-Averaged Navier-Stokes and Large Eddy Simulations of a Turbine Blade at High Subsonic Outlet Mach Number; ASME J. Turbomach., Vol. 137(4): 041001, DOI: 10.1115/1.4028493
[33] Lin, D., Su, X., Yuan, X.; 2018; The Development and Mechanisms of the High Pressure Turbine Vane Wake Vortex; ASME J. Eng. Gas Turbines Power, Vol. 140(9): 092601, DOI: 10.1115/1.4039802
[34] Denton, J.D.; 1993; Loss Mechanisms in Turbomachines; Proceedings of ASME 1993 International Gas Turbine and Aeroengine Congress and Exposition, Cincinnati, OH, USA, 24–27 May 1993, Paper No. 93-GT-435, V002T14A001, DOI: 10.1115/93-GT-435

APPENDIX A: METHOD FOR LOSS COEFFICIENT SCALING TO ACCOUNT FOR TRAILING EDGE THICKNESS

In this section we apply a mass-momentum control volume method to determine a scale factor for the mixed-out average loss coefficient to correct the data for each particular TE design (and associated TE thickness) to a reference value of TE thickness. A method of this kind was first presented by Stewart [29], and has since appeared a number of times in the literature for the evaluation of mixing loss downstream of a vane cascade.

Figure 19a shows a control volume ABCDEFA bounding a region of flow downstream of a simplified representation of a staggered NGV cascade with solid (uncooled) TEs (see e.g. Denton [34]). The flow at inlet to the control volume (AB) is considered to be uniform across the free-stream region, with boundary layers characterised by total displacement and momentum thicknesses δ^* and θ^* respectively. The exit flow

(DE) is fully mixed out. The fluxes and pressures across the periodic boundaries (CD and EA) exactly cancel and can be neglected. Here—for simplicity—we assume an incompressible solution with zero deviation angle ($\delta = 0$): this avoids the need to estimate the suction surface pressure downstream of the throat (p_{SS}) and makes the mixed-out average loss coefficient independent of cascade stagger angle [34]. The resulting mixed-out average total pressure loss coefficient is given by

$$\frac{p_{01} - p_{02}}{\frac{1}{2}\rho v_1^2} = \left(\frac{t + \delta^*}{s\cos\alpha}\right)^2 + \frac{2\theta^*}{s\cos\alpha} - \frac{tC_{pb}}{s\cos\alpha} \tag{7}$$

where C_{pb} is the base pressure coefficient, defined as:

$$C_{pb} = \frac{p_b - p_1}{\frac{1}{2}\rho v_1^2} \tag{8}$$

The first term on the right-hand side in equation (7) represents the loss due to the total blockage of the TE and surface boundary layers. The second term represents the mixed-out average loss coefficient of the boundary layers at the TE, and the third term represents the base pressure loss.

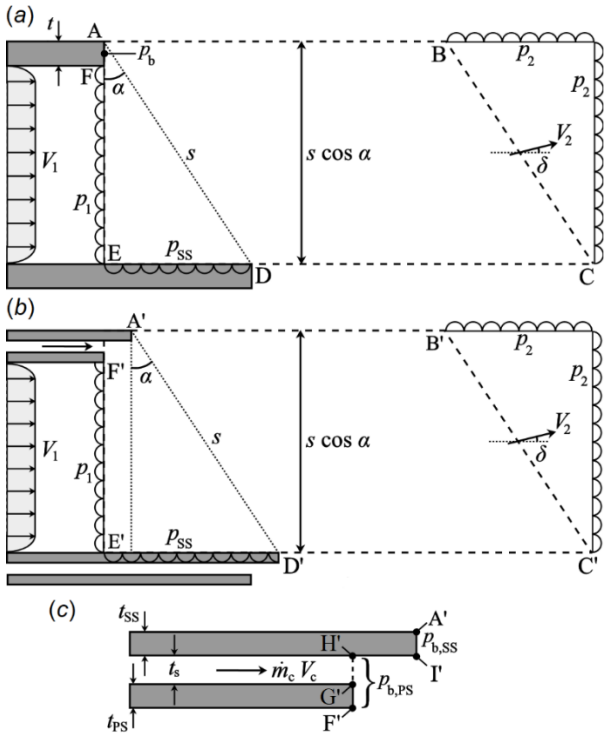


Figure 19: Control volumes for the wake mixing processes downstream of (a) a staggered cascade with a solid TE, and (b) a staggered cascade with a TE slot; (c) inset diagram of the TE geometry for the control volume in (b).

The diagram in Figure 19b shows an adapted control volume in which the solid TE is replaced by separate SS and PS lands, separated by a TE slot, and with an SS-overhang of arbitrary length. A close view of the TE geometry is shown in Figure 19c. The adapted control volume is A'B'C'D'E'F'G'H'I'A'.

In the real cascade, there is a complex static pressure distribution around the base region (see Figure 17). In a complete solution, we would integrate this pressure distribution around the path F'G'H'I'A' to determine the pressure force arising from this control volume boundary. For the purpose of this analysis, however, we define a simplified base region pressure distribution in which a uniform pressure $p_{b,SS}$ acts on the SS TE (A'I'), and a uniform pressure $p_{b,PS}$ acts on the PS TE and the TE slot exit (F'H'). This is justified on the basis that it provides a reasonable first approximation to the base region pressure distributions seen in Figure 17. For each of TE Geometries 1 to 4, we set the values of $p_{b,SS}$ and $p_{b,PS}$ to the CFD-predicted average base region pressures shown in Figure 18a. The pressure force on the inner surface of the SS-overhang (H'I') has no component in the x-direction, and is therefore not required in the case that $\delta = 0$.

We now derive an incompressible solution for the mixed-out average loss coefficient of the adapted scenario (represented in Figure 19b). First applying conservation of mass

$$\rho V_1(s\cos\alpha - k) + \rho V_c t_s = \rho V_2 s\cos(\alpha - \delta) \tag{9}$$

where k is the total TE blockage given by $k = t_{SS} + t_{PS} + t_s + \delta^*$. Then applying conservation of momentum in the x-direction

$$\begin{aligned}\dot{m}_m V_1\left(1 - \frac{\theta^*}{s\cos\alpha - k}\right) + \dot{m}_c V_c - (\dot{m}_m + \dot{m}_c)V_2\cos\delta \\ = p_2 s\cos\alpha - p_1(s\cos\alpha - t_{SS} - t_{PS} - t_s) \\ -p_{b,SS}t_{SS} - p_{b,PS}(t_{PS} + t_s)\end{aligned} \tag{10}$$

Then, taking the assumption that $\delta = 0$ (to simplify the analysis), replacing the mass flow rates $\dot{m}_m$, $\dot{m}_c$ and $(\dot{m}_m + \dot{m}_c)$ in equation (10), with the equivalent terms from equation (9), and rearranging, we get

$$\begin{aligned}p_1 - p_2 = \rho V_2^2 - \rho V_1^2\left(1 - \frac{k + \theta^*}{s\cos\alpha}\right) - \rho V_c^2\frac{t_s}{s\cos\alpha} \\ -(p_{b,SS} - p_1)\frac{t_{SS}}{s\cos\alpha} - (p_{b,PS} - p_1)\frac{(t_{PS} + t_s)}{s\cos\alpha}\end{aligned} \tag{11}$$

A total pressure loss coefficient is derived from the incompressible relations between total and static pressure

$$\frac{p_{01} - p_{02}}{½\rho V_1^2} = \frac{p_1 - p_2 + ½\rho V_1^2 - ½\rho V_2^2}{½\rho V_1^2} \tag{12}$$

then, substituting for $p_1 - p_2$ using equation (11) and simplifying, we get

$$\begin{aligned}\frac{p_{01} - p_{02}}{½\rho V_1^2} = \left(\frac{V_2}{V_1}\right)^2 - 1 + \frac{2k}{s\cos\alpha} + \frac{2\theta^*}{s\cos\alpha} \\ -2\left(\frac{V_c}{V_1}\right)^2\frac{t_s}{s\cos\alpha} - C_{pb,SS}\frac{t_{SS}}{s\cos\alpha} - C_{pb,PS}\frac{(t_{PS} + t_s)}{s\cos\alpha}\end{aligned} \tag{13}$$

where

$$C_{\mathrm{pb,SS}} = \frac{p_{\mathrm{b,SS}} - p_1}{½\rho V_1^2} \tag{14}$$

and

$$C_{\mathrm{pb,SS}} = \frac{p_{\mathrm{b,SS}} - p_1}{½\rho V_1^2} \tag{15}$$

Using the continuity equation (9), we can obtain expressions for the velocity ratios V_2 / V_1 and V_c / V_1, as follows

$$\frac{V_2}{V_1} = \left(1 - \frac{k}{s\cos\alpha}\right)\left(1 + \frac{\dot{m}_c}{\dot{m}_m}\right) \tag{16}$$

$$\frac{V_c}{V_1} = \frac{(s\cos\alpha - k)}{t_s}\frac{\dot{m}_c}{\dot{m}_m} \tag{17}$$

Substituting equations (16) and (17) into equation (13), we get

$$\begin{aligned}\frac{p_{01} - p_{02}}{\frac{1}{2}\rho v_1^2} &= \left(1 - \frac{2k}{s\cos\alpha}\right)\left(2 + \frac{\dot{m}_c}{\dot{m}_m}\right)\frac{\dot{m}_c}{\dot{m}_m} + \frac{2\theta^*}{s\cos\alpha} \\ &+ \left(\frac{k}{s\cos\alpha}\right)^2\left(1 + \frac{\dot{m}_c}{\dot{m}_m}\right)^2 + \frac{2(s\cos\alpha - k)^2}{t_s s\cos\alpha}\left(\frac{\dot{m}_c}{\dot{m}_m}\right)^2 \\ &- \frac{t_{SS}C_{\mathrm{pb,SS}}}{s\cos\alpha} - \frac{(t_{PS} + t_s)C_{\mathrm{pb,PS}}}{s\cos\alpha}\end{aligned} \tag{18}$$

Let us consider the right-hand side of equation (18). The second term is unchanged from equation (7); the final two terms represent the base pressure term from equation (7) split into separate SS and PS parts; the remaining terms represent the total blockage effect of the entire base region, as well as the mixing of the TE coolant flow with the mainstream.

The mixed-out average total pressure, p_{02}, was estimated using equation (18), and used to determine a corresponding KE loss coefficient according to equation (5).

Consider now an adaptation of this theory to compressible flow. Denton and Xu [1] presented a compressible flow solution for the model of Figure 19a. Deckers and Denton [30] extended the analysis to include coolant ejection from a TE slot. A very similar solution procedure was followed in the present study, adapted to represent the model of Figure 19b.

We now express the mainstream mass flow rate at the TE (station 1), and the mixed-out mass flow rate at station 2, using the isentropic capacity function

$$\frac{\dot{m}_m\sqrt{c_p T_{01}}}{p_{01}(s\cos\alpha - k)} = F(M_1, \gamma) \tag{19}$$

$$\frac{(\dot{m}_m + \dot{m}_c)\sqrt{c_p T_{02}}}{p_{02} s\cos(\alpha - \delta)} = F(M_2, \gamma) \tag{20}$$

where

$$F(M,\gamma) = \frac{\gamma}{\sqrt{\gamma - 1}} M\left(1 + \frac{\gamma - 1}{2}M^2\right)^{\frac{\gamma+1}{2(1-\gamma)}} \quad \text{for all } M \le 1 \tag{21}$$

Combining equations (19) and (20) gives the mixed-out average total pressure

$$\frac{p_{02}}{p_{01}} = \left(1 + \frac{\dot{m}_c}{\dot{m}_m}\right)\sqrt{\frac{T_{02}}{T_{01}}}\frac{(s\cos\alpha - k)}{s\cos(\alpha - \delta)}\frac{F(M_1)}{F(M_2)} \tag{22}$$

We consider the isothermal case $T_{02} = T_{01}$, but more generally, T_{02} can be calculated using the energy equation. Again, we make the assumption that $\delta = 0$ to simplify the analysis. We then simultaneously solve equation (22) and the momentum equation in the x-direction, equation (10) (which remains valid for compressible flow conditions), for the mixed-out average Mach number, M_2, and the mixed-out average total pressure, p_{02}, using an iterative process. The mixed-out Mach number, M_2, was iteratively changed, and the corresponding mixed-out conditions of total and static pressure updated using equation (22), until the sum of the base pressure terms, $C_{\mathrm{pb,SS}}t_{SS}/(s\cos\alpha) + C_{\mathrm{pb,PS}}(t_{PS} + t_s)/(s\cos\alpha)$, in equation (10) was equal to the value indicated by the CFD results. This differs from the process proposed in [30] in that known (or predicted) base pressures are used to set the target for the iterative process, rather than being a secondary output from the calculation. We note again that base pressure data was available only from the CFD study. It was therefore necessary to assume that the CFD-predicted base pressure values for each TE overhang length were approximately applicable to the equivalent experiment at the same vane pressure ratio.

Both the incompressible (equation (18)) and compressible (the iterative process described) models were used to estimate mixed-out average total pressure, p_{02}, as a function of SS TE thickness, t_{SS}, for each of the four TE geometries tested in this paper (that is, using base pressure values that approximated the base region pressure distributions in each case, and running the calculation for a range of t_{SS} values). KE loss coefficient, ζ (equation (1)), was then calculated as a function of t_{SS} for each geometry. This leads to four characteristics: ζ_1^* to ζ_4^*. The values of these characteristics at their respective nominal SS TE thicknesses, $t_{SS,1}$ to $t_{SS,4}$, are referred to as the reference values $\zeta_{1,\mathrm{ref}}^*$ to $\zeta_{4,\mathrm{ref}}^*$. We plot the normalised characteristics $\zeta_1^*/\zeta_{1,\mathrm{ref}}^*$ to $\zeta_4^*/\zeta_{4,\mathrm{ref}}^*$ in Figure 20. Plotted in this way, the normalised characteristics pass through unity at the nominal SS TE thickness for that particular geometry.

The abscissa shows t_{SS} normalised with respect to the value for Geometry 1, $t_{SS,1}$. $t_{SS,1}$ is the SS TE thickness which we wish to scale the loss coefficient values for all TE geometries *to*, and is indicated by the left-most vertical dashed line in Figure 20. The other three vertical dashed lines indicate the nominal t_{SS} values for Geometries 2 to 4.

For all geometries, $\zeta^*/\zeta_{\mathrm{ref}}^*$ continuously increases with t_{SS} as expected (rise in TE blockage), and the gradient steadily increases with t_{SS} (in line with equation (18) which shows that the loss due to TE blockage is quadratic in TE thickness).

The scaling factors to correct the loss coefficient for each TE geometry from their uncorrected (i.e. at $t_{SS,n}$) value to their estimated value at thickness $t_{SS,1}$ are read from the ordinate value at which each curve intersects the vertical line $t_{SS} = t_{SS,1}$. These points are marked with circles in Figure 20. We obtain scale factors 0.991, 0.976, and 0.964 using the incompressible model, and 0.985, 0.967, and 0.949 using the compressible model, for Geometries 2, 3, and 4 respectively (the scale factor for Geometry 1 is unity by definition). These values are summarised in Table 7 in the main body of this paper. We note that these scaling functions are intended for correcting for relatively small differences in t_{SS} between our geometries, not for accurate prediction of absolute values of loss coefficient.

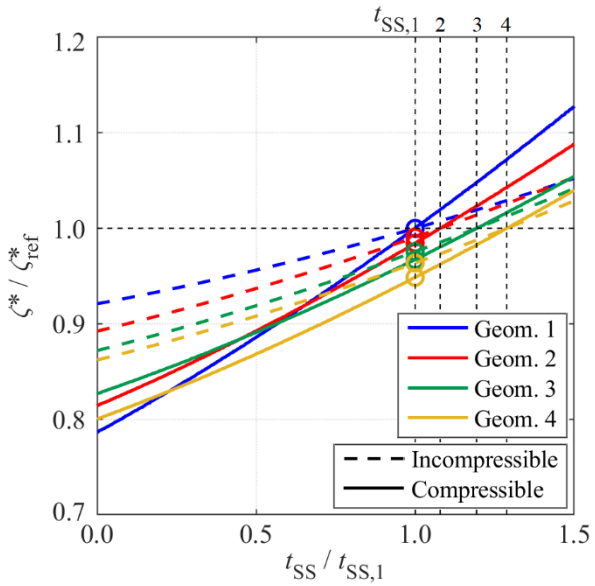


Figure 20: Normalised KE loss coefficient as a function of t_{SS}, for each TE geometry.

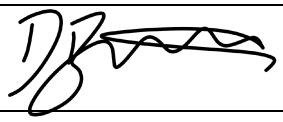
Statement of Authorship for joint/multi-authored papers for PGR thesis

To appear at the end of each thesis chapter submitted as an article/paper

The statement shall describe the candidate's and co-authors' independent research contributions in the thesis publications. For each publication there should exist a complete statement that is to be filled out and signed by the candidate and supervisor **(only required where there isn't already a statement of contribution within the paper itself).**

Title of Paper	Impact of trailing edge overhang length on the loss characteristics of fully cooled transonic nozzle guide vanes
Publication Status	Submitted for Publication
Publication Details	Burdett, D., Povey, T.; 2021; Impact of Trailing Edge Overhang Length on the Loss Characteristics of Fully Cooled Transonic Nozzle Guide Vanes; ASME J. Turbomach., Paper No. TURBO-21-XXXX (*Submitted*)

Student Confirmation

Student Name:			
Contribution to the Paper	Performed experimental testing to collect data, ran numerical simulations, analysed and interpreted experimental and numerical data, developed intellectual arguments, and wrote manuscript.		
Signature		Date	13/02/2021

Supervisor Confirmation

By signing the Statement of Authorship, you are certifying that the candidate made a substantial contribution to the publication, and that the description described above is accurate.

Supervisor name and title: Professor Thomas Povey		
Supervisor comments Dan conducted all of the research himself, and entirely wrote the paper himself, with technical contributions from his supervisor.		
Signature Thomas Povey	Date	19/02/2021

This completed form should be included in the thesis, at the end of the relevant chapter.

8 Discussion and Conclusions

The conclusions drawn from the work presented in this integrated thesis are now summarised.

8.1 Analysis of ultra-low uncertainty gas turbine flow capacity measurement techniques

In this work, the current state-of-the-art in ultra-low uncertainty experimental gas turbine capacity measurement, using semi-transient techniques, is reviewed. Several improvements to the technique (relative to previously published work) are described: modularising the facility working section to allow for rapid interchange of test vane modules; independently metering mainstream and coolant mass flow rates; and optimising the instrumentation to minimise measurement error in vane inlet and exit flow conditions. These changes together (combination of extremely low precision uncertainty, and the capability for rapid interchange of test modules) allow for back-to-back capacity testing of different NGV geometries and for very small capacity changes between those different geometries to be resolved. This makes the experimental setup particularly suited to the academic research environment, facilitating the study and fundamental understanding of capacity sensitivity to secondary influences with much greater flexibility than was previously possible. In this work, this capability is used to examine the effect of cooled trailing edge geometry. The impacts on capacity of other secondary influences including platform leakage flows, vane surface deterioration, and inlet flow disturbances (lean-burn combustor profiles) are all topics of interest for either current ongoing or future research.

Significant consideration is given to the definition of vane capacity in systems with several streams (mainstream, films, and trailing edge coolant) with different inlet conditions of total pressure and temperature. The definition of capacity is somewhat arbitrary, and several alternative definitions can be conceived. From the point of view of determining the absolute value of vane capacity in the engine design process, the precise definition chosen is not of great importance provided it is known and consistently applied (i.e. capacity values are always compared according to the same definition). However, from an academic standpoint certain definitions offer advantages. It is shown that, whilst it is helpful for the coolant stream mass flow rates and

temperatures to be included in the capacity definition (as opposed to referencing the entire flow to the mainstream inlet conditions), the difference arising from the exact way in which this is achieved is minor. Two definitions are proposed, differing in the averaging of inlet total pressure and temperature: either calculating a single capacity term using mass-flow-averaged values of p_0 and T_0, or calculating the mass-flow-weighted sum of individual capacity terms for each stream. These two definitions have similar usefulness in terms of their robustness to changes in the inlet conditions of individual streams—that is, they have approximately equal transportability between, for example, engine and cold experimental rig conditions. However, it is felt that the latter option provides the favoured definition of vane capacity because it offers the possibility—in the correct experiment—to isolate sensitivities to key effects such as trailing edge coolant ejection, by explicitly expressing capacity as a function of the two key controlling pressure ratios. It is argued that this definition may be of more practical use when comparing results from different sources.

A detailed uncertainty analysis is presented, comparing the facility in which the technique was originally developed[1], the current facility, and a proposed future facility in which the uncertainty in capacity has been reduced to a practical limit. The bias errors in the final vane capacity measurement achieved by each of these three facilities are determined to be ±0.535%, ±0.495% and ±0.301% respectively (to 95% confidence). The corresponding precision uncertainties are ±0.028%, ±0.025% and ±0.025% respectively. The current facility therefore yields a reduction in bias uncertainty (relative to the original facility) of ±0.040%. Whilst this may appear a very small improvement, it is important in the context of the engine design and optimisation process. The reduction in bias uncertainty in the current facility with respect to the original facility is shown to arise firstly from reduced uncertainty in vane inlet and exit condition measurements, and secondly from the separate metering of mainstream and coolant mass flow rates. The latter produces a reduction in uncertainty because the separate mass flow measurements are considered to be entirely independent, and the measurement errors are therefore uncorrelated.

[1] Povey, T., Sharpe, M., Rawlinson, A.; 2011; Experimental Measurements of Gas Turbine Flow Capacity Using a Novel Transient Technique; ASME J. Turbomach., Vol. 133: 011005, DOI: 10.1115/1.4000481

This work is intended to serve as a reference point for the current state-of-the-art in experimental gas turbine flow capacity measurement, and also as a manual for best practice in the development and analysis of experiments in this area.

8.2 Impact of trailing edge geometry on the flow capacity of transonic turbine nozzle guide vanes

The capability described above (detection of very small capacity changes between back-to-back tests), alongside a complimentary numerical study, is used to study the influence of varying trailing edge overhang length on vane capacity. A parametric set of trailing edge designs with four incrementally varying overhang lengths is produced on the same set of HP NGV engine parts. In order to do this, an experimental process was pioneered for altering the overhang length of every vane in the fully-annular cascade without removing any vanes from the cascade assembly or compromising its integrity. This process allows us to have confidence that small capacity changes detected between different trailing edge overhang lengths can be attributed to the change in trailing edge geometry without interference from unintended changes in cascade geometry elsewhere (for example, if the cascade assembly were required to be rebuilt, there would inevitably be changes in the precise seating of some vanes and consequently a small shift in capacity, which may be significant in relation to the changes we wish to detect). The combined experimental and numerical study provides the opportunity to understand: the absolute and relative accuracies of the CFD method for vane capacity prediction; the sensitivity of vane capacity to geometry changes of this type; and the fundamental mechanisms for capacity change. The conclusions in each of these areas were as follows:

Absolute and relative accuracies of the CFD method
In terms of absolute values, CFD capacity predictions agree with experimental measurements to within −0.69%, −0.42%, −0.71% and −0.81% for trailing edge Geometries 1 to 4 respectively (see the paper for definitions of the four geometries). The RMS error is 0.67%. Considering that engine designers typically require estimates of NGV capacity accurate to within around 1%, the absolute accuracy of the CFD method for vane capacity prediction is therefore seen to be extremely good. The *relative* accuracy of the CFD (in terms of the capacity *changes* between

trailing edge designs) is good, matching observed experimental changes to within +0.33%, −0.03%, and −0.23% for respective changes of magnitude +1.30%, +2.27% and +2.29%. The proportional RMS error is 12%. The trend in vane capacity with changing trailing edge overhang lengths is very well matched between experiment and CFD. The CFD method was therefore validated for use in aiding understanding of the underlying mechanisms responsible for the observed capacity changes.

Capacity sensitivity to trailing edge overhang length
A monotonic rise in vane capacity is observed as trailing edge overhang length is reduced from Geometry 1 to Geometry 3. Between Geometries 3 and 4, the gradient of the capacity trend reduces significantly (much smaller capacity rise). The experimentally-measured percentage capacity rises with respect to Geometry 1 are +0.97%, +2.31% and +2.52% for Geometries 2 to 4 respectively (nominally equal reductions in overhang length).

Fundamental mechanisms for capacity change.
The fundamental mechanisms responsible for the observed capacity shifts between geometries are analysed in detail. This analysis is split into five areas, drawing the following conclusions:

Coolant stream capacity changes. Changes in both film coolant capacity and trailing edge coolant capacity between trailing edge geometries are shown to be insignificant in relation to the changes in vane capacity.

Changes in surface boundary layers. Vane surface boundary layer displacement thicknesses and associated mass-flow-deficits are estimated (from CFD) at the point of minimum passage width. Whilst there are small differences between the geometries, they are an order of magnitude smaller than the measured capacity changes. It is therefore concluded that this is not a significant mechanism responsible for the vane capacity shift.

Simplistic total pressure loss model. A simple model of the vane is developed which includes a total pressure loss model related to that of Fielding[2], and a repeating area unit to represent changes

[2] Fielding, L.; 1981; The Effect of Irreversibility on the Capacity of a Turbine Blade Row; Proc. Inst. Mech. Eng., Vol. 195, pp. 127–137

in passage area. A typical NGV is a fundamentally 2D system (sonic line far from aligned with the minimum area plane). The intrinsically 1D notion of a throat therefore provides a wholly inadequate description of the system. Even thinking of a particular controlling area is misleading and problematic, due to the necessary arbitrariness with which it must be ascribed in systems of this type. A more complete model of the vane should include several interacting controlling areas, or a more general controlling region. This terminology is considered important as it sets the framework for thinking about the problem. Notwithstanding the inescapable deficiencies of such a simplistic model, the model performs moderately well for very small geometry changes (Geometry 1 to 2) when applied to both experimental and CFD data. For larger geometry changes, the model significantly over-predicts the capacity change, and could not predict the change in behaviour as overhang length became small. Fundamentally, 1D area-loss-models cannot adequately represent the response of the physical system to even small aerodynamic changes and are therefore of little use.

Models of the controlling region. Having dismissed each of the preceding three effects, the flow field through the controlling region is then examined more holistically. Two more complex models of the vane are proposed, representing the two extremes of the tested trailing edge overhang length spectrum. In this case, 'incomplete' means that while these models attempt to convey one important aspect of the interaction in the controlling region (specifically the change in behaviour as overhang length becomes short), they do not, in isolation, explain the capacity trend with reducing overhang length. The first model has two controlling areas, w_{PS} and w_{TE}, which then pass through a third, common controlling area, w_{SS}, which marks the system exit pressure boundary. This model is representative of a long overhang geometry (e.g. Geometry 1). There is a high degree of interaction between the three controlling areas as the characteristic total pressure profile (including the mainstream and trailing edge flows and the wake downstream of the PS trailing edge tip) partially mixes out prior to passing through w_{SS}. If the areas w_{PS} and w_{TE}, and the exit static pressure (at w_{SS}) are all fixed, then the static pressures and mass flow rates at w_{PS} and w_{TE} are dependent on the area ratios w_{PS} / w_{SS} and w_{TE} / w_{SS}, which are in turn dependent

on the overhang length. That is, in this model changing overhang length influences the static pressures and mass flow rates in the controlling region and therefore the vane capacity.

The second model has two independent controlling areas, w_{PS} and w_{TE}, which exhaust to a common static pressure (the system exit pressure boundary). There is no subsequent shared controlling area, significantly reducing the complexity of interaction. This model represents a short or zero overhang geometry (e.g. Geometry 4). Once overhang length becomes sufficiently short to be better represented by the second model, further small changes in overhang length cannot significantly affect the static pressures and mass flow rates at w_{PS} and w_{TE}, and so the vane capacity becomes approximately insensitive to overhang length. It should be noted that we use the term *controlling area* to describe a series of interacting areas, but acknowledge that these areas are arbitrary and are selected only for being easily identifiable and measurable. They are explicitly distinguished from the concept of 'throats' (with their extremely unhelpful connotations of 1D flow) because of the fundamentally 2D nature of the pressure field in typical vane passages.

Aerodynamic flow-field changes. The complex changes in the flow-field between trailing edge geometries are understood by examining full-area and midspan 2D profiles of total and static pressure, Mach number, whirl angle, and local specific capacity, focussing on changes in the controlling region (considered in the framework of the two controlling region models). This analysis is based entirely on CFD data, given the excellent agreement between experiment and CFD for capacity changes between trailing edge geometries. Looking at the controlling region flow field as a whole, as trailing edge overhang length is reduced from Geometry 1 to 3 the static pressure and Mach number fields incrementally shift upstream with respect to the vane passage. Between Geometries 3 and 4, there is almost no further change in the static pressure and Mach number fields. The change in behaviour as overhang length becomes short is in line with a switch between the two schematic models of the controlling region described above (switch-over occurring around the overhang length of Geometry 3).

The data are compared, using the framework of the two incomplete system models, at the controlling areas w_{PS} and w_{SS}. The flow in these planes is fundamentally 2D in nature, and well

described by considering the cross-passage profiles at midspan (with a radial pressure field superimposed). Distributions of static pressure, Mach number and local specific capacity are very similar between all trailing edge geometries when examined at a downstream controlling area (w_{SS}), confirming a similar aerodynamic relationship between pressure distributions at this controlling area and at the far downstream system boundary. When analysed at the w_{SS} plane, the combination of changes in area and local specific capacity poorly reconciles the measured changes in vane capacity, and in particular fail to reflect the change in behaviour as overhang length becomes very short. The distributions of static pressure, Mach number, and local specific capacity at an upstream controlling area (w_{PS}) have far greater sensitivity to trailing edge geometry, due to a complex interaction in the controlling region, analysed as an interaction between two controlling areas. The level of static pressure falls incrementally, and the levels of Mach number and local specific capacity rise incrementally, as overhang length reduces. The combination of changes in area and local specific capacity at this plane very closely reconcile the measured changes in vane capacity between all of the geometries. The difference in capacity reconciliation between the w_{SS} and w_{PS} planes is attributed to w_{SS} planes being affected by the separation downstream of the PS trailing edge tip (the planes are located downstream of the trailing edge slot exit and so some degree of mixing interaction has occurred between the mainstream and trailing edge flows, and importantly for each geometry the w_{SS} plane is located a different distance from the slot exit; whereas the w_{PS} planes are located upstream of the slot exit), something which is not included in the model.

In summary, although the capacity shift between trailing edge geometries *can* be explained using a model which includes changes in area and static pressure at a specific controlling area, a more complete description requires holistic analysis of the aerodynamic change in the entire controlling *region*. Whilst low-order system representations of the type proposed in the paper are tempting (because of their conceptual simplification), they ultimately provide an inadequate description of the system.

8.3 Analysis of averaging methods for non-uniform total pressure fields

This section of work compares representations of average aerodynamic performance parameters—e.g. kinetic energy loss coefficient—including plane-average methods (different flow-weighting schemes) and mixed-out methods. The calculation of average performance parameters is a key part of many studies in the literature, but the exact method by which they are calculated is often given relatively little consideration. It is shown that the choice of method can very significantly influence the apparent results, in some cases obscuring trends in the data. The purpose of this study was to provide guidance for a common practical situation on the accuracy of each method when used to compare two or more experiments, or experiment against CFD.

The methods are compared in terms of their sensitivity to: the axial location of the averaging plane; radial averaging range; and exit Mach number. The underlying physical mechanisms which give rise to the observed sensitivities are discussed. The weighting functions for the plane-average methods (area, volume-flow, and mass-flow-weighting) are strongly influenced by static pressure gradients in the flow. The static pressure field at cascade exit was relatively uniform, but with regions of locally high static pressure directly axially downstream of each trailing edge. Interaction between the total and static pressure fields causes diffusion and acceleration of the flow (flow is diffused as it enters a region of elevated static pressure, and vice versa) and hence changes in flow whirl angle. The high mean exit whirl angle of the flow is shown to generate different alignments of the total and static pressure fields in different axial planes, leading to changes in the local whirl angle distributions between axial planes. Because traverse measurements are made in axial planes (as opposed to streamwise-normal planes), changes in whirl angle distribution affect the volume and mass-flow-rates passing through the traverse plane, and therefore the weighting functions. This effect explains the different axial sensitivities of the plane-averaging methods, as well as the apparently contradictory result that the experimental data has greater circumferential variation in weighting functions compared to CFD.

Plane-averaged KE loss coefficient based on area-averaged total pressure is highly sensitive to axial plane. The axial trend demonstrated in this work is shown to have a large positive peak immediately at the trailing edge (+31.9% above the downstream settled value), and periodic

oscillations over one axial chord length downstream of the trailing edge. The former effect is caused by the over-weighting of the very low momentum wake region, and the latter is caused by the changing influence of the interaction between the total and static pressure fields on the wake characteristics between different axial planes. The data demonstrate that, in this case, the use of an area-weighted-averaging makes it impossible to calculate a meaningful wake mixing rate. Despite the simplicity of area-weighted-averaging (which makes it a common choice in the literature), it is shown to be an extremely poor choice for comparing CFD and experiment or comparing different experiments.

Plane-averaged KE loss coefficients based on mass-flow-averaged and entropy-flux-averaged total pressure are very closely matched in absolute values and axial sensitivity. They slowly and monotonically rise with axial distance downstream of the trailing edge as secondary KE is gradually converted to total pressure loss. The use of one of these methods to represent plane-averaged loss coefficient is recommended where the experimental instrumentation scheme permits and particularly in cases where changes in loss coefficient between different axial planes are to be evaluated. Plane-averaged KE loss coefficient based on volume-flow-averaged total pressure is closely matched to the mass-flow-averaged and entropy-flux-averaged methods, but with small differences near the vane trailing edge. These differences are caused by local density variations where the flow is most non-uniform. Volume-flow-averaging could be said to offer a compromise between axial sensitivity, and practical measurement requirements.

Mixed-out KE loss coefficient values calculated using the Dzung and free-vortex methods are in excellent agreement in terms of absolute values, whilst those calculated from the Amecke and forced-vortex methods are significantly higher than the first two methods. If choosing a single method, the Dzung method might be preferred due to its ease of implementation and unproblematic inclusion of coolant flows. Of course, the user should understand the assumptions inherent in each method and select the one most suited to their application. Mixed-out KE loss coefficients calculated from all four methods are almost independent of axial plane, increasing over one axial chord length downstream of the trailing edge by no more than +3.1%. The data

indicate that the majority of the small rise occurs within a small axial range in which the wakes pass through a local adverse streamwise pressure gradient. This interaction causes an increase in the velocity gradients in the free shear layers at the wake edges, and so increases the entropy generation associated with mixing out of the wake profile. A favourable pressure gradient has the opposite effect, but is very small at the operating point used in these tests. These data show that, whilst mixed-out loss coefficient is approximately insensitive to axial plane, for the purpose of accurately measuring absolute loss coefficient values it is still best to measure in a plane as far downstream of the cascade as the experimental setup allows.

Mixed-out methods provide improved agreement in loss coefficient between experiment and CFD compared to plane-average methods. The average discrepancy (averaged across all data) is 4.3% for mixed-out methods, compared to 14.2% for plane-average methods. Given that local loss coefficient distributions predicted by CFD are evidently under-mixed with respect to experiment, this result is against expectations. This could potentially be explained by the much greater variation in local whirl angle in the experiment, which provides an additional mechanism for mixing loss generation with axial plane. This highlights the importance of using mixed-out methods for comparing absolute KE loss coefficient between experiment and CFD, or in situations where inaccurate prediction of mixing rates is expected.

The axial sensitivity of KE loss coefficient is relatively independent of Mach number—a result that holds true for all plane-average and mixed-out methods. At higher Mach number (particularly above unity), there is a secondary effect that larger gradients of static pressure and density in the flow slightly increase the axial sensitivity (larger amplitude of axial oscillations in both plane-average and mixed-out loss coefficients). Larger gradients amplify the changes in shear layer velocity gradient, and therefore in entropy generation rate. This highlights that, as Mach number becomes supersonic, the choice of averaging method becomes increasingly important. Traverse measurements made close to the trailing edge become more sensitive to the non-uniform static pressure and density fields, which must be well understood.

For the NGV studied, radially averaging over 60% of vane span is shown to be robust for characterising profile loss. This range is sufficiently large to avoid sensitivities due to local radial non-uniformities (particular cooling features etc.) but not so large as to include endwall sensitivities.

8.4 Experimental and numerical analysis of loss characteristics of cooled transonic nozzle guide vanes

A detailed analysis is presented of high-fidelity experimental traverse data downstream of an annular cascade of engine component HP turbine NGVs, in three axial planes. The data address a notable gap in the literature for detailed aerodynamic traverse measurements downstream of *actual engine parts* complete with film and TE cooling flows. They also provide an important benchmark for high-TRL numerical predictions of HP NGV aerodynamic performance. The experimental data are compared with CFD models at a range of fidelity levels (steady and unsteady RANS, excluding and including film cooling). Drawing from the study in the preceding paper, the data are examined using a range of representations: area-surveys of local loss coefficient distribution; circumferential and radial line-profiles; and plane-average and mixed-out average loss coefficient values.

All of the CFD models under-predict the mixing rate of the non-uniform exit flow-field (clearly evident from inspection of area-surveys of local loss coefficient distributions in equivalent axial planes, particularly in the presence of unmixed film flows originating from the last row on the vane PS), and significantly over-predict the average profile loss coefficient (by an average of 17.9%) determined in a given axial plane. Examining the radial profiles of circumferentially-mass-flow-averaged loss coefficient shows that CFD over-predicts loss coefficient by an average (over the profile region) of +2.3%, +22.4%, and +24.9% for uncooled RANS, cooled RANS, and cooled URANS, respectively. From these results, it is inferred that approximately 90% of the over-prediction of loss coefficient by the cooled CFD methods can likely be attributed to over-prediction of the total pressure loss associated with the mixing of surface films. Fully resolving the cooling hole geometries in the mesh, instead of relying on a simple source-terms model, would likely yield a significant improvement. However, this would

of course come at the cost of greatly increased computation time. A potential compromise worthy of trialling in future studies may be to resolve only the rear-most row of film cooling holes on the vane PS which are closest to the traverse planes and are shown to dominate the impact of film cooling on local loss coefficient distributions. Inaccurate prediction of base pressures, boundary layer thicknesses, and the radial migration (down-wash) effect of lower momentum flow are smaller effects contributing to the over-prediction of profile loss coefficient.

The agreement between experiment and CFD for mixed-out loss coefficient was significantly better than for plane-average loss coefficient (average difference of 4.0%, compared with 17.9%—note that the quantitative values in this comparison are slightly different from those in the preceding paper due to the use of different radial ranges). In this case, the greatly improved agreement for total mixed-out loss coefficient arises because the combined under-prediction of plane-average endwall loss coefficient and mixing loss coefficient (the sum of which is the difference between plane-average profile loss coefficient and total mixed-out loss coefficient) is close in size but opposite in sign to the over-prediction of plane-average profile loss coefficient. In axial planes close to the trailing edge, plane-average endwall loss coefficient is well predicted, but the mixing loss coefficient due to residual secondary KE is significantly under-predicted (potentially explained by the very low variation in local whirl angle as described in the preceding paper). In axial planes further downstream, the mixing loss coefficient due to residual secondary KE is accurately predicted, but plane-average endwall loss coefficient is significantly under-predicted (due to under-prediction of the rate of boundary layer growth on the exit duct walls). Again, it is concluded that the use of a mixed-out loss coefficient, ideally covering the full vane span from hub to case endwalls, is strongly recommended when comparing results between experiment and CFD.

Local distributions of loss coefficient downstream of the NGV cascade are examined in detail, with a specific focus on the impacts of geometric features characteristic of complex, 3D engine component vanes. Two key conclusions are drawn from this analysis. Firstly, the experimental wake profile of local loss coefficient has a distinctive radial pattern caused by the

presence of internal rib cooling features within the TE slot. Loss coefficient is locally *reduced* directly downstream of solid ribs inside the slot (lower coolant flow rate) and elevated in the spaces between the ribs (higher coolant flow rate). This suggests that the local coolant flow rates over the vane span are distributed just below the stationary point on the trend of loss coefficient with trailing edge coolant flow rate (described by many studies in the literature). This is a significant effect, and the sort that would be difficult to detect without testing engine components. CFD methods failed to reproduce the deviations in the radial loss coefficient profile, instead predicting locally *higher* loss coefficient directly downstream of the solid ribs, and vice versa (i.e. opposite variation to that observed in experiment). A potential explanation for this discrepancy is proposed in which, whilst the overall coolant mass flow rate is similar, the *local* flow rate between the ribs is inflated due to the under-prediction of mixing and thus moves to a higher point on the trend where loss coefficient is falling. It is felt that there is scope for further investigation of this effect in future, for example analysing CFD predictions with different local distributions of coolant mass flow at the slot exit plane.

Secondly, significant differences in circumferential distributions of local loss coefficient are observed between different radial sections in the same axial plane—in particular, the wake is deeper and narrower near the hub compared to midspan and higher radii, indicating that a notably lesser degree of mixing out has taken place. This effect is caused by the radial variations in lean, sweep and exit turning angle of the 3D vane geometry, which in combination generate a radial distribution of streamwise path length travelled by the flow between the trailing edge and a given axial traverse plane. That is, the wake profile measured near the hub is less mixed out than that at midspan in the same axial plane, because the flow has travelled a shorter distance from the trailing edge. This demonstrates that care must be taken when interpreting data downstream of complex, 3D vane geometries. Whilst traversing in flat axial planes is easy and convenient, it can distort the data significantly. A corollary of this radial variation is that axial trends in characteristic parameters of the wake profiles (both peak local loss coefficient and wake width) measured at different radial heights do not collapse to a common trend when presented in terms of axial

distance. However, when presented as functions of streamwise path length the collapse to a common characteristic is compelling. The characteristic shapes are consistent with the interactions between the total and static pressure fields (causing diffusion and acceleration of the flow, and changes in the velocity gradients in the shear layers) described in the preceding paper. This analysis provides a basis for a wake profile decay model based on local streamwise path length. This is an extremely important outcome for predicting thermal and aerodynamic rotor forcing effects in the complete HP turbine stage.

Finally, the sensitivity of midspan loss coefficient to exit Mach number is examined. In the subsonic range, increasing Mach number reduces both the peak local loss coefficient and the wake width, and consequently the average loss coefficient. When Mach number exceeds unity, an increase in wake width and a corresponding increase in average loss coefficient are observed in the experimental data. In contrast, CFD indicates a continued reduction in wake width, and whilst there is a rise in average loss coefficient, this can only be detected by calculating the *mixed-out* average loss coefficient (line-average loss coefficient at midspan continues to fall). The change in behaviour, and rise in average loss coefficient, as Mach number becomes supersonic is associated with the introduction of a shockwave just upstream of the SS trailing edge. Based on the evidence available, the difference in behaviour between the experimental and CFD data is attributed to two effects. Firstly, the trailing edge shockwave is somewhat poorly resolved in CFD and is therefore 'smeared out' to give a region of adverse static pressure gradient as opposed to a sharp discontinuity. An adverse pressure gradient increases the velocity gradients in the wake shear layers and therefore increases mixed-out loss coefficient. Secondly, the shockwave may in reality be moving unsteadily, causing increased mixing close to the trailing edge for the same level of mixed-out loss coefficient. Such an effect is not expected to be predicted by RANS CFD.

8.5 Impact of trailing edge overhang length on the loss characteristics of fully cooled transonic nozzle guide vanes

Finally, detailed analysis of high-fidelity traverse measurements downstream of fully-cooled transonic HP NGVs is brought together with the comparison of data from the four different TE geometries with progressively shortening SS-overhang length. This study assesses the impact of

TE overhang length on the aerodynamic performance of fully-cooled transonic HP NGVs, and in so doing aims to fill a gap in the literature by performing a very detailed analysis of loss characteristics for a parametric series of well-defined cooled TE designs (constrained by achievable manufacturing limits) using fully-cooled engine parts. The experimental data are compared against unsteady (URANS) CFD results, building on the comparison between these data sets presented in the previous paper. The performance of the four TE designs are compared by examining: local distributions of KE loss coefficient and exit whirl angle; average values of KE loss coefficient; wake mixing rates; base region pressure distributions predicted by URANS; and unsteady wake region pressure signal fluctuations in the URANS data.

The SS-overhang length was changed between the four TE geometries by incrementally removing material from the SS TE tip. Consequently, the SS TE thickness increased due to the taper of the engine part geometry (by as much as +28.8% between Geometries 1 and 4). To make a fair comparison between geometries, a correction is performed to account for the effect of changing TE thickness on TE loss. A failure to ensure a fair comparison between SS-overhang and centred-ejection TE designs in terms of minimum metal thickness (most commonly by instead matching the ultimate TE thickness between the designs, which masks a major advantage of the SS-overhang geometry in practice) is an issue affecting several of the studies in the existing literature. The correction was performed by using a control volume method to estimate KE loss coefficient as a function of SS TE thickness for each of the four TE geometries, using base pressure distributions predicted by URANS to tailor the simplified control volume representation to each case of SS-overhang length, and evaluating scale factors to adjust each design case to a common TE thickness.

A corrected (for changes in TE thickness) mixed-out average profile KE loss coefficient was used as the representation of overall loss. A mixed-out average (as opposed to the average in a particular traverse plane) gives the best representation of overall loss generation by the vane (i.e. both loss already manifest, and inevitable additional loss due to mixing out of secondary KE) and removes the sensitivity to secondary KE at a particular plane. This is particularly important when comparing experimental and numerical data because of the well-known tendency of

URANS to under-predict the mixing rate. Profile loss coefficient values are compared in order to isolate the effect of the change in TE design, having established that secondary and endwall losses do not change significantly with overhang length. The sensitivity of secondary and endwall losses is considered by comparing local distributions of KE loss coefficient in the vicinity of the TE-endwall junctions. The form of the secondary vortex loss cores changes very little with SS-overhang length. The only significant change is a circumferential shift in the location of the hub and case endwall junction loss cores as the overhang length is shortened, due to some vestigial overhang material left in the TE-endwall corner. This is a result of the method used for altering the overhang length in the experimental programme.

The unsteady behaviour of each TE geometry is compared by analysing the temporal variation of the wake region pressure field at strategically-located monitor points in the URANS CFD solutions. Fluctuations in the pressure signal are characterised by the RMS amplitude, and the frequency (expressed as a Strouhal number based on the mean exit flow velocity and the TE thickness). The unsteady characteristics are, for the most part, uniform between three different spanwise locations, providing further confirmation that the effect of changing overhang length is 2D in nature. In Geometries 1 to 3, the magnitude of unsteady pressure fluctuations is small (RMS value of fluctuations varying from 0.06–0.13% of the local time-mean isentropic dynamic head). There is a large rise in the magnitude of unsteady pressure fluctuations (by a factor of approximately 8) in the base region when SS-overhang length becomes short, and a fall in shedding frequency (Strouhal number falls from an average of 0.28 to 0.20). This is attributed to a change in vortex shedding mode, from one in which small vortices are shed at relatively high frequency from the extended SS TE tip (Mode 1 shedding), to one in which larger eddies are shed (at lower frequency) from the entire base region (Mode 2 shedding). Changes observed in the experimental data are seen to be compatible with this conclusion, although unsteady pressure measurements are not available from the ECAT experiment. Smaller spanwise fluctuations in radial profiles of local KE loss coefficient, and lower and broader peaks in circumferential profiles of local KE loss coefficient, are both seen in the experimental data for the shorter overhang lengths, and both of these effects are symptomatic of enhanced mixing close to the TE. However,

the shift in vortex shedding mode appears to occur at slightly longer overhang length in the experimental data than in the URANS CFD data (between Geometries 2 and 3, rather than between Geometries 3 and 4). The change in vortex shedding mode additionally provides explanation for the difference in wake mixing rates between TE geometries. Both the rate of decay of circumferential-peak loss coefficient, and the rate of growth of wake width, are more strongly biased close to the TE in cases where Mode 2 shedding occurs, due to an enhanced mixing rate close to the TE. Aside from this effect, changing overhang length has minimal impact on wake mixing rate.

URANS CFD predicts a gradual increase in corrected mixed-out average profile loss coefficient as overhang length is reduced, before plateauing at very short overhang length. The experimental data are largely in agreement with URANS in terms of the trend in mixed-out average profile loss coefficient between TE geometries, but show an additional +12.6% increase in corrected mixed-out average loss coefficient at intermediate overhang lengths, which is not captured by the CFD. The discrepancy is thought to be caused by shed pressure waves associated with Mode 2 vortex shedding in the transonic range in the experimental data, which are not captured in the CFD simulations (a known limitation of the URANS method). In this hypothesis, the additional loss would arise because pressure waves shed on the PS of the TE propagate towards and impinge upon the SS of the adjacent vane, stimulating rapid thickening of the boundary layer and therefore additional total pressure loss. It should be noted, however, that a shift in vortex shedding mode in the experiment is unconfirmed since no unsteady experimental pressure measurements were made. Whilst URANS may be adequate for predicting the shift in shedding mode (although at slightly different overhang length), it appears to be poor at accurately predicting shed pressure waves. A more sophisticated numerical method (i.e. LES) would give greater insight into this theory.

Notwithstanding the boundary layer thickening effect associated with shed pressure waves, the CFD data indicate only small changes in boundary layer loss coefficient between all four TE geometries. The corrected mixed-out profile KE loss coefficient characteristic is therefore

assumed to be dominated by changes in base pressure drag and aerodynamic changes in the vane passage.

Comparing the base region pressure distributions (static pressure over a path following around the SS TE, TE slot exit plane, and PS TE at midspan) predicted by URANS CFD shows a substantial fall in PS average base region pressure with decreasing overhang length (specifically a substantial fall between Geometries 1 and 3 but very little further drop between Geometries 3 and 4—virtually a mirror image of the trend in vane capacity seen in the earlier study) but very little sensitivity to overhang length of the SS average base region pressure. The different behaviours of the PS and SS base regions are explained by changes in the entire vane aerodynamics, associated with upstream migration of the low-pressure region due to uncovered turning downstream of the TE. This migration is shown in the study of vane capacity presented in the earlier paper. As the SS-overhang is progressively shortened, the location of the SS TE moves upstream. For the specific geometry studied, this displacement is similar in magnitude to the displacement of the static pressure contours. Therefore the sensitivity of SS base region pressure to overhang length is low. In contrast, the location of the PS TE remains fixed as overhang length reduces, and so the PS base region pressure has far greater sensitivity to upstream migration of the static pressure contours. It is tempting to attempt to draw a simple association between a fall in base region pressure and a rise in pressure drag and therefore overall (mixed-out average) loss. Interestingly however, and contrary to some previous studies, preliminary analysis suggests that there is not a simple relationship between the two for these particular geometries: the changes in base region pressure are associated with changes in overall vane aerodynamics at the same nominal operating pressure ratio. The latter effect is significant, suggesting that the overall loss trend cannot be understood by simply considering the base region pressure trend in isolation without considering a more holistic analysis of the aerodynamic change within the entire vane passage. This is an interesting area for future exploration.